ACOUSTIC SENSITIVITY OF THE VESTIBULAR SYSTEM AND MECHANICAL ANALYSIS OF THE TECTORIAL MEMBRANE IN MAMMALS

Gareth Paul Jones

Submitted for the degree of Doctor of Philosophy September 2011

DECLARATION

I hereby declare that this thesis has not been, and will not be, submitted in whole or in part to another University for the award of any other degree.

_____

Gareth Paul Jones

ACKNOWLEDGEMENTS

I thank my supervisors Professor Ian Russell and Dr. Andrei Lukashkin for their invaluable advice and guidance during my time as a DPhil student and in the preparation of this thesis. I also thank the BBSRC for providing the funding for my studentship.

I thank my parents, David and Marylynn Jones, for the continual support and encouragement that they have provided throughout my prolonged stay in education.

I thank my work colleagues (and friends) for creating an enjoyable and supportive working environment, particularly James Hartley for building almost every piece of equipment in our lab (and for knowing how to fix it), Thomas Weddell for his help and advice and Terri Roberts for her skilled assistance in creating sensitive pieces of equipment out of Falcon tubes and insulation tape.

Finally I also thank a number of my friends for kindly contributing their time and efforts to proof reading my work, particularly Nicola Harman, Adele Carvil, Emma Haynes, and also my mother, Marylynn Jones. They have all unwittingly become fully accountable for any typos remaining in this documeant.

PREFACE

The research presented in this thesis is the work of Gareth P. Jones under the supervision of Ian J. Russell and Andrei N. Lukashkin. This work covers two distinct topics related to mammalian hearing; the retained acoustic sensitivity of the mammalian vestibular system and the mechanical properties of the mammalian tectorial membrane (TM).

This thesis contains 7 chapters and 1 appendix. Chapter 1 contains a general introduction to mammalian hearing and to the vestibular system and Chapter 2 describes the materials and methods used in both the vestibular and TM experiments.

Chapters 3-6 are results chapters and include specific introductions to the experiments performed, results and discussion of results. Chapter 3 covers the topic of the acoustic sensitivity of the mammalian vestibular system and was previously published in the Journal of the Association for Research in Otolaryngology in Sept. 2010 (Jones et al., 2010). Chapter 3 is a reproduction of this paper, edited slightly to conform to the formatting of this document. The methods are included in the chapter, with additional methodological detail that was omitted from the published paper included in Chapter 2. The references have also been merged with the main REFERENCES section. For this paper the collection of DPOAE and CAP recordings to assess the hearing of the *Nox3* mice was performed by Dr. Victoria A. Lukashkina. Chapters 4-6 investigate the material properties of the mammalian TM (Jones et al., 2011) and the methods for the experiments presented in these chapters are contained entirely in Chapter 2.

Chapter 7 contains a general discussion of the data presented in this thesis and suggestions for future work in the two topic areas. Chapters 2 and 7 are split in to two sections relating to the vestibular and TM work respectively. All references cited in the text are listed alphabetically in the references section.

APPENDIX 1 contains a video of the dissections performed to isolate the TM from the mouse cochlea.

UNIVERSITY OF SUSSEX

Gareth Paul Jones

Acoustic sensitivity of the vestibular system and mechanical analysis of the tectorial membrane in mammals

SUMMARY

This thesis cover two separate topics related to the function of the mammalian inner ear.

- Acoustic sensitivity of the vestibular system.

Data are presented showing facilitation of the auditory startle response by tones outside the range of the mouse cochlea. The sensation of these low frequency tones is demonstrated to be mediated via the acoustically sensitive sacculus of the vestibular system by data collected from *Nox3*$^{-/-}$ mice. These mice lack the otoconia of the vestibular system and, unlike the wild-type mice, only show facilitation to tones within the range of the mouse cochlea, and not in response to tones <4 kHz.

- The mechanical properties of the tectorial membrane (TM).

The mechanical properties of the TM are investigated using a laser interferometer-based method for tracking the longitudinal propagation of a radially shearing travelling wave in segments of TM isolated from the basal and apical regions of the wild-type cochlea. The properties of these travelling waves (wave propagation velocity and wave amplitude decay) are tracked over a range of stimulus frequencies (1-20 kHz). The viscoelastic properties, shear storage modulus (G') and shear viscosity (η), are estimated over this frequency range and are found to be lower in the apical TM segments compared to the basal TM segments, indicating the apical region of the TM is less stiff than the basal region. These data are compared to data collected from TM segments isolated from the basal cochlear region of three mutant groups, each lacking expression of TM-specific proteins; α-tectorin (*Tecta*$^{Y1870C/+}$), β-tectorin (*Tectb*$^{-/-}$) and otoancorin (*Otoa*$^{EGFP/EGFP}$), using the same laser interferometer-based method. The viscoelastic properties are estimated for each of the mutants and indicate varying degrees of loss of structural integrity in their respective TM segments. Reflective difference between the wild-types and mutants are also observed and compared.

CONTENTS

LIST OF FIGURES

Equations

Tables

Figures

ABBREVIATIONS

ASR	Auditory Startle Response
BF	Best Frequency
BM	Basilar Membrane
CAP	Compound Action Potential
CF	Characteristic Frequency
CN	Cover Net
DPOAE	Distortion Product OtoAcoustic Emission
HB	Hair Bundle
HS	Hensen's Stripe
IHC	Inner Hair Cell
MB	Marginal Band
MET channel	Mechano-Electrical Transducer channel.
OA	Otoconia-Absent
OHC	Outer Hair Cell
OoC	Organ of Corti
OP	Otoconia-Present
OW	Oval Window
Re	Relative to
RL	Reticular Lamina
RM	Reissner's Membrane
RW	Round Window
SD	Standard Deviation
SE	Standard Error
SL	Spiral Limbus
SM	Scala Media
SSM	Striated Sheet Matrix
ST	Scala Tympani
SV	Scala Vestibuli
TM	Tectorial Membrane
VEMP	Vestibular Evoked Myogenic Potential

VARIABLES

α	Amplitude decay constant ($1/\sigma$, m^{-1})
G'	Shear storage modulus (Pa)
η	Shear viscosity (Pa·s)
ρ	Density (Kgm^{-3})
P_M	Probe with background Masker
P_0	Probe Only
r	Longitudinal distance (m)
σ	Space constant ($1/\alpha$, m)
v_r	Velocity of radial shear (ms^{-1})
v_s	Travelling wave propagation velocity (ms^{-1})

1 GENERAL INTRODUCTION

Auditory perception serves a number of important roles in mammals, from a defence against predators to a facilitator of complex social interactions. Terrestrial mammals have extremely diverse hearing requirements that are reflected in the anatomy and perceptual range of their individual ears as well as in their vocalisations. Humans, for example, typically inhabit an acoustic niche between 20 Hz and 20 kHz, whereas some other mammals, such as echolocating bats, can produce and perceive sounds at frequencies over 100 kHz (Vater and Kössl, 2011).

1.1 Anatomy of the mammalian ear

The mammalian ear is organised into three functionally distinct regions; the outer ear, middle ear and inner ear. The outer and middle ears are primarily designed to collect acoustic energy, apply basic filtering, and couple energy on to the fluid filled inner ear (Figure 1.1). The inner ear is responsible for both the sensation of acoustic information through the cochlea, and the sensations of rotation and linear acceleration through the vestibular system. Because of the evolutionary relationship between these two systems the sensations of hearing and balance are inextricably anatomically and functionally linked.

1.1.1 The outer and middle ears

The outer ear is formed of the pinna, a cartilaginous structure that collects acoustic stimuli and funnels it into the auditory canal. The anatomy of the outer ear varies greatly between species, depending on its specific acoustic demands. The large pinnae of species such as humans and mice act as “collecting horns” that increase sound pressure as it travels along the narrowing auditory canal to the tympanic membrane (also known as the ear drum, Figure 1.1) (Geisler, 1998). The pinnae also apply basic filtering to incoming acoustic stimuli; resonance in the ear canal boosts particular frequencies and interference of frequencies around the pinnae provides clues to the elevation of a sound source (Middlebrooks and Green, 1991). In humans, frequencies most prevalent in human speech are selectively boosted (Purves et al., 2001; Pickles, 2008).

The tympanic membrane forms the interface between the outer and middle ears and transmits energy to the ossicles, the bones of the middle ear. The middle ear is a gas filled cavity containing three hinged bones, the malleus, incus and stapes. These bones connect the tympanic membrane to the oval window of the cochlea and together act as an impedance matching device, significantly reducing the reflection of acoustical energy as it moves from the low-impedance gaseous medium of the outer ear to the high-impedance aqueous media in the inner ear (Purves et al., 2001; Pickles, 2008). The malleus and incus rotate together to apply

force to the stapes, which directs pressure into the oval window, creating a pressure difference between the oval and round windows of the cochlea (Pickles, 2008). Efficiency of transmission of acoustic energy through the middle ear depends on the transfer function and varies between species (Moller, 1963; Saunders and Johnstone, 1972). In addition, two muscles connecting to the malleus and stapes can actively affect the transfer function by contracting and stiffening ossicular chain. This muscular feedback can reduce the energy of lower frequency sounds to protect the inner ear from high intensity sounds or to improve the sensation of higher frequencies (Pickles, 2008).

1.1.2 The inner ear

The mammalian inner ear has evolved to serve two distinct purposes. The evolutionarily ancient otolithic organs and semi-circular canals of the vestibular system are responsible for the sensation of gravity and movement; providing the essential and constant feedback required by an individual to navigate in space and control their own body (Angelaki and Cullen, 2008). The cochlea, a more recent evolutionary offshoot of the vestibular system, is adapted to tackle an arguably even more complex task; the sensation of sound. The remarkable intensity range of the cochlea allows the perception of acoustic stimuli louder than a gunshot as well as sounds so quiet they carry only enough energy to cause sub-angstrom displacement of the basilar membrane (well below the magnitude of thermal noise). This sensitivity is achieved while maintaining a frequency resolution of 0.2-0.5% difference and a temporal resolution of 6-10 μs covering up to 10 octaves (Dallos, 1992). These vast and contradictory requirements are accomplished by intricate passive gradients within the cochlea and a complex active feedback system powered by the electrically motile outer hair cells (Dallos, 1992; Lukashkin et al., 2009).

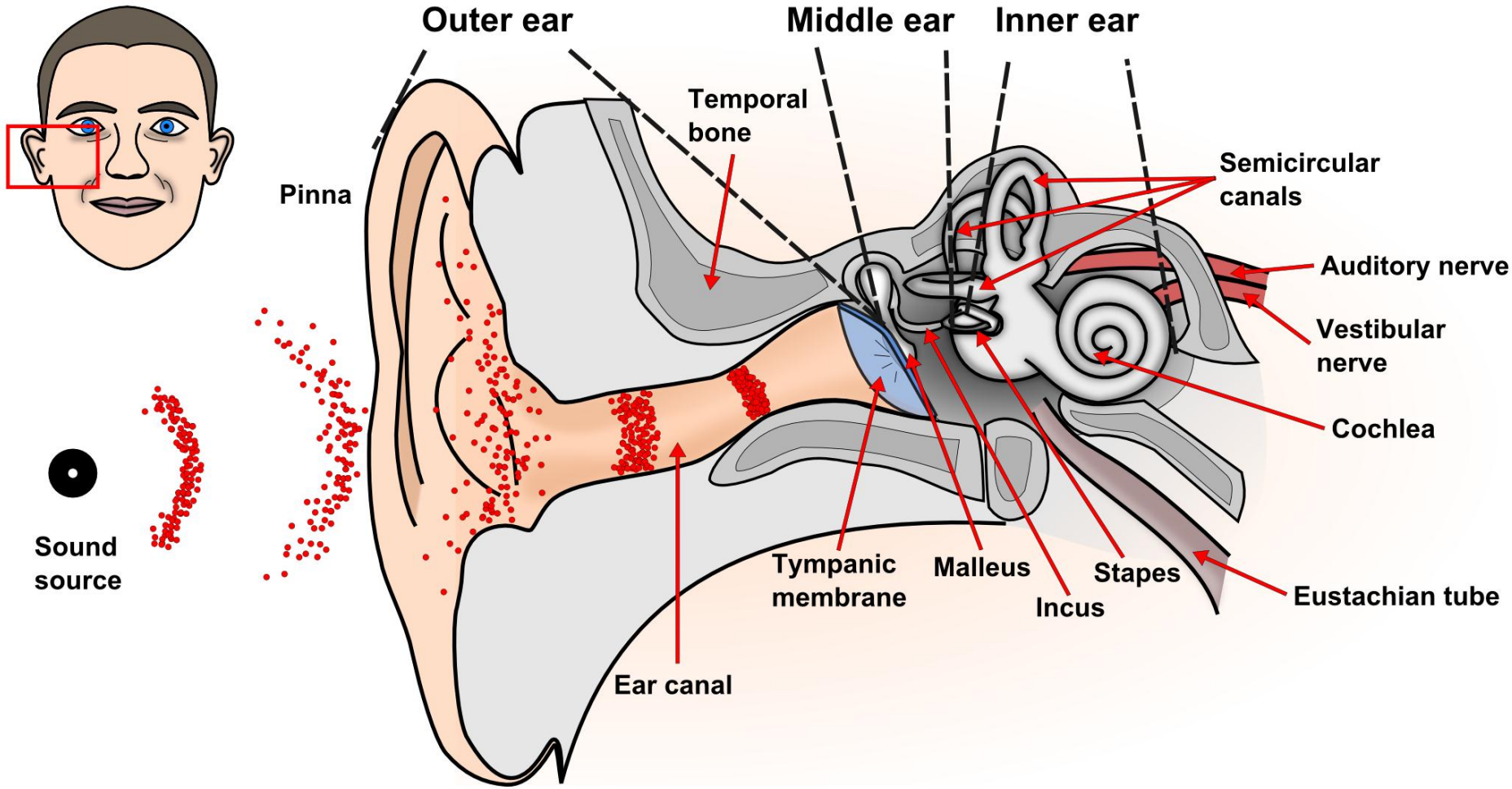

Figure 1.1 The anatomy of the outer, middle and inner ears (right ear, viewed as a cross-section of the head along the frontal plane). Modified from Pickles (2008).

1.2 The vestibular system

The vestibular system is an evolutionary early sensory system located alongside the cochlea within the vestibule of the inner ear. In mammals its primary role is maintaining balance and interpreting movements of the head. In fish and amphibians it also serves as a primitive auditory system, generally with one or two otolithic organs sensing auditory stimuli and further otolithic organs and the semicircular canals maintaining balance (Lowenstein and Roberts, 1951; Popper and Fay, 1973; Popper et al., 1982). Pathologies of the vestibular system, such as vestibular neuritis, can be crippling, with symptoms including nausea, vertigo, and loss of balance. Other senses that are reliant on vestibular feedback, such as vision, can also be seriously disrupted (Baloh, 2003).

1.2.1 Anatomy of the vestibular system

Five separate sensory organs make up the mammalian vestibular labyrinth, all of which contribute to the sensation and control of balance, rotation and acceleration of the head. Although the primary function of the vestibular system in mammals is no longer the sensation of auditory stimuli, there is evidence that it has retained some ability to detect low frequency sounds, particularly via the sacculus, both within and without the frequency range of the cochlea (McCue and Guinan, 1994; Todd et al., 2000; Murofushi et al., 2005b).

Of the five mammalian vestibular organs, the two otolithic organs, the utricle and saccule, detect linear acceleration and the three semicircular canals detect rotation of the head (Fernandez and Goldberg, 1976a; Fernandez and Goldberg, 1976b; Fernandez and Goldberg, 1976c). Each system functions by depolarising or hyperpolarising two types (I and II) of directionally sensitive hair cells that are structurally related to those in the cochlea (Figure 1.2). The type I and type II cells do not correspond to specific afferent neuron populations (Eatock and Songer, 2011) and the functional difference between them remains unclear, although they can typically be distinguished based on their innervation patterns (Ricci et al., 1997) and differing numbers of stereocilia (Moravec and Peterson, 2004). Vestibular hair cells are formed of a cell body with actin filament-based stereocilia and a microtubulin-based Kinocilium protruding from the cuticular plate (Geisler, 1998). Displacement of the stereocilia on the top of the hair cells towards the kinocilium causes polarisation of the cell and increased neurotransmitter release. During periods of no stimulation, the hair cells maintain a significant level of spontaneous activity, which is reduced by movements causing the displacement of the stereocilia away from the kinocilium (and hence hyperpolarisation of the cell) (Purves et al., 2001).

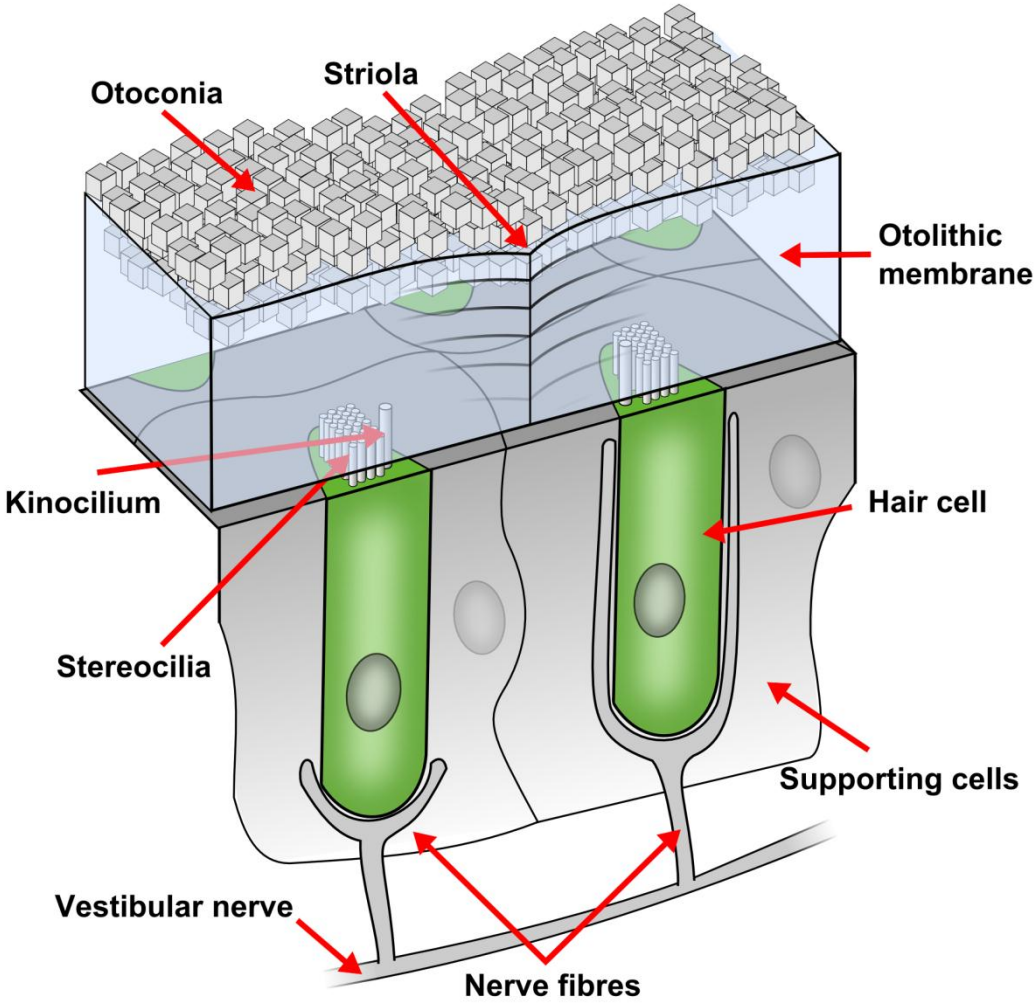

Figure 1.2 Vestibular hair cells in the otolithic organs.

The utricle and saccule both contain otoconia; calcium carbonate particles in the form of calcite, contained within the otolithic membrane. This gives both organs a significant inertial mass, and causes movement of the otoliths to lag relative to the head during linear acceleration. During motion the otolithic membrane shears against the tips of hair cells located in the macula (30,000 in the human utricle and 16,000 in the human saccule) (Watanuki and Schuknecht, 1976). Each hair cell is directionally sensitive and the arrangement of hair cells within the utricle and saccule include areas of oppositely polarised (orientated) hair cells that are divided by an area called the striola. Combining information from the otolithic organs from both sides of the head produces mostly unambiguous movement information – the saccule and utricle are aligned along different planes and each movement produces a unique pattern of excitation and inhibition of hair cells within each. This alignment allows the utricle to respond primarily to movement in the horizontal plane and the sacculus to respond to movement along the vertical plane, including gravity (Kandel et al., 2000; Purves et al., 2001).

Rotation and angular acceleration of the head in any dimension is detected by the three perpendicular semicircular canals, each orientation along a different plane. In humans the semicircular canals are 8 mm long tubes that start and end in the utricle (Purves et al., 2001). Each tube contains endolymph and has a thickened area of epithelium known as the crista ampullaris, which contains a patch of around 7000 hair cells polarised in the same direction. The hair cells are innervated by the relative motion of the endolymph pushing against a gelatinous mass called the cupula, which is anchored (hinged) at one end. As the head rotates, the fluid pushes the cupula, shearing it against the hair cells. Depending on the direction, the hair cells are either depolarised or hyperpolarised. During such rotation the contralateral canals respond oppositely (with depolarisation occurring on the side of the head in the direction of motion).

1.2.2 Acoustic sensitivity of the vestibular system

Although the primary role of the mammalian vestibular system is maintaining balance, some of its end organs were involved in auditory perception before the evolution of the cochlea in lower animals. Teleost fish, for example, have three semi-circular canals and three otolithic organs in the inner ear. Of these, the semi-circular canals and the utricle are devoted to balance and the remaining two otolithic organs, the lagena and sacculus, are involved in hearing. The otolithic organs in these fish are similar to those of land vertebrates, containing an otolithic mass connected to a sensory epithelium with type II mechanosensory hair cells. As with vestibular hair cells in mammals they are directionally specified by the orientation of the kinocilium on each (Popper et al., 1982).

In higher vertebrates the cochlea has replaced the sacculus as a more sophisticated organ of hearing. However, the sacculus does still have projections to the cochlear nerve and, given its evolutionary history, is the most likely candidate for an acoustically sensitive organ in the mammalian vestibular system. Neural responses of possible vestibular origin have already been observed in a diverse range of vertebrates including squirrel monkeys (Young et al., 1977), cats (McCue and Guinan, 1995), pigeons (Wit et al., 1984), guinea pigs (Cazals et al., 1983a; Cazals et al., 1983b; Didier and Cazals, 1989), toads (Moffat and Capranica, 1976) and humans (Todd and Cody, 2000; Todd et al., 2000; Todd, 2001; Sheykholeslami and Kaga, 2002; Todd et al., 2003; Murofushi et al., 2005a; Todd et al., 2008).

The functional purpose of auditory sensitivity of the sacculus in vertebrates is unclear. It is possible that it is simply an epiphenomenon of evolution, existing for the lack of evolutionary pressure for it to disappear. However, as an evolutionarily ancient system, the vestibular

system has extensive connections to a wide range of brain regions, such as the brain stem, cerebellum and hypothalamus. Stimulation of the vestibular system can result in both short-latency reflexes and affective sensations. It is possible that, like other vestibular responses, acoustic sensitivity of the sacculus still has a functional role in mammals (McCue and Guinan, 1994; Todd et al., 2000; Todd, 2001), particularly in species that lack low frequency cochlear-mediated hearing (Jones et al., 2010).

Stimulation of the vestibular system can give rise to a number of unconscious motor reflexes and conscious sensations. During the vestibulo-ocular reflex (VOR), for example, stimulation of the semicircular canals instructs the eye muscles to act antagonistically to the movement of the head, allowing the eyes to continue looking at the same point in space as the head turns, without requiring conscious processing (Robinson, 1968). Other motor reflexes include vestibular evoked muscle contractions, which are discussed below. Certain types of stimulation can give rise to conscious sensations such as nausea and enjoyment. Vestibular stimulation may play an important role in the excitement of theme park rides and, potentially, enjoyment of music with low frequency beats in the range of saccular acoustic sensitivity. Such affective associations may be significant in the context of the auditory startle experiments presented in Chapter 3 (p. 70) – the mice may be able to associate the preceding vestibular stimulation with the impending startle stimuli, leading to a modification of the response. However, conscious perception of vestibular stimulation is not necessarily required for modification to take place, which provides at least two possible mechanisms for modification to occur (Todd et al., 2000).

Evidence also exists that vocal sounds produced by an individual can be within the frequency and level range of the sacculus, raising the possibility that auditory sensitivity of the vestibular system may play a role in the monitoring of self-produced vocalisations (Todd et al., 2000). This may not be applicable to all mammals – mouse auditory vocalisations tend to be well above the frequency range of the sacculus (Willott, 2001; Holy and Guo, 2005), for example, but for some, such as humans, voice pitches have a lower limit of <100 Hz. The level of sound produced in the human vocal tract is unclear, with estimates ranging between 94-130 dB SPL, but with its proximity to the vestibular labyrinth it is possible it is loud enough to be transmitted to the sacculus at a level above threshold. Involvement of the vestibular system in the perception of another's speech is less likely, given that (during normal speech) the sound level reaching the inner ear is likely to be much less than 90 dB SPL at all frequencies (Todd et al., 2000).

1.2.2.1 Vestibular evoked myogenic potentials.

Vestibular evoked myogenic potentials (VEMPs) are short latency responses recorded from muscles in response to high level, low frequency stimuli. Most research into VEMPs has focused on electromyography (EMG) recording from the sternocleidomastoid (SCM) muscle; a positive-negative peak observed at p13-n23 that increases in size as sound pressure is raised (Figure 1.3) (Ferber-Viart et al., 1999). In patients with vestibular system or vestibular nerve pathologies the p13-n23 peak is eliminated. However, the peak is still observed in patients with sensorineural hearing loss. Conversely, longer latency components present in VEMP recordings (n34, p44) from healthy subjects are not present in recordings from patients with sensorineural hearing loss, whereas the p13-n23 peak is (Sheykholeslami and Kaga, 2002). The p13-n23 peak is generated ipsilaterally in response to unilateral stimuli while the n34 and p44 peaks are generated bilaterally following unilateral stimulation, presumably by cochlear afferents (Todd et al., 2000; Wang and Young, 2003).

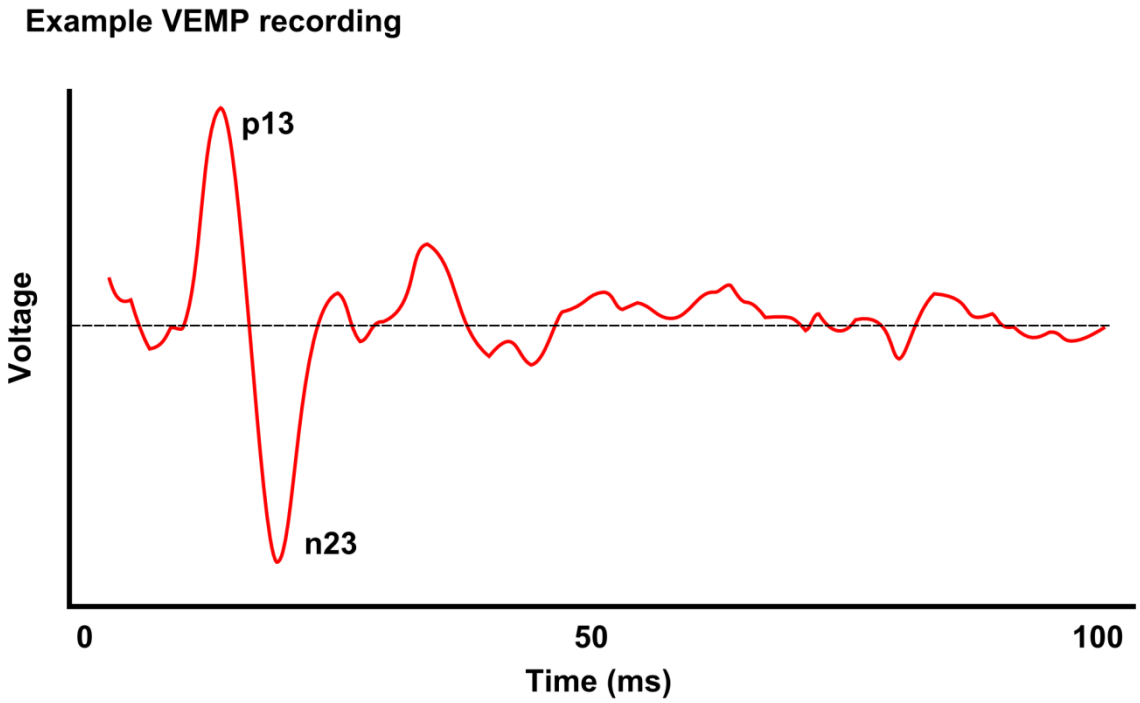

Figure 1.3 Example VEMP recording. Averaged EMG recordings from an individual SCM muscle in response to bilateral stimulation with a 200 Hz, 10 ms tone pulse at 110 dB SPL. The p13-n23 peak becomes visible above 85 dB SPL and increases in amplitude as the sound level increases. Adapted from Todd (2001).

Evidence indicates that VEMPs are generated in the saccular vestibular afferents and travel along an oligosynaptic pathway to the neck muscles. The extremely short latency of the response (~10-20 ms) (Bickford et al., 1964; Cody and Bickford, 1969; Colebatch et al., 1994) indicates the muscular reflex involves no higher processing, similar to other vestibular reflexes (VOR, etc.). A similar response, but affecting other muscles, has also been described in a

patient with Tullio's phenomemon, where auditory stimulation caused contraction of a leg muscle via vestibular sensation (Ferber-Viart et al., 1999). VEMPs are typically recorded while the SCM muscles are held in a constant state of contraction by turning the head contralateral to the side being stimulated. Electrodes on the SCM muscle record the potential changes in the muscle.

Compared to the latency of voluntary muscle contractions (100 ms) and neck muscle contraction during the auditory startle reflex (50 ms), the latency of VEMPs is much shorter (<10-20 ms) (Todd et al., 2000). Unlike the auditory startle response (ASR, Chapter 2.2.1, p. 49), which also causes muscle twitches, the VEMP response can be stimulated at high frequencies without significant habituation. These differences in response latency indicate that different systems are used to generate each response – a low threshold cochlea-mediated system in the case of the ASR, and a higher threshold vestibular-mediated system in the case of VEMPs.

The physiological role of VEMPs is unclear, but it is likely to be related to vestibular reflexes involving the vestibulocollic pathway and cervical muscles. Stimulation of the saccular nerve has been shown to cause excitation and inhibition in neck motor neurons, depending on the side relative to unilateral stimulation (Rapoport et al., 1977). VEMPs, however, are not always observed bilaterally in response to unilateral stimulation, although if involved in head-turning, it would make sense to cause excitation and inhibition of antagonistic muscles. It is important to note that VEMP amplitudes depend on the level of contraction of the muscle when the stimulus is presented, which will of course be unequal unless the head is not rotated, even if the signal is bilateral.

1.2.2.2 Frequency tuning of the sacculus

VEMPs have provided a useful tool for analysing the frequency range of the sacculus in humans. VEMP responses increase linearly with sound pressure level (when the neck muscles are in a constant state of contraction), with the greatest response to frequencies between 300-350 Hz. This response rapidly drops off as frequency increases or decreases and the range is similar to the resonant frequencies of fish swim bladders (412±300 Hz). It has been proposed that frequencies between 50-800 Hz and above 90 dB SPL are capable of evoking continuous and phase locked responses in the saccular nerve (Todd et al., 2000). Another method, involving recording from acoustically responsive irregularly discharging (ARID) vestibular afferents located in the inferior vestibular nerve of the cat, also shows some tuning characteristics. These ARID fibres maintain an irregular firing rate and synchronise in response

to tone bursts of between 100-2500 Hz, with the most responsive frequencies being between 200-1000 Hz, at a threshold of around 90 dB SPL (McCue and Guinan, 1994; McCue and Guinan, 1995).

1.2.2.3 Neural projections

The vestibular system is well connected to the autonomic nervous system; these connections occur at numerous levels, including in the brainstem, cerebellum and hypothalamus. It is possible, given the autonomic nervous system (ANS) is highly developed in Teleost fishes (where the sacculus is one of the primary auditory organs), that these connections still exist between the sacculus and ANS (Popper et al., 1982; Meredith and Butler, 1983).

The vestibular system has afferent projections to four vestibular nuclei; the lateral, medial, superior and inferior vestibular nuclei (LVN, MVN, SVN and IVN, respectively). Fibres from the LVN and IVN, which receive projections from the utricle and semicircular canals, continue along the vestibulospinal tract to anterior horn cells in various levels of the spinal cord and act to co-ordinate motor movements. The sacculus projects to the IVN and MVN, which continue to the vestibulospinal tract and cervical cord, respectively (Mensinger et al., 1997; Purves et al., 2001; Highstein and Holstein, 2006). Evidence from primates shows that lesions of areas of the vestibular ganglion innervating the cochlea in rhesus monkeys causes degeneration of afferent fibres leading to the MVN and IVN (Stein and Carpenter, 1967).

The amphibian auditory system represents a transition between evolutionarily older vestibular-based hearing and newer high frequency systems, and comprises of two papillae responsible for low-mid and high frequency hearing, and an acoustically sensitive sacculus. Both the papilla and sacculus project to the forebrain and midbrain along similar pathways. The saccular projections to the forebrain reach a number of areas involved in reproductive behaviour, including the hypothalamus and striatum. It is hypothesised that these connections are maintained in higher animals and provide vestibular access to reward areas of the brain not directly connected to the cochlea (Todd, 2001).

1.2.2.4 Relevance to mammalian hearing

The behavioural relevance of acoustic sensitivity of the vestibular system may depend on the hearing range of the animal. Humans, for example, can hear 20 Hz and above, so are able to perceive (via the cochlea) low frequency tones that may also stimulate the vestibular system. Conversely the cochleae of mice, which are used as the experimental animals in Chapter 3 (p. 70), are unable to detect tones in the low frequency vestibular range. The frequency range of the mouse cochlea is approximately 4-80 kHz, depending on level. There is large strain

variation, and age variation within some strains. Generally, there are two areas of peak sensitivity that coincide with behaviourally relevant frequency ranges. The area of best sensitivity at lower range is around 10-18 kHz and at ultrasonic frequencies, 40 and 70±10 kHz (Willott, 2001; Müller et al., 2005).

Hearing thresholds vary depending on detection criteria and age; behavioural thresholds tend to be than neural thresholds, of which single unit recordings from inferior colliculus neurons are the most sensitive (Figure 1.4). For the mouse, relative thresholds increase as frequency decreases below ~4 kHz. Figure 1.4, B shows thresholds required to elicit the ASR (which are higher than the threshold of perception at a given frequency). For CBA mice, ABR recordings indicate that frequencies below approximately 4-5 kHz require high levels (>80 dB SPL) to elicit a response, therefore, in the context of the experiments presented in Chapter 3, the masker tones of <3 kHz at <80 dB SPL should not be detected by the cochlea (Müller et al., 2005).

1.2.2.5 Nox3 mice

In order to investigate the involvement of the vestibular system in the results presented in Chapter 3, *Nox3* mice are used. Homozygous *Nox3* mutants lack a functioning copy of the gene encoding NADPH oxidase 3. These mice suffer from impaired otoconial morphogenesis, preventing the development of a fully functional vestibular system, while not impairing development (Paffenholz, 2004) or function (Jones et al., 2010) of the auditory system.

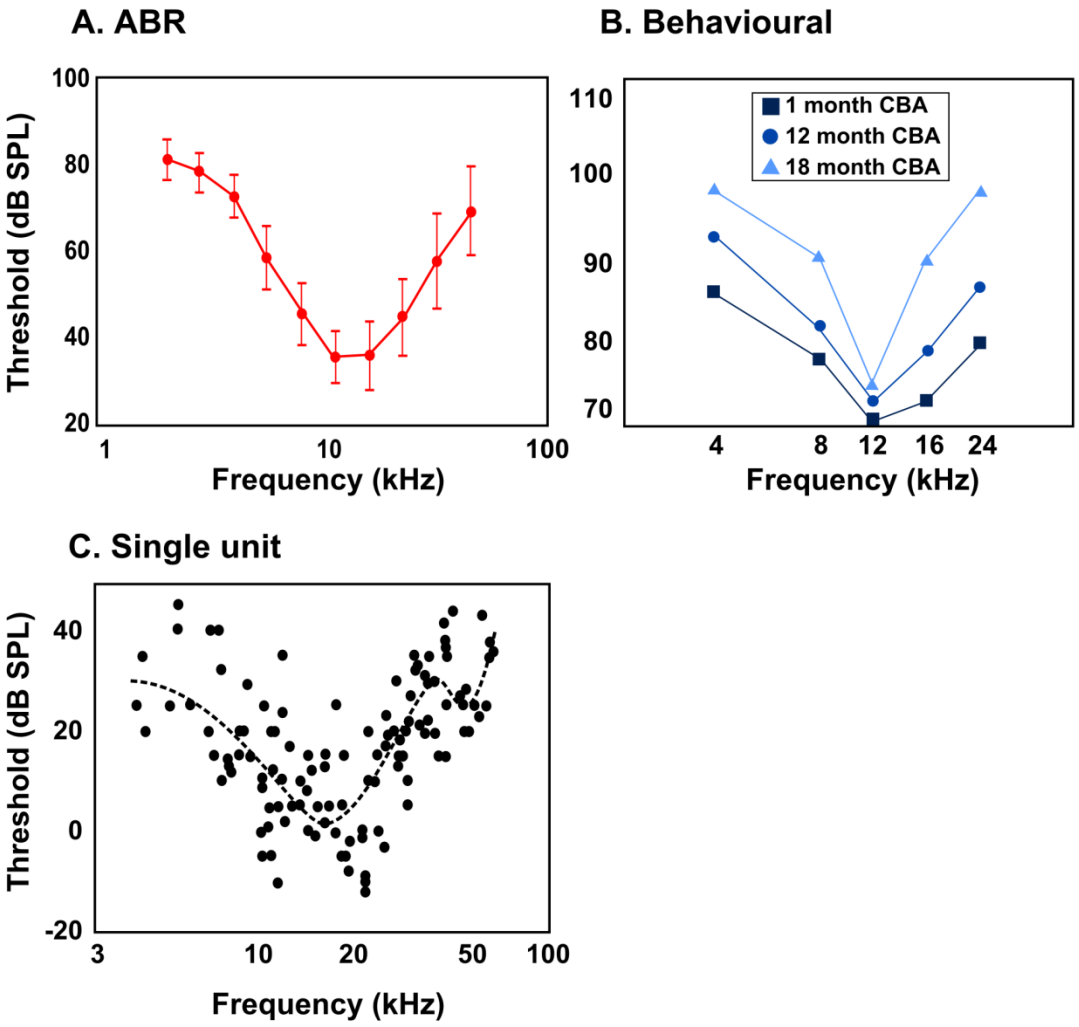

Figure 1.4 Thresholds of hearing. **A**. Thresholds of hearing at different frequencies obtained through auditory brainstem recording (adapted from Müller et al., 2005). **B**. Behavioural thresholds (adapted from Parham and Willott, 1988). **C**. Single unit recordings from individual neurons in the inferior colliculus (adapted from Egorova et al., 2001).

1.3 The cochlea

The mammalian cochlea is a small bony labyrinth located in the inner ear and is a specific evolutionary adaptation of the mechanosensory properties of the vestibular system, tuned to detect higher frequency sound stimuli over a greater level range. It is responsible for the sensation of acoustic energy entering the ear via vibration of its oval window; this energy is transferred from the bones of the middle ear, though the oval window and into the inner ear where it causes relative pressure changes between the fluids of the cochlea. These pressure waves vibrate the basilar membrane (BM) and propagate along the organ of Corti. The organ of Corti is a sensory epithelium containing supporting cells, two types of hair cells (inner and outer) and two acellular membranes (the BM and tectorial membrane, TM) (Figure 1.5). The inner hair cells (IHCs) are excited by mechanical displacement in a similar fashion to the hair cells of the vestibular system, and project afferent connections to the brain. Outer hair cells (OHCs) receive efferent innervation and act as active amplifiers of BM vibration, while also improving frequency and temporal resolution via a complex active feedback mechanism (Purves et al., 2001; Pickles, 2008).

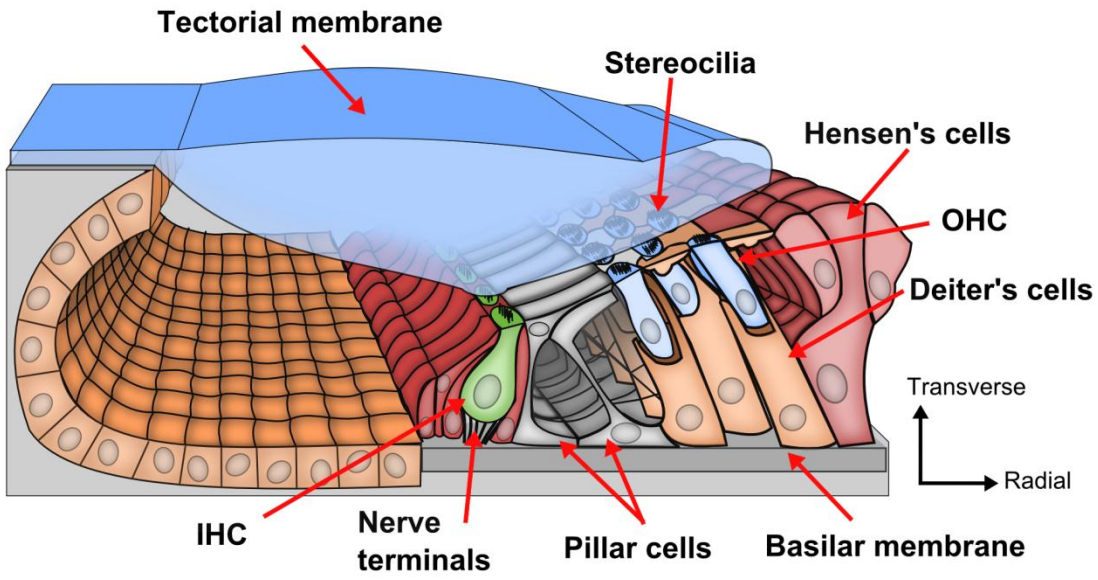

Figure 1.5 Transverse section through the organ of Corti. Adapted from Geisler (1998).

1.3.1 Anatomy and passive mechanical properties

In some vertebrates, in which the frequency requirements of the auditory system are much less demanding than those of mammals (ie., the frequency range is lower and smaller), such as frogs and birds, the spatial decomposition of sound is achieved by electrically tuned sensory hair cells (Crawford and Fettiplace, 1981). However, in mammals the tuning of the tonotopic

map is a mechanical phenomenon, and the anatomy of the cochlea directly influences a number of passive mechanical gradients along its length.

The cochlea is divided into three fluid filled ducts, the scala vestibule, scala media and scala tympani. The scala media, which lies between the other two scalae and contains the organ of Corti, is filled with high K^+, low Na^+ concentration endolymph (Sterkers et al., 1988). It is separated from the high Na^+ perilymph in the scala vestibuli (above) by Reissner's membrane and the scala tympani (below) by the BM. Although the BM is the physical separation between the scala media and scala tympani, it is permeable to perilymph and the reticular lamina forms the chemical barrier (Salt et al., 1986). The scalae spiral longitudinally from the base (near the oval window), around the modiolus (the bony centre of the spiral), to the apex of the cochlea. The oval window is a membranous opening of the scala vestibuli and movement of the stapes footplate displaces the membrane, moving the fluid of the scala vestibuli. At the apex the scala vestibuli and scala tympani join via an opening called the helicotrema, through which remaining fluid pressure passes and moves back along the scala tympani to the round window at the base of the cochlea. The cochlear fluid is incompressible and the round window moves counter phase to the oval window, allowing the movement of fluid and setting up the pressure differences between the scala media and scala tympani that drive the BM during hearing (Figure 1.6). As the impedance of Reissner's membrane is negligible, the pressure in the scala media and scala vestibuli are the same (Voss et al., 1996; Olson, 1998).

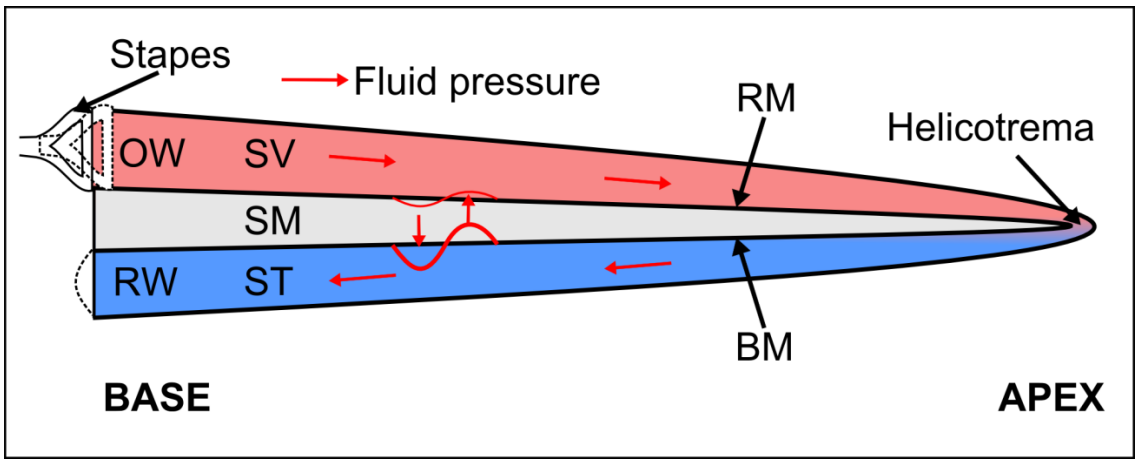

Figure 1.6 Uncoiled cochlea. Pressure differences between the scalae cause a transverse travelling wave to propagate longitudinally along the BM.

1.3.1.1 Organ of Corti

The organ of Corti is located in the high K^+ environment of the scala media, at the division between the scala media and scala tympani. It consists of the cells and structures responsible

for the spatial decomposition and sensation of sound. These include two sets of electromechanical hair cells, the BM and TM, efferent and afferent nerves, and supporting cells. Relative to the organ of Corti, the endolymph of the scala media creates a voltage difference of around +80-100 mV (Békésy, 1952) known as the endocochlear potential. The K^+ concentration of the scala media (and hence the endocochlear potential) is maintained by the stria vascularis (Tasaki and Spyropoulos, 1959) and forms the basis of the ionic current that activates the sensory cells of the organ of Corti during stimulation.

1.3.1.2 Supporting cells

The supporting cells in the organ of Corti are not directly involved in the transduction of auditory stimuli, but do perform a range of essential functions such as maintaining the ionic gradients that power the endocochlear potential (stria vascularis), providing structural rigidity (Hensen's cells and Deiter's cells), modulating OHC electromotility and possibly coupling energy longitudinally (Deiter's cells) (Bohnke and Arnold, 1998; Yu and Zhao, 2009).

1.3.1.3 Hair cells

The hair cells of the organ of Corti can be divided into two morphologically and functionally distinct types, the inner hair cells (IHCs) and outer hair cells (OHCs) (Figure 1.7). A human cochlea contains around 15,000 hair cells, with one row of IHCs situated on the inner edge of the spiral lamina of the organ of Corti and three rows of OHCs at the base, increasing to five at the apex, located towards the outer edge of the spiral lamina (Glueckert et al., 2003; Pickles, 2008). IHCs receive mostly afferent innervation and are responsible for the conversion of mechanical energy in to the neural activity representing the sensation of sound. OHCs receive mostly efferent stimulation and are electromechanically motile, feeding energy back in to the cochlea. On top of both IHCs and OHCs are rows of hair bundles formed of rigid, actin filament-based stereocilia (Flock and Cheung, 1977; Tilney et al., 1980) that deflect in response to fluid movement between the reticular lamina (RL) and Hensen's stripe of the TM (in the case of IHCs) or shearing between the TM relative to the RL (in the case of OHCs). The stereocilia on each hair cell are organised in rows of increasing height, and adjacent rows are coupled to the next by elastic tip links (formed of cadherin 23 and protocadherin 15) and horizontal top connectors (Goodyear et al., 2005; Kazmierczak et al., 2007). Unlike the hair cells of the vestibular system, there is no microtubule-based kinocilium present in fully developed cochlear hair cells. During acoustic stimulation the stereocilia are deflected as a group in the radial direction and pivot around their base in the cuticular plate (Hudspeth and Jacobs, 1979). These movements are directionally sensitive, with deflection of the hair bundle towards the tallest row of stereocilia causing excitation and depolarisation of the cell body

(Figure 1.8) (Flock, 1965; Russell et al., 1986a; Russell et al., 1986b; Russell and Richardson, 1987; Russell et al., 1989; Evans and Dallos, 1993). Displacement towards the modiolus has the opposite effect and hyperpolarises the cell, inhibiting its response. Depolarisation and hyperpolarisation of the cells is mediated by mechanoelectrical transduction (MET) channels located near the tips of the stereocilia (Kros et al., 1992; Beurg et al., 2009). MET channels are non-specific and allow any ions to flow through, as indicated by their resting potential of 0 mV and linear current/voltage relationship (Crawford et al., 1991; Kros, 1996). These channels are hypothesised to be connected to the tip links (Fettiplace and Hackney, 2006), with the probability of MET channels opening increasing during stimulation in the excitatory direction (as tension on the tip links increases) (Pickles et al., 1984; Richardson et al., 2011). The probability of MET channels opening has a sigmoidal dependence on hair bundle deflection (Figure 1.8) (Kros et al., 1992; Russell et al., 1992; Netten and Kros, 2000; Ricci et al., 2003) and in the case of OHCs, the TM biases the hair bundles into their most sensitive position. This bias is lost in mutants lacking a TM (for example *Tecta*$^{\Delta ENT/\Delta ENT}$) and in these mutants OHC hair bundles rest in a similar position as IHC hair bundles (Legan et al., 2000).

The resting potentials of IHCs and OHCs are -45 mV and -70 mV, respectively (Russell and Sellick, 1978; Russell and Sellick, 1983). During excitation of the cell, MET channels open allowing K^+ and Ca^{2+} to flow in down their electrochemical gradients (created by the high concentration of K^+ in the endolymph of the scala media and the +80 mV endocochlear potential). Ca^{2+} has the effect of blocking MET channels and hence may be involved in adaptation in the hair bundles (Ricci et al., 2003).

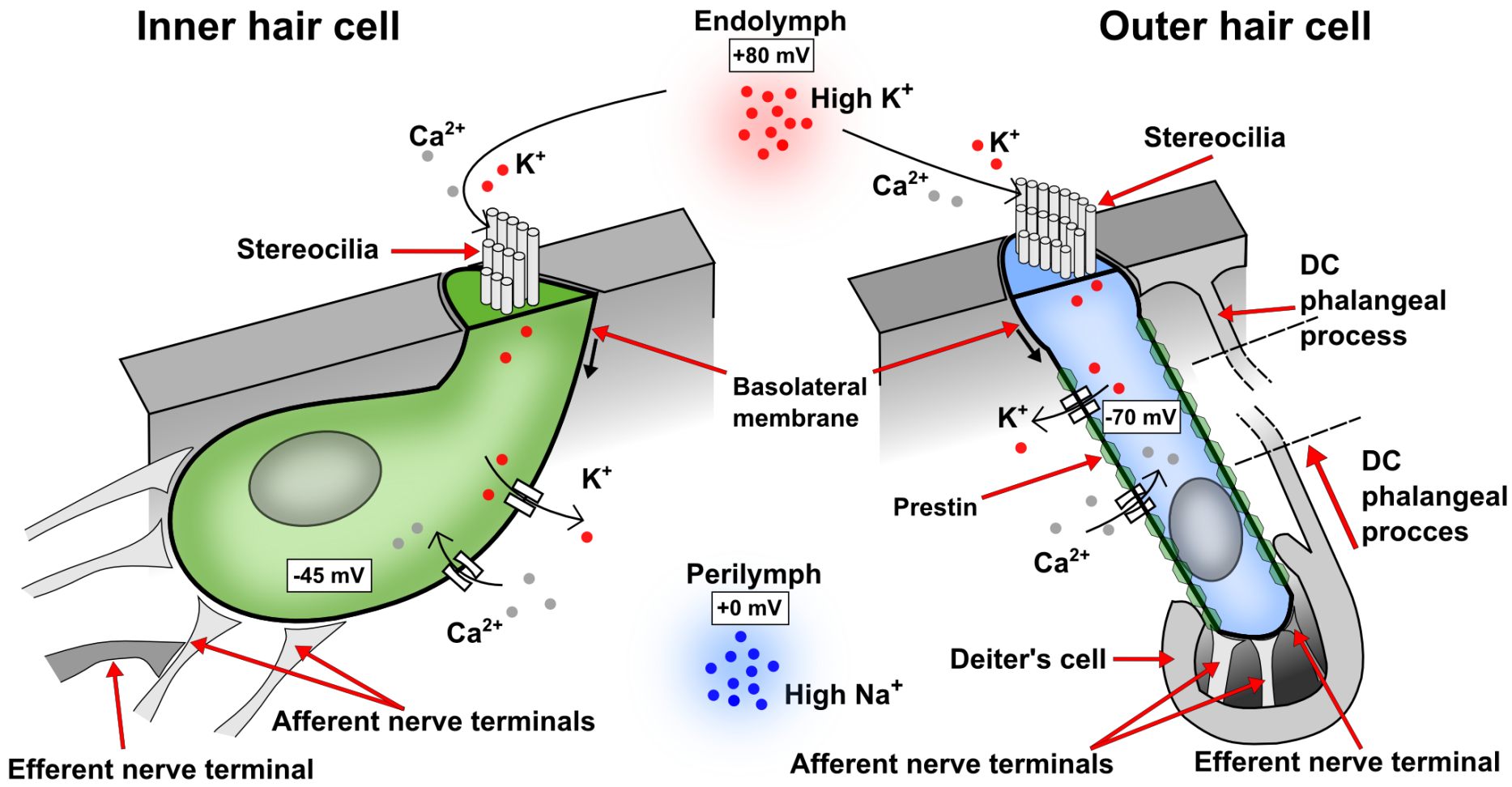

Figure 1.7 Cochlear hair cells. IHCs (left) are responsible for transduction of acoustic vibrations while OHCs (right) are mechanically active and receive mostly efferent innervation.

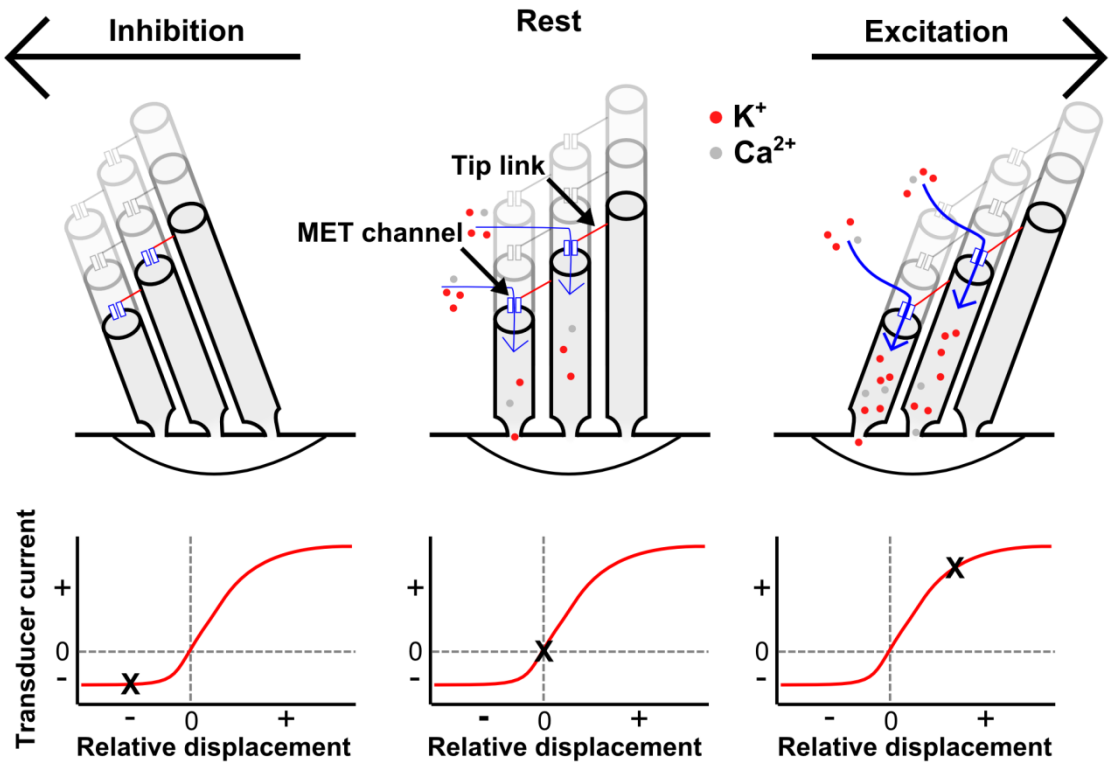

Figure 1.8 Inhibition and excitation of hair bundle stereocilia. Radial shear of the hair bundles causes relative movement between rows of stereocilia, opening or closing the MET channel depending on the direction of shear. For OHCs the "rest" position of the stereocilia are biased into the most sensitive region of their mechanoelectrical transduction curves (Russell et al., 1992).

1.3.1.4 Basilar membrane

Two collagen-rich acellular membranes are present in the organ of Corti, the tectorial membrane (TM, described in detail in Chapter 1.3.1.4, p. 34) and the basilar membrane (BM). Both are involved in the stimulation of the hair cells and the spatial decomposition of frequencies along the length of the cochlea. The resonant properties of the BM vary longitudinally and depend on a number of factors including the stiffness, width and mass of the BM, damping, and the dimensions of the scalae. Stiffness of the BM decreases by two orders of magnitude from the base to the apex of the cochlea (Zwislocki and Cefaratti, 1989), causing higher frequencies to resonate near the base and lower frequencies towards the apex (Békésy, 1960). If transverse vibration of the BM is measured from a specific point, its phase lag (relative to movement of the stapes) is frequency dependant. The dependence of frequency on longitudinal position of the resonant peak spatially links specific acoustic frequencies to specific regions of sensory cells, and provides the tonotopical map that is the basis for frequency discrimination in the cochlea (for example Müller et al., 2005). The point at which a particular frequency resonates on the BM is known as its best frequency (BF) or characteristic frequency (CF), when associated with cochlear amplification (Chapter 1.3.2,

p. 42). In a passive system (for example, in the dead or compromised cochlea used in von Békésy, 1960; Békésy, 1970), in regions of the cochlea basal to the BF (temporally, before the travelling wave reaches its BF), the system is stiffness-dominated, meaning that initially the travelling wave encounters a very stiff section of the BM and causes little displacement (conserving energy). As the wave continues down the stiffness gradient of the BM its velocity decreases and its amplitude increases, dissipating more energy until it peaks at the BF. After this point the system becomes mass dominated, the remaining energy is quickly lost and the wave damped to zero. In such a system, the spatial element has a finite length and the sharpness of the BF peak is directly related to the overall frequency resolution.

1.3.1.5 Tectorial membrane

The TM is located above the hair cells of the cochlea and interacts with OHCs via direct coupling of the longest stereocilia of the hair bundle to the Kimura's membrane on the underside of the TM (Kimura, 1966; Zwislocki, 1986; Goodyear et al., 2005) and is viscously coupled to the IHCs by the subtectorial fluid (Dallos et al., 1972; Freeman and Weiss, 1990a; Freeman and Weiss, 1990b; Freeman and Weiss, 1990c). The importance of the TM in healthy auditory function is well established, although it was traditionally assumed to be simply a surface against which the OHCs could shear during stimulation. However, its composition, mechanical function and effect on the cochlear amplifier, which have been the focus of significant attention in recent years, remain unclear (reviewed in: Freeman et al., 2003a; Freeman et al., 2003b; Richardson et al., 2008; Lukashkin et al., 2010).

1.3.1.5.1 Composition

The TM has a similar structure to connective tissue and is a polyelectrolyte gel. It is acellular, 97% water, and consists of a non-diffusible matrix of charged macromolecules and diffusible ions (Tanaka, 1981). Its dry weight comprises several types of collagen fibres, proteoglycans (charged glycosaminoglycans, GAGs, attached to a protein backbone) and non-collagenous glycoproteins (Figure 1.9) (Freeman et al., 2003b).

The polyelectrolyte nature of the TM (Weiss and Freeman, 1997) means its chemical, electrical, mechanical and osmotic properties are interlinked and its structure is therefore susceptible to environmental changes (Freeman et al., 2003b). Swelling of the TM occurs when the pH is increased ≥9 or decreased ≤6 (Weiss and Freeman, 1997), when osmotic pressure of its surrounding environment is decreased (Shah et al., 1995), or when the concentration of Na^+ in its environment is increased (relative to its usual environment in the scala media). Conversely, increasing osmotic pressure leads to an increased concentration of Ca^{2+} in the

TM's environment and causes the TM to shrink (Shah et al., 1995). The structural dependence on ionic concentration is governed by two mechanisms involving the matrix's macromolecules. Binding of ions to these molecules can affect the conformation of the molecules (and hence the structural organisation of the matrix) or the fixed charge of the macromolecules, altering the osmotic pressure of the gel (Freeman et al., 2003b).

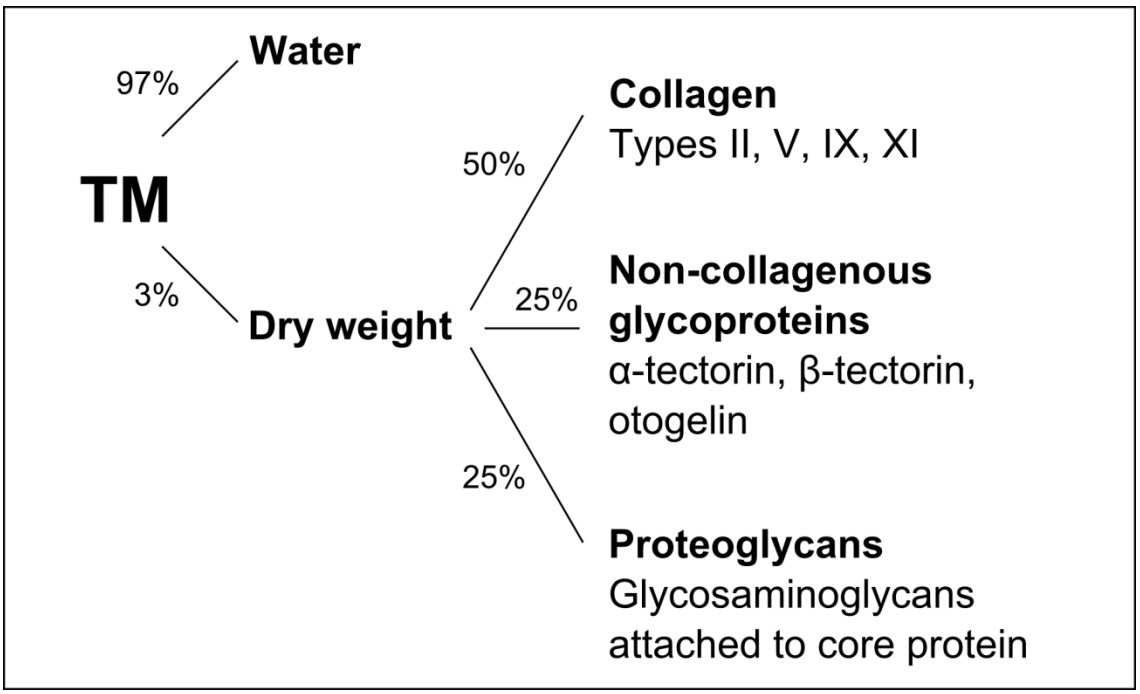

Figure 1.9 The molecular composition of the TM.

Radially the TM is divided into the limbal, middle and marginal zones (Figure 1.10, A-B), with the limbal and marginal zones forming the two connections between the TM and organ of Corti. The marginal zone, consisting of the marginal bank and marginal net, extends over the outer row of OHCs and attaches to the outermost row of Deiter's cells (or Hensen's cells) (Lim, 1972). The limbal zone attachment is mediated by the inner ear specific protein otoancorin and it anchors on the inside of the cochlear turn at the spiral limbus. Henson's Stripe divides the middle and marginal zones of the TM and the marginal zone overlies the IHCs and all rows of OHCs, with the tallest stereocilia on each of the OHCs imbedded in the underside. Although the stereocilia of the IHCs do not contact the TM, the TM is required for them to be effectively driven by the fluid in the subtectorial space (Legan et al., 2000; Nowotny and Gummer, 2006). A cover net of closely packed collagen fibrils sits on top of the TM (Kronester-Frei, 1978), the makeup of which changes slightly over each radial zone (Sugiyama et al., 1992).

1.3.1.5.1.1 Collagen

Collagen fibres make up around 50% of the protein weight of the TM (Figure 1.9) (Thalmann et al., 1986). A number of types of collagen fibres have been identified in the TM, including types II, V, IX and XI (Richardson et al., 1987). Type II fibres contribute to the vast majority of the collagen content and are orientated radially along the length of the TM (Lim, 1972; Kronester-Frei, 1978), forming the structural basis for its radial stiffness. The other collagen types, along with the other macromolecules of the matrix, control the spacing and orientation of the type II fibres.

1.3.1.5.1.2 Proteoglycans

Proteoglycans are heavily glycosylated proteins, containing a core protein and covalently bonded glycosaminoglycans (GAGs) (Kjellen and Lindahl, 1991). Two types of GAGs are present in the mammalian TM, chondroitin sulphate and keratan sulphate (Richardson et al., 1987; Munyer and Schulte, 1991; Thalmann et al., 1993). These molecules are negatively charged by polysaccharide groups and bind cations, providing a mechanism by which they can affect TM mechanics.

1.3.1.5.1.3 Glycoproteins

The glycoproteins of the TM, α-tectorin, β-tectorin and otogelin, make up approximately 25% of the TMs protein weight (Richardson et al., 1987; Cohen-Salmon et al., 1997) and are expressed exclusively in the inner ear. In the TM they organise the striated sheet matrix, which makes the structure of the TM significantly more complex compared to other mammalian polyelectrolyte gels (Goodyear and Richardson, 2002). α-tectorin and β-tectorin are specific to the TM and otogelin is expressed in the TM and the cupulae and otolithic membranes of the vestibular system (Cohen-Salmon et al., 1997; Legan et al., 1997). Over recent years mutations to TECTA and TECTB, the genes encoding for α-tectorin and β-tectorin respectively, have been identified in humans suffering from hereditary hearing loss (Verhoeven et al., 1998). Mouse models for *Tecta*, *Tectb* and *Otog* have allowed for the study of their role in TM morphology and the function of the TM in normal hearing (Legan et al., 1997; Legan et al., 2000; Simmler et al., 2000a; Simmler et al., 2000b; Legan et al., 2005; Russell et al., 2007; Xia et al., 2010) (Chapter 5, p. 107).

1.3.1.5.2 Structure of the tectorial membrane

The structure of the TM varies both radially and longitudinally. Longitudinally the total radial width and the thickness of the TM increase from base to apex; the cross sectional area increases nearly 3x from 1845 μm^2 in the base to 5278 μm^2 in the apex (Russell et al., 2007). Of

the radial divisions of the TM, the limbal zone is the widest (radially) at ~45 µm in the base (Gueta et al., 2007) and the thinnest (transversally) at ~10 µm thick (Ghaffari, 2008). *In vivo* the inside edge of the limbal zone attaches to the spiral limbus of the organ of Corti. The middle zone is ~30 µm (Gueta et al., 2007) wide in the base and is the thickest zone, increasing from 21.6 µm thick to 36.4 µm in the apex (Russell et al., 2007). The marginal zone overlies the reticular lamina and the tallest stereocilia of the OHCs imbed into Kimura's membrane on the underside of the TM (Kimura, 1966). In the base the marginal zone is ~13 µm wide (Gueta et al., 2007) and tapers in thickness from ~20 µm at the interface between the middle and marginal zones to ~10 µm at the marginal edge (Figure 1.10).

1.3.1.5.3 Mechanical and viscoelastic properties of the tectorial membrane

The radial and longitudinal changes in the structure of the TM correlate with changes to its mechanical properties. The stiffness and mechanical properties of the TM have been measured *in vitro* (Békésy, 1953; Békésy, 1960), *in vivo* (Zwislocki et al., 1988; Zwislocki and Cefaratti, 1989), in isolated preparations (Freeman et al., 2003a; Freeman et al., 2003b; Shoelson et al., 2004; Gueta et al., 2006; Ghaffari et al., 2007; Ghaffari et al., 2010), and *in situ* in a hemicochlea preparation (Richter et al., 2007). The methods used to assess stiffness have involved probing the TM (Békésy, 1953; Békésy, 1960; Zwislocki and Cefaratti, 1989; Shoelson et al., 2004; Gueta et al., 2006; Richter et al., 2007), vibration with a magnetic bead (Abnet, 1998; Abnet and Freeman, 2000) and vibration at auditory frequencies (Ghaffari et al., 2007; Ghaffari et al., 2010). Békésy (1953) was the first study to note that the TM had both elastic and viscous properties.

Anisotropy of the TM is one of the defining features of the mammalian cochlea (Gavara et al., 2011). Data from atomic force microscopy (AFM) probing studies show that both the transversal stiffness and radial stiffness of the TM reduce from base to apex (-4.0 $dBmm^{-1}$ and 4.9 $dBmm^{-1}$, respectively) (Richter et al., 2007). This longitudinal reduction in stiffness occurs mostly in the marginal zone, with Young's modulus decreasing from 210±5 kPa to 24±4 kPa, base to apex, whereas the stiffness properties of the thinner limbal zone and the thicker middle zone (relative to the marginal zone) do not change longitudinally (Gueta et al., 2006). Radially stiffness varies, with the limbal zone being the stiffest and the middle zone the most compliant. In the marginal zone (where stiffness varies longitudinally) it is within the same order of magnitude as the stiffness of the OHC hair bundles along the length of the cochlea (Shoelson et al., 2004; Gueta et al., 2006).

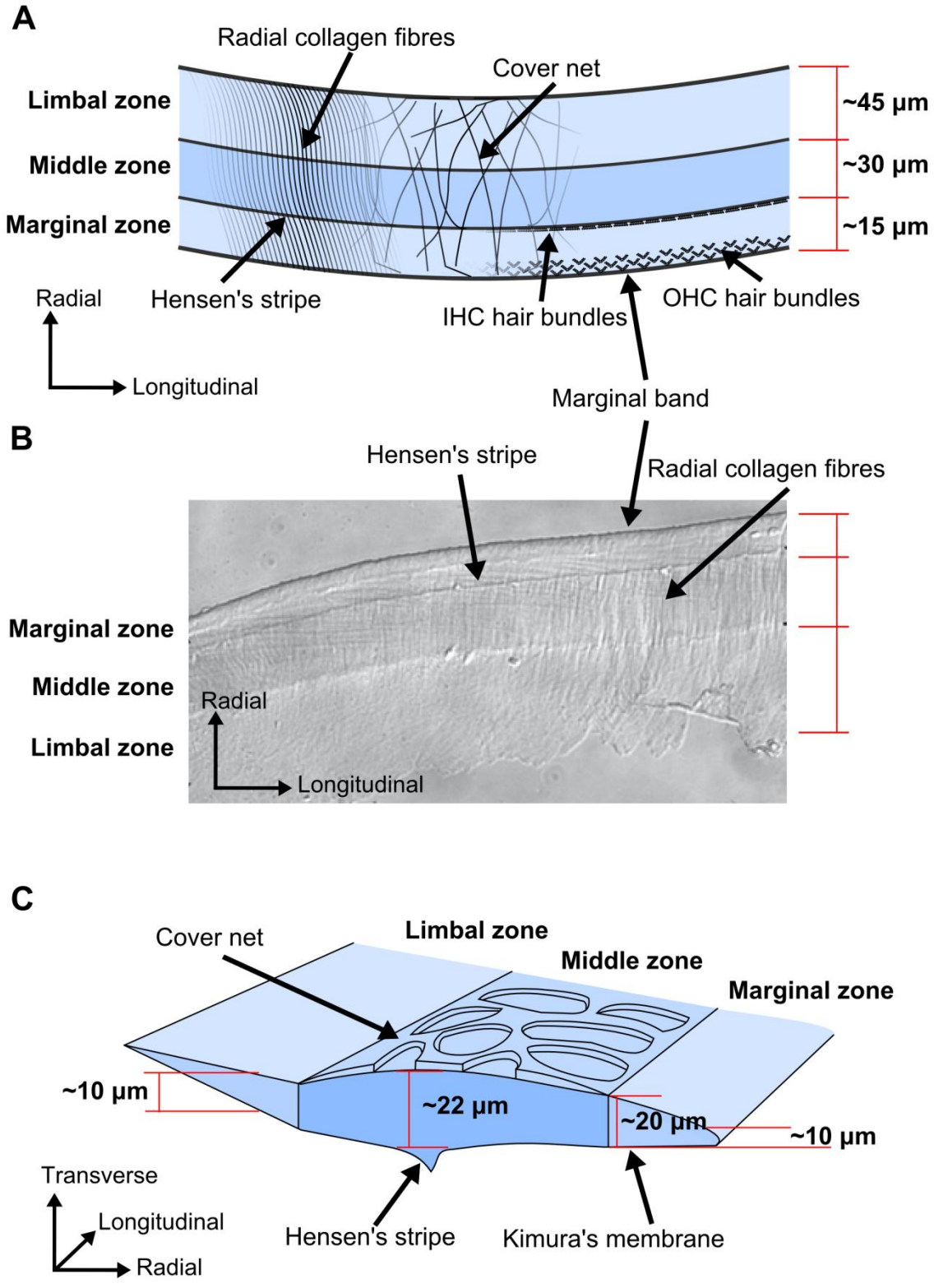

Figure 1.10 The structure of the TM. **A**. From above. **B**. From above (adapted from Gueta et al., 2007). **C**. Transverse section.

However, there are several complications to the probing methods; probing the TM *in situ* not only tests the compliance of the TM but rather it's combined compliance with the other structures in the organ of Corti and probing of isolated preparations may also test the compliance of the surrounding environment (particularly in the case of the thin limbal zone). Additionally because of the viscoelastic nature of the TM (Abnet and Freeman, 2000; Freeman et al., 2003a; Freeman et al., 2003b; Ghaffari et al., 2007) its properties are dynamic and change depending on the frequency, amplitude or velocity of stimulation (in a similar fashion to thixotropic materials such as custard). Static and quasistatic measurements may not give an accurate representation of TM properties at higher frequency stimulation, particularly compared to the higher frequency ranges of mammalian hearing.

1.3.1.6 Anatomical and mechanical gradients in the cochlea

Significant mechanical stiffness gradients occur both radially and longitudinally in the organ of Corti (Figure 1.11). Radially the stiffness of the supporting structures ensures that transverse movement of the BM results in minimal movement of the IHCs, while maximising the movement at the OHCs. Longitudinally the overall stiffness of the organ of Corti reduces from base to apex. This correlates with the equivalent stiffness changes in the BM and the TM (Richter et al., 2007) and also a decrease in hair bundle stiffness in both sets of hair cells (Strelioff and Flock, 1984). The longitudinal gradients in the TM (discussed in Chapter 1.3.1.5.3, p. 38) set up the mechanical basis through which the TM can resonate at reducing frequencies from basal to apical positions, in a similar fashion to the BM, allowing the TM to act as a second frequency analyser.

In addition to base to apex reduction in hair bundle stiffness, the length of the hair bundles of IHCs and OHCs increases while the number of stereocilia in each hair bundle decreases (Lim, 1986; Davis, 2003). Functionally this means that in the base there are more, shorter stereocilia composing each hair bundle. These hair bundles are stiffer but are more sensitive, with greater angular rotation of the shorter hair bundle occurring from the same amount of transverse BM vibration than compared to the longer hair bundles in the apex. The larger number of stereocilia in basal regions counteracts the loss of MET channels (and subsequent smaller transducer currents) resulting from the stereocilia being shorter. As a consequence of the greater overall number of stereocilia and larger individual channel conductance in the basal region (Ricci et al., 2003; He et al., 2004), mechanotransduction currents are larger (and adapt more quickly) than in the apical region (Fettiplace and Ricci, 2003). The number of rows of OHCs varies between species, but in humans the number of rows increases from three to five from the base to apex. The length of the OHCs also increases base to apex as the angle of the

reticular lamina relative to the BM increases (Lim, 1980; Brownell et al., 1985). This length increase causes an increase in membrane capacitance (Davis, 2003).

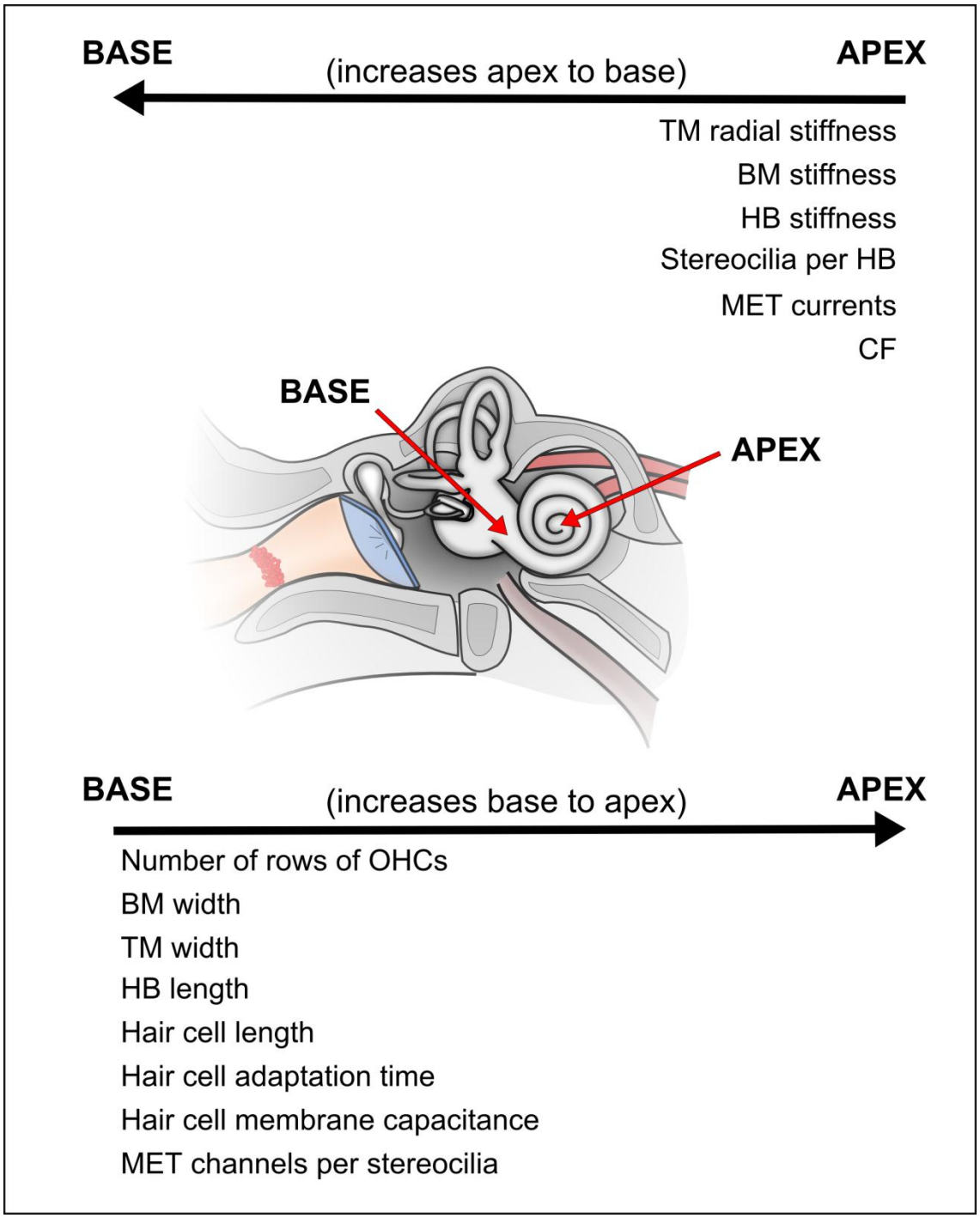

Figure 1.11 Anatomical, mechanical and functional gradients in the cochlea.

1.3.2 Active sensation of sound

During acoustic stimulation the BM is driven by the pressure differences between the scala media and scala tympani; a transverse, longitudinally propagating travelling wave is established by higher pressure in the scala media pushing downwards on the BM and higher pressure in the scala tympani pushing upwards (Figure 1.11). This travelling wave is deconstructed into its composite frequencies by the BM, with maximum transverse displacement of the organ of Corti occurring at the CF of a given BM position and decaying rapidly thereafter. Changes in the mechanical properties of the BM along the length of the cochlear mean that different frequencies resonate in different spatial locations; higher frequencies cause the BM to resonate near the base of the cochlea, and lower frequency sounds cause resonance further towards the apex of the cochlea. Although the passive structural gradients provide the basis for this frequency analysis, they cannot alone account for the frequency, temporal and level sensitivity observed in the cochlea *in vivo.*

A number of models of passive sharpening mechanisms have been proposed (review: Nilsson, 1978), however, data showing differences between healthy and compromised cochleae (Ruggero and Rich, 1991; Robles and Ruggero, 2001) and observations of evoked and spontaneous otoacoustic emissions (Kemp, 1978; Kemp and Chum, 1980; Zurek, 1981) indicate the existence of an active component of hearing. This concept was first suggested in 1948 (Gold, 1948), and later termed the “cochlear amplifier” (Davis, 1983). Active feedback requires amplification (or negative damping) of transverse BM vibrations to be effective (Russell et al., 1992; Nilsen and Russell, 1999; recent review: Ashmore et al., 2010). Direct evidence for cycle-by-cycle negative damping (Lukashkin et al., 2007) and power gain (Ren et al., 2011a) has been demonstrated in the mammalian cochlea. Such an amplification system is required to overcome viscous damping and to apply gain to low level stimulation (while possibly also compressing high levels of stimulation), without compromising frequency or temporal resolution. The exact mechanism by which active mechanical feedback can boost levels is a matter of debate, but if this amplification occurs only near the CF (Russell and Nilsen, 1997; Ren et al., 2011b), rather than the entire cochlear partition between the base and CF (Neely and Kim, 1983), it may be also be involved in frequency tuning; recent experimental evidence from *Tectb*$^{-/-}$ mice has shown that reducing longitudinal coupling of OHCs (and hence reducing the spatial extent of the amplifier) sharpens frequency tuning (Russell et al., 2007).

1.3.2.1 Force generation

Significant evidence exists that the source of the energy added to the cochlear amplifier is the OHCs, but the method of force generation is still a matter of debate between two possible, not

necessarily mutually exclusive, mechanisms; evolutionarily conserved hair bundle motility and prestin-based somatic motility.

In non-mammalian land vertebrates, hair bundle motility, where the stereocilia "push back" with the MET channel closing mechanism, is the sole feedback mechanism. Two forms of this mechanism exist; slow myosin motor based and fast Ca^{2+} dependant pathways affecting the mechanotransducer. Spontaneous oscillation of up to 80 nm displacement at 5-50 Hz has been observed in the hair bundles of the bull frog sacculus. Blocking the transduction channels with gentamicin reversibly stops oscillations and drugs affecting the activity of the slow-myosin motor affect the rate of oscillation (Martin et al., 2003). This mechanism is too slow to be relevant to the higher frequency ranges required by mammals, bats, etc., whereas the fast Ca^{2+} dependant mechanisms may be fast enough, but may not be powerful enough (Meaud and Grosh, 2011). One mechanism for Ca^{2+} dependent conformational changes has been observed in isolated rat OHCs, where a stimulus caused active force generation in the same direction (Kennedy et al., 2005; Kennedy et al., 2006) and another in turtle hair cells that generates force in the opposite direction to the stimulation (Ricci et al., 2000).

OHCs were first shown to elongate in response to hyperpolarisation and shorten in response to depolarisation by Brownell et al. (1985). This electro-mechanotransduction is directly coupled to the BM and works up to 100 kHz *in vivo* in the guinea pig (nearly twice the range of the guinea pig and adequate to cover 80 kHz upper range of hearing in mice) (Grosh et al., 2004). In the mouse cochlea, the response of OHCs is frequency dependant and controlled by their longitudinal position in the cochlea, a requirement for the feedback of the OHCs to contribute to tuning (Kössl and Russell, 1992). OHC somatic motility is powered by the basolateral membrane protein prestin. Prestin is specific to the OHCs of the mammalian inner ear and can produce electromotility in other eukaryotic cells exposed to voltage changes when artificially expressed (Zheng et al., 2000; Mellado Lagarde, 2008; Mellado Lagarde et al., 2008; Weddell et al., 2011b). Recent evidence has shown that the prestin-based somatic motility of OHCs is not limited by the OHC membrane time constant, as previously thought (Johnson et al., 2011).

1.3.2.2 Tectorial membrane

Regardless of the specific mechanism used to generate force by the OHCs, the timing of their feedback is dependent on the TM. The TM is the most structurally complex of the acellular gels of the inner ear (Goodyear and Richardson, 2002) and *in vivo* resonates at a longitudinal position at a frequency half an octave below the CF of the position (Gummer et al., 1996; Hemmert et al., 2000; Lukashkin et al., 2010). It performs two important roles in the active

sensation of acoustic stimulation: Movement of the TM relative to the RL affects gain by allowing efficient stimulation of IHCs by the fluid in the subtectorial space (Legan et al., 2000) and affects frequency tuning and gain by interacting with the stereocilia of the OHCs (Russell et al., 2007). The tallest stereocilia of IHCs are not embedded in the TM and stimulation via the subtectorial fluid is likely to be complex and involves Hensen's stripe (Nowotny and Gummer, 2006).

Data from various mouse mutants have demonstrated how morphological changes or removal of the TM can affect cochlear tuning and sensitivity (McGuirt et al., 1999; Legan et al., 2000; Simmler et al., 2000b; Legan et al., 2005; Russell et al., 2007; Xia et al., 2010). These data have made it apparent that both the radial properties and the longitudinal properties of the TM need to be considered when modelling cochlear mechanics. Traditionally, longitudinal coupling in the TM has been neglected and each cochlear place modelled independently. At each of these points the radial properties have been modelled between two extremes; as infinite radial and bending stiffness with a pivot at the spiral limbus (Figure 1.12, A) (Davis, 1958; Davis, 1965; Johnstone and Johnstone, 1966; Rhode and Geisler, 1967; Billone and Raynor, 1973; Neely and Kim, 1983; Steel, 1983) and as a simple mass load in which radial stiffness is negligible (Figure 1.12, C) (Zwislocki et al., 1988; Zwislocki and Cefaratti, 1989; Mammano and Nobili, 1993). Between these two extremes of stiffness and mass, models can include radial resonance in the TM (Zwislocki and Kletsky, 1979; Allen, 1980; Neely and Kim, 1986; Gummer et al., 1996) (Figure 1.12, B).

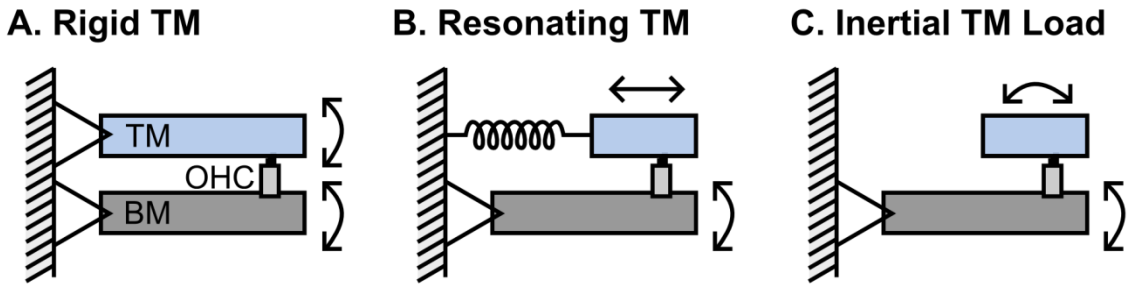

Figure 1.12 Models of radial TM motion. **A**. Infinite radial and bending stiffness, pivoting around the spiral limbus. **B**. A resonating model with mass and finite stiffness. **C**. A mass load with negligible radial stiffness. Adapted from Abnet (1998).

There is experimental evidence for the TM being a second (and multi-modal) resonator in the cochlea, with its maximal radial resonance occurring at half an octave below the CF of each cochlear position (Allen and Fahey, 1993; Gummer et al., 1996; Hemmert et al., 2000). In such a system the timing between the radial resonance of the TM and the transverse resonance of the BM is critical. Gummer et al. (1996) compares the difference in feedback provided by a

compliant or inertial TM, when assuming that OHCs are inhibited when BM displacement is towards the scala vestibule and that hair bundle displacement lags the OHC intracellular receptor potential by 90°. Under these conditions (not considering OHC motility due to extracellular potentials), inertial loading of the TM causes amplification of the BM displacement (Figure 1.13) (Gummer et al., 1996; reviewed by Lukashkin et al., 2010).

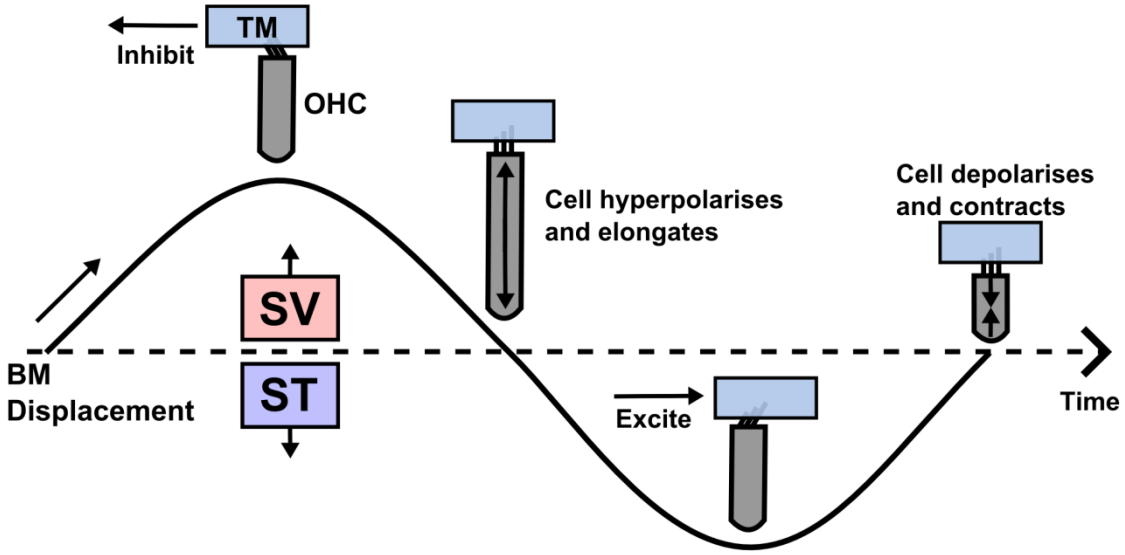

Figure 1.13 Interaction between OHCs and radial TM resonance. When the TM provides an inertial load to the OHC hair bundles BM motion is amplified. Adapted from Gummer et al. (1996).

Models without longitudinal coupling consider radial stiffness in isolated cochlear positions. However, recent experimental evidence (discussed in Chapter 5.2.1, p. 110), not only indicates that the longitudinal mechanical properties of the TM can support energy propagation over physiologically significant distances, but that disruption of this coupling can cause hearing pathology. A recent model takes the longitudinal propagation of energy in the TM into account and concludes that the TM has a significant influence on cochlear tuning (Meaud and Grosh, 2010).

1.3.3 Summary

Active feedback in hearing by the cochlear amplifier builds upon the multiple passive gradients present in the components of the cochlea to enhance the level range and frequency and temporal resolution of mammalian hearing and to overcome viscous damping (Lukashkin et al., 2007). In this system force is produced by electromotility of the OHCs and the application and timing of this feedback is controlled by the interaction between the resonances of the TM and BM (Gummer et al., 1996; Lukashkin et al., 2010). Traditionally the involvement of longitudinal coupling has only been considered important in the BM, but recent data has shown that

energy can propagate longitudinally in isolated TM segments (Abnet and Freeman, 2000; Ghaffari et al., 2007). Other experimental data has shown the importance of longitudinal coupling in the TM *in vivo* (Legan et al., 2005; Russell et al., 2007) and it is considered in recent mathematical models (Meaud and Grosh, 2010).

1.4 Thesis aims

This thesis looks at two distinct areas of hearing; the retained acoustic sensitivity of the vestibular system and the material properties of the TM in the cochlea. The broad aims of each of the results chapters are:

Chapter 3 – to determine if the vestibular system is acoustically sensitive to low frequencies in mice, which have a cochlea that is insensitive to frequencies <4 kHz and, if so, to determine which end organs might be involved.

Chapter 4 – to develop a laser-interferometer based method for tracking induced travelling waves in isolated TM segments and to compare the mechanical properties of segments from the apical and basal turns of the wild-type cochlea.

Chapter 5 – to compare the mechanical properties of TM segments from the basal turn of cochleae from *Tecta*$^{Y1870C/+}$, *Tectb*$^{-/-}$ and *Otoa*$^{EGFP/EGFP}$ mice to wild-types.

Chapter 6 – to compare the reflective properties of segments of the TM in *Tecta*$^{Y1870C/+}$, *Tectb*$^{-/-}$ and *Otoa*$^{EGFP/EGFP}$ mice and wild-type mice, and attempt to correlate any observed difference to structure.

2 MATERIALS AND METHODS

2.1 Introduction

This materials and methods chapter is split in to two sections relating to the behavioural experiments presented in Chapter 3 (p. 70) and the tectorial membrane (TM) laser interferometry experiments presented in Chapters 4 (p. 87), 5 (p. 107) and 6 (p. 144).

All procedures involving animals were performed in accordance with UK Home Office regulations and with approval of the local ethics committee.

2.2 Methods: Acoustic sensitivity of the vestibular system

Experiments were performed in an acoustically shielded booth in order to measure the magnitude of the auditory startle response (ASR) of an individual mouse, using a lab built accelerometer. Combinations of two acoustic stimuli were used; a “probe” tone to elicit startle and a “masker” tone of varying frequency. The saliency of the masker tone, which included frequency and level combinations both within and without the cochlear range of the mouse, was assessed by comparing the probe-elicited ASR in the presence of the masker tone to the ASR elicited by the probe on its own.

The stimulus presentation paradigm, distortion product otoacoustic emission (DPOAE) and neural compound action potential (CAP) procedures, the details of the *Nox3* mutant mice, and the basic methods used in the collection of data are described in Chapter 3 (p. 70), which is a reproduction of the paper published in JARO in 2010 (Jones et al., 2010). This section includes additional methodological detail omitted from this published version (detailed equipment set up, background to the auditory startle response, vestibular dissections, etc.).

2.2.1 Auditory startle response

The ASR is a well characterised reflex to acoustic stimulation (Ison and Hoffman, 1983; Koch, 1999; Willott, 2001). It has a short latency and involves a short, sharp twitch of body and facial muscles in response to intense or surprising stimuli. The ASR has been documented in many mammals, and can be used as a measure of stimulus saliency in mice. The obvious behavioural response to acoustic stimuli in mice can be quantitatively measured by recording either the amplitude of displacement or the acceleration of the “jump” elicited in the mouse. The baseline of the ASR is non-zero and the response amplitude can be modified by both internal factors (such as emotional state; Davis et al., 1997; Plappert and Pilz, 2002, motor activity; Wecker and Ison, 1986; Plappert et al., 1993, input from other sensory modalities; (Yeomans et al., 2002, etc.) and external factors relative to the animal (such as background noise (Hoffman and Fleshler, 1963; Davis, 1974), pre-pulses (Hoffman and Ison, 1980), or modification of the eliciting stimulus, etc.). Sound pressure level, frequency (or frequency spectrum), rise time, etc. all contribute to the stimulus saliency and hence the behavioural response to the eliciting startle tone (Willott, 2001).

Modification of the ASR can occur at different levels (with different latencies) and can be entirely unconditioned or involve behavioural conditioning (Brown et al., 1951; Davis et al., 1993; Walker and Davis, 1997). Experimental paradigms involving pre-pulse inhibition (PPI), for example, do not require prior behavioural conditioning and can have a facilitatory (Lang et al.,

1990; Schmid et al., 1995) or inhibitory (Hoffman and Ison, 1980) effect on startle amplitude. PPI is used to access how parameters of a tone affect the startle response – a tone that does not elicit a startle response is typically presented ~100 ms before the startle stimulus. The inhibition (or facilitation) of the startle reflex can then be used to determine the salience of the preceding tone (Hoffman and Ison, 1980). In cases where background noise alters the startle response, the relationship between noise and startle amplitude is complex, with lower levels of background noise facilitating startle and higher levels inhibiting it (Ison and Russo, 1990). Conditioned cues presented in a behaviourally perceivable time before the startle stimulus (other tones, tactile stimuli, etc.) can facilitate the reflex (Walker and Davis, 1997). Notably, cues preceding the startle stimuli do not usually decrease the size of the response, which would be a reasonable prediction given they may serve as a warning and reduce the element of surprise (Koch, 1999).

Startle reflexes can be elicited exclusively by individual sensory modalities or as a combination of a number of modalities; with a larger startle reflex often observed as the result of input from more than one sensory system (Yeomans et al., 2002). For example, air puff stimuli contain a tactile component (moving air contacting the skin) and an auditory component (the noise made generating the puff). In deafened rats, the startle reflex is smaller in response to the tactile component alone than in rats with normal hearing, who receive input from the auditory system as well as the somatosensory system. Cross-modal summation of the startle reflex between the auditory and vestibular systems has been demonstrated (Li and Yeomans, 1999; Li et al., 2001) and is strongest when the stimuli are timed to reach the point of summation simultaneously. Vestibular stimulation preceding acoustic stimulation by 5-7.5 ms optimally increases the startle reflex by 3-5x. This summation may take place in the spinal cord, where the vestibulospinal tract and reticulospinal tracts converge after passing through the vestibular nucleus and caudal pontine reticular nucleus, respectively (Li et al., 2001).

2.2.2 Dissection

Cochlear dissections were performed after completion of all behavioural experiments (immediately after terminal DPOAE recordings, if applicable). The entire inner ear was removed into a Petri dish containing Hank's Balanced Salt Solution (HBSS: 138 mmol NaCl, 5.33 mmol KCl, 0.441 mmol KH_2PO_4, 4.17 mmol $NaHCO_3$, 0.338 mmol Na_2HPO_4, 5.56 mmol D-Glucose) and the stapes removed. In wild-type mice the sacculus was visible as a bright white mass directly below the (removed) stapes. Surrounding bone between the oval window and stapes, and around the base of the cochlea was also removed in order to make

this visual inspection as clear as possible (Figure 2.1). The presence or absence of the otoconia of the sacculus was visually confirmed and recorded.

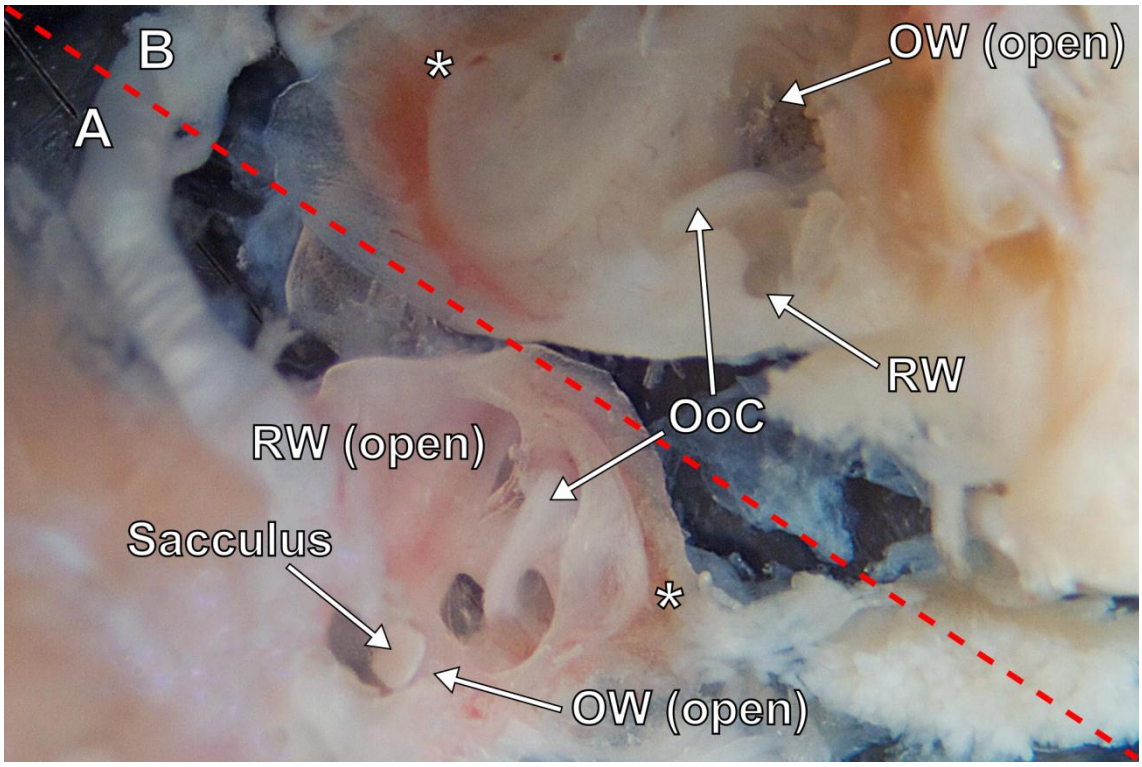

Figure 2.1 Cochlear dissection of *Nox3* mice. **A**. In wild-types the sacculus was clearly visible as a white mass though the oval window after removal of the stapes. **B**. In the *Nox3*$^{-/-}$ mice it was not visible due to the lack of otoconia. Asterisks mark the apical end of each cochlea

2.2.3 Equipment setup

All experiments were conducted in an acoustically shielded booth (IAC, UK) and stimulus delivery and response recording were controlled by a PC running Matlab 2006b (The MathWorks, Inc.) (Figure 2.2). Two pure tones for sound stimulation (one for the masker and one for the probe) were generated digitally and converted to analogue by a DT3010/32 data acquisition board (Data Translation) at a rate of 200 kHz and presented through a pair of loudspeakers. Two attenuators controlled by the computer via USB set the level of the stimulation for both speakers. Startle responses were recorded by an analogue accelerometer (laboratory designed and constructed) and digitized by the same data acquisition board at a rate of 200 kHz. The experimental chamber was arranged with both loudspeakers in front of the mouse to ensure binaural stimulation (Figure 3.2, p. 75).

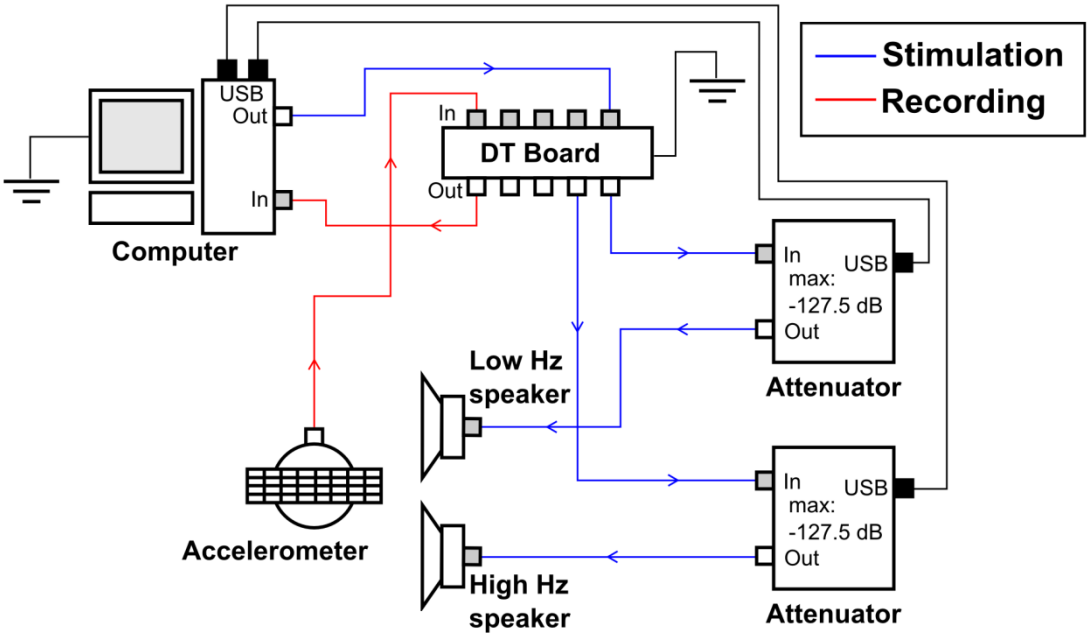

Figure 2.2 Schematic of the electronic equipment used in the ASR experiments. Two speakers delivering the probe and masker tones are controlled by the computer via a DT3010/32 data acquisition board. The amplitude of the startle response is recorded with an accelerometer via the same DT3010/32 board.

2.3 Methods: Mechanical properties of the tectorial membrane

In order to launch travelling waves along isolated segments of TM, apical or basal segments were removed by cochlear dissection and mounted in a fluid filled chamber between a vibrating and stationary support. On stimulation of the vibrating support the longitudinal propagation of the travelling wave was tracked at multiple points along the length of the TM using a laser interferometer focused through a viewing window on to the marginal edge of the TM.

2.3.1 Mice

In total five mouse strains were used in the collection of data for the experiments presented in Chapters 3 (p. 70) and 4 (p. 87). These included wild-types (CBA/Ca and S129 background strains) (Chapter 3) and three mutant groups *Tecta*$^{Y1870C/+}$, *Tectb*$^{-/-}$ and *Otoa*$^{EGFP/EGFP}$, all of which were on CBA/Ca backgrounds (Chapter 4). All the mouse colonies were maintained at the University of Sussex and mice were used between 1-6 months of age.

2.3.2 Dissection and mounting

The dissections were performed under a light microscope, in a Petri dish containing artificial endolymph (AE: 174 mmol KCl, 2.00 mmol NaCl, 0.0261 mmol $CaCl_2$, 3.00 mmol D-glucose, 5.00 mmol HEPES, pH=7.3). The inner ear was removed from the skull and the cochlea was opened with forceps. The TM was detached from the spiral limbus (if necessary) using a tungsten probe with a tip diameter of <0.1 mm mounted on a syringe needle (Figure 2.3 and Figure 2.4). Usually the entire TM was removed in one piece in the wild-type, *Tecta*$^{Y1870C/+}$ and *Otoa*$^{EGFP/EGFP}$ mice. In the *Otoa*$^{EGFP/EGFP}$ mice the TM is not attached to the spiral limbus and would simply fall off. Qualitatively The TM was noticeably more brittle in the *Tectb*$^{-/-}$ mice and tended to break while being detached. Larger pieces of TM were cut by eye with a scalpel blade into segments between 350-1000 µm long. Sections referred to as “basal” are from the basal 3rd of the cochlea and “apical” segments are from the apical 3rd of the cochlea (Figure 2.5). The length of these segments varied depending on the region; the tighter curve in the apical regions generally limited the usable length to less than that of basal regions. A video of an example dissection is included in APPENDIX 1 (p. 188). Once detached and cut a single TM segment was transferred into the pre-prepared experimental chamber using a glass tipped pipette for mounting.

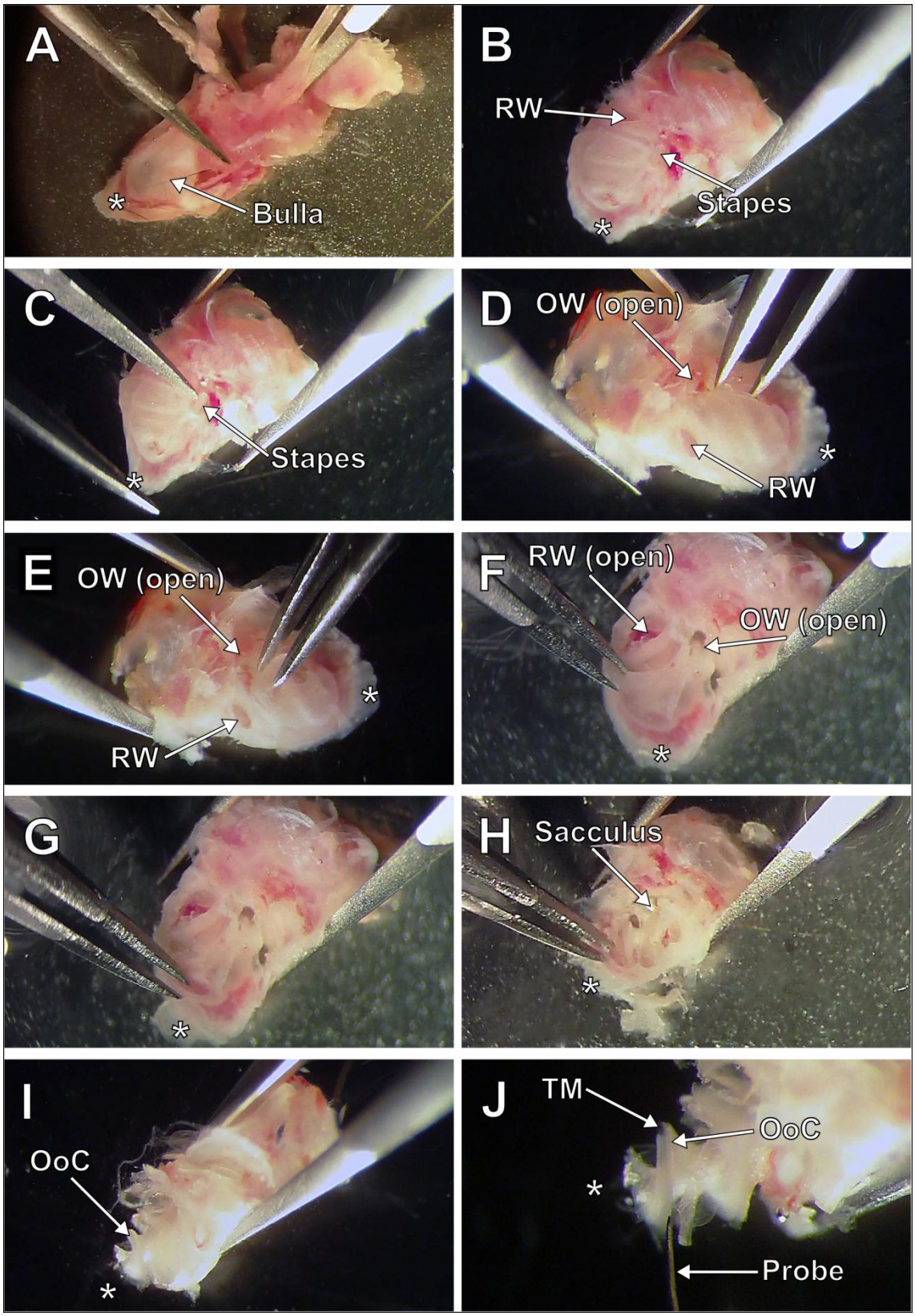

Figure 2.3 Cochlear dissection I, asterisks mark the apical end of the cochlea (see also APPENDIX 1, p. 188). **A**. The inner ear was removed from the skull and placed into a dish containing AE. The Bulla was then removed with forceps. **B-H**. The stapes was removed (**C**) and the top bony wall of the cochlea was chipped away with forceps. **I-J**. The back bony wall of the cochlea was chipped away, exposing the organ of Corti (OoC) and TM. A tungsten probe was gently pushed between the TM and OoC in order to detach the TM from the OHCs and SL.

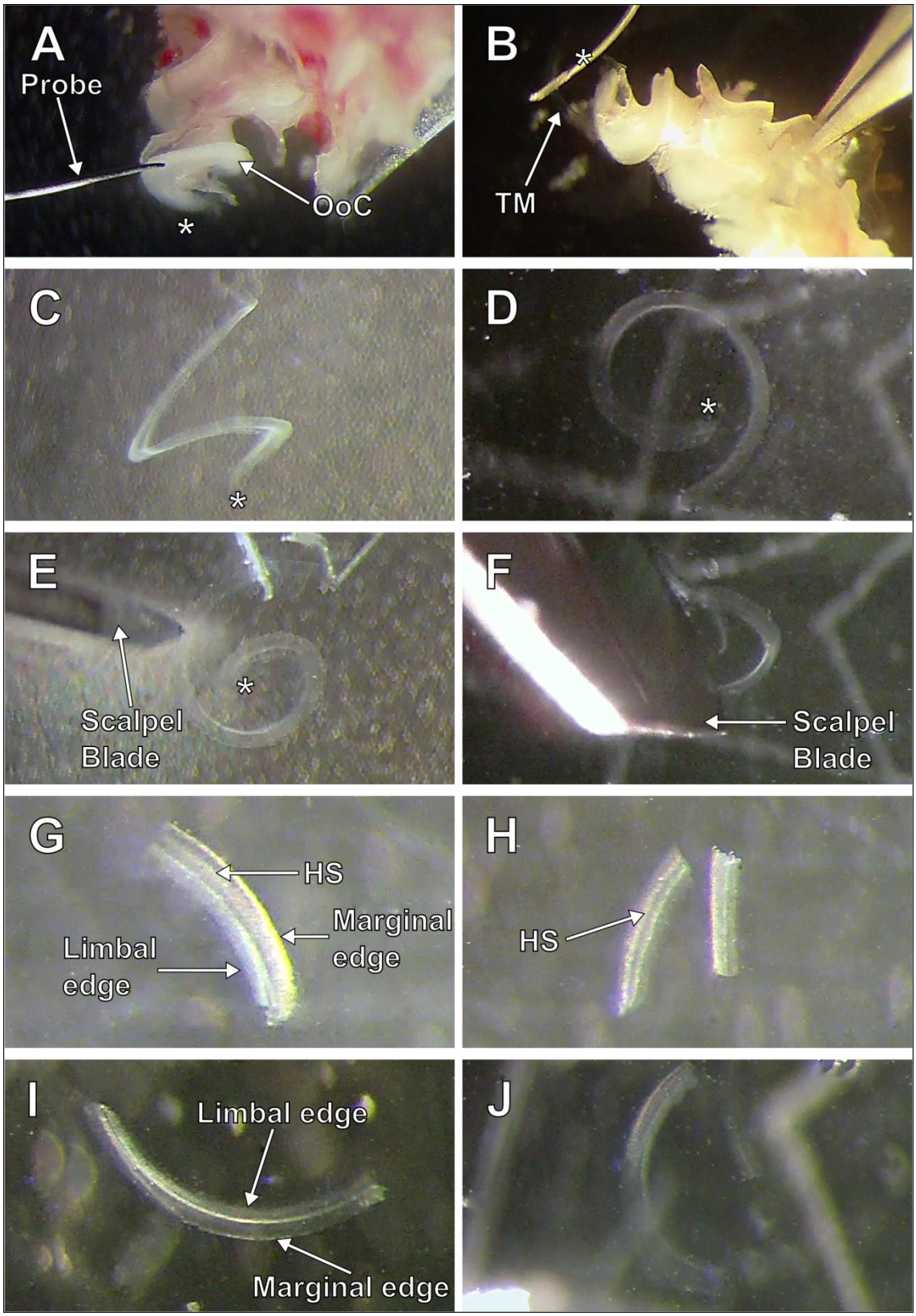

Figure 2.4 Cochlear dissection II, asterisks mark the apical end of the cochlea (see also APPENDIX 1, p. 188). **A-B**. The TM was detached using the tungsten probe. **C**. A whole isolated TM from the side. **D**. An isolated segment of TM viewed from the top. **E-F**. The detached TM was cut into usable segments with a scalpel blade. **G-J**. Individual segments of TM viewed from above.

2.3.3 Experimental chamber

The experimental chamber contained a vibrating and a stationary support on which a single TM segment was mounted. The chamber was filled with AE so that the prepared TM was submerged to a depth of at least 4 mm. The walls of the chamber were constructed from shaped silicone gel (Dow Corning 732) and the front wall contained a viewing window (cut from a microscope cover slip, Figure 2.6, A) through which the laser interferometer could be focused on to the prepared TM segment. The viewing window was angled slightly to avoid reflecting light straight back into the laser and was positioned so that the distance between it and the lasers focal point on the TM (~15 mm) was well outside the lasers depth of focus (20 µm). In order to reduce vibration, the base of the chamber was insulated by two glass microscope slides separated by a ~20 mm of soft foam. All experimental equipment (the chamber, the laser interferometer and the stationary support) was set up on a gas vibration isolation table located inside a Faraday cage.

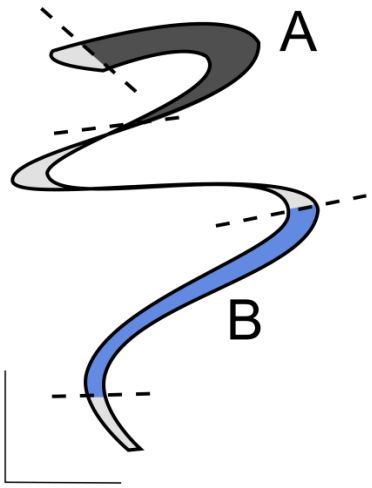

Figure 2.5 "Apical" and "basal" TM segments. Apical segments were taken from the final turn in the apex (**A**) of the cochlea, indicated by the shaded grey region. Basal segments were taken from the first cochlear turn in the base (**B**) as indicated by the shaded blue region.

Stimulation of the vibrating support was delivered by a piezo (Thorlabs AE0203D04 3.5x4.5x5 mm, unloaded resonance=261 kHz) mounted inside the experimental chamber. The piezo was attached at an angle of 90^{o} to an araldite block stuck to the bottom of the chamber by araldite (Figure 2.6, B). Vibration of the piezo was perpendicular to the viewing window and parallel to the chamber base, and the vibrating support on which the TM was mounted during experiments was attached in the same plane as the vibration. The vibrating support was either constructed from a small (~5x10x<1 mm) piece of glass or platinum. The mounting of the piezo was such that it was loaded only at each end, to avoid skewing the vibration by loading the side walls. The glass stationary support (~10x10x<1 mm) was mounted on a mechanically isolated stand (verified by laser interferometer recordings of the stationary support during stimulation of the vibrating support) external to the chamber and lowered in to place prior to the TM being added to the chamber (Figure 2.6, C).

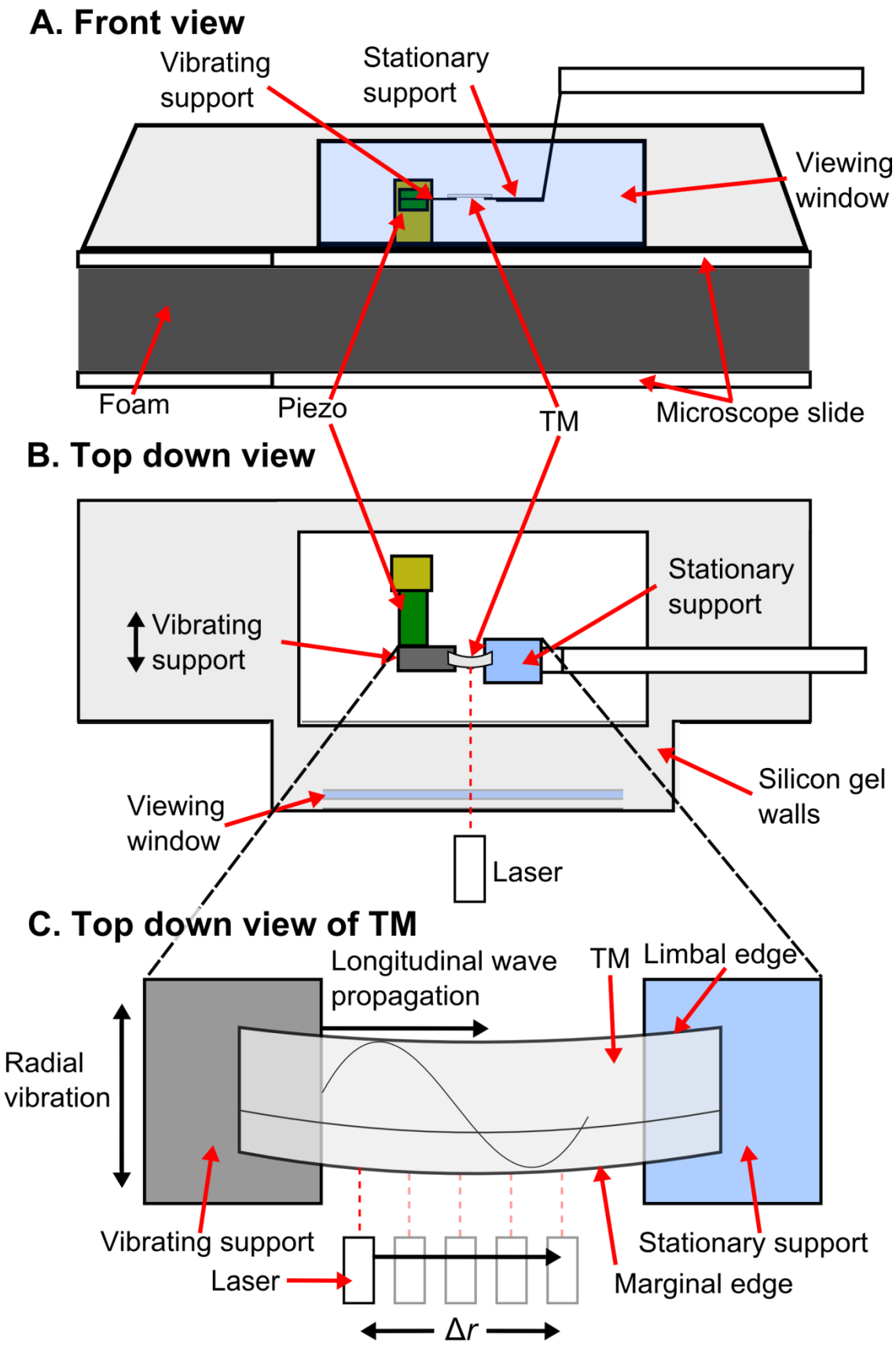

Figure 2.6 Schematic of the experimental chamber. **A**. The front ("lasers-eye view") of the chamber. **B**. Top down view of the chamber. **C**. Enlarged, top down view of the TM mounted on the stationary and vibrating supports.

To prepare the chamber prior to adding the TM, Cell Tak (BD Biosciences) mixed with AE was applied to both supports. This was allowed to dry and then rinsed with reverse osmosis water. The chamber was then rinsed with, and then filled with AE. The TM segment was added to the chamber and allowed to settle between the two supports. It was then gently pressed at each end against the supports with the back curve of the tungsten probe and allowed to adhere to the Cell Tak for ~20 minutes before commencement of the experiment. The attachment of the TM segment to the supports was verified after completion of the experiment by slowly increasing the distance between the supports. Where the attachment had been adequate for the preceding experiment, the TM segment would stretch slightly before breaking or detaching from a support.

2.3.4 Equipment setup

All experiments were conducted in a quiet room on a gas isolation table and inside a Faraday cage. Stimulus delivery and signal processing were controlled via a DT3010/32 data acquisition board (Data Translation) by a PC running Matlab 2006b (The MathWorks, Inc.) (Figure 2.7). A single USB attenuator (Figure 2.8) controlled the amplitude of stimulation delivered to the stimulating piezo and a 10 Ω piezo driver counteracted the effect of reducing piezo amplitude with frequency (Figure 2.9, A) (caused by an increase in capacitance of the piezo with frequency). Slight dips in piezo amplitude were observed at 5 and 15 kHz, which were presumably caused by a resonance created by the mounting (loading) of the piezo. However, as the absolute change in amplitude in these frequencies was very small (~20 nm, relative to nearby frequencies) and frequency was the main determinant of radial velocity of the piezo (v_r) (Figure 2.9, B), these resonances had no noticeable effect in the collected data.

2.3.5 Laser interferometer

A self-mixing homodyne laser-diode interferometer was used to record the phase and amplitude of the stimulated travelling wave in the TM and is described in detail in Lukashkin et al. (2005). The laser detects the phase dependant changes in intensity of light reflected back from moving surfaces. It is able to detect sub-nanometre displacements of very low-reflective surfaces (such as the BM) and through semi-opaque obstructions (such as the round window). At half intensity the lasers spot has a diameter of 5 µm and a depth of focus of 20 µm.

A max-averaging signal processing algorithm was used to mitigate movements of the preparation due to noise. The laser is at its most sensitive when the operating point is in quadrature (at Q1 or Q2, Figure 2.10, A). Movements away from these operating points result in a smaller signal being recorded for the same target displacement (Figure 2.10, B). The wave

length of the laser is 670 nm, allowing a working range of 670/4=167 nm around a quadrature point. This means that the maximum amplitude the laser can record is 167/2=84 nm. The max-averaging algorithm repeats recordings a set number of times (typically *n*=10 or 20) and uses the largest amplitude, which would have been recorded when the laser was closest to either of its most sensitive operating points (Q1 or Q2). This process allows the detection of sub-nanometre displacements even with relatively large amplitude background noise/movement (Lukashkin et al., 2005).

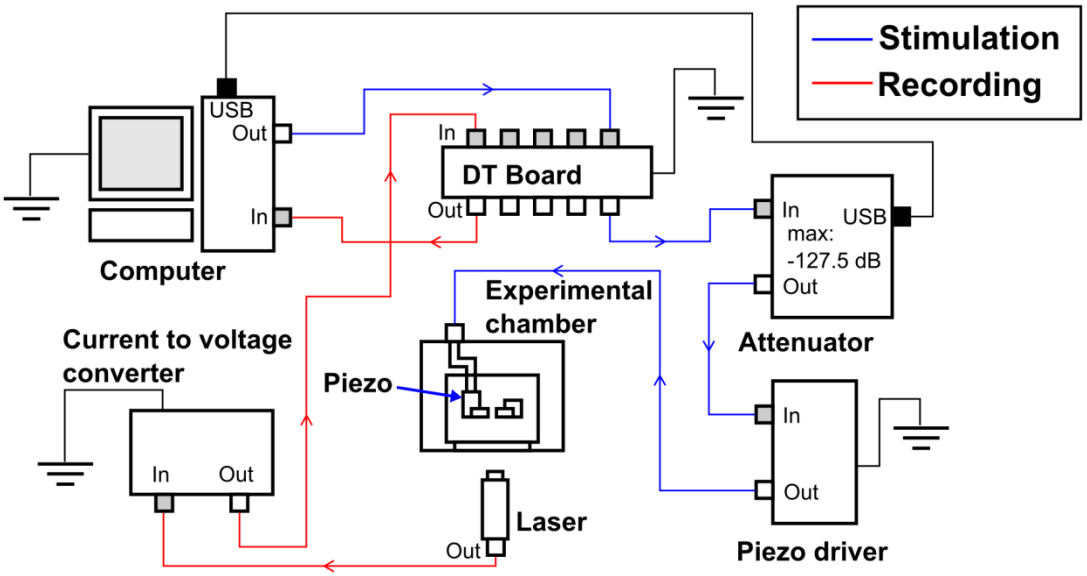

Figure 2.7 Schematic of the electronic equipment used in the TM experiments. Stimulus delivery and signal recording were controlled by a PC via a DT3010/32 data acquisition board.

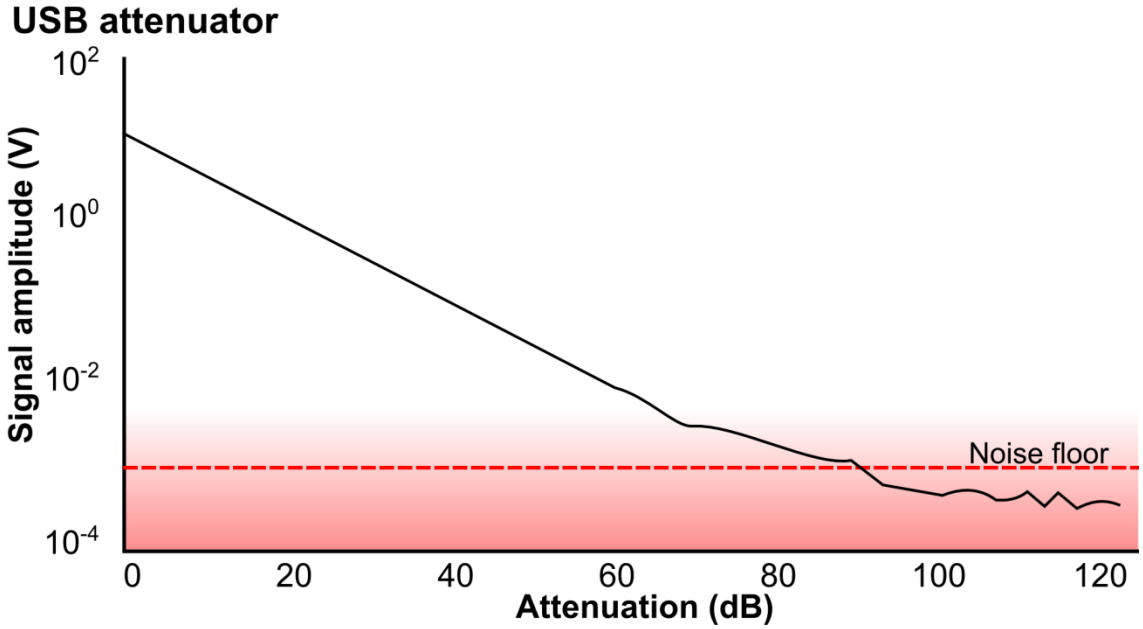

Figure 2.8 Characteristics of the USB attenuator; the relationship between attenuation (dB) and signal amplitude (V) delivered to the piezo. The USB attenuator accurately attenuated the analogue signal reaching the piezo driver from the DT3010/32 board down to the noise floor (~80 dB).

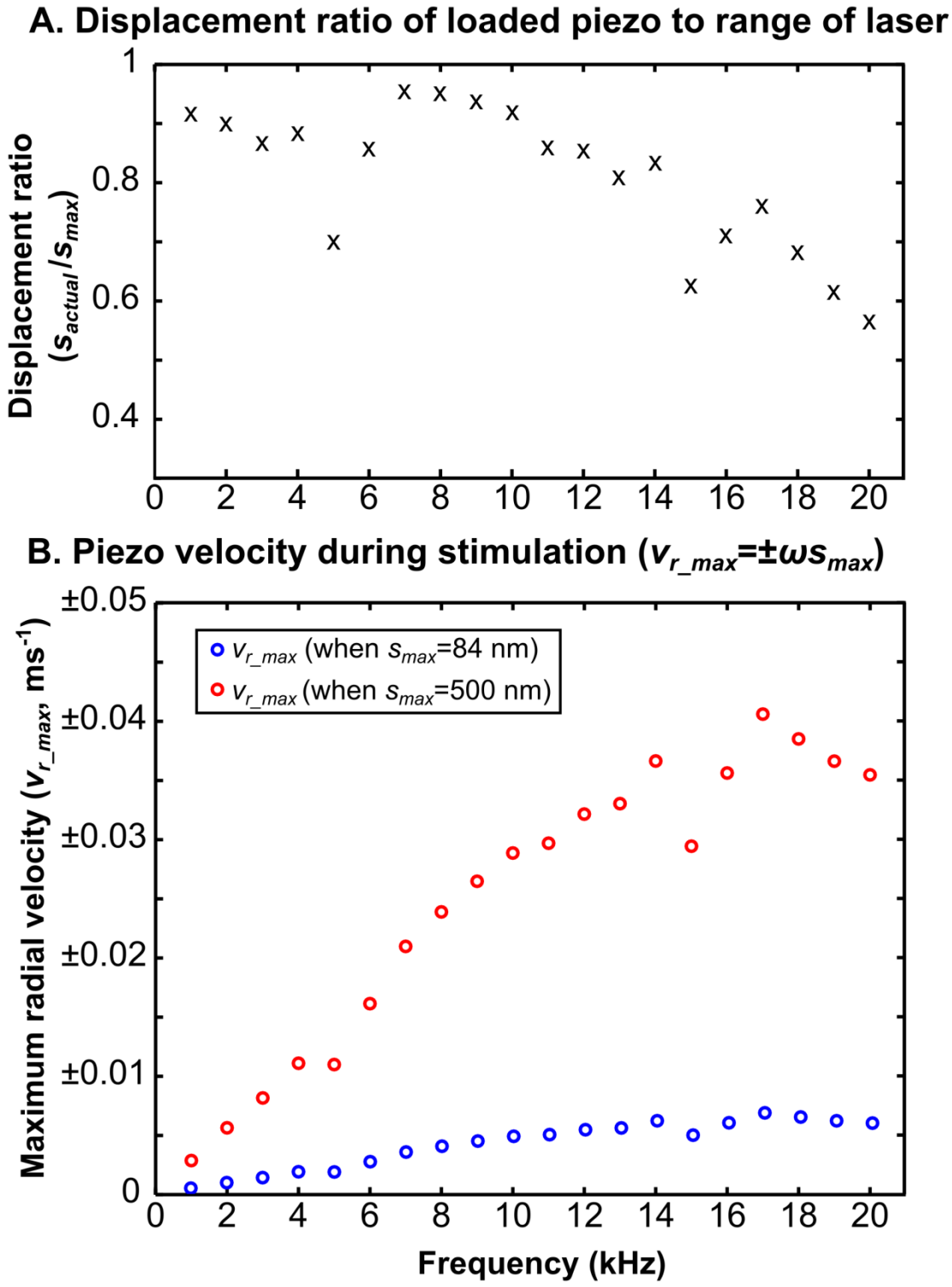

Figure 2.9 Maximum radial amplitude and velocity of piezo stimulation. **A**. The ratio of piezo amplitude (s_{actual}) to maximum piezo amplitude (s_{max}) as a function of frequency (s_{max}, was set by attenuation level). The piezo's amplitude decreased slightly with frequency, this effect was significantly reduced by the piezo driver. **B**. The radial velocity (v_r) of the piezo as a function of stimulus frequency and s_{max}. Maximum radial stimulation velocities (v_{r_max}) are slower when the amplitude is smaller, which may have an effect on fluid coupling around the TM, although this is mitigated by using a smaller stimulation amplitudes. The blue circles show the radial velocity as a function of frequency for the piezo with an amplitude-frequency relationship shown in **A**, when the maximum displacement is set to the maximum rage of the laser interferometer (84 nm, approximately 10 dB attenuation applied by the USB attenuator). The red circles show the velocity-frequency relationship with the amplitude-frequency profile shown in **A**, where the maximum radial displacement is 500 nm.

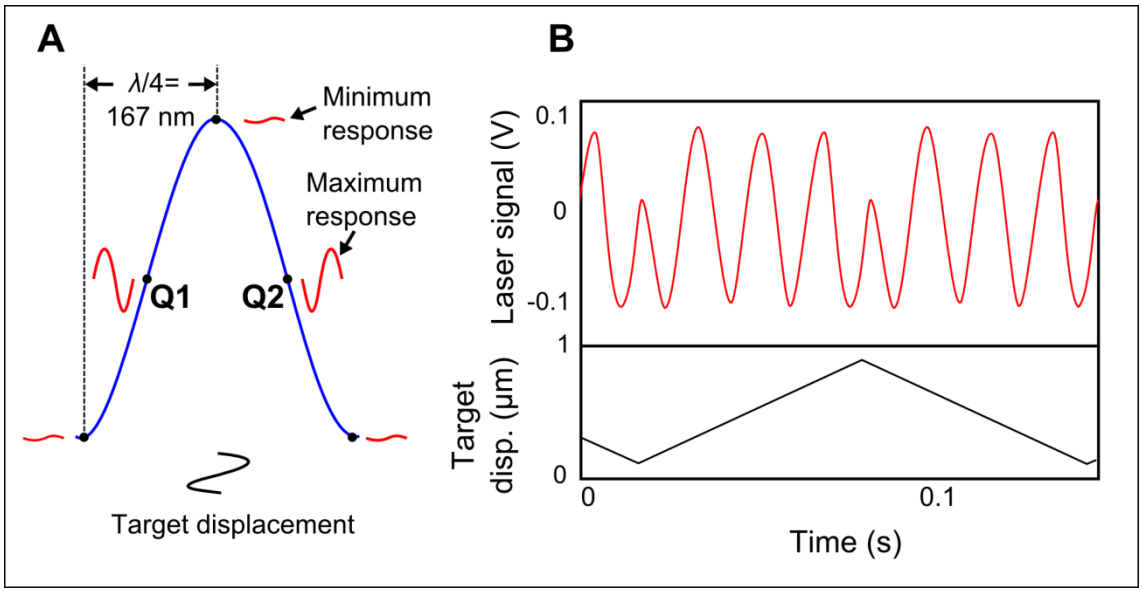

Figure 2.10 Dependence of laser sensitivity on distance to target. **A**. The maximum laser response is recorded from the quadrature points, Q1 and Q2. **B**. Movement of the laser relative to the target shifts the operating point and changes signal amplitude. The max averaging signal analysis algorithm corrects for this shift. Adapted from Lukashkin et al., 2005.

2.3.6 Experimental procedure

The laser interferometer was focused on to the marginal edge of the TM so that the light entering the chamber was approximately parallel with the end of the vibrating support. The usable length of the mounted TM was measured using a micromanipulator on which the laser was mounted; the laser was moved from one end of the TM to the other and the distance recorded (accurate to about 20-30 µm). To avoid potential interference by reflection from the vibrating support, the first longitudinal position on the TM was defined as being 60-100 µm away from the edge of the vibrating support. Recording commenced from this point and the laser was stepped along the TM (in 10 or 20 µm steps) until it came within 100 µm of the stationary support or a distance of at least 300 µm was covered for each TM preparation.

Sinusoidal stimulation of 1-20 kHz was generated in Matlab and converted to an analogue signal by a DT3010/32 board at a rate of 500 kHz. Amplitude of the stimulation was controlled by an attenuator and a piezo driver. The attenuator controlled the absolute displacement and the piezo driver reduced the relative loss of radial displacement with frequency (Figure 2.9, A). The attenuator level was set to ensure the maximum vibration was within the linear range of the laser interferometer (max 84 nm displacement), around 10 dB (Figure 2.8). The velocity of stimulation is a product of frequency and amplitude ($v_{max}=\pm\omega * s_{max}$, where ω=angular velocity and s_{max}=maximum displacement) and the velocity as a function of frequency for set amplitudes is shown in (Figure 2.9, B).

Radial stimulation (Figure 2.11) of 1-20 kHz was applied to the TM in steps of 1 kHz at every longitudinal position (typically n=3 or 5 for each position). Phase and amplitude of the travelling wave were recorded by the laser interferometer at each location at each frequency and were digitised by the same DT3010/32 board at a rate of 500 kHz. Phase data was recorded between -180 and 180°. Amplitude data required calibration to control for differing reflectance at each point along the TM. The recorded voltage from the laser (between 0-10 V) is the product of the reflectance of the surface and the displacement of the surface. In order to calibrate the amplitude, a piezo with known displacement on which the laser interferometer was mounted was vibrated at 1 kHz while the target was kept stationary (typically n=3 for each longitudinal position). The level of attenuation of the stimulus was stepped down from 20 to 0 dB in steps of 2 dB (increasing the displacement of the laser with each step). The maximum amplitude in this range shows the maximum amount of displacement detectable within the linear range of the laser (84 nm, Figure 2.12). The corresponding voltage of this point gave a reference voltage at which displacement=84 nm at the reflectance of the point. The amplitude data was compared to this value: Voltage/calibration voltage*84=amplitude in nm. The raw data and amplitude calibration runs were saved on the computer for later analysis.

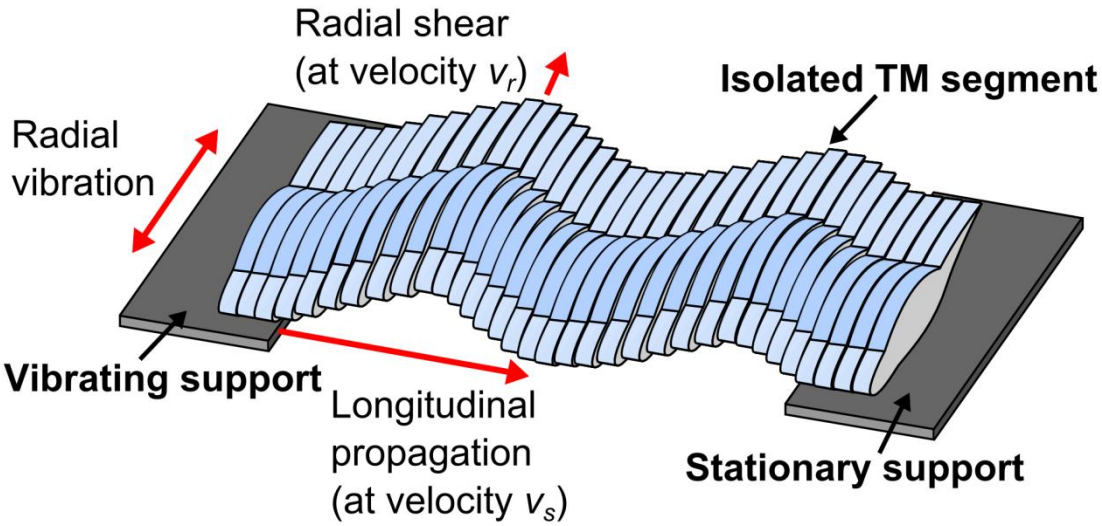

Figure 2.11 Planes of vibration *in vitro*. Vibration was applied to the isolated TM segment in the radial plane, resulting in a radially shearing, longitudinally propagating travelling wave. *In vivo* the TM shears radially near the CF, whereas the BM displaces in the transverse plane.

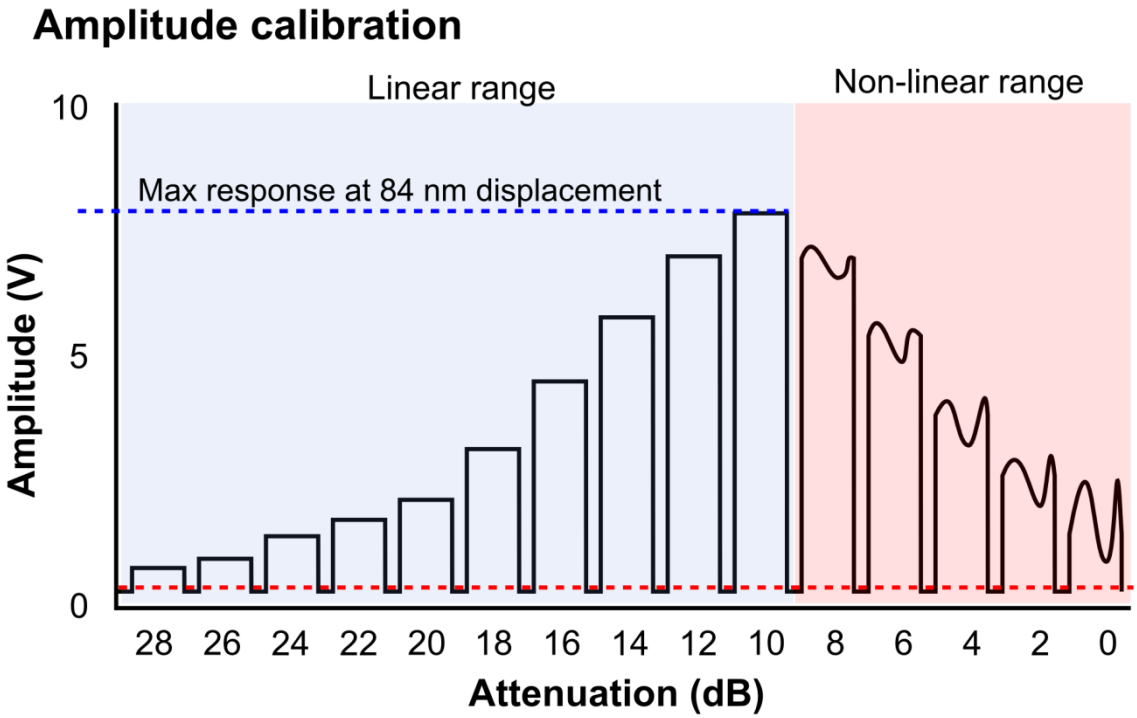

Figure 2.12 Calibration of the laser signal amplitude. As attenuation is stepped down (increasing the amplitude of radial displacement of the second piezo on which the laser is mounted) the amplitude signal from the laser increases. When the laser is moved by a distance greater than its maximum range (84 nm, relative to its stationary target) its response becomes non-linear and drops in amplitude (here ≤8 dB attenuation). The prior point of maximum stimulation (here 10 dB attenuation) provides a references voltage that corresponds to 84 nm. The voltage ratio between experimental data collected from the same longitudinal position and this reference voltage controls for the reflectivity of the surface and gives its actual displacement.

2.3.7 Data analysis

Analysis of the raw data was conducted after completion of the experiment and involved a number of steps in which the phase and amplitude data were analysed separately, most of which were automated and performed by scripts running in Matlab 2006b.

2.3.7.1 Phase

1. **Extraction of the phase angle from the raw data**

   Due to the inherent 180^{o} phase ambiguity in the laser recordings the actual phase was determined for each frequency at each longitudinal position by using a region of the raw recording where no phase jump occurred (Figure 2.13). This was usually at the point corresponding to the maximum amplitude of the response. Phase was extracted for each frequency at each point for each *n* (3-5) by an automated script running in Matlab 2006b. The data was averaged across *n* with care taken to avoid averaging any phase jumps caused by the 180^{o} ambiguity. For example, if *n*=3 and one good phase reading could be extracted at +180^{o} and two at 0^{o} then simply taking the mean (60^{o}) of

these values would not be representative of the true phase. To avoid this problem the script took a modal average of the available phase data points in order to find the "modal group" (in this example, 0°, and indicated by blue circles in Figure 2.14, A). Any outliers (in this example, the +180° point, and those indicated by red crosses in Figure 2.14, A) were then corrected by ±180° to minimise their difference relative to the modal group. After correction of outliers a mean of the points available at each longitudinal position was then taken and average phase lag plotted for each frequency as a function of longitudinal distance (Figure 2.14, B, blue line).

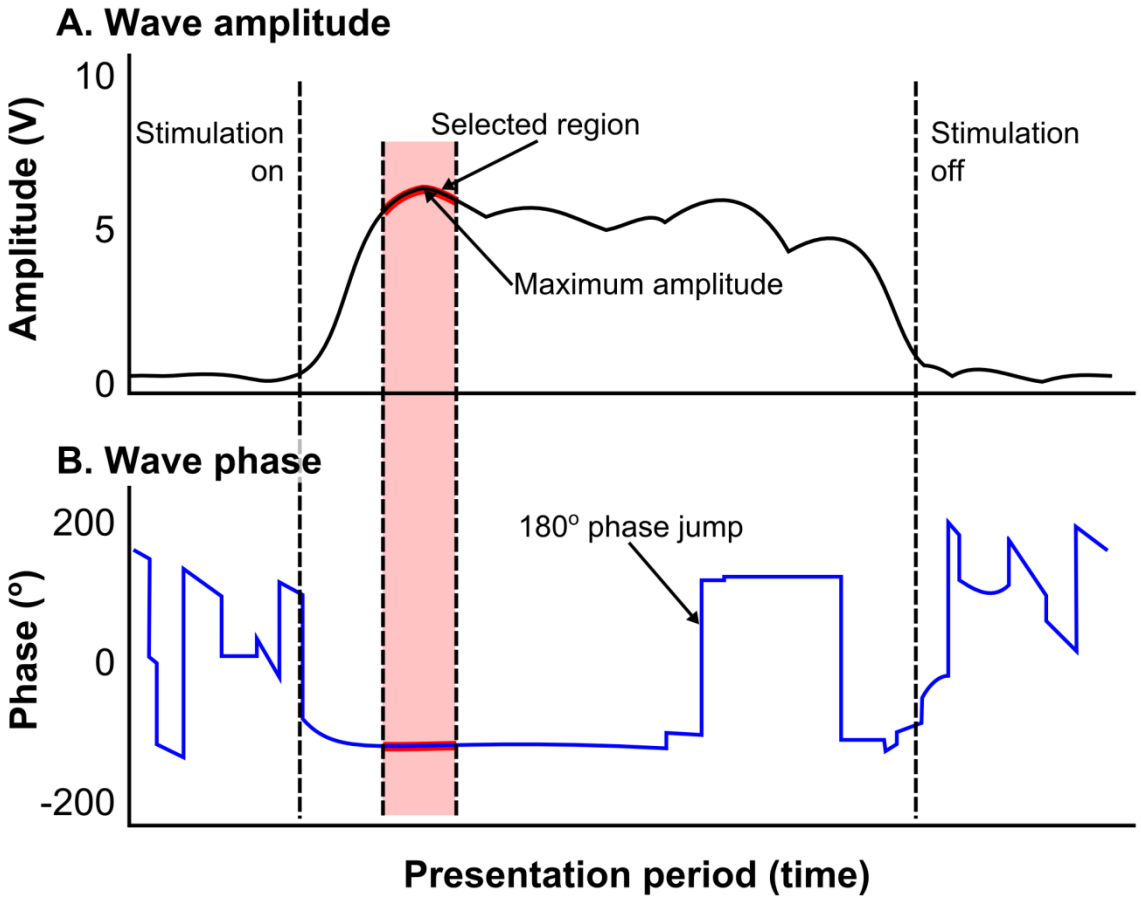

Figure 2.13 Extraction of phase from raw data (single stimulus presentation). An automated script running in Matlab 2006b sampled phase data from a section of phase in which no 180° jump occurs (the first region checked corresponds to the point of maximum amplitude).

2. **Unwrapping the phase data (for each frequency as a function of longitudinal distance)**

   Phase data was unwrapped for each individual experiment at each frequency (as a function of longitudinal distance) as shown in Figure 2.14, B. Unwrapping corrected for the phase ambiguity inherent in recording values greater than the +180 to -180°. Any value that fell below -180° would be recorded as positive. For example, -190° would be

recorded as +170°; these jumps are clear in the data and were be corrected for by adding or subtracting 360° relative to the rest of the data, as visualised in Figure 2.14, B, (black arrows). The final result of this process is shown in Figure 2.14, C which is the phase lag as a function of longitudinal distance for a single frequency from a single experiment.

Note that an average of the phase lag for each frequency between each group was taken at this point to calculate the phase roll-off as a function of longitudinal distance (as presented in Figure 4.1, A-C, p. 91 and Figure 5.1, A-C, p. 118) and for use in calculating the travelling waveform (as presented in Figure 4.7, A-D, p. 102; Figure 4.8, A, p. 104; Figure 5.11, A-D, p. 132; Figure 5.13, A-D, p. 134; and Figure 5.15, A-D, p. 136, see Chapter 2.3.7.3 below).

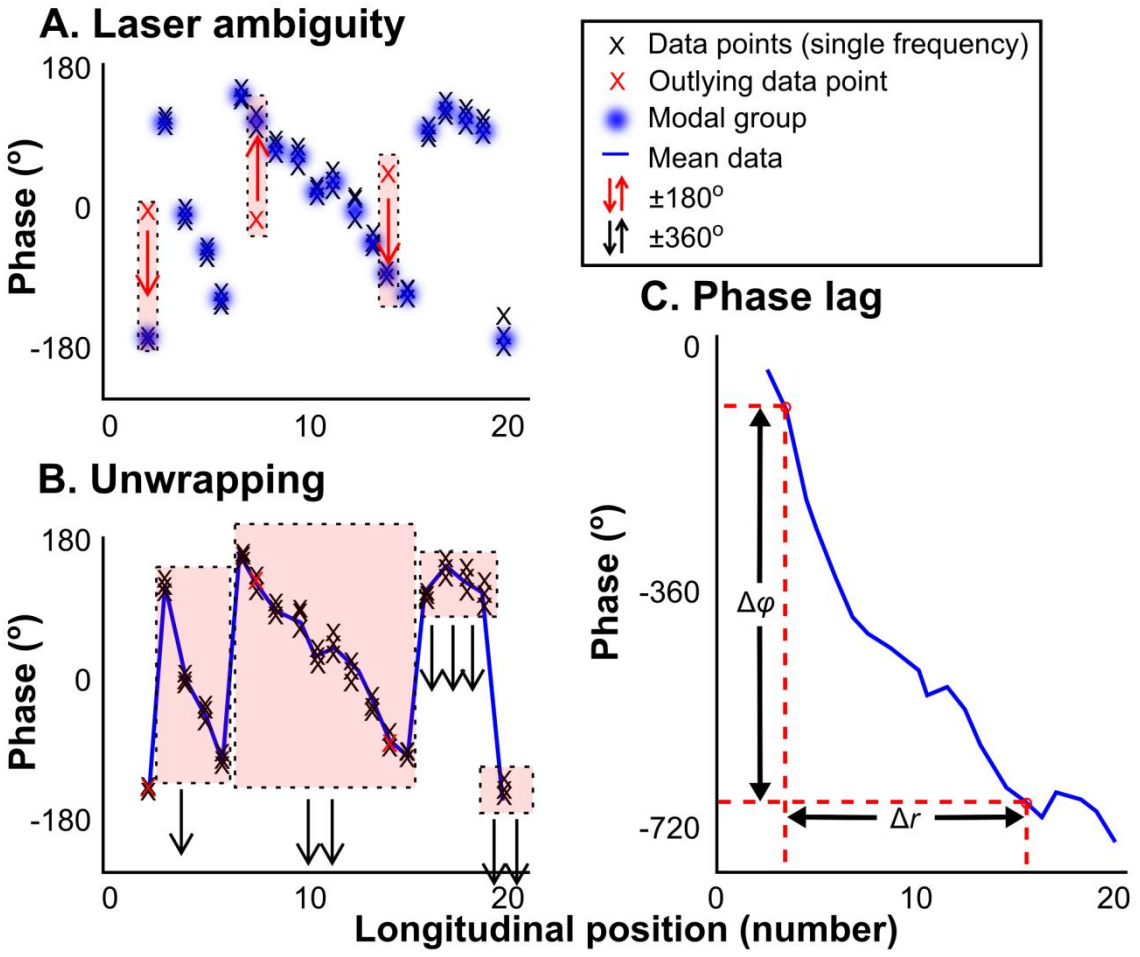

Figure 2.14 Analysis of the phase data; phase lag as a function of longitudinal distance calculated for each frequency. **A**. The 180° laser ambiguity was accounted for by finding the modal group and adjusting outliers by ±180° to minimise difference. **B**. The mean of each longitudinal position was taken and unwrapped. **C**. The phase roll-off as a function of distance and two points between which velocity of the wave was calculated are highlighted (red dots).

3. **Calculation of the travelling wave propagation velocity for each frequency**

   Travelling wave propagation velocity (v_s) was calculated individually for each frequency (in each experiment) from the phase roll-off as a function of longitudinal distance (as shown in Figure 2.14, C). A clean section of phase was selected and the change in phase ($\Delta\varphi$) and change in longitudinal distance (Δr) were used in Equation 2.1.

$$v_s = \frac{\omega * \Delta r}{\Delta \varphi} \qquad \textbf{Equation 2.1}$$

4. **Averaging of the propagation velocity data between experiments**

   The mean travelling wave propagation velocity was calculated for each group (wild-type CBA/Ca basal, wild-type CBA/Ca apical, wild-type S129 basal, *Tecta*$^{Y1870C/+}$ basal, *Tectb*$^{-/-}$ basal and *Otoa*$^{EGFP/EGFP}$ basal), as presented in Figure 4.3 (p. 96) and Figure 5.3 (p. 121).

5. **Estimation of the viscoelastic moduli by fitting a homogenous isotropic Voigt body model to the average velocity data (as a function of frequency) for each group**

   Shear storage modulus (G', kPa) and shear viscosity (η, Pa·s) were estimated for each group (wild-type CBA/Ca basal, wild-type CBA/Ca apical, wild-type S129 basal, *Tecta*$^{Y1870C/+}$ basal, *Tectb*$^{-/-}$ basal and *Otoa*$^{EGFP/EGFP}$ basal) by fitting Equation 2.2 to the average travelling wave propagation velocity as a function of frequency (as presented in Figure 4.4, p. 97 and Figure 5.4, p. 122) (Chen et al., 2004).

$$v_s = \sqrt{\frac{2(G'^2 + \omega^2\eta^2)}{\rho(G' + \sqrt{G'^2 + \omega^2\eta^2})}} \qquad \textbf{Equation 2.2}$$

2.3.7.2 Amplitude

1. **Calibration**

   Calibration was applied to the recorded amplitudes at each frequency for each longitudinal position.

2. **An exponential decay ($y=A_{(0)}*e^{-\alpha*x}$) was fit to the amplitude data as a function of longitudinal distance at each frequency**

   Exponential decay curves were fit to the wave amplitude decay as a function of longitudinal distance (example Figure 2.15, A, black line) for each individual and for each frequency (as presented in Figure 4.5, p. 99; Figure 5.5, p. 125; Figure 5.7, p. 127; and Figure 5.9, p. 129). The plots of mean amplitude decay with longitudinal distance

are normalised to a representative 100 nm at x=0 (ie. $A_{(0)}$=100 nm) for the sake of simple interpretation, as this was close to the actual maximum radial displacement of the piezo (~80 nm).

3. **The decay constant was averaged for each frequency between experiments**

   Mean decay (α) and space (σ) constants were calculated for each group at each frequency (as presented in Figure 4.6, p. 100; Figure 5.6, p. 126; Figure 5.8, p. 128; and Figure 5.10, p. 130).

2.3.7.3 Waveforms

1. **Amplitude decays normalised to 100 nm displacement at 0 µm**

   Absolute values for TM displacement varied somewhat between preparations, with maximum displacement at the lower frequencies generally ~80 nm and varying proportionally for the higher frequencies (see Figure 2.9, A). This variation was most likely due to the quality of the attachment of the TM to the vibrating support. To control for this, relative amplitude decay rather than absolute amplitude was considered; the mean α (which describes decay independently of absolute amplitude) was used for each group at each frequency to produce a representative fit normalised to $A_{(0)}$=100 nm, ie. $y=100*10^{-9}*e^{-\alpha*x}$ (Figure 2.15, A, as presented in Figure 4.5, p. 99; Figure 5.5, p. 125; Figure 5.7, p. 127; and Figure 5.9, p. 129).

2. **Phase data was averaged between experiments before calculation of propagation velocity for each individual**

   Steps 1-2 of the phase analysis regime were performed. At this point the phase roll-off for each frequency (example shown in Figure 2.14, C) were normalised and averaged across experiments for each group (wild-type CBA/Ca basal, wild-type CBA/Ca apical, $Tecta^{Y1870C/+}$ basal, $Tectb^{-/-}$ basal and $Otoa^{EGFP/EGFP}$ basal, as presented in Figure 4.1 (p. 91) and Figure 5.1 (p. 118).

3. **The average phase data was "re-wrapped" and fit with a sine function ($y=c*\sin(d*x+f)$)**

   The Averaged phase roll-offs for each frequency for each group were "re-wrapped" ($y=\sin(\varphi/(360/\pi))$) and then fit with a sine function $y=c*\sin(d*x+f)$ (Figure 2.15, B).

4. **The fitted sine functions were multiplied by the normalised exponential functions**

   The average decay (normalised to representative 100 nm radial displacement at 0 µm longitudinal distance) was applied to the fitted sine function (Figure 2.15, C, examples shown in Figure 4.5, p. 99; Figure 5.5, p. 125; Figure 5.7, p. 127; and Figure 5.9, p. 129).

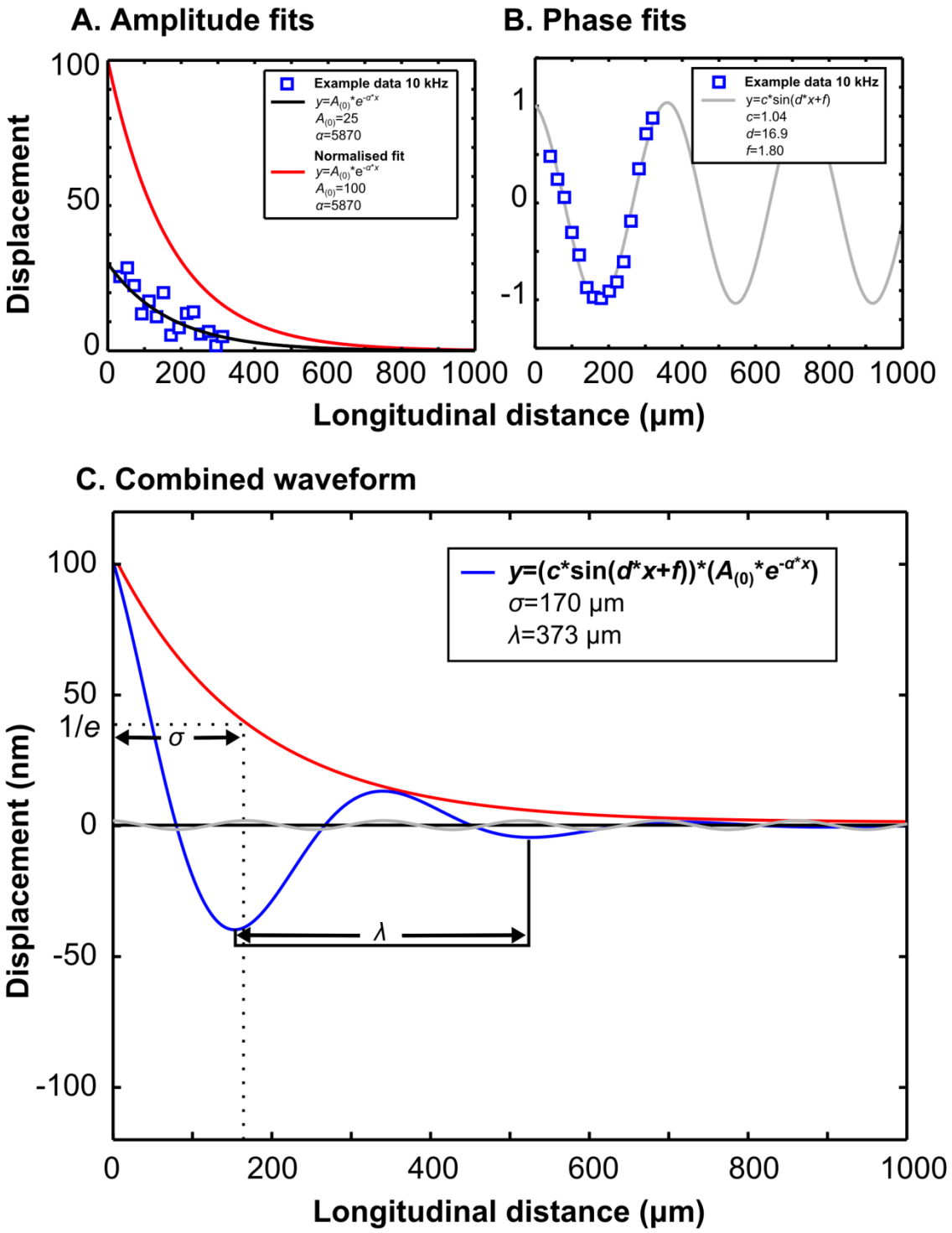

Figure 2.15 The fits applied to the amplitude and phase data. **A**. An exponentially decaying curve was fit to the amplitude data for each individual TM (black line). As the absolute values varied somewhat between experiments, the rate of decay, α, was used to produce a representative fit for each group at each frequency (red line, which represents a single frequency) where $A_{(0)}$=100 nm. **B**. A sine function was fit to the "re-wrapped" average phase data at each frequency for each group. **C**. The representative amplitude fit (red line) and the phase fit (grey line) were multiplied to produce a representation of the average travelling waveform (blue line).

2.3.7.4 Statistical analysis and fitting

All statistical analysis and curve fitting was performed in Matlab 2006b. The fitted viscoelastic moduli are presented ±SD and are compared, where appropriate, with Student's t-test. Values from previous work are quoted as published (usually mean±SD) and calculated mean values, such as travelling wave propagation velocity (v_s) are presented ±SD and are plotted on graphs as ±SE for visual clarity. *n*s are listed in tables and figures.

In the phase lag and amplitude decay graphs in Chapters 4 and 5 linear regressions is used to visually highlight certain gradients. Statistical information is provided for each fit, however is not intended to constitute a rigorous statistical test; for example, multiple comparisons are not account for. This information is provided for the sake of visual interpretation and in lieu of more a sophisticated model of analysis that will be the subject of future work (see Chapter 7.2.10, p. 166).

In Chapter 6 Matlab's anova1 function was used to perform a one-way analysis of variance on large pools of raw laser reflectivity data, followed by use of the multicompare function to assess individual significance of comparisons between each group. This function corrects for multiple comparisons and provides a convenient visualisation of the comparisons.

3 THE VESTIBULAR SYSTEM MEDIATES SENSATION OF LOW-FREQUENCY SOUNDS IN MICE

Gareth P. Jones, Ian J. Russell, Victoria A. Lukashkina, Andrei N. Lukashkin,

School of Life Sciences, University of Sussex, Falmer, Brighton, BN1 9QG, UK

3.1 Abstract

The mammalian inner ear contains sense organs responsible for detecting sound, gravity and linear acceleration, and angular acceleration. Of these organs the cochlea is involved in hearing while the sacculus and utriculus serve to detect linear acceleration. Recent evidence from birds and mammals, including humans, has shown the sacculus, a hearing organ in many lower vertebrates, has retained some of its ancestral acoustic sensitivity. Here we provide not only more evidence for the retained acoustic sensitivity of the sacculus, but also that acoustic stimulation of the sacculus has behavioural significance in mammals. We show that the amplitude of an elicited auditory startle response is greater when the startle stimuli are presented simultaneously with a low frequency masker, including masker tones that are outside the sensitivity range of the cochlea. Masker-enhanced auditory startle responses were also observed in otoconia-absent *Nox3* mice, which lack otoconia but have no obvious cochlea pathology. However, masker-enhancement was not observed in otoconia-absent *Nox3* mice if the low-frequency masker tones were outside the sensitivity range of the cochlea. This last observation confirms that otoconial organs, most likely the sacculus, contribute to behavioural responses to low-frequency sounds in mice.

KEY WORDS: cochlea; vestibular; sacculus; *Nox3* mouse; auditory startle; auditory masker.

3.2 Introduction

Mammals have a remarkable sense of hearing, with auditory ranges specifically adapted to their particular acoustic niche. This sensitivity is achieved mainly by the cochlea; a relatively new evolutionary adaptation compared to the much more ancient vestibular system. Recent studies have demonstrated however, that parts of the mammalian vestibular system, notably the sacculus, historically one of the first acoustically sensitive organs (Popper et al., 1982), have retained the ability to detect acoustic stimuli previously associated only with the cochlea. There is further evidence that this stimulation may have behavioural significance (Todd, 2001). Acoustic sensitivity of the sacculus in mammals might be expected as consequences of both its evolutionary history and anatomical location. In mice, for example, the sacculus is located behind the oval window membrane, directly in the line of vibration caused by movement of the stapes. It is clearly visible through the oval window once the stapes has been removed.

The vestibular systems of birds and mammals including cats (McCue and Guinan, 1994; McCue and Guinan, 1995), monkeys (Young et al., 1977), guinea pigs (Cazals et al., 1983b; Didier and Cazals, 1989) and pigeons (Wit et al., 1984) have been found to respond to acoustic stimuli, often with good evidence that the vestibular afferents innervating the sacculus are the most acoustically sensitive. Evidence from primates indicates that afferent projections from the sacculus reach the medial vestibular nucleus or inferior vestibular nucleus, which then projects bilaterally to the spinal cord (Stein and Carpenter, 1967). In humans, for example this pathway mediates Vestibular Evoked Myogenic Potentials (VEMPs), in which acoustic excitation of the vestibular system causes twitches in various muscles, most obviously the cervical muscles (Bickford et al., 1964; Ferber-Viart et al., 1999). Although the typical stimuli used are also within the human auditory range, an auditory origin of the VEMPS is ruled out by the fact that they still occur in patients with hearing loss (Sheykholeslami and Kaga, 2002; Wang and Young, 2003; Murofushi et al., 2005a).

With its ability to respond to acoustical stimulation, the vestibular system has the potential to extend the hearing range of mammals and hence their ability to detect low frequency sounds of behavioural significance. For example, the frequency range of the mouse cochlea, defined by sensitivity to sound stimulation below 80 dB SPL, is approximately 4-75 kHz, although this varies depending on age and mouse strain (Nyby, 2001). There are three areas of peak sensitivity that coincide with behaviourally relevant frequency ranges; the area of best sensitivity at the lower range is around 10-18 kHz and at ultrasonic frequencies, 40 kHz and 70 kHz ±10 kHz (Nyby, 2001; Müller et al., 2005).

In this paper we investigate whether mice can respond to low-frequency sounds. We demonstrate that low-frequency pure tones, which have stimulus parameters outside the sensitivity range of the mouse cochlea (Müller et al., 2005; Taberner and Liberman, 2005), can facilitate auditory startle responses (ASRs) caused by a high-frequency tone that is within the range of the frequency and sensitivity of the cochlea (Figure 3.1). This facilitation disappears in vestibular deficient mice proving that the vestibular system in mice can mediate the detection of low-frequency sounds.

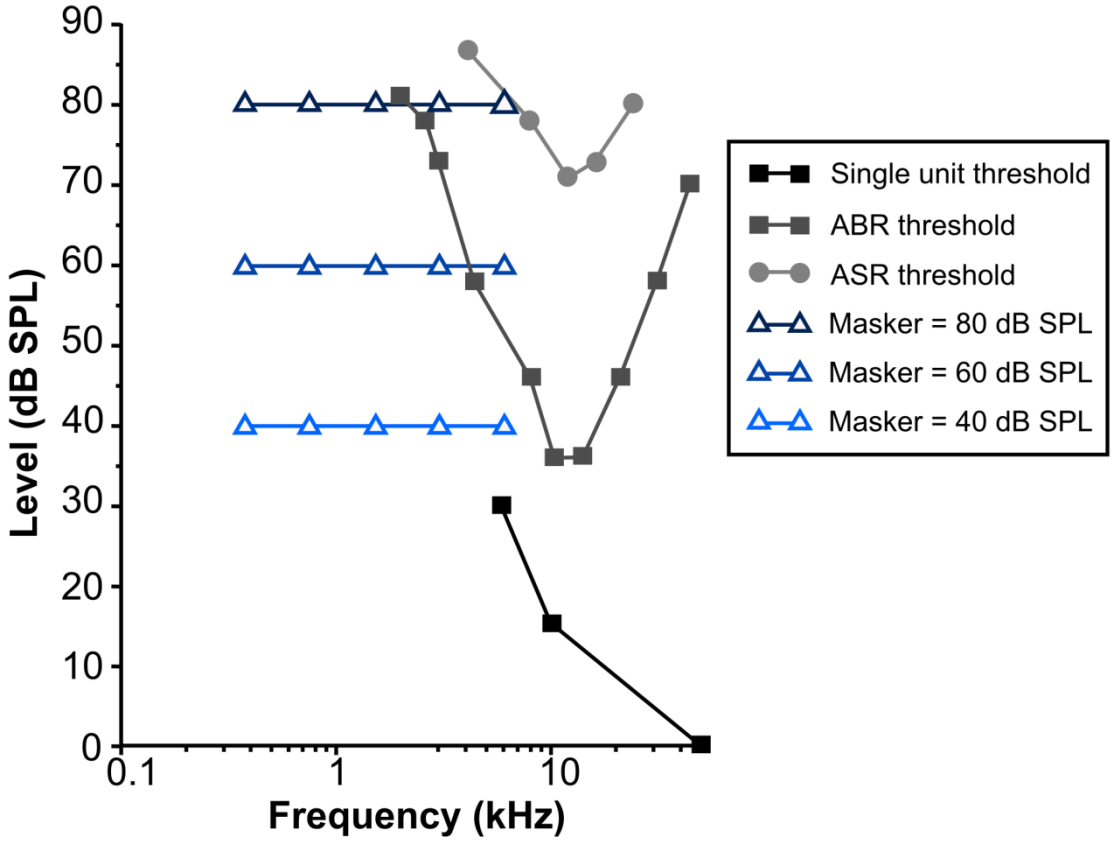

Figure 3.1 ASR, ABR, and single unit thresholds for CBA mice compared to the levels and frequencies used as background maskers in the experiments. Only the higher levels (60 dB SPL and 80 dB SPL) at the higher frequencies (3 kHz and 6 kHz) are above ABR threshold. Single unit recording from inferior colliculus neurons indicate that the higher frequencies may be detectable at 40 dB SPL. ASR threshold curve modified from Parham and Willott (1988). ABR threshold curve modified from Müller et al. (2005). Single unit threshold curve modified from Egorova et al. (2001).

3.3 Methods

3.3.1 Auditory startle response

The ASR is a short latency motor reflex in response to loud, abrupt sounds, common to most mammals. It is often used as a behavioural method to assess hearing in mice; ASR protocols are most revealing when a startle eliciting stimulus (probe) is used in conjunction with additional stimuli (maskers). The ASR can be modified by maskers presented simultaneously or preceding the startle stimulus. For example, Carlson and Willott (2001) employed simultaneous masker tones of different frequencies in conjunction with a probe stimulus to reveal facilitation of the elicited ASR. However, masker frequencies below the auditory range of the mouse cochlea have not been included in previous studies. The experiments described in this paper test the hypothesis that low frequency pure tones are detected by mice and are capable of modifying the ASR in a similar fashion to audible background tones.

3.3.2 Mice

In total two strains of mice were used; wild-type CBA/CaJ maintained at the University of Sussex and *Nox3 C57BL6/J* mice originally obtained from The Jackson Laboratory and then maintained and out bred to a CBA/CaJ background at the University of Sussex. All mice were housed individually for at least a week prior to experimentation and were used between 6-8 weeks old to avoid any complications caused by age related hearing changes. The *Nox3* mice carry a series of recessive mutations that knock out the NADPH oxidase 3 gene, preventing the development of the otoconia in the sacculus and utricle in homozygous mutants with consequent vestibular deficits (henceforth referred to as otoconia-absent *Nox3* mice) (Paffenholz, 2004). The ASR from CBA/CaJ mice was initially measured to provide baseline data because this particular mouse strain demonstrated a larger ASR amplitude. For the sake of clarity, results for the CBA/CaJ mice are presented separately to the otoconia-present *Nox3* mice as the absolute size of their ASRs varied slightly due to a small difference in weight between the litters of each type used.

3.3.3 Equipment setup

All experiments were conducted in an acoustic booth (IAC, UK). Pure tones for sound stimulation and white noise for sound calibration were generated digitally, converted to analogue by a DT3010/32 data acquisition board (Data Translation) at a rate of 200 kHz and presented through a pair of loudspeakers, one for the startle eliciting “probe” tone (2.5” Motorola piezo tweeter) and one for the background “masker” tone (3” Eurotec 8Ω loudspeaker). Sound pressure was monitored using a Bruel & Kjaer 4133 ¼ inch microphone.

The sound system was calibrated free field *in situ* for frequencies between 100-70,000 Hz. Known sound-pressure levels were expressed in dB SPL re: 2×10^{-5} Pa. Startle responses were recorded via an analogue accelerometer (laboratory designed and constructed) and digitized by the same data acquisition board at a rate of 200 kHz. The experimental chamber was arranged with both loudspeakers in front of the mouse to ensure binaural stimulation. The wire mesh cage was mounted on the accelerometer and was small enough to restrict the mouse's movements, which would otherwise diminish the ASR amplitude (Figure 3.2, A). Stimuli were presented only during periods in which the mouse was settled, as determined from video observation and accelerometer output.

3.3.4 Experimental paradigm

Each experiment involved manipulating 2 variables; masker frequency and probe level, with the masker level kept constant. The probe frequency was determined prior to starting the experiments by finding the most salient startle eliciting frequency. For both the CBA and the *Nox3/CBA* mice this was 14 kHz and was not changed over the course of the experiments. Suitable probe levels for eliciting the ASR were also determined prior to starting the experiments; for the CBA mice probe levels of 80 and 90 dB SPL were used and for the *Nox3/CBA* mice, 90 dB SPL (80 dB SPL was not used for the *Nox3/CBA* mice as it did not elicit a large enough ASR). Individual mice were subject to 3 experiments; one for each masker level (40, 60, and 80 dB SPL), separated by at least 24 hours. Each possible combination of stimulus conditions was presented to the mouse in randomised blocks. For example, for the CBA mice, the block size was 12 – containing all possible combinations of 2 different probe levels and 6 different masker conditions (Table 3.1). These blocks of presentations were repeated until a total of 120 presentations (10 for each masker frequency) had been performed (or a 1 hour time limit was reached). The "masker off" conditions were used as a baseline against which masked responses for the same probe level were normalised.

The presentation order of each individual probe/masker combination is shown in Figure 3.2, B (without masker) and Figure 3.2, C (with masker). The onset of the masker always preceded that of the probe by 2 seconds and was on for a total of 3 seconds. The probe stimulus had a rise/fall time of 2 ms to increase its startle saliency, whereas the masker tone had a longer 10 ms rise/fall time in order to avoid it potentially eliciting a startle at its onset at the higher levels.

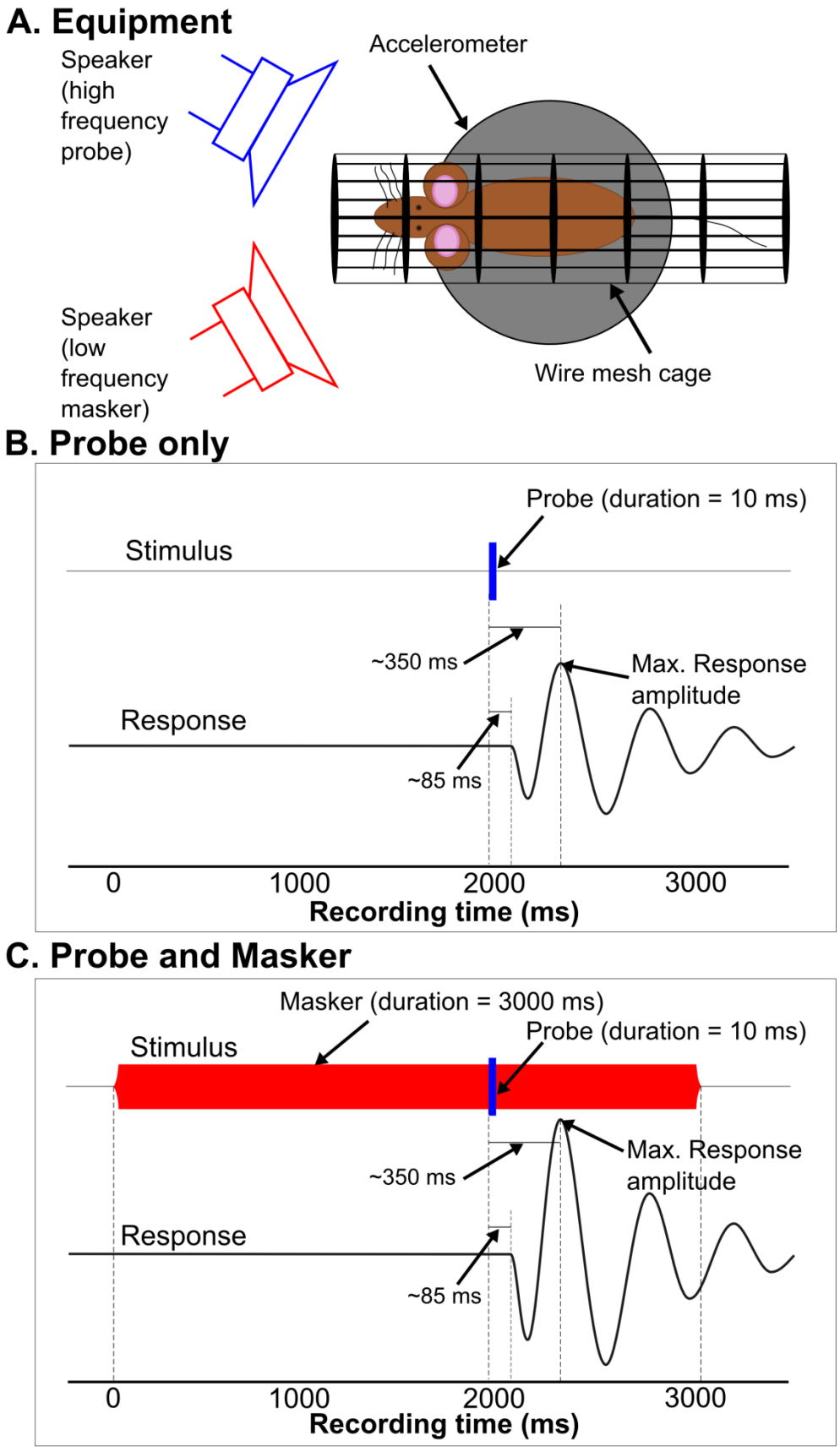

Figure 3.2 Startle chamber schematic and the temporal order of presentations. **A**. Schematic of the presentation chamber. **B**. The temporal order of probe alone presentations **C**. The temporal order of probe and masker presentations. The onset of the masker preceded that of the probe by 2000 ms and continued for a total of 3000 ms.

Probe level (dB SPL)	Masker frequency (kHz)					
80	Masker off	0.375	0.75	1.5	3	6
90	Masker off	0.375	0.75	1.5	3	6

Table 3.1 The 12 possible probe and masker combinations, using 2 probe levels and 6 masker frequencies (including no masker). Each block of 12 was randomised before presentation.

ASRs were normalised by dividing the ASR to the combination of probe tone and masker (P_M) by the ASR to the probe tone alone (P_0). In Figure 3.3, Figure 3.5, Figure 3.6, and Figure 3.7 the normalised data are expressed as the "Startle Ratio" (P_M/P_0). After normalisation, multi-way repeated measures ANOVAs were performed with startle ratio as the dependent on the data. Post-hoc two way *t*-tests were then performed on each masker frequency/level combination against the normalised response to the probe on its own to indicate which masker conditions significantly facilitated the ASR amplitude. These comparisons were judged significant at p=0.01 (Bonferroni correction of p=0.05 for 5 multiple comparisons) and are indicated on the graphs with asterisks. Data and statistical analysis were performed in Matlab R2006b (The MathWorks, Inc.) and Origin 7 (OriginLab Corporation).

All *Nox3/CBA* mice used were bred from heterozygous parents and were phenotyped after completion of the experiments. Attempts to use behavioural assays to identify the otoconia-absent *Nox3* mice proved unreliable and the mice were not genotyped due to cost and lack of necessity, as such all experiments using the mice were conducted blind. The homozygous mutants were identified post mortem, after completing all experiments by inner ear dissection. The presence (or lack) of otoconia in the sacculus was checked visually via the oval window after removal of the stapes. Out of a total of 38 dissections from 4 separate litters, 10 otoconia-absent mice were identified, 6 of which were prior used in the ASR experiments. The numbers of mice for each group used in the behavioural experiments are 8, 4, 4 for CBA mice, otoconia-present mice and otoconia-absent mice respectively. The numbers of otoconia-present mice used for the CAP and DPOAE experiments are 5 and 9 respectively. The corresponding numbers for otoconia-absent mice are 3 and 3 (see Figure 3.4).

To measure distortion product otoacoustic emissions (DPOAEs) and compound action potentials of the auditory nerve (CAPs), mice were anaesthetized with ketamine (0.12 mg/g body weight i.p.) and xylazine (0.01 mg/g body weight i.p.) for DPOAE procedures or with Urethane (ethyl carbamate, 2 mg/g body weight, i.p.) for CAP procedures. The animals were

tracheotomized, and their core temperature was maintained at 38°C. To measure CAPs, a caudal opening was made in the ventrolateral aspect of the right bulla to reveal the round window. CAPs were measured from the round window membrane using glass pipettes filled with artificial perilymph with tip diameters of 50-100 μm (recording bandwidth > 30 kHz). Signals were amplified with a recording bandwidth of DC-100 kHz.

To measure DPOAEs and CAPs, sound was delivered via a probe with its tip within 1 mm of the tympanic membrane and coupled to a closed acoustic system comprising two MicroTech Gefell 1 inch MK102 microphones for delivering tones and a Bruel & Kjaer 3135 ¼ inch microphone for monitoring sound pressure at the tympanum. The sound system was calibrated *in situ* for frequencies between 1-70 kHz using a measuring amplifier and known SPLs were expressed in dB SPL re: $2x10^{-5}$ Pa. White noise and tone pulses with rise-fall times of 0.2 ms were synthesized by a Data Translation 3010 data acquisition board, attenuated, and used for sound system calibration and the measurement of electrical and acoustical cochlea responses. To measure DPOAEs, the levels of the f2 tone were set 10 dB SPL below that of the f1 tone with the frequency ratio of f2/f1 set to 1.23. DPOAE threshold curves were constructed from measurements of the level of the f2 tone that produced a 2f1–f2 DPOAE with a level of 0 dB SPL. System distortion during DPOAE measurements was 80 dB below the primary tone levels. On the basis of laser diode interferometer measurements from the spiral lamina and bony wall of the mouse cochlea (Legan et al, 2000; unpublished data), only sound pressure and not linear acceleration was delivered to the cochlea at levels and frequencies within the range of the sound system used in these experiments.

All procedures involving animals were performed in accordance with UK Home Office regulations with approval from the local ethics committee.

3.4 Results

3.4.1 Wild-type mice

Multi-way repeated measures ANOVA of the ASRs recorded from the CBA mice (Figure 3.3) with startle ratio as the dependent variable and probe level, masker level and masker frequency as factors showed significant effects of probe level (p<0.001, F=30.6, df=1), masker frequency (p<0.001, F=92.6, df=5) and masker level (p<0.001, F=47.1, df=2). Interactions were also observed between masker frequency and masker level (p<0.001, F=11.7, df=10); ASRs recorded in the presence of masker tones increased in amplitude with masker level and frequency (Figure 3.3). Data points shown to be significantly different (two way t-test) to the probe only baseline are marked with an asterisk (p=0.01 or better). These maskers included frequencies within and below the range of the mouse cochlea (Figure 3.1). Facilitation in the presence of masker frequencies, which are below the frequency range and sensitivity of the cochlea (masker frequencies 1.5 kHz, 0.75 kHz and 0.375 kHz), caused facilitation when presented at levels of 60 dB SPL and above. No significant facilitation was observed for any of the masker frequencies when presented at the lowest masker level (40 dB SPL), except for at 6 kHz.

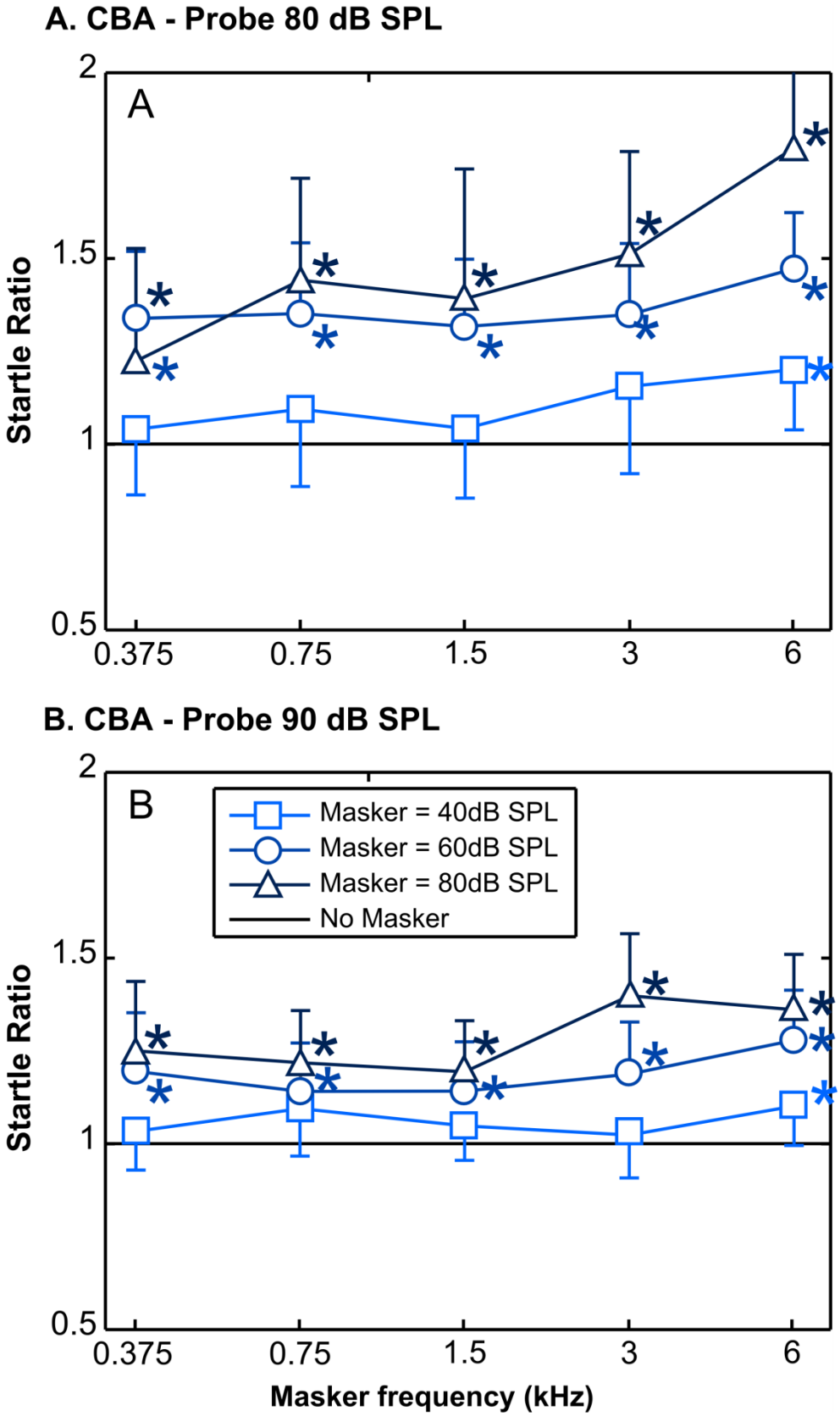

Figure 3.3 Startle ratio as a function of masker frequency for CBA mice (startle amplitude, compared to that due to the probe tone on its own, y=1). **A**. 80, 14 kHz probe. **B**. 90 dB SPL, 14 kHz probe. In this and all subsequent figures, startle ratio is the ASR due to the combination of probe tone and masker (P_M) divided by the ASR to the probe tone alone (P_M/P_0). Error bars indicate standard deviation; asterisks indicate significance at p≤0.01; n=7 for 40 and 60 dB SPL points for both probes; n=8 for all 80 dB SPL maskers.

3.4.2 *Nox3* mice

Cochlea function in homozygous *Nox3* mutant mice that lack otoconia is not affected (Paffenholz, 2004). This observation was confirmed in our study through the measurement of similar DPOAE and CAP audiograms from *Nox3* mice regardless of the presence or absence of otoconia in the macula of the sacculus (Figure 3.4).

The ASRs recorded from the otoconia-present littermates of the otoconia-absent *Nox3* mice exhibited similar facilitation to the CBA mice (Figure 3.5), whereas this facilitation differed for the otoconia-absent mice (Figure 3.6). Multi-way repeated measures ANOVA with startle ratio as the dependent variable and phenotype, masker frequency and masker level as factors showed significant effects of phenotype (p<0.001, F=40.7, df=1), masker frequency (p<0.001, F=14.3, df=4) and masker level (p<0.001, F=37.1, df=2). Interactions occurred between phenotype and masker frequency (p<0.001, F=5.27, df=4) and between masker frequency and masker level (p<0.001, F=4.14, df=8). As with the CBA mice, the ASR of otoconia-present mice was facilitated for all masker frequencies when presented at 80 dB SPL. Facilitation at lower masker levels (40 dB SPL and 60 dB SPL) occurred only at 6 kHz (Figure 3.5). This facilitation was again generally greater for higher frequencies (3 kHz and 6 kHz) but still present for the masker frequencies below the mouse's auditory range (1.5 kHz, 0.75 kHz and 0.375 kHz). Again facilitation increased with masker level for all frequencies, although with a higher threshold; between 60-80 dB SPL compared to between 40-60 dB SPL for the CBA mice. The ASRs of otoconia-absent *Nox3* mice were facilitated only by masker frequencies well within the auditory range of the mouse cochlea, at frequencies 3 kHz (at 80 dB SPL) and 6 kHz (at 60 dB SPL and above) (Figure 3.6). No significant facilitation was observed for the lower frequency maskers at any level.

Figure 3.7 shows a comparison of the 80 dB SPL masker levels for each group of mice. Multi-way ANOVA of this data with startle ratio as the dependent variable and phenotype and masker frequency as factors indicates significant effects of phenotype (p<0.001, F=11.0, df=2), masker frequency (p<0.001, F=61.5, df=5) and interaction between phenotype and masker frequency (p<0.001, F=4.86, df=10).

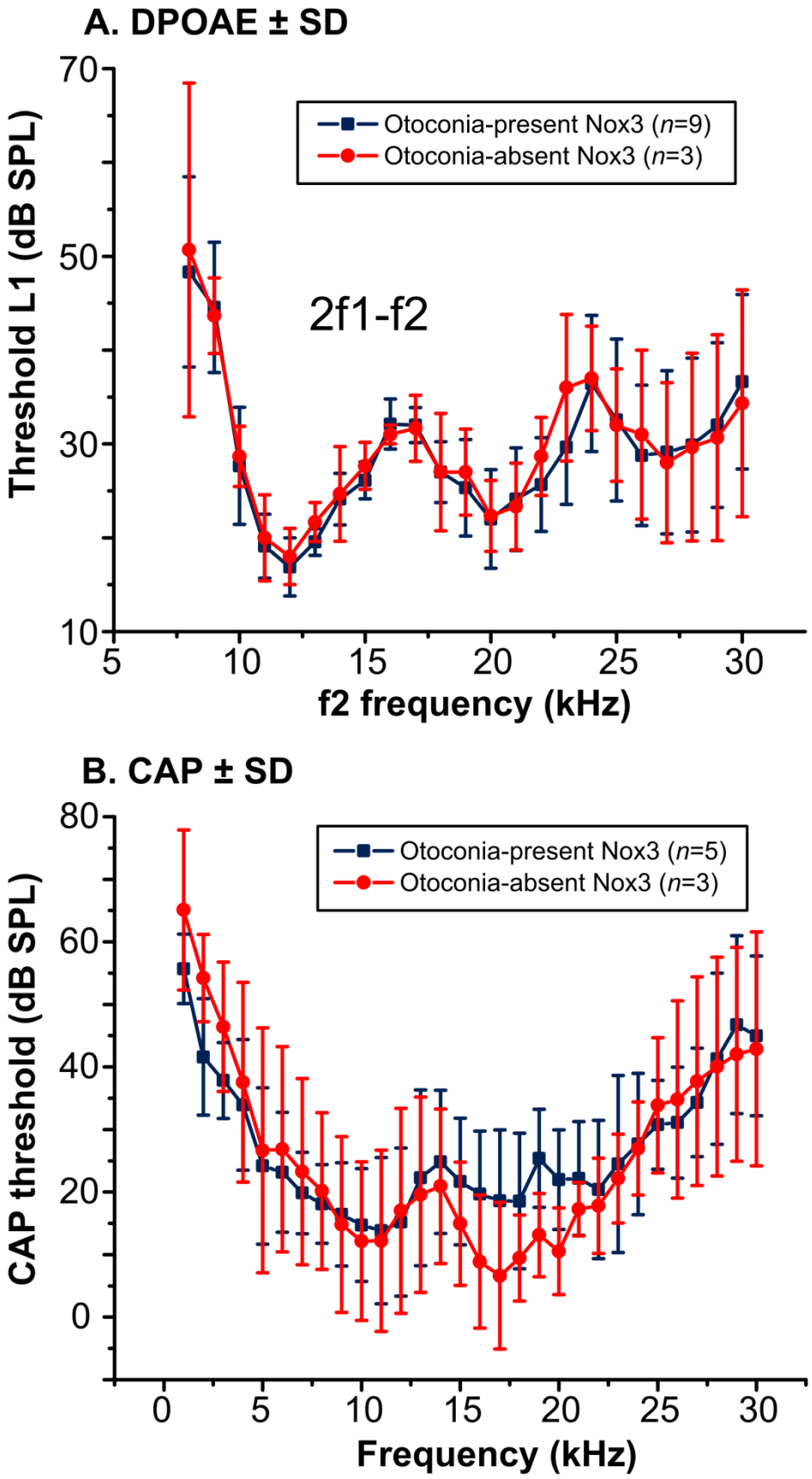

Figure 3.4 Threshold levels of acoustical responses for the *Nox3* mice. **A**. Threshold level L1 (mean±SD) of the low-frequency primary f1 required to generate 0 dB SPL DPOAE at frequency 2f1-f2 for different frequencies of the high-frequency primary f2 **B**. CAP threshold levels (mean±SD) for pure-tone stimulation.

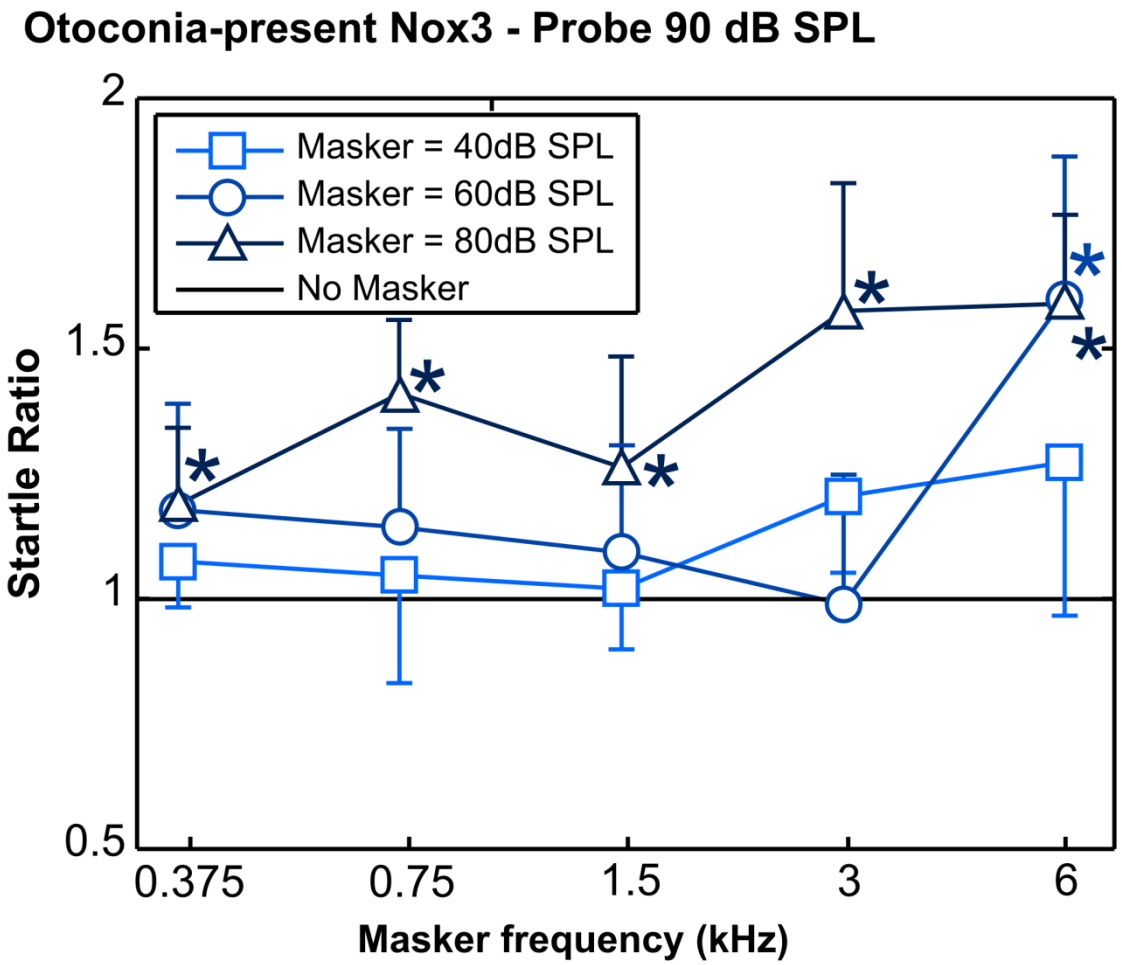

Figure 3.5 Startle ratio as a function of masker frequency for otoconia-present *Nox3* mice (startle amplitude, compared to that due to the probe tone on its own, *y*=1). *n*=4 for all points, error bars ±SD.

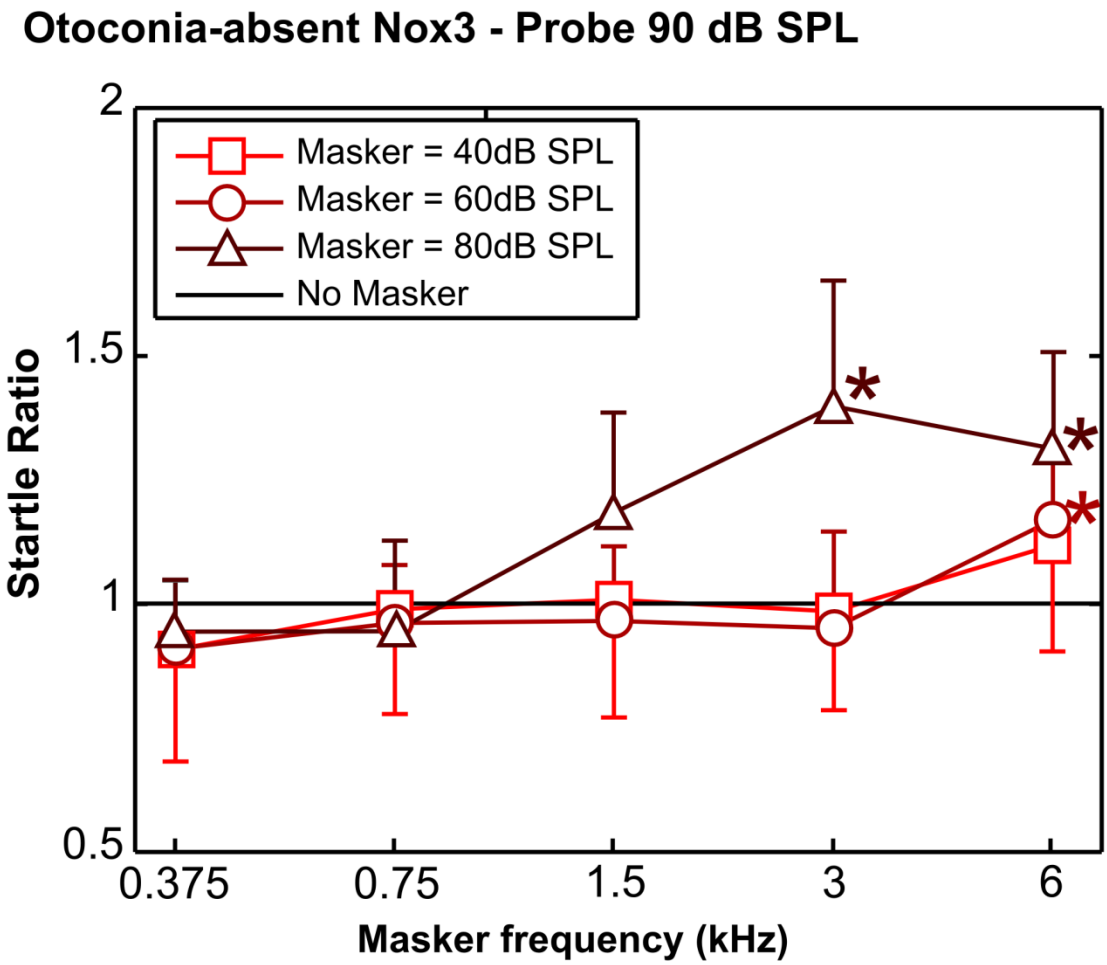

Figure 3.6 Startle ratio as a function of masker frequency for otoconia-absent *Nox3* mice (startle amplitude, compared to that due to the probe tone on its own, y=1). n=4 for all points, error bars ±SD.

3.5 Discussion

3.5.1 Otoconia-present *Nox3* mice

ASRs measured in CBA and otoconia-present *Nox3* mice were facilitated at all masker frequencies that were tested. The maskers at 3 kHz and 6 kHz are within the frequency range of the cochlea and were delivered at levels within its range of sensitivity. It is highly likely, therefore, that the facilitation of the ASRs at these frequencies was mediated via the cochlea and auditory nerve. Effective facilitation of the ASR was also achieved with maskers at frequencies (0.375, 0.75, 1.5 kHz) and levels (80 dB SPL) outside the frequency – sensitivity range of the mouse cochlea, as measured from threshold, single unit, auditory nerve data (Taberner and Liberman, 2005) and auditory brainstem responses (Figure 3.1). The facilitation must, therefore, be a result of input from another sensory modality that is also excited, albeit indirectly, by sound pressure (see methods).

3.5.2 Otoconia-absent *Nox3* mice

In contrast to the CBA and otoconia-present *Nox3* mice, ASRs recorded from the otoconia-absent *Nox3* mice were not facilitated by masker frequencies below 3 kHz (Figure 3.7), even though DPOAE and CAP audiograms from otoconia-present or otoconia-absent *Nox3* mice are indistinguishable (Figure 3.4). The *Nox3* mutation is reported to affect only the otoconia of the vestibular system (Paffenholz, 2004). In agreement with this observation, our dissections of the peripheral auditory system did not reveal any other abnormalities in the gross structure of the inner ear at the macroscopic level, with the cochlea and vestibular apparatus appearing to be similar in both otoconia-present and otoconia-absent *Nox3* mice. The ASR thresholds were very similar for all 3 groups of mice, although the ASR amplitude was slightly smaller for the *Nox3* mice, due to individuals in these litters of mice being slightly smaller than the mice in the CBA litters.

On the basis of our observations that tones with frequencies below 3 kHz facilitate ASRs caused by audible tones in otoconia-present *Nox3* mice but not in otoconia-absent *Nox3* mice, where the otoconia are missing from the gravitational receptors, we propose that at least two systems are implicated in the ASR facilitation. The cochlea mediates facilitation with the masker tones above 3 kHz and the vestibular system (most likely the sacculus) mediates facilitation for masker tones with frequencies below 3 kHz. This proposal is also supported by the finding that one of the two peaks observed in VEMPs is of vestibular origin with the other of cochlea origin (Ferber-Viart et al., 1999). Cross modal modification of the ASR by the sacculus/utricle has been described previously using free fall rather than acoustic stimulation

of the vestibular system (with the facilitation being greatest when the stimulation of each modality was temporally synchronised relative to the point of summation) (Yeomans et al., 2002).

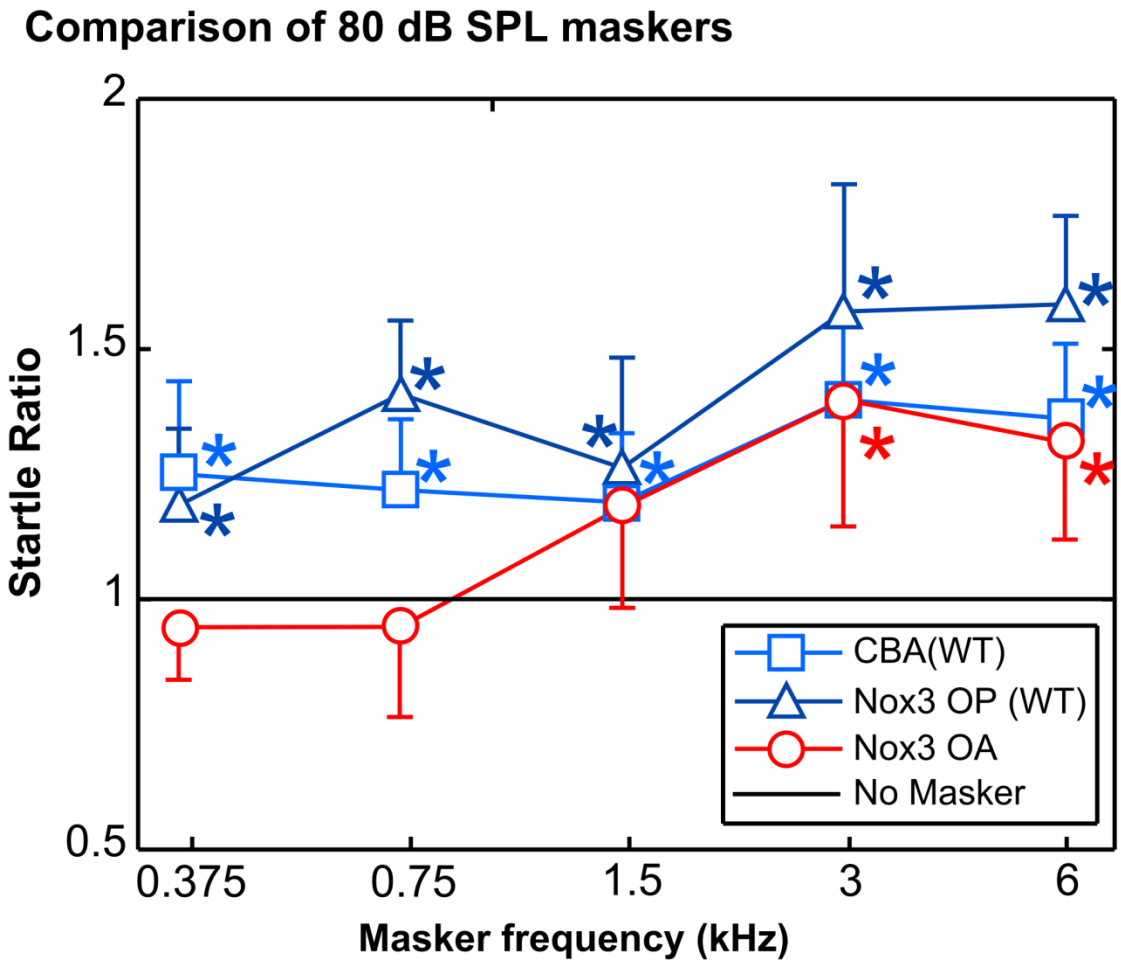

Figure 3.7 Startle ratio, as a function of masker frequency (80 dB SPL) for CBA, otoconia-present (OP) *Nox3*, and otoconia-absent (OA) *Nox3* mice (startle amplitude, compared to that due to the probe tone on its own, y=1). Error bars ±SD.

The neuronal circuitry underlying the ASR is thought to involve the caudal pontine reticular nucleus (PnC) innervating motor neurons and receiving input from brainstem nuclei including the dorsal cochlea nucleus (DCN), cochlear root nucleus (CRN), medial cochlear nucleus (MCN) and lateral superior olive (LSO) (Koch, 1999). Of these innervating nuclei, the CRN pathway has the shortest latency and depolarises cells in the PnC to close to firing threshold. It is hypothesised that any further input from the other nuclei will then elicit a startle response (Koch, 1999). It has been shown that the sacculus has projections reaching the DCN (Burian and Gstoettner, 1988), providing a possible mechanism by which it can facilitate the ASR. Perhaps a more parsimonious explanation for the augmentation of the acoustically activated ASR through acoustic activation of the vestibular system is that the vestibular signals activate

the limbic system, ie. rumbling, low-frequency, vibrations cause anxiety, thereby eliciting a stronger startle response. Support for this latter suggestion has yet to be forthcoming because, for example, Schanbacher (1997) discovered that lesions of the amygdala do not affect the enhancement of the auditory startle response by background noise. These proposed mechanisms also predict that, as observed in the data presented in this paper, vestibular stimulation by acoustic stimuli is not necessarily capable of eliciting an ASR independently of acoustic stimuli within the range of the cochlea (at least not by the same auditory pathway). Acoustic stimulation of the vestibular system can, however, contribute to a concurrent ASR elicited by a cochlear pathway (which activates the PnC).

The data in this paper supports and extends previous studies showing the retained acoustic sensitivity of the mammalian sacculus and for the first time demonstrates how this detection has a physiologically significant effect on an important behavioural reflex.

3.6 Acknowledgements

We thank Mr James Hartley for technical support. GPJ was supported by a research studentship from the BBSRC. Research was supported by the MRC.

4 MECHANICAL PROPERTIES OF THE WILD-TYPE MOUSE TECTORIAL MEMBRANE

4.1 Abstract

The tectorial membrane (TM) is viscoelastic and is able to propagate travelling waves over a significant longitudinal distance. The characteristics of this travelling wave depend on the physical properties of the TM and are measured using a new method; a laser interferometer focused on the marginal edge of isolated TM segments. Phase and amplitude data are recorded from the basal and apical regions of wild-type mice. From these data the capacity of the TM to couple energy longitudinally along the cochlea and its viscoelastic properties (shear storage modulus, G' and shear viscosity, η) are estimated and wave amplitude tracked (decay constant, α and corresponding space constant, σ). The values are compared between the two regions and indicate that apical TM segments are mechanically and structurally different to those from the basal region of the cochlea.

4.2 Introduction

In the cochlea of the mammalian inner ear, the TM is positioned above, and in contact with, the longest stereocilia of the outer hair cells (OHCs) (Lim, 1972). These electrically motile hair cells actively feed energy into the system with timing mediated by the interaction of the motion between the TM and BM, providing the mechanical basis for the cochlea's extraordinary sensitivity and frequency resolution (Gummer et al., 1996; Lukashkin et al., 2010). Only recently has much attention been paid to the material and mechanical properties of the TM (Abnet and Freeman, 2000; Freeman et al., 2003a; Freeman et al., 2003b; Richardson et al., 2008; Lukashkin et al., 2010). Exactly how the TM interacts with the OHC hair bundles has implications for the gain and timing of the cochlea amplifier, and measurements from *Tectb*$^{-/-}$ mice show how the mechanical properties of the TM can affect tuning and sensitivity (Russell et al., 2007). It has been hypothesised the TM controls the spatial extent of OHC excitation (ie. the number of OHCs coupled), which is reduced in the *Tectb*$^{-/-}$ mice (Lukashkin et al., 2010). Previous estimates of the structural properties of the TM have been made (Abnet and Freeman, 2000; Shoelson et al., 2004; Gueta et al., 2006; Gu et al., 2008; Gavara and Chadwick, 2009), but not under physiologically realistic conditions. Due to the viscoelastic nature of the TM (Freeman et al., 2003a), its properties are dynamic, meaning they vary with stimulus properties such as frequency and amplitude. Recent work by Ghaffari et al. (2007, 2008, 2010) improves on previous static TM measurements by stimulating isolated TM segments with acoustic frequencies (1-18 kHz). Radial sinusoidal displacement was applied to one end of an isolated segment of TM by a piezo, resulting in the establishment of a travelling wave that propagates away from the piezo. The properties of the travelling wave, such as the relationship between stimulus frequency and propagation velocity, or spatial decay of the wave's amplitude with longitudinal distance, can be used to estimate the TM's mechanical properties. The data presented in this chapter takes another step towards realistic measurement conditions by using a new laser interferometer based method to track the induced travelling waves along isolated segments of TM. The sensitivity of the laser interferometer (0-84 nm) allows physiologically realistic stimulus amplitudes to be used at acoustic frequencies (1-20 kHz). This is significant as both frequency and amplitude of stimulation affect the velocity at which the TM is radially displaced during stimulation. The velocity of stimulation has implications both for fluid effects inside the TM gel and for fluid damping relative to the external fluid in the isolated preparations.

Data was collected from two wild-type groups; CBA/Ca (the wild-type litter mates of *Tectb*$^{-/-}$ mutants, including a combination of Tectb$^{+/+}$ and Tectb$^{+/-}$ mice) and wild-type mice on

an S129 background. Amplitude and phase data from apical and basal regions were collected from the CBA/Ca group. Phase data from the basal region were collected from the S129 group. Both of these groups of mice exhibit normal hearing, with no phenotypical difference between the $Tectb^{+/+}$ and $Tectb^{+/-}$ (Russell et al., 2007) mice composing the CBA/Ca group. The data collected from the S129 background strain were used as both verification of phenotypical normality of the $Tectb^{+/-}$ in the CBA/Ca group and, along with comparisons to similar methodologies, verification of the laser interferometer method as well.

4.2.1 Mechanical investigation of the tectorial membrane

The viscoelastic properties of the TM, G' and η, were estimated from the relationship between wave propagation velocity and stimulus frequency based on a linear Voigt body description of a viscoelastic medium (Equation 2.2, p. 66) (Chen et al., 2004). The wave propagation velocity was calculated using Equation 2.1 (p. 66). Change in phase with distance (phase roll-off) was tracked for stimulus frequencies 1-20 kHz over the length of a basal or apical TM segment in 1 kHz steps. Longitudinal coupling of energy along the TM was measured by tracking radial displacement amplitude longitudinally for frequencies 2-20 kHz and calculating the exponential decay. The decay for each stimulus frequency was fit with an exponential decay cure ($y=A_{(0)}*e^{-\alpha*x}$) and the decay constant, α, used to calculate the distance over which the wave decays by a factor of $1/e$ (the space constant, σ). The waveforms of the propagating travelling waves were generated from the normalised exponential decays and sine waves fit to the average rate of phase roll-off at each frequency ($y=c*\sin(d*x+e)$).

Phase and amplitude data are presented with linear fits to the 1-10 and 11-20 kHz stimulus frequency ranges. Linear regression was used to compare these fits to $y=0$ and to visualise the relationships of these measurements to the stimulus frequency, rather than as a definitive statistical analysis of the relationship. As such, an indication of possible statistical significance of individual fits is presented at the $p=0.05$ level, without correcting for multiple comparisons.

4.2.2 Aims

1. To establish and test the new laser interferometer-based method for tracking travelling waves in *ex vivo* segments of TM.
2. Estimate the viscoelastic properties of the TM from measurement of wave propagation velocity as a function of frequency. And compare these values between TM segments from apical and basal cochlear regions.

3. Measure the spatial extent of longitudinal coupling in the TM from the amplitude decay of propagating travelling waves, and compare these values between TM segments from apical and basal cochlear regions.
4. Calculate the waveform of the travelling waves and compare between TM segments from apical and basal cochlear regions.
5. Establish a baseline set of data against which the properties of TM mutant mice can be compared.

4.3 Results

4.3.1 Phase delay

For all wild-type groups, phase lag with longitudinal distance generally increased as a function of stimulus frequency (1-20 kHz) (Figure 4.1, A-C). For the two basal groups, the greatest phase lag averaged 375° (1.04 cycles) over a longitudinal distance, *r*, of 390 µm (wild-type CBA/Ca basal at 17 kHz, Figure 4.1, A) and 310° degrees (0.86 cycles) over 350 µm (wild-type S129 basal at 13 kHz, Figure 4.1, B). The maximum phase roll-off for these basal groups was 0.96 and 0.89 °µm^{-1}, respectively (Figure 4.2). The maximum phase lag was greater in the apical region, averaging 355° (0.99 cycles) over a distance of 280 µm (at 19 kHz) at a rate of 1.27 °µm^{-1} (Figure 4.1, C).

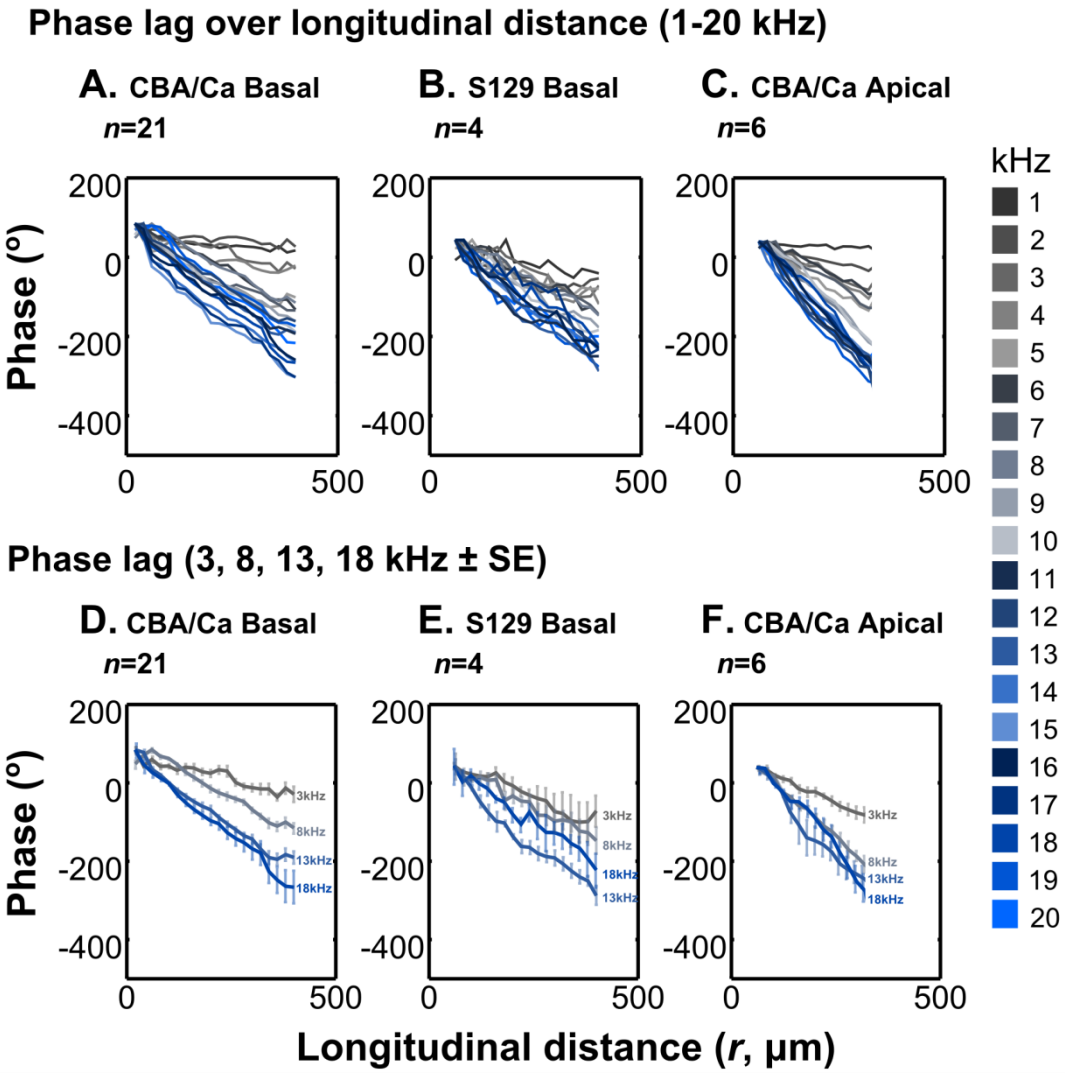

Figure 4.1 Comparison of the phase lag between the wild-type TM segments (normalised to 0° at 100 µm). **A-C**. Phase lag at each stimulus frequency between 1-20 kHz increased as a function of longitudinal distance for basal (A, B) and apical (C) segments from wild-type mice. D-E. Phase lag as a function of longitudinal distance for stimulus frequencies 3, 8, 13 and 18 kHz. For visual clarity error bars are shown as standard error.

For all three wild-type groups the general trend was a monotonic increase of maximum phase lag with stimulus frequency for frequencies ≤10 kHz, which slowed markedly for frequencies ≥11 kHz (Figure 4.2, A-C). There was variability within this trend; for example the greatest average phase lag for each group (as quoted above) did not necessarily occur at 20 kHz, although the error bars in Figure 4.2 indicate they do fit within the general trend. This was due to an increase in variability of the phase measurements at the highest stimulus frequencies and the closer grouping of maximum phase lag of the higher stimulus frequencies. The variability in the phase measurement was due partly to the decrease in amplitude of the stimulating piezo with increasing frequency; at 19 and 20 kHz, the stimulus amplitude was closer to the noise floor. Phase measurements at 18 kHz, however, provide a good trade-off between frequency and amplitude of the stimulus and Figure 4.1, D-E shows phase lag as a function of stimulus frequency between 3-18 kHz in 5 kHz steps. At 18 kHz the total phase lag over a distance of 390 µm in the basal region of the cochleae of wild-type CBA/Ca mice averaged 337^{o}=0.86 $^{o}\mu m^{-1}$, over a distance of 350 µm, in the basal region of the cochleae of wild-type S129 mice phase lag averaged 255^{o}=0.72 $^{o}\mu m^{-1}$, and over a distance of 280 µm in the apical region of the cochleae of wild-type CBA/Ca mice phase lag averaged 315^{o}=1.13 $^{o}\mu m^{-1}$ (3, 8, 13 and 18 kHz summarised in Table 4.1).

The total phase lag as a function of stimulus frequency over the available longitudinal stretches of TM for each group is plotted in Figure 4.2, A-C. The slopes are indicated by linear fits; dashed black regression lines for stimulus frequencies in the steep 1-10 kHz range and dashed red regression lines in the 11-20 kHz range. The fits to the lower stimulus frequency range (1-10 kHz, dashed black regression lines) for each group have gradients that appear significantly different to y=0: wild-type CBA/Ca basal gradient=21.0 $^{o}Hz^{-1}$, p<0.001, wild-type S129 basal gradient=16.8 $^{o}Hz^{-1}$, p<0.001 and wild-type CBA/Ca apical gradient=22.8 $^{o}Hz^{-1}$, p<0.001. Whereas none of the fits to the higher frequency range (11-20 kHz, dashed red regression lines) appear significantly different to y=0: wild-type CBA/Ca basal gradient=4.66 $^{o}Hz^{-1}$, p=0.440, wild-type S129 basal gradient=-3.28 $^{o}Hz^{-1}$, p=0.304 and wild-type CBA/Ca apical gradient=2.96 $^{o}Hz^{-1}$, p=0.183. The corresponding phase roll-off for each group (Figure 4.1, D-F) exhibited the same trend; fits to lower stimulus frequencies appeared significantly different from y=0 and the plateau at the higher stimulus frequencies did not appear significant from y=0. 1-10 kHz frequency fits: wild-type CBA/Ca basal gradient=0.0537 $^{o}\mu m^{-1}Hz^{-1}$, p<0.001, wild-type S129 basal gradient=0.0481 $^{o}\mu m^{-1}Hz^{-1}$, p<0.001 and wild-type CBA/Ca apical gradient=0.0813 $^{o}\mu m^{-1}Hz^{-1}$, p<0.001. 11-20 kHz frequency fits: wild-type CBA/Ca basal gradient=0.0119 $^{o}\mu m^{-1}Hz^{-1}$, p=0.440, wild-type S129 basal

gradient=-0.0094 $^{o}\mu m^{-1}Hz^{-1}$, p=0.304 and wild-type CBA/Ca apical gradient=0.0106 $^{o}\mu m^{-1}Hz^{-1}$, p=0.183. The gradients of these fits represent the rate of change of phase roll-off with frequency (ie. acceleration of phase change) and indicate that it varies between lower (1-10 kHz) and higher (11-20 kHz) stimulus frequencies in both apical and basal wild-type TM segments.

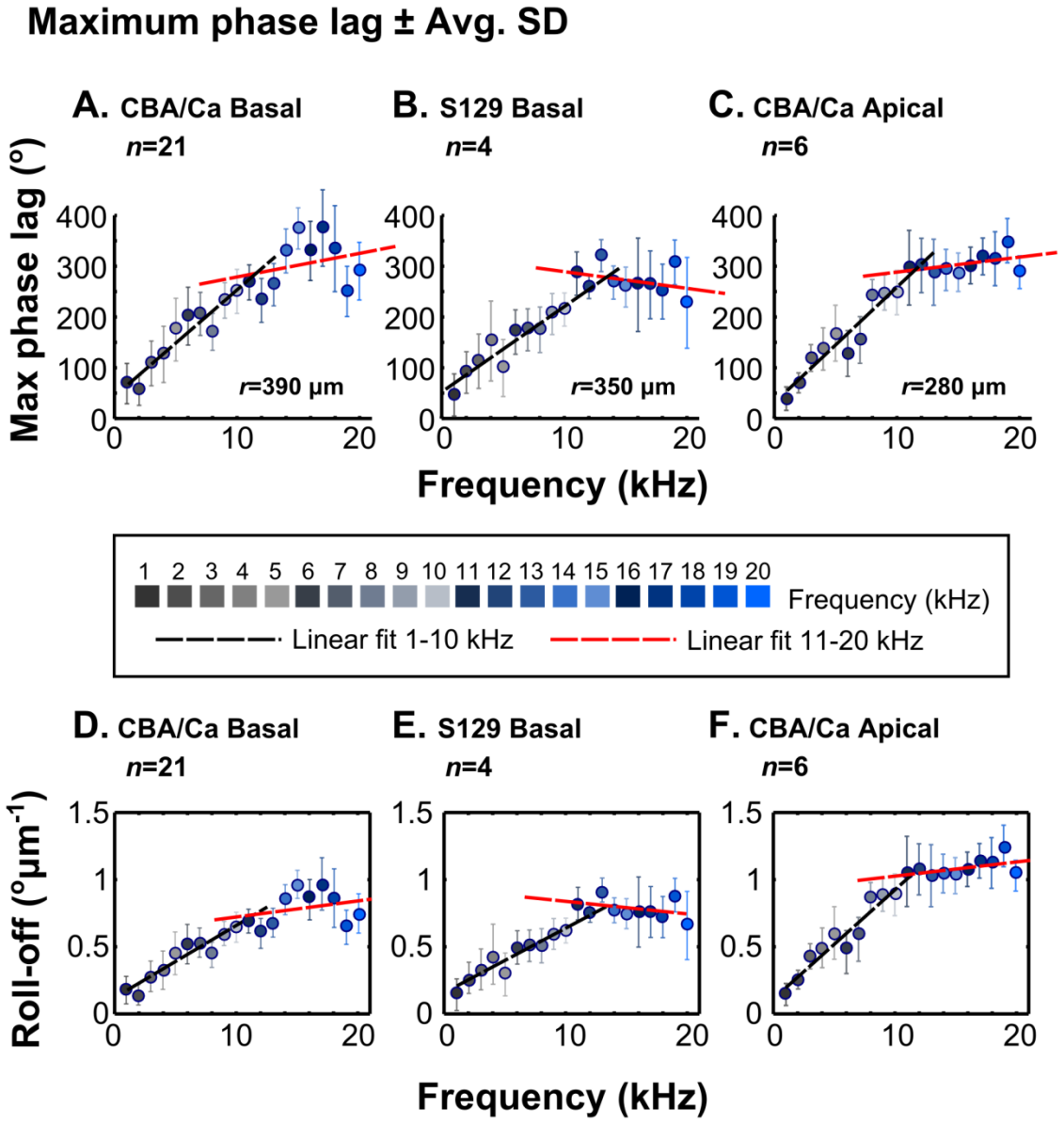

Figure 4.2 Comparison of the total phase lag and phase roll-off between the wild-type TM segments. **A-C**. The maximum average phase lag as a function of frequency over a set longitudinal distance, *r*, for each wild-type group. Error bars are the average standard deviation of the preceding longitudinal points. The maximum phase lag for the wild-type CBA/Ca apical group (**C**) where *r*=280 µm is similar to that of the wild-type CBA/Ca basal group (**A**) over a longer distance (*r*=390 µm). Dashed black regression lines show linear fits for the 1-10 kHz stimulus frequency range and dashed red regression lines show linear fits for the 11-20 kHz stimulus frequency range. **D-F**. The average phase roll-off for each group. In both the basal (**D** and **E**) and apical (**F**) regions the linear fits (dashed black and dashed red regression lines) indicate that phase acceleration as a function of stimulus frequency is greater for the 1-10 kHz than 11-20 kHz frequency range.

Overall, comparing between the fits for wild-type CBA/Ca basal and apical groups, between 1-20 kHz, phase roll-off increased 4.88x (0.17 °µm^{-1} at 1 kHz to 0. 83 °µm^{-1} at 20 kHz) in basal TM segments (Figure 4.2, D) and 6x (0.19 °µm^{-1} at 1 kHz to 1.14 °µm^{-1} at 20 kHz) in apical TM segments (Figure 4.2, F). The majority of this change occurs at the lower stimulus frequencies (1-10 kHz): 3.8x (0.17 °µm^{-1} at 1 kHz to 0.65 °µm^{-1} at 10 kHz) for basal TM segments (Figure 4.2, D, dashed black regression line) and 4.8x (0.19 °µm^{-1} at 1 kHz to 0.92 °µm^{-1} at 10 kHz) for apical TM segments (Figure 4.2, F, dashed black regression line). The plateaus at the higher stimulus frequencies (11-20 kHz) account for a smaller proportion of the overall change: 1.17x (0.71 °µm^{-1} at 11 kHz to 0.83 °µm^{-1} at 20 kHz) for basal segments (Figure 4.2, D, dashed red regression line) and 1.1x (1.04 °µm^{-1} at 11 kHz to 1.14 °µm^{-1} at 20 kHz) for apical TM segments (Figure 4.2, F, dashed red regression line).

Group (wild-types)	Stimulus frequency (kHz)	Phase lag (°)	Longitudinal Distance (*r*, µm)	Phase roll-off (°µm^{-1})
CBA/Ca Apical (*n*=6)	3	120	280	0.40
CBA/Ca Apical (*n*=6)	8	244	280	0.87
CBA/Ca Apical (*n*=6)	13	289	280	1.03
CBA/Ca Apical (*n*=6)	18	315	280	1.13
CBA/Ca Basal (*n*=21)	3	111	390	0.28
CBA/Ca Basal (*n*=21)	8	173	390	0.44
CBA/Ca Basal (*n*=21)	13	266	390	0.68
CBA/Ca Basal (*n*=21)	18	337	390	0.86
S129 Basal (*n*=4)	3	115	350	0.33
S129 Basal (*n*=4)	8	178	350	0.51
S129 Basal (*n*=4)	13	324	350	0.93
S129 Basal (*n*=4)	18	255	350	0.72

Table 4.1 Summary of phase lag and phase roll-off at each stimulus frequency for the wild-type TM segments (colour coded by stimulus frequency).

The error bars in Figure 4.2, A-F are the average standard deviation of every longitudinal point preceding the end point. It is important to note that the greater variability indicated at higher

stimulus frequencies is due mainly to the greater overall phase lag at these frequencies. For example, in absolute terms the 10% variability of 90^{o} total roll-off is less than 10% variability of 300^{o} total roll-off. The same effect is seen on the error bars of the Figure 4.1, D-F as an effect of distance rather than stimulus frequency (albeit slightly smaller, as these bars are presented as standard error for the sake of visual clarity).

4.3.2 Propagation velocity of the travelling wave

The propagation velocity of the travelling wave can be calculated from the phase data using Equation 2.1. This equation takes into the account the frequency of stimulation as well as the change in phase. This means that although there is a plateauing of phase roll-off for the higher stimulus frequencies (Figure 4.2, A-C), velocity continues to increase with frequency (Figure 4.3). The propagation velocities presented in Figure 4.3 are calculated over the longest section of clean phase available for each stimulus frequency for each mouse (rather than directly from the average phase lag over a set distance, as presented in Figure 4.1, A-C). The error bars in Figure 4.3 are mean±SE from the average velocity calculated.

Propagation Velocity increased as a function of stimulus frequency in both the apical and basal regions (Figure 4.3). The velocities calculated for the two basal groups were very similar, as predicted by the phase data, although the wild-type S129 group was more variable because of the lower *n*. In measurements from apical TM segments this increase was monotonic from 2.03±0.708 ms^{-1} (mean±SD) at 1 kHz to 5.94±1.07 ms^{-1} at 20 kHz (2.93x). A similar (generally) monotonic increase in velocity was also seen in the basal TM segments; 4.24±2.60 ms^{-1} at 1 kHz to 8.93±2.16 ms^{-1} at 20 kHz (2.11x) for the wild-type CBA/Ca basal group and 3.95±1.07 ms^{-1} at 1 kHz to 10.1±1.40 ms^{-1} at 20 kHz (2.56x) for the wild-type S129 basal group. There was a local minimum at 4-5 kHz (~3.3 ms^{-1}) in the data from basal turn TM segments, which was due to the small amount of phase roll-off for stimulus frequencies ≤5 kHz; as roll-off decreases, velocity approaches infinity. In practice, a longer measurement distance is required to measure velocity at lower stimulus frequencies when roll-off is small.

4.3.3 Viscoelastic properties

The viscoelastic properties, G' and η, were estimated by fitting the velocity data to Equation 2.2 (Chen et al., 2004) (Figure 4.4). Both basal groups showed very similar properties; G'=11.0±6.73 kPa (mean±SD), η=0.305±0.0469 Pa·s for the wild-type CBA/Ca group (Figure 4.4, A) and G'=11.4±4.18 kPa, η=0.319±0.0289 Pa·s for the wild-type S129 group (Figure 4.4, B). Estimates for G' and η were significantly lower in the wild-type CBA/Ca apical region; G'=4.75±2.10 kPa (t-test, p=0.378), η=0.156±0.0140 Pa·s (p<0.001) (Figure 4.4, C). These values

correspond to a 2.28x in *G'* and a 1.99x reduction in η between the basal and apical segments of the TM for the wild-type CBA/Ca group (Table 4.2).

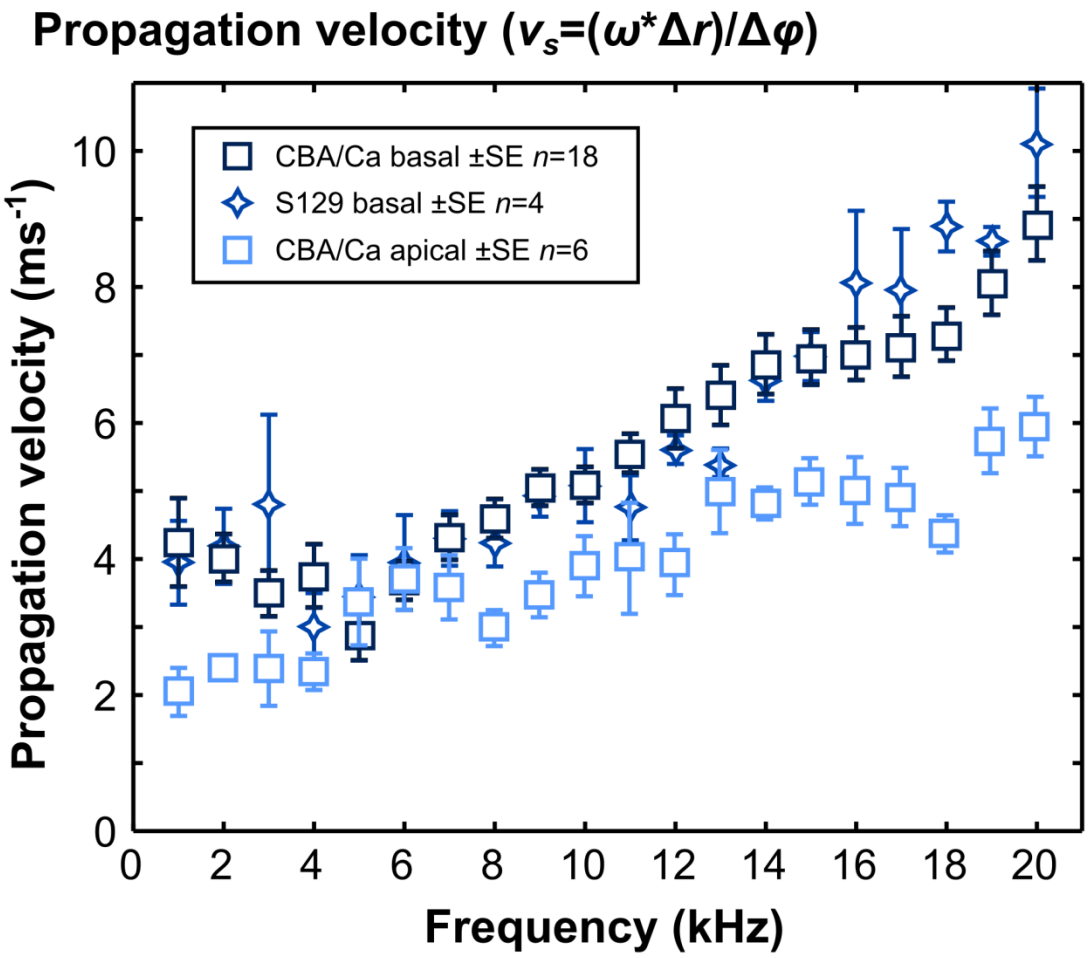

Figure 4.3 Comparison of wave propagation velocities between the wild-type TM segments. Wave propagation velocity increased as a function of frequency in both the basal (darker blues) and apical (light blue) TM segments from wild-type mice.

Group (wild-types)	Viscoelastic properties	
	G' ±SD (kPa)	η ±SD (Pa·s)
CBA/Ca Apical (*n*=6)	4.75±2.10	0.156±0.0140
CBA/Ca Basal (*n*=18)	11.0±6.73	0.305±0.0469
S129 Basal (*n*=4)	11.4±4.18	0.319±0.0289

Table 4.2 Summary of the estimated viscoelastic properties for the wild-type TM segments (colour coded by group).

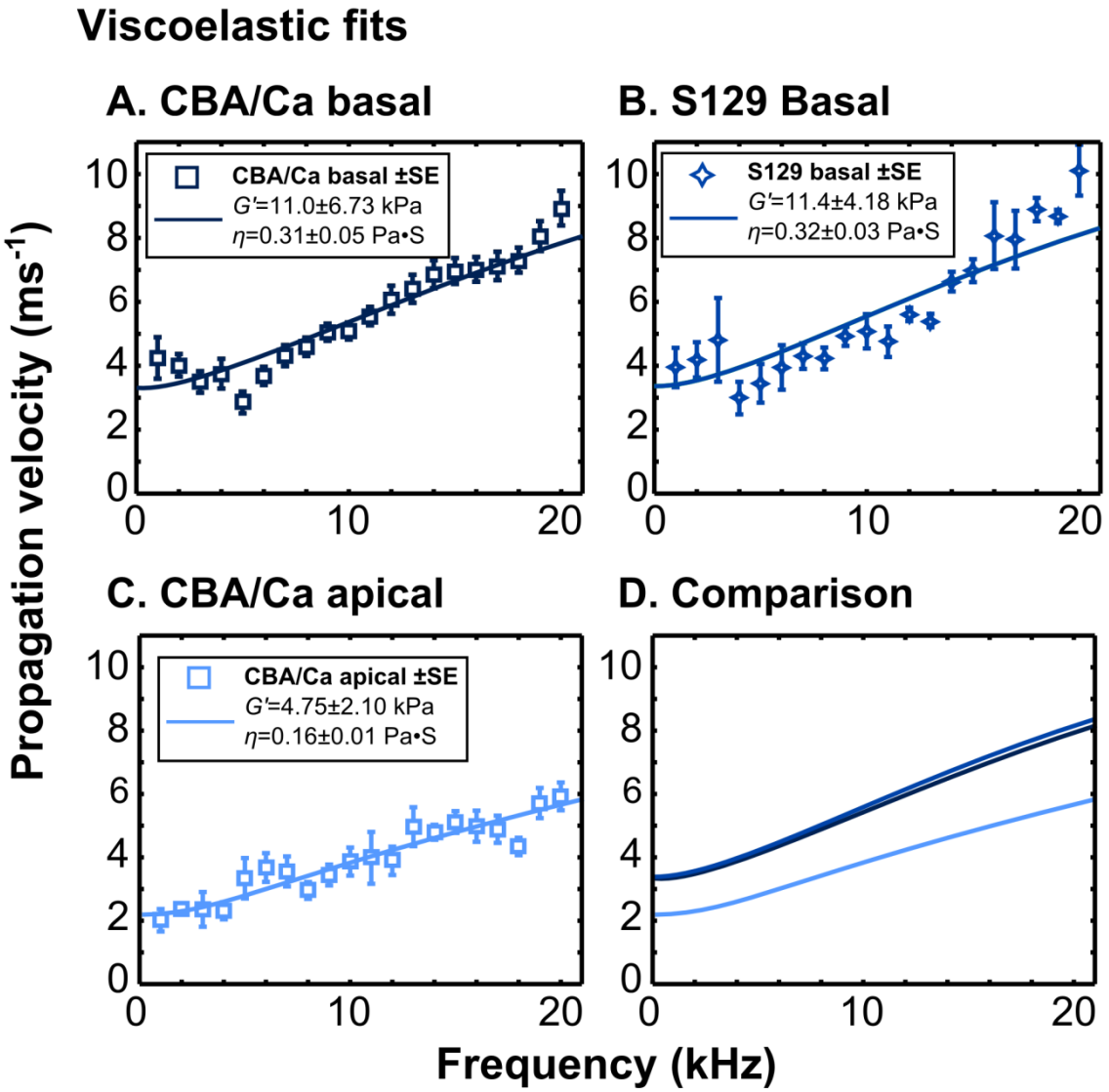

Figure 4.4 The viscoelastic coefficient fits of the travelling wave propagation velocity for the wild-type TM segments (mean±SD, values quoted in figure rounded to fit figure). **A**. Wild-type CBA/Ca basal TM segments G'=11.0±6.73 kPa, η=0.305±0.0469 Pa·s. **B**. Wild-type S129 Basal TM segments G'=11.4±4.18 kPa, η=0.319±0.0289 Pa·s. **C**. Wild-type CBA/Ca apical TM segments G'=4.75±2.10 kPa, η=0.156±0.0140 Pa·s. **D**. Comparison of the fits.

4.3.4 Spatial decay of the travelling wave

Amplitude decay was measured in the basal and apical TM segments of the wild-type CBA/Ca group for stimulus frequencies 2-20 kHz. The decay constant, α, as a function of longitudinal distance was fit with an exponentially decaying curve ($y=A_{(0)}*e^{-\alpha*x}$) at each stimulus frequency. Examples of these fits are shown in Figure 2.14, A (p. 65). Examples of the decay curves as a function of longitudinal distance (0-1000 µm) for the basal and apical regions of the CBA/Ca group are shown in Figure 4.5, A-D (normalised to representative 100 nm radial displacement at 0 µm longitudinal distance). The longitudinal space constant, σ ($\sigma=1/\alpha$; the distance over which the initial amplitude decays by a factor of $1/e$) is shown alongside α in Figure 4.6, A-B.

Due to the exponential relationship between α and σ, σ needs exponentially more resolution to resolve as α decreases (and as σ increases). The variability in the fitted α value to the raw amplitude data is a result of a number of factors contributing to the noise floor and is constant across values of σ. Practically this means that error of the σ increases exponentially as α becomes less negative and limits the accurate measurement of σ to ~≤600 µm. As such σ>600 µm is classified as >600 µm rather than as a specific value (Table 4.3).

Stimulus frequency (kHz)	**Wild-type CBA/Ca Basal** (*n*=5)		**Wild-type CBA/Ca Apical** (*n*=5)	
	α ±SD X10^3	**σ (µm)**	**α ±SD X10^3**	**σ (µm)**
2	2.93±0.63	341	3.22±1.20	311
4	3.10±1.34	323	3.08±1.48	325
7	1.46±1.05	>600	3.74±1.81	267
9	2.64±1.28	379	5.89±1.80	170
10	2.94±0.49	340	5.50±1.08	182
12	2.08±1.06	481	4.09±0.767	244
14	2.97±0.71	337	5.30±1.39	189
15	2.04±0.48	490	5.06±1.42	198
18	1.66±0.58	>600	4.75±1.29	211
20	1.92±1.06	521	4.17±0.83	240

Table 4.3 Summary of the space and decay constants for the wild-type CBA/Ca TM segments (colour coded by stimulus frequency).

At the lower stimulus frequencies (2-7 kHz, Figure 4.5, A) α did not appear to vary significantly between the basal and apical TM segments and σ was similar (4 kHz, mean±SD: α=3.10±1.34, σ=323 µm and α=3.08±1.48, σ=325 µm, respectively). However, for stimulus frequencies ≥8 kHz, α increased in the apical region relative to the basal region (Table 4.3). As with phase roll-off as a function of stimulus frequency, α for the lower (1-10 kHz) and higher (11-20 kHz) stimulus frequency ranges can be roughly approximated with linear fits (Figure 4.6, A, dashed black and dashed red regression lines). In the basal TM segments, where there is little change in α with stimulus frequency (σ stays approximately within the 300-500 µm range) these fits have similar gradients across the whole 2-20 kHz stimulus frequency range and do not appear significantly different from y=0 (1-10 kHz stimulus frequency range: gradient=-44.7 Hz^{-1}, p=0.715, 11-20 kHz stimulus frequency range: gradient=-77.4 Hz^{-1}, p=0.392). However in the apical TM segments, the reduction of σ relative to the basal TM segments is mostly accounted for in the 1-10 kHz stimulus frequency range, with the linear fit appearing significantly different to y=0: gradient=349 Hz^{-1}, p=0.0416. There is little change for the 11-20 kHz stimulus frequency range and the linear fit does not appear significant compared to y=0: gradient=-28.3 Hz^{-1}, p=0.801. Comparing the difference in α between the apical and basal TM

segments (α_{apical}-α_{basal}), Figure 4.6, B) showed the relative difference between the TM segments more clearly. In the basal TM segments α is very similar for stimulus frequencies ≤4 kHz. Relative to the basal TM segments, the apical TM segments then show an increase in α (and a corresponding decrease in σ) between 4-10 kHz. For the 11-20 kHz stimulus frequency range this decline plateaued and there was little change in α as a function of stimulus frequency, relative to basal TM segments (Figure 4.6, dashed red regression line).

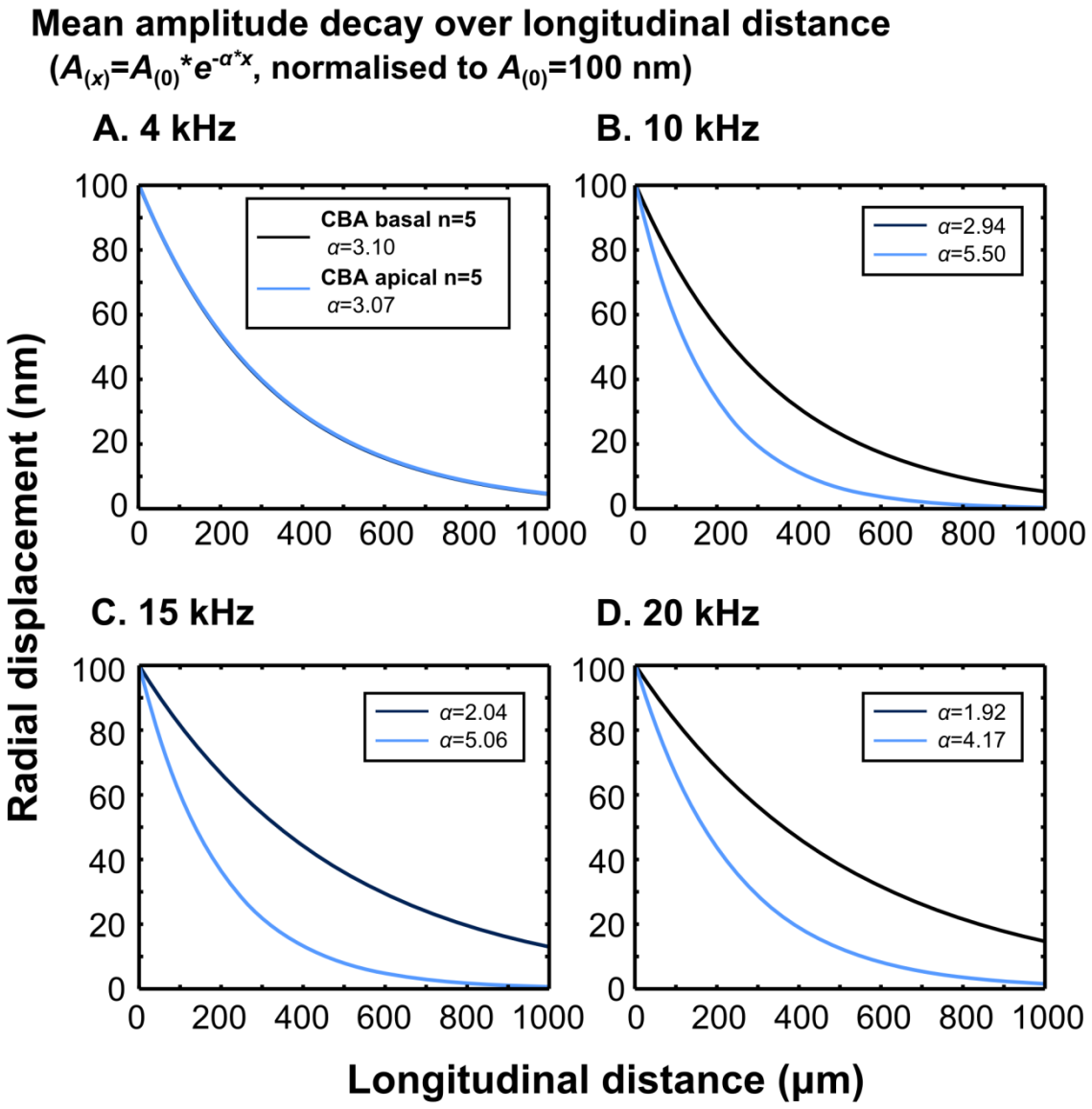

Figure 4.5 Examples of amplitude decay for the wild-type CBA/Ca TM segments. **A-D**. Comparisons of amplitude decay as a function of longitudinal distance between basal and apical segments of TM from wild-type CBA/Ca mice at 4 (**A**), 10 (**B**), 15 (**C**) and 20 kHz (**D**). The decay is exponential ($y=A_{(0)}*e^{-\alpha*x}$) where $A_{(0)}$ is plotted as 100 nm radial displacement at the point of stimulation (0 µm) and α is the corresponding value in Table 4.2.

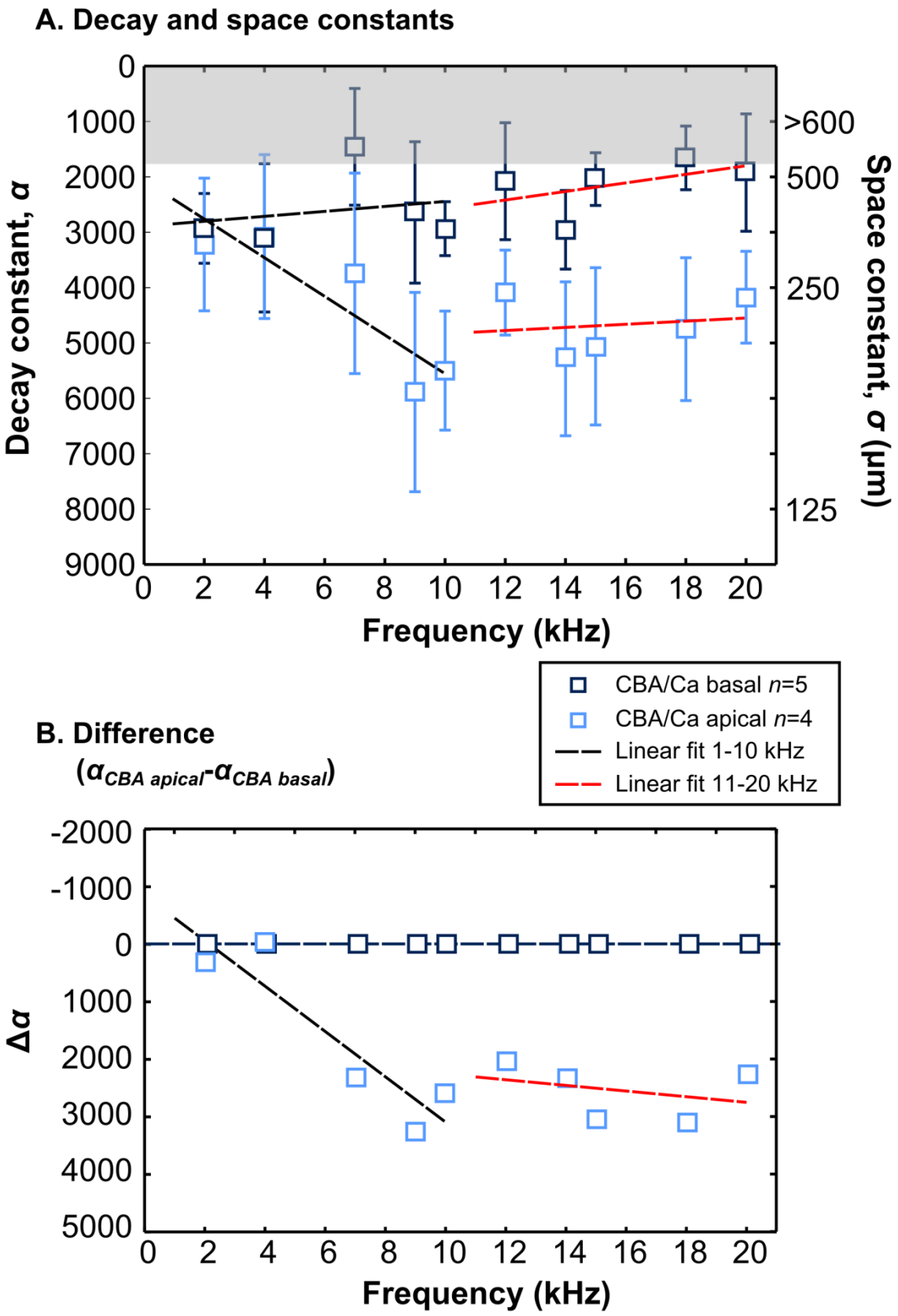

Figure 4.6 Spatial decay as a function of stimulus frequency for the wild-type CBA/Ca TM segments. **A**. Mean decay constants, α (and corresponding space constants, σ) for the wild-type CBA/Ca basal and apical groups. Error bars are standard deviation of α. Dashed black and dashed red regression lines show linear fits to the 1-10 kHz and 11-20 kHz stimulus frequency ranges, respectively **B**. The difference in mean α between the wild-type CBA/Ca apical and basal TM segments (α_{apical}-α_{basal}).

4.3.5 Waveform of the travelling wave

The waveform of the propagating travelling wave is a product of both its wavelength (λ) and amplitude decay (α). The waveform was calculated by fitting a sine wave to the average phase roll-off data at each stimulus frequency. The exponential decay functions fit to the amplitude data (plotted as a representative 100 nm radial displacement at 0 µm longitudinal distance) were then applied to the sine waves. Examples of these waveforms are shown in Figure 4.7, A-D. At 4 kHz (Figure 4.7, A) α and phase roll-off (and hence λ) were similar between the basal and apical TM segments, and the corresponding waveforms were similar. At 10, 15 and 20 kHz (Figure 4.7, B-D) α increased in the apical TM segments and λ decreased (as phase roll-off was greater). As a consequence the travelling waveforms in apical TM segments lag the basal waveforms and propagated over a shorter longitudinal distance. Comparisons of the waveforms as a function of stimulus frequency are shown in Figure 4.8, A-B. In apical TM segments the waveforms propagate over shorter distances and bunch at the higher stimulus frequencies. The longitudinal position of the first positive peak of the waveforms is tracked and compared between groups in Figure 4.9.

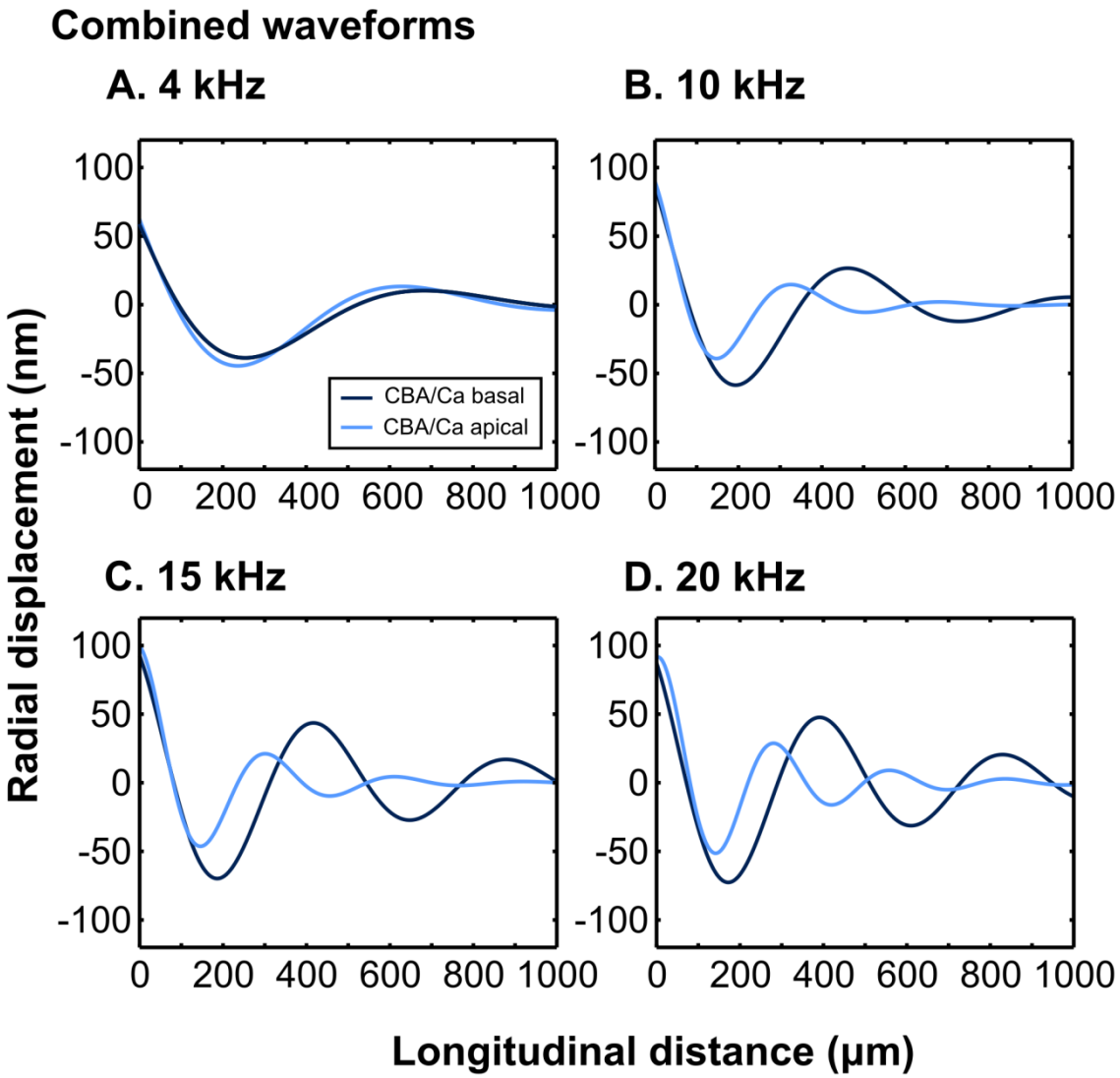

Figure 4.7 Waveforms of the travelling waves for the wild-type CBA/Ca TM segments. **A-D**. Comparisons between the travelling waveforms from the apical (light blue) and basal (darker blue) TM segments for stimulus frequencies 4 (**A**), 10 (**B**), 15 (**C**) and 20 kHz (**D**). Waveforms were calculated from the rate of amplitude decay, α (fit with an exponential decay of the form $y=A_{(0)}*e^{-\alpha*x}$) and the phase data (fit with a sine wave of the form $y=c*\sin(d*x+f)$).

4.4 Discussion

4.4.1 Summary

The data presented provide evidence for the viscoelastic nature of isolated TM segments and reveal differences in the mechanical properties of the TM between the apical and basal turns of wild-type mice. The isolated segments of TM are able to propagate radially shearing travelling waves longitudinally, at acoustic stimulus frequencies (1-20 kHz), and at physiologically realistic amplitudes, over significant longitudinal distances (several hundred microns). These waves have similar velocities to the BM travelling wave (Ren and Nuttall, 2001; Ren, 2002). The material properties of the TM affect the characteristics of the waves; both wave propagation velocity and the spatial extent of the waves are affected by the stiffness of the TM, providing two possible mechanisms by which longitudinal coupling in the TM can affect the gain and timing of feedback in the cochlea. The space constants and viscoelastic moduli indicate that longitudinal coupling is stronger in basal TM segments compared to apical segments. The longer space constants and reduced phase roll-off in the basal segments show travelling waves propagate further (and faster) than in the floppier apical segments.

The robustness of the laser interferometer based method to track these waves in the TM is demonstrated. The estimates for the viscoelastic properties are within the same order of magnitude, and show similar trends to other published data (Abnet, 1998; Abnet and Freeman, 2000; Shoelson et al., 2004; Masaki et al., 2006; Ghaffari et al., 2007; Richter et al., 2007; Gu et al., 2008; Ghaffari et al., 2010). The similarities between the phase and velocity data recorded from the wild-type S129 mice compared to the wild-type CBA/Ca mice provides further verification of the method and also further verification that the heterozygous Tectb$^{+/-}$ mice are indistinguishable from wild-type mice.

4.4.2 Wave velocity is reduced in the apical region

Phase roll-off is quicker in apical segments of TM, indicating travelling wave velocities are reduced compared to the basal region. As stimulus frequency increases, wave propagation velocity increases in both basal and apical regions. Estimates of the viscoelastic properties of the TM based on this stimulus frequency/propagation velocity relationship indicate that the apical TM is less able to propagate energy longitudinally than the basal TM (Table 4.2). In both the apical and basal regions, the rate of increase of phase roll off is greater for the 1-10 kHz frequency range than the basal 11-20 kHz frequency range.

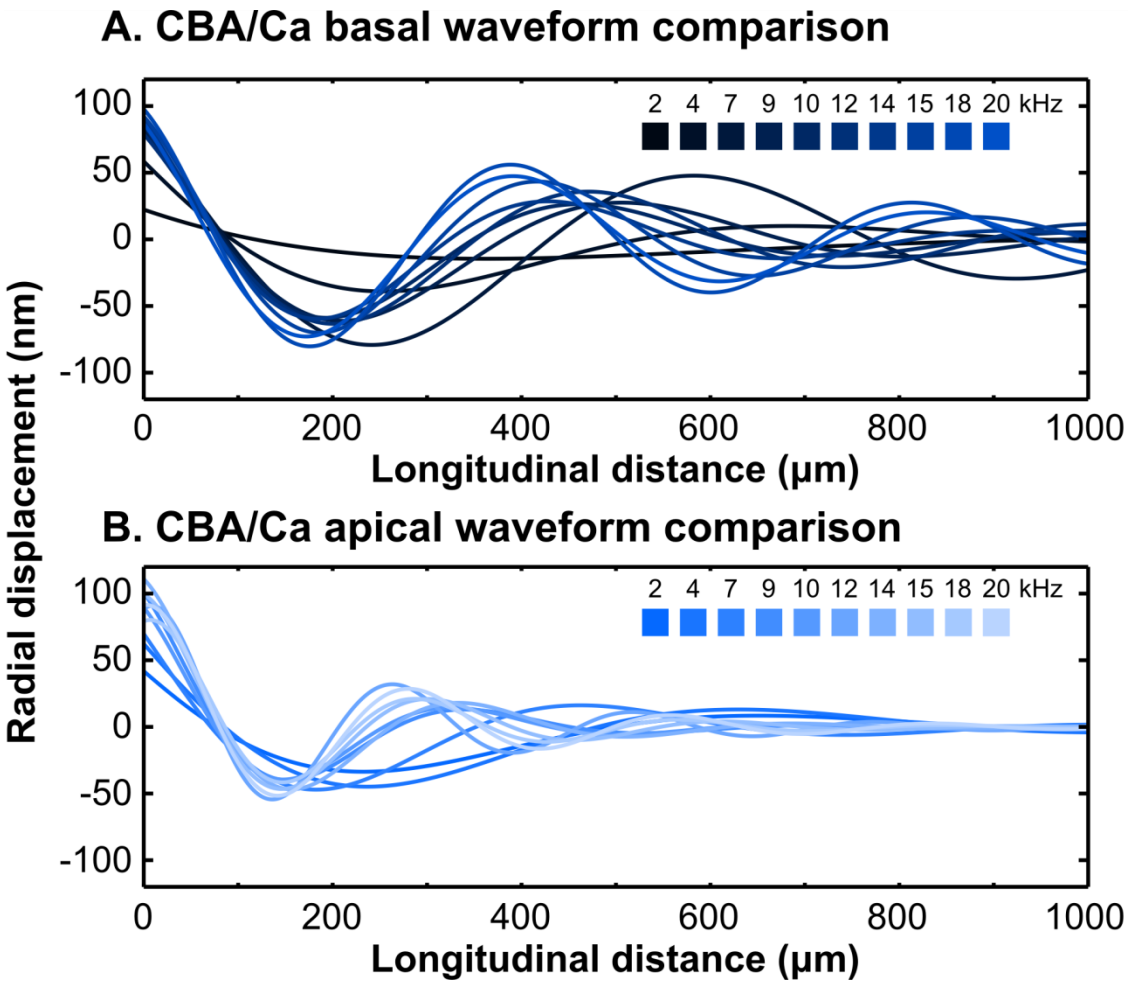

Figure 4.8 Comparison of the travelling waveforms of the travelling waves for the wild-type CBA/Ca TM segments for stimulus frequencies 2-20 kHz. **A.** Basal TM segments. **B.** Apical TM segments.

4.4.3 Spatial coupling is reduced in the apical region

The amplitude data shows that longitudinal coupling in the TM is reduced in the apical segments for stimulus frequencies >10 kHz compared to the basal segments. This means that, at these frequencies, there is likely to closer spatial coupling of hair cells in the apical region of the intact cochlea than in the basal region. Reducing the spatial coupling of hair cells has the effect of increasing the sharpness of frequency tuning by reducing the longitudinal distance over which mechanical feedback from the OHCs can act (Russell et al., 2007; Lukashkin et al., 2010). The difference in the relationship between stimulus frequency and wave amplitude decay may be the result of a shift in radial resonance over the length of the TM. The apical turn of the CBA/Ca mouse cochlea is not optimised to detect frequencies above ~10 kHz (Müller et al., 2005) and the fact that the higher stimulus frequencies decay at a faster rate may be an indication that the TM is not designed to longitudinally propagate the energy of these frequencies in this region. The higher stimulus frequencies (>10 kHz) are within the range of

the basal half of the mouse cochlea and it is reasonable to hypothesise that higher stimulus frequencies, above the resonance range of this region of the cochlea, may decay at a greater rate than those tested. In the BM the travelling wave diminishes very quickly after the point of resonance. Such reduction in coupling makes sense in the context of the tuning characteristics of the healthy cochlea where TM resonance is below the BM resonance (0.5 octaves difference in the apical region) (Gummer et al., 1996; Hemmert et al., 2000).

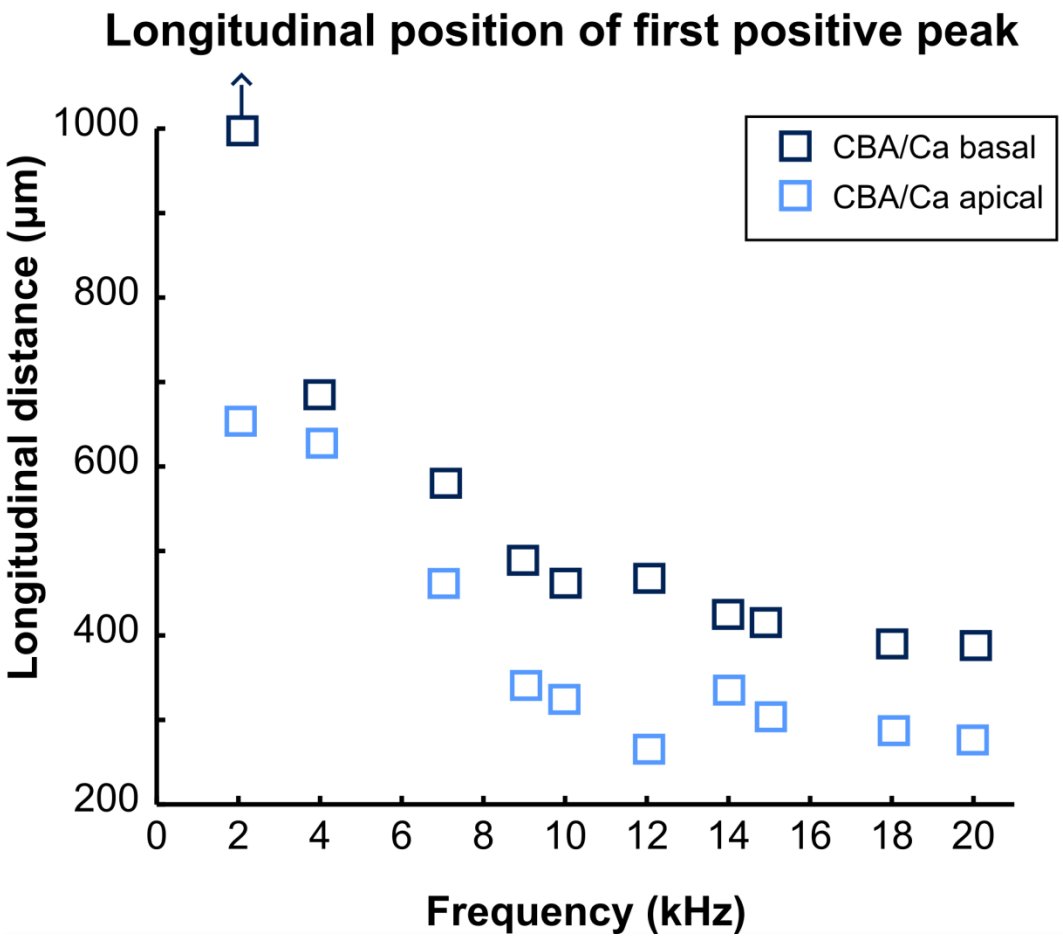

Figure 4.9 Longitudinal position of the first positive peak of the waveforms in wild-type CBA/Ca TM segments. The longitudinal position of the first positive peak from wild-type CBA/Ca TM segments occurs at ~50% of the distance of that of the basal TM segments.

4.4.4 Waveforms

The combined waveforms for the frequency range tested do not necessarily reveal the shape (or existence) of a TM travelling wave *in vivo*. In the intact cochlea the energy source is not at one end of the TM, as it is in the experimental set up, rather it occurs at the CF via transverse vibration of the BM and mechanical feedback from the OHCs. Also the loading and damping in the experimental environment are very different compared to inside the intact cochlea. The propagation of a travelling wave is further complicated by multimodal vibration of the TM

(Gummer et al., 1996; Hemmert et al., 2000). It is possible that the travelling wave propagation is restricted to a region in which the shear resonance of the TM dominates (1 to 0.1 octaves below the CF). However, despite these differences and complications, the data shows that for the same stimulation in the experimental chamber, the induced travelling wave changes as the mechanical properties of the TM change (ie. between the apical and basal regions). This implies that energy propagation via the TM is different in basal and apical regions, similar to the changes in resonance of the TM and BM longitudinally.

4.4.5 Conclusions

A decrease in the stiffness of the TM over the length of the cochlea is predicted by the reduction in the low resonance notch in neural tuning curves that is attributed to the TM resonance (Zwislocki, 1986; Allen and Fahey, 1993; Gummer et al., 1996; Hemmert et al., 2000; Lukashkin et al., 2010). The respective 2.28x and 1.99x decreases of G' and η between the basal and apical TM segments reflect this change in stiffness. The reduction in the space constant of wave amplitudes in the apical region is also indicative of this reduction in stiffness, at the higher stimulus frequencies. The amplitude data for the lower stimulus frequencies implies that, at those frequencies, the TM is still as capable of propagating energy longitudinally as in the basal region.

If travelling waves in the TM are able to propagate *in vivo*, then longitudinal coupling in the TM is likely to affect tuning and sensitivity in the cochlea (as observed in Russell et al., 2007; Ghaffari et al., 2010). Discrepancies between BM responses and IHC and auditory nerve response indicate that vibration of the organ of Corti is complex (Mountain and Cody, 1999) and longitudinal coupling in the TM, in addition to its resonant properties, may account for some of this complexity.

5 MECHANICAL PROPERTIES OF THE TECTORIAL MEMBRANES OF *TECTA*$^{Y1870C/+}$, *TECTB*$^{-/-}$ AND *OTOA*$^{EGFP/EGFP}$ MUTANT MICE

5.1 Abstract

The mechanical properties of the basal region of three tectorial membrane (TM) mutants groups, *Tecta*$^{Y1870C/+}$, *Tectb*$^{-/-}$ and *Otoa*$^{EGFP/EGFP}$, are assessed by stimulating the longitudinal propagation of a travelling wave. The wave is tracked at multiple points by a laser interferometer focused on the marginal edge of an isolated segment of TM and its phase and amplitude are recorded. From the phase data velocity of the travelling wave as function of stimulus frequency is calculated and its viscoelastic properties (shear storage modulus, *G'*, and shear viscosity, η) are estimated. The amplitude data (decay constant, α and space constant, σ) are used to calculate the spatial extent of wave propagation. Each mutant group is compared to the wild-type CBA/Ca data presented in Chapter 4 (p. 87) and found to be mechanically less rigid than the wild-type.

5.2 Introduction

The mechanical properties of TM segments isolated from the basal region of the cochleae of α-tectorin, β-tectorin and otoancorin mutants are investigated and are compared to the basal wild-type data presented in Chapter 4 (p. 87). These groups all exhibit hearing pathologies linked to the attachment and condition of the TM.

Despite its key position above the organ of Corti and in contact with the longest stereocilia of the outer hair cell (OHC) hair bundles, the importance of the TM for frequency tuning and OHC stimulation in the mammalian cochlea has, until recently, been mostly neglected. In traditional models of the cochlea the TM is assumed to be simply an inert or resonating mass against which the OHC hair bundles shear. However, recent evidence from mice lacking key TM proteins has shed light on the importance of the TM for gain, tuning and for stimulation of the inner hair cells (IHCs) (Lukashkin et al., 2010; Richardson et al., 2011). *Tectb*$^{-/-}$ mice lack the protein β-tectorin, which is specific to the inner ear (the TM in the cochlea and the otoconial membranes in the vestibular system). In these mice the TM remains attached to the organ of Corti, but neural recordings show a dramatic increase in the sharpness of frequency tuning, along with a mild sensitivity loss (Russell et al., 2007). The morphology of the TM in these mice is severely disrupted and it has been hypothesised that interactions between the travelling waves in the TM and basilar membrane (BM) control the spatial coupling of OHCs during amplification (Russell et al., 2007; Lukashkin et al., 2010). In the *Tectb*$^{-/-}$ mice reduced longitudinal stiffness reduces the spatial limit of energy coupling and hence the cochlear-frequency range over which energy from (fewer) OHCs is propagated is also reduced; leading to the observed sharpened tuning (Russell et al., 2007; Lukashkin et al., 2009; Lukashkin et al., 2010). Previously atomic force microscopy and other mechanical techniques have been used to investigate the material properties of the TM (Abnet and Freeman, 2000; Shoelson et al., 2004; Gueta et al., 2006; Ghaffari et al., 2007; Richter et al., 2007; Ghaffari et al., 2010; Gueta et al., 2011). The material properties of the TM are dynamic and vary depending on stimulation frequency and amplitude (Freeman et al., 2003a). Only two of these studies (Ghaffari et al., 2007; Ghaffari et al., 2010) have used acoustic-frequency stimulation to assess the viscoelastic and spatial coupling properties of wild-types and *Tectb*$^{-/-}$ TM mutants. No study of the dynamic material properties of the α-tectorin or otoancorin mutants has yet been conducted and the mechanical correlates to the structural abnormalities (discussed below and summarised in Table 5.1) are unclear.

		TM morphology						
Mutant	**Affected proteins**	**Collagen**	**Appearance**	**HS**	**MB**	**CN**	**Dimensions**	**Attachments**
***Tecta*$^{\Delta ENT/\Delta ENT}$** (Legan et al., 2000)	α-tectorin, β-Tectorin, otogelin	Randomly orientation, missing SSM	Detached and associated with RM	Missing	Missing	Missing	Abnormal	No attachment to OHCs or SL
***Tecta*$^{\Delta ENT/+}$** (Legan et al., 2000)	NA	Phenotypically as wild-type	Phenotypically as wild-type	Present	Present	Present	Phenotypically as wild-type	Attached to OHCs and SL
***Tecta*$^{Y1870C/Y1870C}$** (Legan et al., 2005)	α-tectorin	Randomly orientation, missing SSM	Detached and associated with RM	Missing	Missing	Missing	Abnormal	No attachment to OHCs or SL
***Tecta*$^{Y1870C/+}$** (Legan et al., 2005)	α-tectorin, otogelin	Orientated perpendicular to upper surface	Kimura's membrane detached, unusual shape, increased sub tectorial space	Missing	Missing	Missing	"Significantly thinner "	Weak attachments to OHCs and SL
***Tecta*$^{C1509G/C1509G}$** (Xia et al., 2010; Gueta et al., 2011)	α-tectorin	Severe disruption of fibrils surrounding TM edge	Short in radial direction (basal)	Missing	Disrupted	Disrupted	Abnormal	Loose connection to SL, detached from OHCs
Tecta$^{C1509G/+}$ (Xia et al., 2010; Gueta et al., 2011)	α-tectorin	Partial disruption of fibrils surrounding TM edge	Short in radial direction (basal)	Missing	Present	Disrupted	Thicker transversally, shorter radially	Attached to SL and first row of OHCs only in the base
***Tectb*$^{-/-}$** (Russell et al., 2007)	β-tectorin	Randomly orientation, missing SSM	Frayed at apical end	Missing	Present in basal region, missing in apical region	Present	2x thicker but normal radial width at apical end	Attached to OHCs and SL
***Otog* (various)** (Simmler et al., 2000a; Simmler et al., 2000b)	Otogelin	Disrupted	Phenotypically similar to wild-type				Phenotypically similar to wild-type	Attached to OHCs and SL
***Otoa*$^{EGFP/EGFP}$** (Zwaenepoel, 2002; Lukashkin et al., unpublished data)	Otoancorin	Phenotypically as wild-type	Similar to wild-type	Missing	Present, possible disruption	Present, possible disruption	Similar to wild-type	Attached to OHCs, not SL

Table 5.1 Summary of morphological properties of mutant tectorial membranes. The three groups for which mechanical data is presented in this chapter are highlighted (colour coded by group). Abbreviations: CN: Cover net, HS: Hensen's stripe, MB: Marginal band, RM: Reissner's membrane, SL: Spiral limbus, SSM: Striated sheet matrix.

Viscoelastic and spatial coupling data from the TMs of the *Tectb*$^{-/-}$ mice described by Ghaffari et al. (2010) support the hypothesis that the extent of spatial coupling is reduced in *Tectb*$^{-/-}$ mutants (Russell et al., 2007; Lukashkin et al., 2010). In segments of isolated TM, from both basal and apical regions, the propagation velocity of travelling waves was reduced and the corresponding estimates for the viscoelastic properties, shear storage modulus (*G'*) and shear viscosity (η) are lower. In addition to this, the reduced spatial spread of longitudinal energy is observed in the shorter space constants (σ, the distance over which the wave amplitude decays by a factor of 1/*e*) in the *Tectb*$^{-/-}$ mutants. Both these factors have implications of timing and feedback in the active cochlea.

5.2.1 The mutants

The three mutant groups, *Tectb*$^{-/-}$, *Tecta*$^{Y1870C/+}$ and *Otoa*$^{EGFP/EGFP}$, presented in this chapter have mutations specific to the TM (and other restricted locations in the inner ear that do not affect hearing). These three mutants (along with others) are summarised in Table 5.1.

5.2.1.1 Tecta

α-tectorin is a protein specific to the acellular gels of the inner ear and is found in the otoconial membranes of the otolithic organs and the TM, but not the cupulae of the semicircular canals (Legan et al., 1997; Goodyear and Richardson, 2002). A number of mutations for the gene coding for α-tectorin, TECTA, have been described and all cause hereditary hearing loss (Govaerts et al., 1998; Verhoeven et al., 1998; Plantinga et al., 2006), of these mutations the hearing phenotypes of *Tecta*$^{\Delta ENT/\Delta ENT}$ (Legan et al., 2000), *Tecta*$^{Y1870C/+}$ (Legan et al., 2005) and *Tecta*$^{C1509G/C1509G}$ (Xia et al., 2010) have been characterised in mouse models.

In *Tecta*$^{\Delta ENT/\Delta ENT}$ mice Exon 3 is skipped resulting in the deletion of 96 amino acids within the entactin G1-like domain of the α-tectorin protein. This results in a number of abnormalities in the ultrastructure of the TM, its supporting structures and also in the otoconial membranes of the utricle and saccule of the vestibular system. The TM in these mice is completely detached from the sensory epithelium and the spiral limbus and lacks Hensen's stripe and the marginal band. *Tecta*$^{\Delta ENT/+}$ mice are unaffected and are identical to wild-types. The ultrastructure of the *Tecta*$^{\Delta ENT/\Delta ENT}$ mice is severely disrupted; as well as lacking α-tectorin, no β-tectorin or otogelin are present. Consequently the characteristic striated sheet matrix is completely absent and instead collagen fibrils are disorganised and arranged randomly instead of radially (Legan et al., 2000; Richardson et al., 2008). Despite the total detachment of the TM, the BM responses in the *Tecta*$^{\Delta ENT/\Delta ENT}$ mice are tuned, but the second sensitivity peak (attributed to the TM) at ~0.5 octaves below the BM CF is not present. The OHCs are unaffected; their hair bundles are

correctly orientated, and cochlear microphonic recordings demonstrate they can still be driven via fluid coupling. There is however a marked frequency-dependant 35 dB loss of sensitivity in BM responses and lack of biasing of the OHC hair bundles towards the most sensitive operating point, which is indicated by asymmetry in the recorded cochlear microphonics. CAP threshold recordings from these mice also show that the (IHCs) respond to hair bundle displacement by BM velocity (coupled through the fluid) rather than BM displacement, as when the TM is present (Legan et al., 2000).

Mice with a homozygous missense mutation to *Tecta*$^{C1509G/C1509G}$ also exhibit asymmetric cochlear microphonics. In these mice the TM is loosely connected to the spiral limbus but detached from the OHCs. In the heterozygous *Tecta*$^{C1509G/+}$ mice the attachment to the spiral limbus is stronger, but in the base the TM is shorter radially, resulting in attachment to the hair bundles of the first row of OHCs only (Xia et al., 2010). Humans heterozygous for this mutation suffer partial hearing loss (Pfister et al., 2004) and both *Tecta*$^{C1509G/+}$ and *Tecta*$^{C1509G/C1509G}$ mice have increased ABR and DPOAE thresholds (25-40 dB and 30-50 dB, respectively) (Xia et al., 2010). Morphologically, disorganisation of the TMs collagen fibres has been observed in the both *Tecta*$^{C1509G/+}$ and *Tecta*$^{C1509G/C1509G}$ mice and structurally Young's modulus is reduced in both groups compared to wild-types (49±9, 33±5, and 109±11 kPa, respectively) in the mid turn and even more so in the basal turn (75±11, 45±7 and 295±15 kPa, respectively) (Gueta et al., 2011).

Y1870C is a semi-dominant missense mutation to *Tecta*. Similar to the *Tecta*$^{\Delta ENT/\Delta ENT}$ mice, the TM in *Tecta*$^{Y1870C/Y1870C}$ is completely detached for the spiral limbus and organ of Corti and as such the hearing impairments in these mice are similar (Legan et al., 2000; Legan et al., 2005). However, the TMs of *Tecta*$^{Y1870C/+}$ mice are still attached to the spiral limbus and the hair bundles of the OHCs, while simultaneously showing severe structural impairment. In these mice the connection of the TM to the spiral limbus is weakened, Kimura's membrane is detached from the underside of the TM (but still in contact with the OHC hair bundles) and the marginal band, cover net and Henson's stripe are missing (Legan et al., 2005; Masaki et al., 2010). The TM also has an unusual shape with an increased subtectorial space between the TM and the IHCs. The internal striated sheet matrix in the TM is disrupted and, instead of organising radially, collagen fibres orient themselves perpendicular to the upper surface and protrude through (Legan et al., 2005). Overall there is a slight reduction of the tectorin content (both α and β) of *Tecta*$^{Y1870C/+}$ TMs and shear impedance of the TM at stimulus frequencies between 10-9000 Hz reduced by a factor of 3x (Masaki et al., 2010).

The phenotype of *Tecta*$^{Y1870C/+}$ is distinctly different from those of *Tecta*$^{\Delta ENT/\Delta ENT}$ and *Tecta*$^{Y1870C/Y1870C}$. Cochlear microphonics recorded from OHCs show that the cells are healthy and the symmetrical shape of the cochlear microphonic, along with similarity to wild-types, indicates that the mechanical coupling between the TM and hair bundles is the same as in wild-type mice. Mechanical tuning of the BM in *Tecta*$^{Y1870C/+}$ mice is very similar to wild-types; both iso-response and DPOAE tuning curves have similar shapes to wild-types but are less sensitive (8 dB and 13.5 dB, respectively) (Legan et al., 2005).

5.2.1.2 Tectb

β-tectorin is another protein specific to the acellular gels of the inner ear and is present in the same locations as α-tectorin; the TM and otoconial membranes, but not the cupulae (Legan et al., 1997).

Mice homozygous for a targeted deletion of exons 1-4 of β-tectorin coding gene, *Tectb*, lack expression of the protein β-tectorin (Russell et al., 2007). The TM of a *Tectb*$^{-/-}$ mouse is still attached to the spiral limbus and the hair bundles of the OHCs, however, it lacks an organised striated sheet matrix. The collagen fibrils of the TM are arranged in a random matrix of filaments formed by α-tectorin (Russell et al., 2007; Richardson et al., 2008). In the basal region the dimensions of the TM remain the same as those in wild-type mice but increase to twice the cross-sectional area of a wild-type by the very apical end of the TM (11544±1130 μm^2 compared to 5278±730 μm^2, respectively). In the enlarged areas the radial width remains the same as wild-types, but the transverse thickness of the TM is increased. Other TM structures, including the cover net, marginal band and Kimura's membrane, are all present, although Henson's stripe is missing along the entire length of the TM and the marginal band absent in the apical region (Russell et al., 2007).

The radial stiffness of the TM in *Tectb*$^{-/-}$ mice is unaffected in the basal region of the cochlea; this is indicated by recordings of the extracellular OHC receptor potentials from the basal turn when stimulating the cochlea with a 10 kHz tone. At this frequency (2-3x octaves below basal CFs) the radial stiffness of the TM dominates its material properties. The magnitude and phase of the OHC receptor potentials recorded are the same as wild-types, showing that the mutant TM is still able to effectively deflect the OHC hair bundles (assuming no compensatory gain increase in the OHCs) (Russell et al., 2007).

Unlike the radial stiffness, the longitudinal stiffness of the TM in *Tectb*$^{-/-}$ is reduced, including in the grossly-normal basal region. This is indicated both by enhanced frequency tuning shown in BM isoresponse recordings and neural masking tuning curves, and also by measurement of the

viscoelastic properties of isolated segments of TM by Ghaffari et al. (2010). Russell et al. (2007) showed that BM recordings from *Tectb*$^{-/-}$ mice are 10 dB less sensitive at the 53 kHz place on the BM while simultaneously exhibiting a reduced bandwidth of the sensitivity peak at the CF ($Q_{10\ dB}$=18.9 dB for wild-types compared to $Q_{10\ dB}$=9.6 dB for *Tectb*$^{-/-}$ mice). The low frequency resonance (a small peak of BM sensitivity at a lower frequency to the CF and attributed to the TM) is also absent in *Tectb*$^{-/-}$ mice (Russell et al., 2007). Similar changes were seen in the neural masking tuning curves – wild-types and *Tectb*$^{-/-}$ mice had roughly the same sensitivity but the mutants were much more sharply tuned than wild-types. This increase in frequency tuning was attributed to a reduced spread of excitation longitudinally along the cochlea of mutants; the TM effectively couples the energy over a shorter longitudinal distance (and hence from fewer OHCs), reducing the interaction between adjacent frequency places.

Recent data from Ghaffari et al. (2010) proposes two possible properties of TM travelling waves that could contribute to the differences in sensitivity and frequency resolution observed in the *Tectb*$^{-/-}$ mice. The wavelength (and hence propagation velocity) and spatial decay constant of the travelling waves are reduced in *Tectb*$^{-/-}$, with the most dramatic reduction (relative to the same region in wild-types) in the apical, low frequency region. Ghaffari et. al. (2010) also estimated the viscoelastic properties of the TM from the travelling wave propagation velocities. In the basal third of the cochlea these values reduced from G=42±10 kPa (mean±SD) and η=0.23±0.007 Pa·s in wild-type mice to G=18±1 kPa and η=0.17±0.006Pa·s in the *Tectb*$^{-/-}$ mutants.

5.2.1.3 Otoa

Otoancorin is an inner ear specific protein found at the interface between the sensory epithelia in the semicircular canals, cochlea and otolithic organs, and their overlying acellular gels. In the developed cochlea it is expressed in the limbal attachment zone of the TM to the spiral limbus, and briefly during development at the medial attachment of the TM to the OHC hair bundles (Zwaenepoel, 2002). Humans identified with a missense mutation in otoancorin, D356V, have hereditary, moderate to severe hearing loss (Walsh et al., 2006). In the mouse model *Otoa*$^{EGFP/EGFP}$, the first coding exon of the Otoa gene is replaced with a gene encoding enhanced green fluorescent protein (EGFP), entirely preventing the expression of otoancorin. In these mice the TM is completely detached from the spiral limbus but still attached to the OHC hair bundles. α-tectorin, β-tectorin, and otogelin are all expressed normally, but Hensen's stripe is missing from the TM and there is possible structural abnormality in the marginal band (Lukashkin et al., unpublished data). Cochlea microphonic data from these mice show that the OHCs function normally and tuning and sensitivity of the BM is unaffected. However, the low

frequency notch of insensitivity (attributed to the TM) is missing from the BM tuning curves and the threshold levels of CAP recordings from the auditory nerve are raised by ~40 dB at most frequencies, indicating that the partly detached TM does not effectively drive the IHCs (Weddell et al., 2011a).

5.2.2 Mechanical investigation of the tectorial membrane

In the data presented here, the viscoelastic properties of the TM, G' and η, were estimated from the relationship between wave propagation velocity and stimulus frequency based on a linear Voigt body description of a viscoelastic medium (Equation 2.2, p. 66) (Chen et al., 2004). The wave propagation velocity is calculated using Equation 2.1 (p. 66). Change in phase with distance (phase roll-off) was tracked for stimulus frequencies 1-20 kHz over the length of basal TM segments in 1 kHz steps. Longitudinal coupling of energy along the TM was measured by tracking radial displacement amplitude longitudinally for frequencies 2-20 kHz and calculating the exponential decay. The decay for each stimulus frequency was fit with an exponential decay cure ($y=A_{(0)}*e^{-\alpha*x}$) and the decay constant, α, used to calculate the distance over which the wave decays by a factor of $1/e$ (the space constant, σ). The combined waveforms of the propagating travelling waves were generated from the normalised exponential decays and sine waves fit to the average rate of phase roll-off at each stimulus frequency ($y=c*\sin(d*x+f)$).

Phase and amplitude data are presented with linear fits to the 1-10 and 11-20 kHz stimulus frequency ranges. Linear regression was used to compare these fits to $y=0$ and to visualise the relationships of these measurements to the stimulus frequency, rather than as a definitive statistical analysis of the relationship. As such, an indication of possible statistical significance of individual fits is presented at the $p=0.05$ level, without correcting for multiple comparisons.

5.2.3 Aims

1. Compare phase roll-off between the mutant groups as a function of stimulus frequency and longitudinal distance.
2. Estimate viscoelastic properties of basal TM segments of three mutant groups *Tecta*$^{Y1870C/+}$, *Tectb*$^{-/-}$ and *Otoa*$^{EGFP/EGFP}$ from the relationship between wave propagation velocity and stimulus frequency.
3. Measure the extent of longitudinal coupling in each mutant group by tracking amplitude decay of the travelling wave.
4. Compare this data to basal wild-type data and attempt to determine any links between specific mechanical properties to the known information about the morphological pathologies in each mutant group.

5. Examine the consequence on the travelling wave that any changes in wavelength and amplitude decay in each group have, and the relationship of these changes to cochlear mechanics.

5.3 Results

Each mutant group is presented along with reference wild-type data from the wild-type CBA/Ca basal group analysed in Chapter 4 (p. 87). This group contains a mixture of *Tectb*$^{+/-}$ and *Tectb*$^{+/+}$ mice which are phenotypically indistinguishable and have identical hearing and TM structure to the background CBA/Ca strain.

5.3.1 Phase delay

For all three mutant groups phase lag increased as a function of distance and stimulus frequency (Figure 5.1, A-F). Roll-off was generally greater for higher stimulus frequencies and increased approximately monotonically with distance for all three mutant groups (Figure 5.2, A-C): 340^{o} (0.94 cycles) over a longitudinal distance, *r*, of 320 µm (*Tectb*$^{-/-}$ at 12 kHz), 410^{o} (1.14 cycles) over 340 µm (*Tecta*$^{Y1870C/+}$ at 19 kHz) and 410^{o} over 320 µm (*Otoa*$^{EGFP/EGFP}$ at 20 kHz). The maximum phase roll-off for these groups was 1.06, 1.21 and 1.28 ^{o}µm^{-1}, respectively (Figure 5.2, D-F).

The *Tectb*$^{-/-}$ and *Tecta*$^{Y1870C/+}$ basal TM segments showed similar trends as the wild-type CBA/Ca basal TM segments presented in Chapter 4, with a grouping of total phase lag for stimulus frequencies ≥11 kHz (Figure 5.1, A-B). Because of this grouping effect and a slight increase of phase variability with stimulus frequency the greatest average phase lag for each group (as quoted above) did not necessarily occur at 20 kHz (although the error bars in Figure 5.2, A-B indicate they do fit within the general trend). 18 kHz provides a good trade-off between frequency and amplitude of the stimulus and Figure 5.1, D-F shows the phase lag at 18 kHz and other stimulus frequencies descending in 5 kHz steps for visual clarity. At 18 kHz the total phase lag over a distance of 340 µm in the *Tecta*$^{Y1870C/+}$ basal TM segments averaged 373^{o}=1.10 ^{o}µm^{-1}, over a distance of 340 µm in the *Tectb*$^{-/-}$ basal TM segments phase lag averaged 337^{o}=0.91 ^{o}µm^{-1}, and over a distance of 320 µm in the *Otoa*$^{EGFP/EGFP}$ basal TM segments phase lag averaged 386^{o}=1.21 ^{o}µm^{-1} (3, 8, 13 and 18 kHz summarised in Table 5.2).

The total phase lag as a function of stimulus frequency over the available longitudinal stretches of TM for each group is plotted in Figure 5.2, A-C. Similar to the wild-type groups (in both basal and apical TM segments), the phase roll-off varied as a function of stimulus frequency for the *Tectb*$^{-/-}$ basal TM segments (Figure 5.2, B), but not in the *Tecta*$^{Y1870C/+}$ basal TM segments (Figure 5.2, A) or *Otoa*$^{EGFP/EGFP}$ basal TM segments (Figure 5.2, C). In all three groups the monotonic increase in total phase-lag with stimulus frequency (over the longitudinal distance, r, Figure 5.2, A-C) and corresponding phase roll-off (Figure 5.2, D-F) can be approximated by linear fits to the lower (1-10 kHz) and higher (11-20 kHz) stimulus frequency ranges (indicated

by dashed black and dashed red regression lines in Figure 5.2, A-D). In all three mutant groups the gradients for the both total phase lag and phase roll-off as functions of stimulus frequency appeared significantly different from *y*=0 for the 1-10 kHz frequency range: *Tectb*$^{-/-}$ basal gradient=14.4 $^{o}Hz^{-1}$ (total phase lag over 320 µm, Figure 5.2, B) and gradient=0.0452 $^{o}\mu m^{-1}Hz^{-1}$ (phase roll-off, Figure 5.2, E), $p<0.001$. *Tecta*$^{Y1870C/+}$ basal gradient=34.0 $^{o}Hz^{-1}$ (total phase lag over 340 µm, Figure 5.2, A) and gradient=0.100 $^{o}\mu m^{-1}Hz^{-1}$ (phase roll-off, Figure 5.2, D), $p<0.001$. *Otoa*$^{EGFP/EGFP}$ basal gradient=19.4 $^{o}Hz^{-1}$ (total phase lag over 320 µm, Figure 5.2, C) and gradient=0.0607 $^{o}\mu m^{-1}Hz^{-1}$ (phase roll-off, Figure 5.2, F), $p<0.001$. The *Tectb*$^{-/-}$ basal group plateaued in the 11-20 kHz frequency range: *Tectb*$^{-/-}$ gradient=2.15 $^{o}Hz^{-1}$ (total phase lag over 320 µm, Figure 5.2, B) and gradient=0.00670 $^{o}\mu m^{-1}Hz^{-1}$ (phase roll-off, Figure 5.2, E), $p=0.501$. However the *Tecta*$^{Y1870C/+}$ basal and *Otoa*$^{EGFP/EGFP}$ basal groups did not: *Tecta*$^{Y1870C/+}$ gradient=8.22 $^{o}Hz^{-1}$ (total phase lag over 340 µm, Figure 5.2, A) and gradient=0.0242 $^{o}\mu m^{-1}Hz^{-1}$ (phase roll-off, Figure 5.2, D), $p=0.015$. *Otoa*$^{EGFP/EGFP}$ gradient=17.3 $^{o}Hz^{-1}$ (total phase lag over 320 µm, Figure 5.2, C) and gradient=0.0540 $^{o}\mu m^{-1}Hz^{-1}$ (phase roll-off, Figure 5.2, F), $p<0.001$. The *Tecta*$^{Y1870C/+}$ basal and *Otoa*$^{EGFP/EGFP}$ basal groups showed a linear increase in total phase lag and phase roll-off as functions of stimulus frequency across the whole 1-20 kHz stimulus frequency range, with the linear relationship appearing strongest in the *Otoa*$^{EGFP/EGFP}$ group.

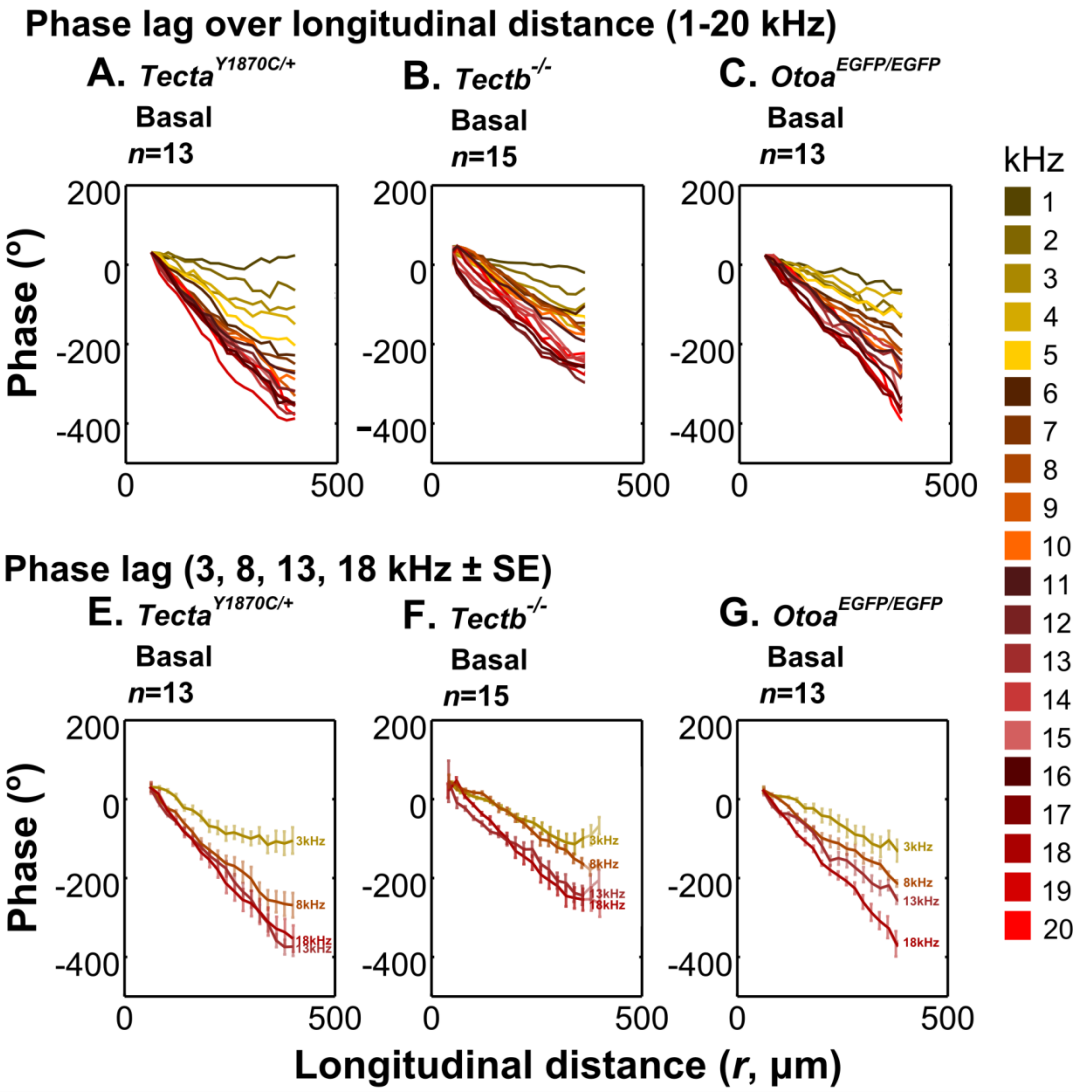

Figure 5.1 Comparison of the phase lag between the mutant TM segments (normalised to 0° at 100 µm). **A-C**. Phase roll-off for stimulus frequencies 1-20 kHz increased as a function of longitudinal distance for basal TM segments from all three mutant groups. **D-E**. Phase lag as a function of longitudinal distance for stimulus frequencies 3, 8, 13 and 18 kHz. For visual clarity error bars are standard error.

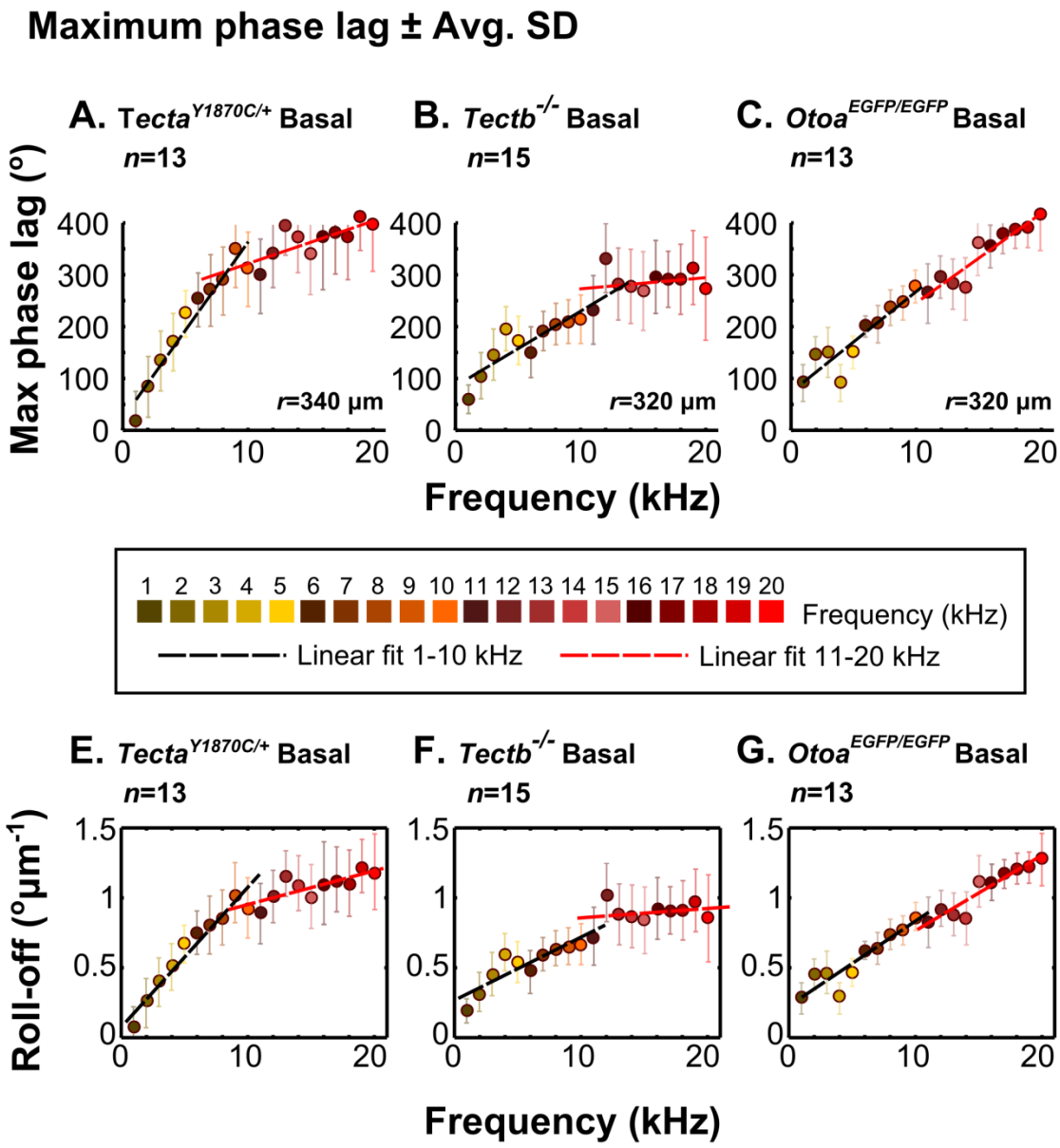

Figure 5.2 Comparison of the total phase lag and phase roll-off between the mutant TM segments. **A-C**. The maximum average phase lag as a function of stimulus frequency over a set longitudinal distance, *r*, for each mutant group. Error bars are the average standard deviation of the preceding longitudinal points. Dashed black regression lines show linear fits to the lower stimulus frequency range (1-10 kHz) and dashed red regression lines show linear fits to the higher stimulus frequency range (11-20 kHz). **D-F**. The average phase roll-off for each group. In the *Tectb*$^{-/-}$ basal and *Tecta*$^{Y1870C/+}$ basal groups (**D** and **E**) the linear fits (dashed black and dashed red regression lines) indicate that phase acceleration as a function of stimulus frequencies is greater for the 1-10 kHz frequency range than the 11-20 kHz frequency range. For the *Otoa*$^{EGFP/EGFP}$ basal TM segments (**C**), acceleration of the rate of phase roll-off does not vary as a function of stimulus frequency.

Group	Stimulus frequency (kHz)	Phase lag (°)	Distance (r, µm)	Phase roll-off (°µm^{-1})
Tecta$^{Y1870C/+}$ Basal (*n*=13)	3	137	340	0.40
Tecta$^{Y1870C/+}$ Basal (*n*=13)	8	291	340	0.86
Tecta$^{Y1870C/+}$ Basal (*n*=13)	13	396	340	1.16
Tecta$^{Y1870C/+}$ Basal (*n*=13)	18	373	340	1.10
Tectb$^{-/-}$ Basal (*n*=15)	3	146	320	0.46
Tectb$^{-/-}$ Basal (*n*=15)	8	214	320	0.64
Tectb$^{-/-}$ Basal (*n*=15)	13	282	320	0.88
Tectb$^{-/-}$ Basal (*n*=15)	18	337	320	0.91
Otoa$^{EGFP/EGFP}$ Basal (*n*=13)	3	150	320	0.47
Otoa$^{EGFP/EGFP}$ Basal (*n*=13)	8	237	320	0.74
Otoa$^{EGFP/EGFP}$ Basal (*n*=13)	13	282	320	0.88
Otoa$^{EGFP/EGFP}$ Basal (*n*=13)	18	386	320	1.21

Table 5.2 Summary of phase lag and phase roll-off at each stimulus frequency for the mutant TM segments (colour coded by stimulus frequency).

5.3.2 Propagation velocity of the travelling wave

The propagation velocities calculated for each group using Equation 2.1 were similar between the mutant basal TM segments and were notably different from the wild-type CBA/Ca basal TM segments (Figure 5.3). In all three mutant groups the propagation velocity increased monotonically as a function of stimulus frequency (mean±SD). *Tecta*$^{Y1870C/+}$ basal: 1.50±1.14 ms^{-1} at 1 kHz increasing to 5.44±1.03 ms^{-1} at 20 kHz (3.63x). *Tectb*$^{-/-}$ basal: 1.41±0.627 ms^{-1} at 1 kHz increasing to 5.19±0.881 ms^{-1} at 20 kHz (3.68x). *Otoa*$^{EGFP/EGFP}$ basal: 1.33±0.574 ms^{-1} at 1 kHz increasing to 6.03±1.20 ms^{-1} at 20 kHz (4.53x). Compared to the wild-type CBA/Ca basal TM segments (shown in blue in Figure 5.2 for reference) the propagation velocities calculated from the mutant TM segments were slower at all stimulus frequencies except for the local 5 kHz minima for the wild-type CBA/Ca mice. Although slower overall, the individual increases in velocity from 1-20 kHz were greater for the mutant groups (quoted above) compared to the wild-types (2.11x in the CBA/Ca basal and 2.93x in apical TM segments).

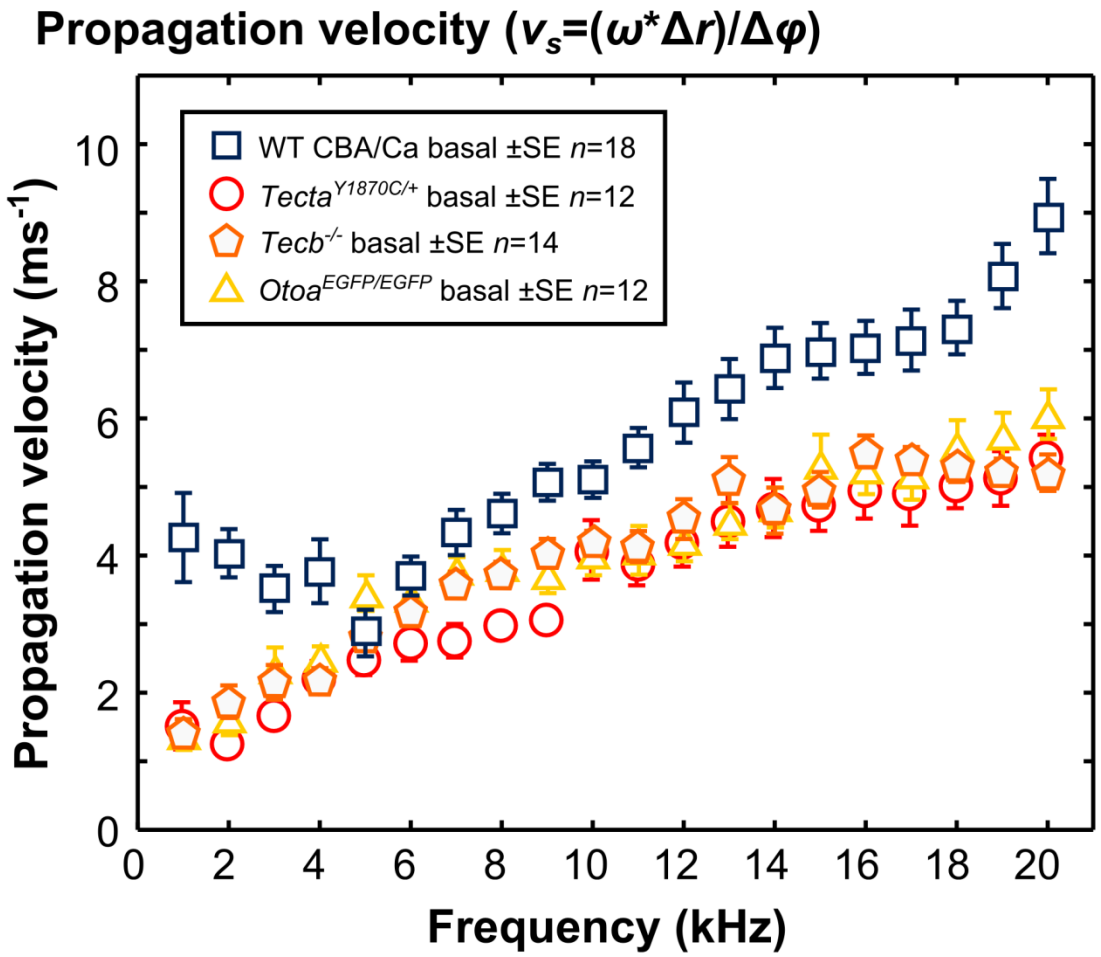

Figure 5.3 Comparison of wave propagation velocities between mutant basal and wild-type CBA/Ca basal TM segments. Wave propagation velocity increased as a function of stimulus frequency for all groups, although was general slower in mutant TM segments (*Tecta*$^{Y1870C/+}$, red; *Tectb*$^{-/-}$, orange; and *Otoa*$^{EGFP/EGFP}$, yellow) than the wild-types (CBA/Ca, blue).

5.3.3 Viscoelastic properties

The viscoelastic properties, *G'* and *η*, estimated for the basal mutant TM segments were significantly lower for each mutant group compared to the same cochlear region in wild-types (*G'*=11.0±6.73 kPa, *η*=0.305±0.0469 Pa·s for wild-type CBA/Ca basal, mean±SD). *G'*=1.43±1.96 kPa (t-test, $p<0.001$), *η*=0.125±0.0172 Pa·s ($p<0.001$) for *Tecta*$^{Y1870C/+}$ basal, *G'*=-0.0983±0.642 kPa ($p<0.001$), *η*=0.128±0.0153 Pa·s ($p<0.001$) for *Tectb*$^{-/-}$ basal, and *G'*=-0.0284±0.720 kPa ($p<0.001$), *η*=0.133±0.0157 Pa·s ($p<0.001$) for *Otoa*$^{EGFP/EGFP}$ basal (Figure 5.4, Table 5.3).

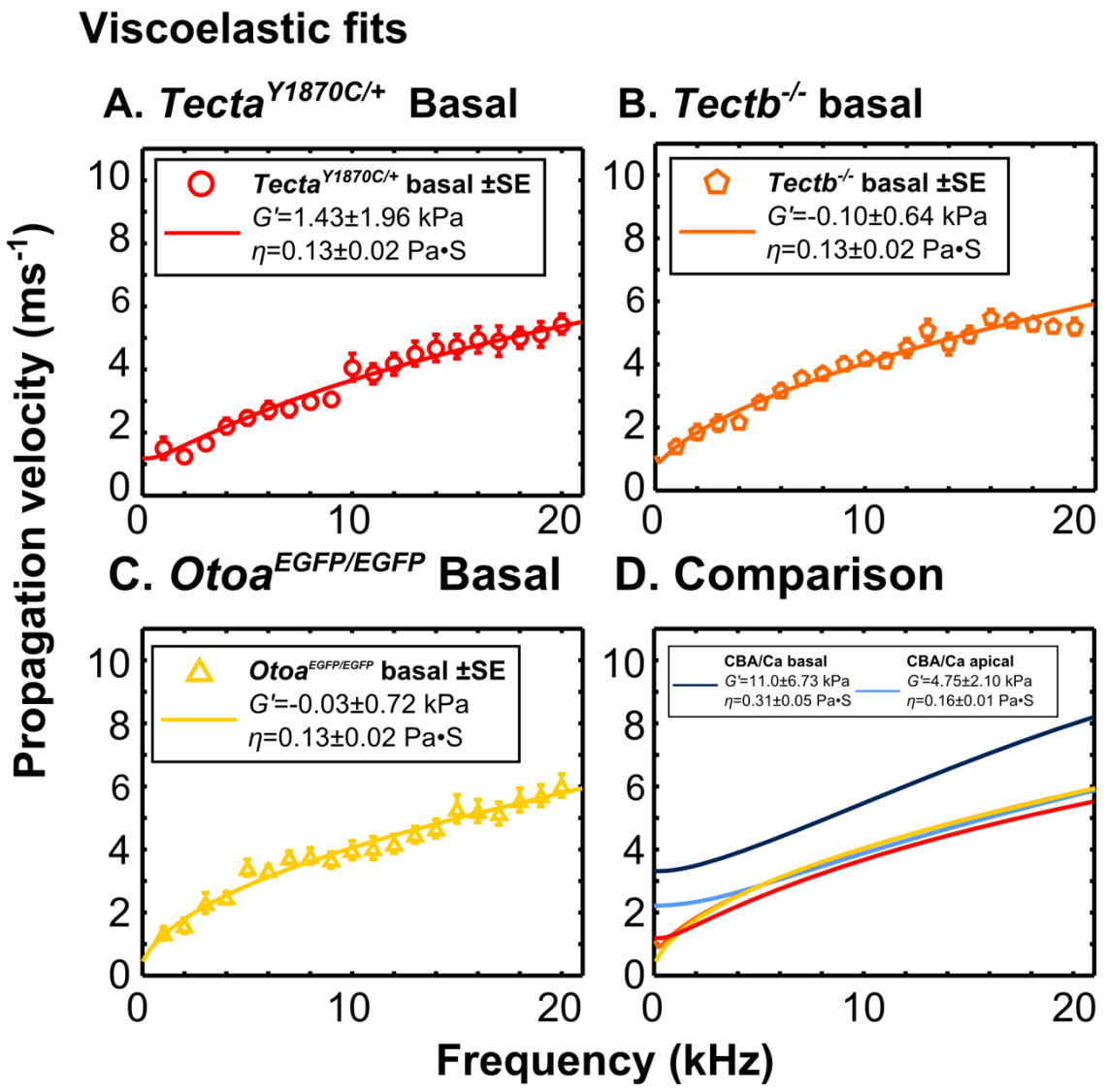

Figure 5.4 The viscoelastic coefficient fits of the travelling wave propagation velocity for the mutant TM segments (mean±SD, values in figure rounded to fit figure). **A**. Tectb$^{Y1870C/+}$ basal TM segments *G'*=1.43±1.96 kPa, *η*=0.0125±0.0172 Pa·s **B**. *Tectb*$^{-/-}$ basal TM segments *G'*= -0.0983±0.642 kPa, *η*=0.128±0.0153 Pa·s. **C**. *Otoa*$^{EGFP/EGFP}$ basal TM segments *G'*=-0.0284±0.720 kPa, *η*=0.133±0.0157 Pa·s. **D**. Comparison of the fits for the mutant TM segments in **A-C** and the wild-type CBA/Ca basal and apical TM segments (Chapter 4).

Group	Viscoelastic properties	
	G' **±SD (kPa)**	***η*** **±SD (Pa·s)**
Tecta$^{Y1870C/+}$ **Basal** (*n*=12)	1.43±1.96	0.125±0.0172
Tectb$^{-/-}$ **Basal** (*n*=14)	-0.0983±0.642	0.128±0.0153
Otoa$^{EGFP/EGFP}$ **Basal** (*n*=12)	-0.0284±0.720	0.133±0.0157

Table 5.3 Summary of the estimated viscoelastic properties for the mutant TM segments (colour coded by group).

5.3.4 Spatial decay of the travelling wave

Amplitude decay was measured for the basal mutant TM segments tween 2-20 kHz (summarised in Table 5.4). The decay constant, α, as a function of longitudinal distance was fit with an exponentially decaying curve ($y=A_{(0)}*e^{-\alpha*x}$) at each stimulus frequency. Examples of the decay curves (normalised to representative 100 nm radial displacement at 0 µm longitudinal distance) as a function of longitudinal distance (0-1000 µm) for each group are shown in Figure 5.5, A-D (*Tecta*$^{Y1870C/+}$ basal), Figure 5.7, A-D (*Tectb*$^{-/-}$ basal) and Figure 5.9, A-D (*Otoa*$^{EGFP/EGFP}$ basal), with the corresponding wild-type CBA/Ca basal decay curves plotted for reference. α as a function of stimulus frequency and wave space constants, σ ($\sigma=1/\alpha$; the distance over which the initial amplitude decays by a factor of $1/e$), are shown in Figure 5.6, A-B (*Tecta*$^{Y1870C/+}$ basal), Figure 5.8, A-B (*Tectb*$^{-/-}$ basal) and Figure 5.10, A-B (*Otoa*$^{EGFP/EGFP}$ basal. Because of the exponential relationship between α and σ (and the requirement of exponentially increasing resolution to accurately determine longer σ), σ>600 µm is classified as >600 µm rather than as a specific value. For the *Tecta*$^{Y1870C/+}$ basal TM segments, α decreases roughly linearly across 2-20 kHz frequency range (meaning σ decreases roughly exponentially) (Figure 5.6, A-B). When this trend is approximated with linear regression fits, the lower (1-10 kHz) and higher (11-20 kHz) stimulus frequency ranges have similar gradients (1-10 kHz gradient=106 Hz^{-1}, 11-20 kHz gradient=188 Hz^{-1}) and do not appear significantly different from $y=0$ (p=0.267, p=0.0656, respectively; dashed black and dashed red regression lines, Figure 5.6, A). Compared to the wild-type CBA/Ca basal TM segments the difference in α deviates at ~15 kHz (as indicated by error bars in Figure 5.6, A), after which σ is shorter in the *Tecta*$^{Y1870C/+}$ basal mice (≥2.28x at 20 kHz). For the *Tectb*$^{-/-}$ basal TM segments amplitude decay increased rapidly as a function of stimulus frequency over the 1-10 kHz frequency range (Figure 5.8, A-B, dashed black regression line: gradient=267 Hz^{-1}, p=0.004) and then plateaued for the higher 11-20 kHz frequency range (Figure 5.8, A, dashed red regression line: gradient=-94 Hz^{-1},

p=0.517). Compared to the wild-type CBA/Ca basal TM segments (Figure 5.8, B) σ was much shorter at stimulus frequencies ≥9 kHz (≥2.96x at 20 kHz). Qualitatively the basal *Tectb*$^{-/-}$ basal amplitude decay data looks more similar to the wild-type CBA/Ca apical data (Figure 4.6, A-B, p. 100) than to the basal wild-type CBA/Ca basal data. α as a function of stimulus frequency for the *Otoa*$^{EGFP/EGFP}$ basal TM segments was linear across the whole 2-20 kHz range and was similar to the wild-type CBA/Ca wild-type basal data <18 kHz (Figure 5.10, A-B). The linear fits to the 1-10 kHz (Figure 5.10, A, dashed black regression line) and 11-20 kHz (Figure 5.10, A, dashed red regression line) frequency ranges had similar gradients and did not appear significantly different from y=0 (1-10 kHz: gradient=130 Hz^{-1}, p=0.165, 11-20 kHz: gradient 111 Hz^{-1}, p=0.0994).

Stimulus frequency (kHz)	***Tecta*$^{Y1870C/+}$ Basal** (n=5)		***Tectb*$^{-/-}$ Basal** (n=5)		***Otoa*$^{EGFP/EGFP}$ Basal** (n=4)	
	α ±SD X10^3	**σ (µm)**	**α ±SD X10^3**	**σ (µm)**	**α ±SD X10^3**	**σ (µm)**
2	3.46±0.980	289	2.55±0.659	392	2.10±0.948	476
4	2.94±1.02	340	2.82±0.751	355	1.98±1.35	505
7	3.59±1.63	279	4.04±1.86	248	3.00±2.33	333
9	4.47±1.53	224	4.14±0.832	242	2.30±0.675	435
10	4.72±1.31	212	4.68±0.711	214	3.36±0.683	298
12	3.45±1.40	290	6.70±1.89	149	3.11±0.864	322
14	3.84±0.620	260	4.89±1.04	204	3.52±0.790	284
15	4.30±0.578	233	4.76±1.12	210	2.94±1.17	340
18	4.91±0.898	204	5.55±1.55	180	3.81±0.890	262
20	4.04±1.04	248	5.24±1.50	191	3.96±0.710	253

Table 5.4 Summary the space and decay constants for the mutant TM segments (colour coded by stimulus frequency).

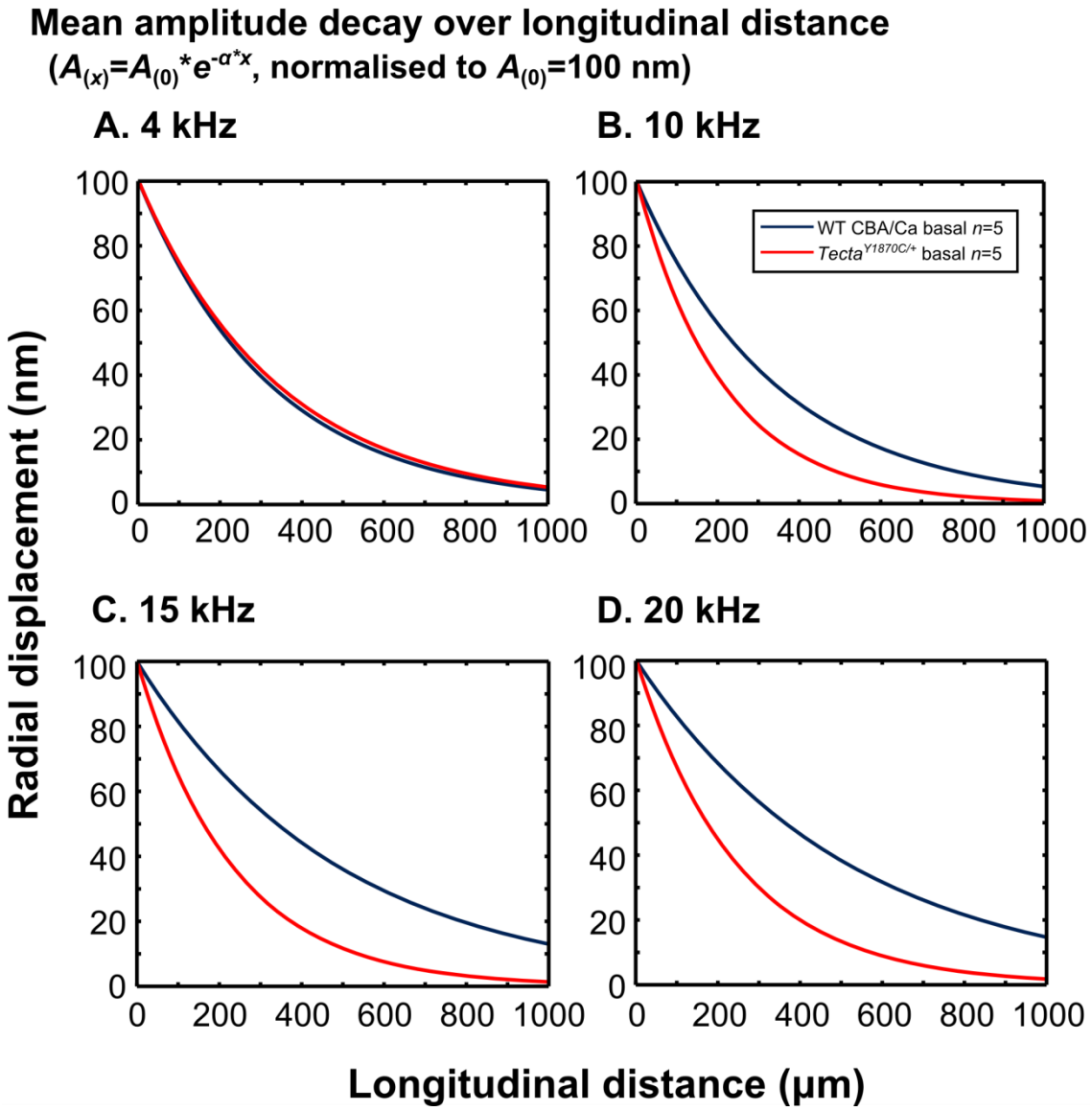

Figure 5.5 Examples of amplitude decay for the *Tecta*$^{Y1870C/+}$ basal TM segments. **A-D**. Amplitude decay of the travelling wave as a function of longitudinal distance for *Tecta*$^{Y1870C/+}$ basal TM segments (red line) at 4 (**A**), 10 (**B**), 15 (**C**) and 20 kHz (**D**). The decay is exponential ($y=A_{(0)}*e^{-\alpha*x}$) where $A_{(0)}$ is plotted as 100 nm radial displacement at the point of stimulation (0 μm) and α is the corresponding value in Table 5.4. Wild-type CBA/Ca basal data (blue lines) are plotted for reference.

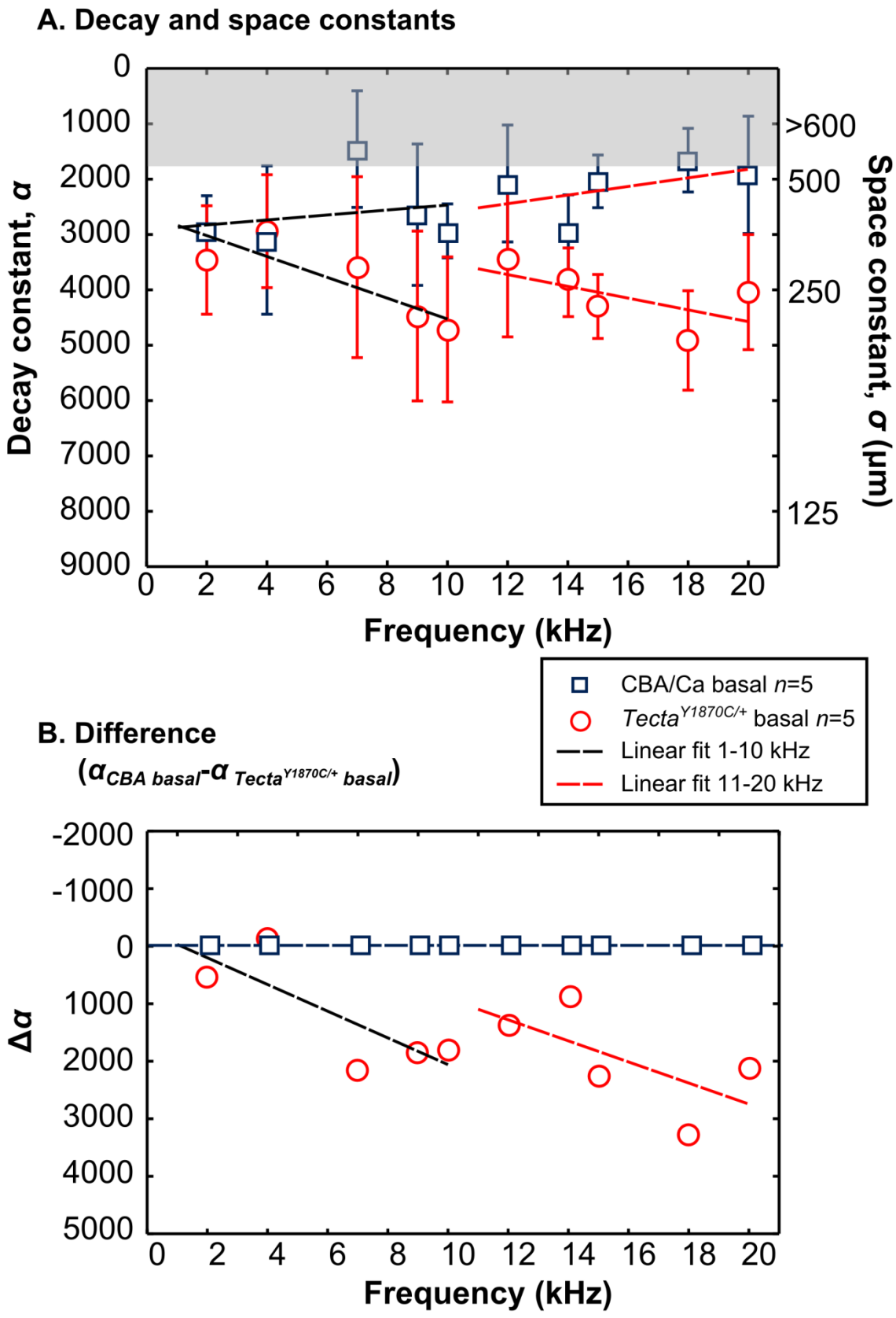

Figure 5.6 Spatial decay as a function of stimulus frequency for the *Tecta*$^{Y1870C/+}$ basal TM segments. **A**. Mean decay constants, α (and corresponding space constants, σ) for the *Tecta*$^{Y1870C/+}$ basal TM segments, with wild-type CBA/Ca basal data plotted for reference. Error bars are standard deviation of α. Dashed black and dashed red regression lines show linear fits to the 1-10 kHz and 11-20 kHz stimulus frequency ranges. **B**. The difference in mean α between the wild-type CBA/Ca basal and *Tecta*$^{Y1870C/+}$ basal TM segments ($\alpha_{CBA\ basal}$-$\alpha_{\mathrm{TectaY1870C/+\ basal}}$).

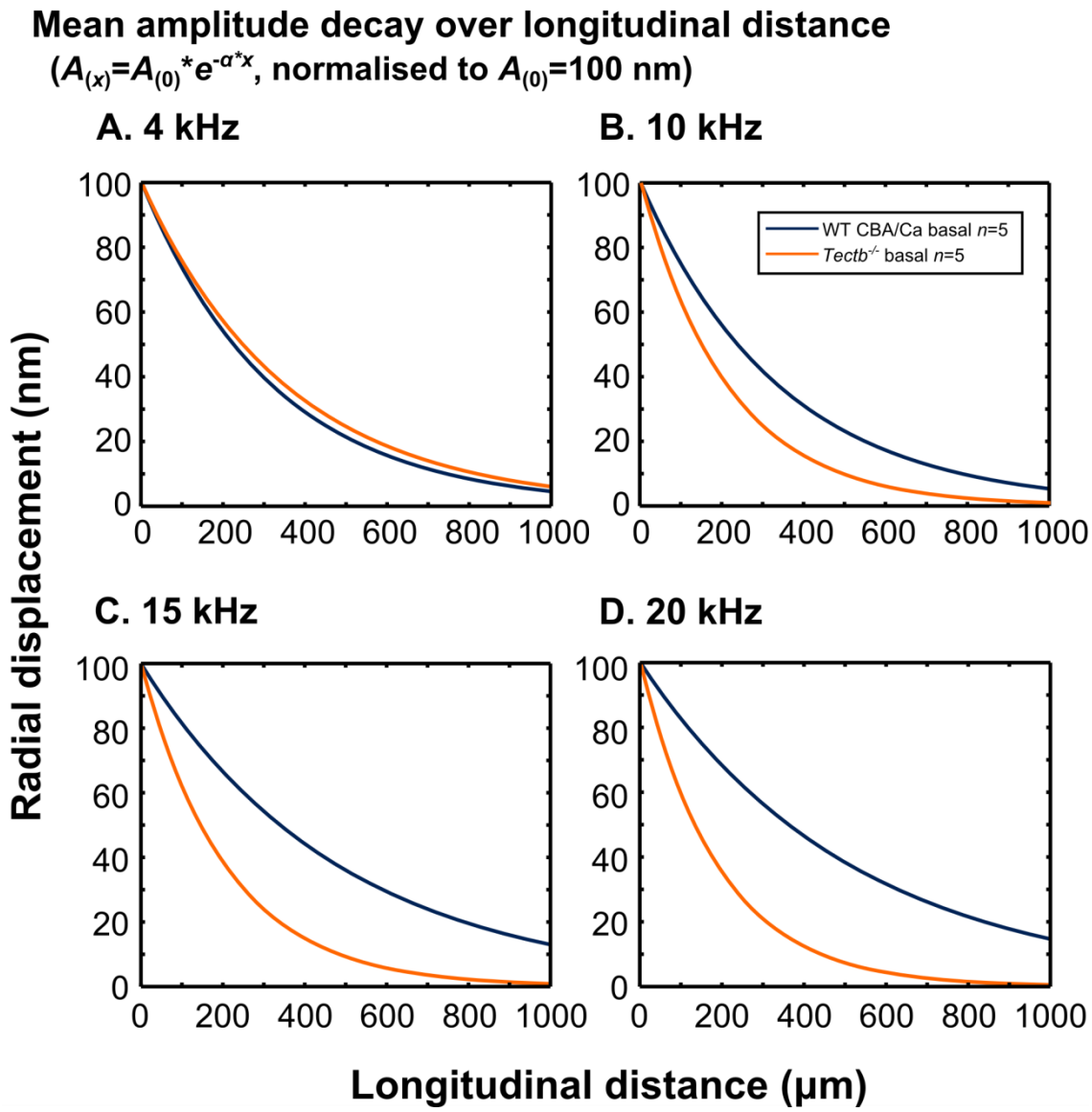

Figure 5.7 Examples of amplitude decay for the *Tectb*$^{-/-}$ basal TM segments. **A-D**. Amplitude decay of the travelling wave as a function of longitudinal distance for *Tectb*$^{-/-}$ basal TM segments (orange line) at 4 (**A**), 10 (**B**), 15 (**C**) and 20 kHz (**D**). The decay is exponential ($y=A_{(0)}*\exp^{-b*x}$) where $A_{(0)}$ is plotted as 100 nm radial displacement at the point of stimulation (0 µm) and α is the corresponding value in Table 5.4. Wild-type basal CBA/Ca data (blue lines) are plotted for reference.

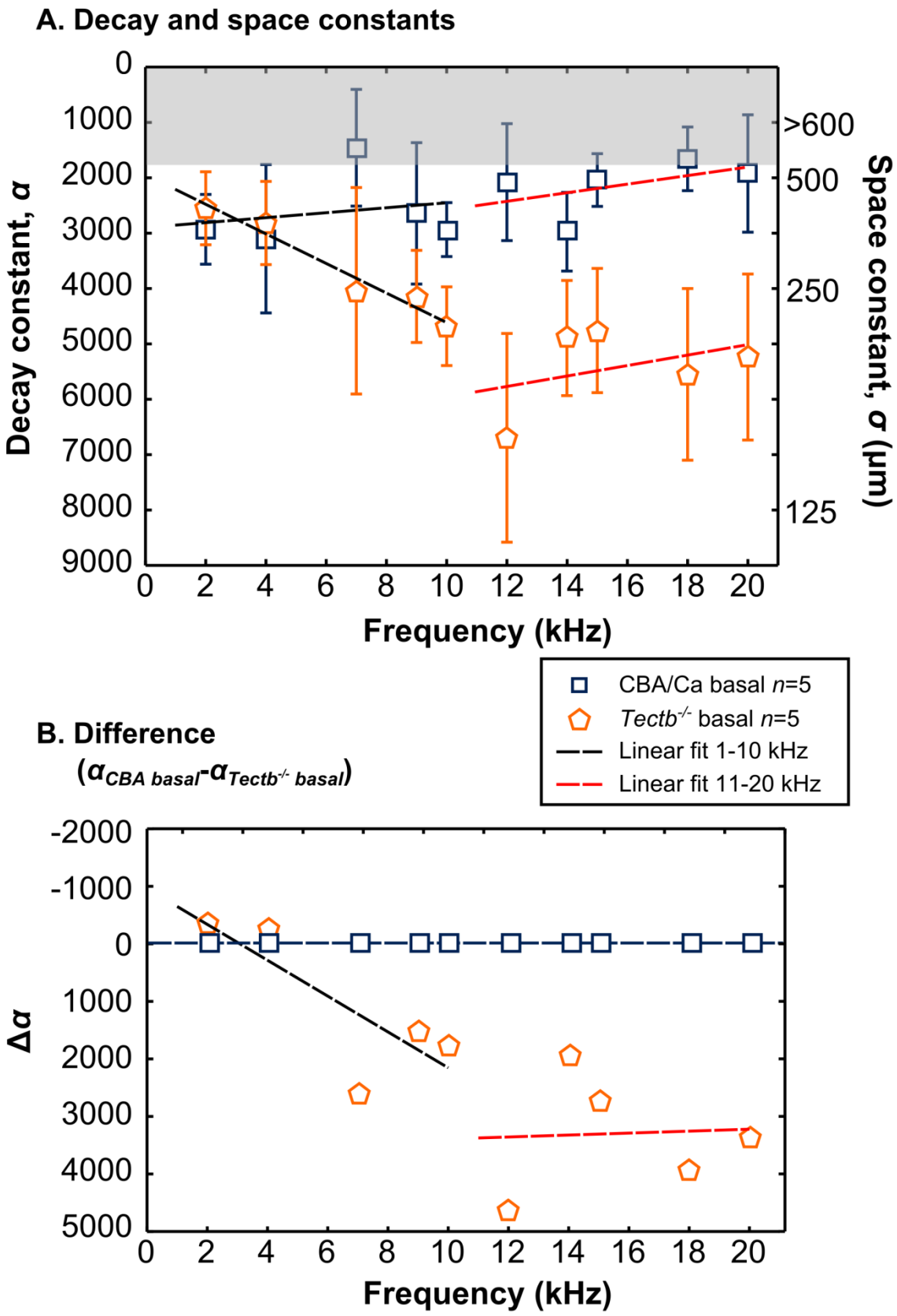

Figure 5.8 Spatial decay as a function of frequency for the *Tectb*$^{-/-}$ basal TM segments. **A**. Mean decay constants, α (and corresponding space constants, σ) for the *Tectb*$^{-/-}$ basal Tm segments, with wild-type CBA/Ca basal data plotted for reference. Error bars are standard deviation of α. Dashed black and dashed red regression lines show linear fits to the 1-10 kHz and 11-20 kHz stimulus frequency ranges. **B**. The difference in mean α between the wild-type CBA/Ca basal and *Tectb*$^{-/-}$ basal TM segments ($\alpha_{CBA\ basal}$-$\alpha_{\text{Tectb-/- basal}}$).

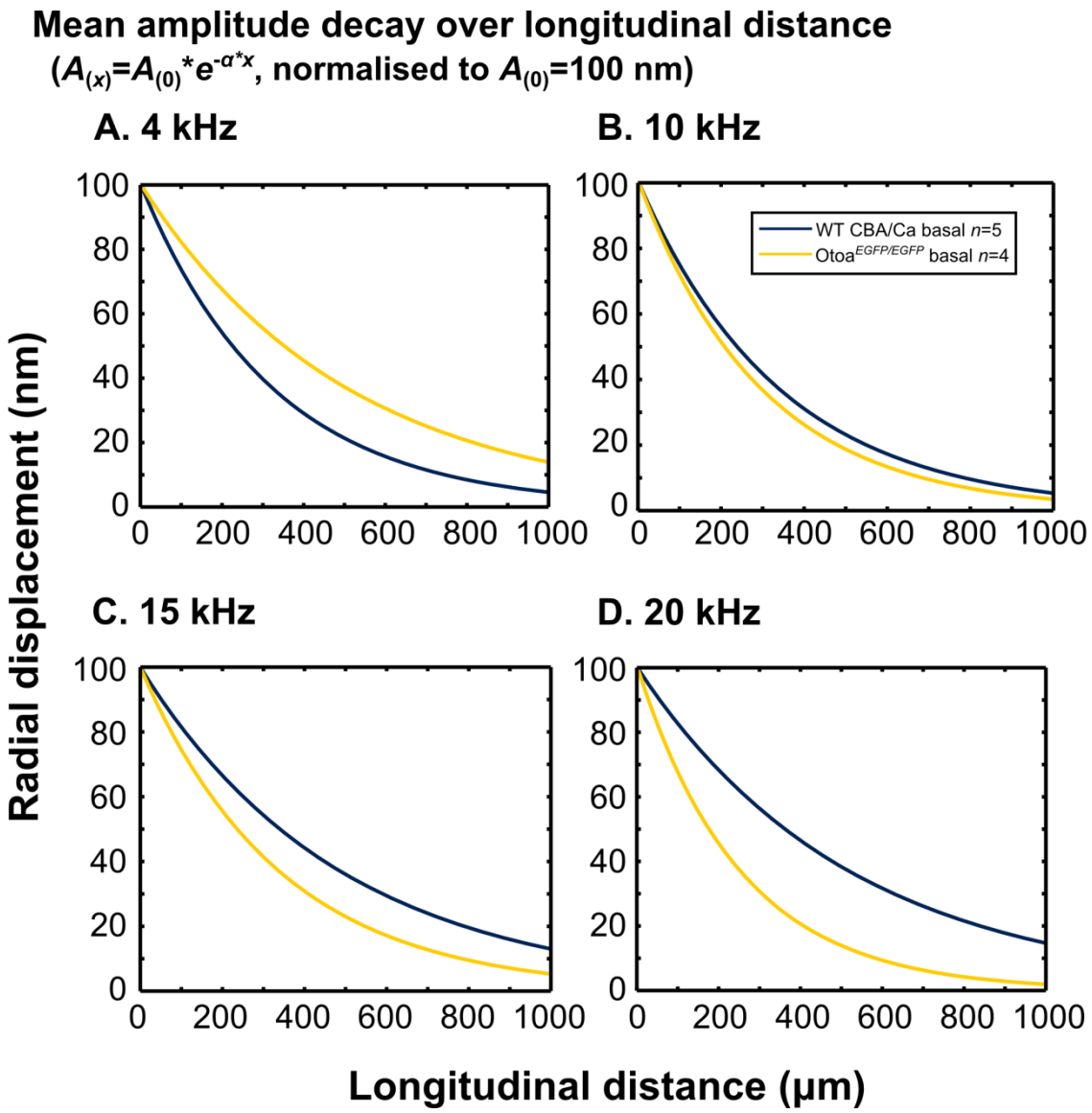

Figure 5.9 Examples of amplitude decay for the *Otoa*$^{EGFP/EGFP}$ basal TM segments. **A-D**. Amplitude decay of the travelling wave as a function of longitudinal distance for *Otoa*$^{EGFP/EGFP}$ basal TM segments (yellow line) at 4 (**A**), 10 (**B**), 15 (**C**) and 20 kHz (**D**). The decay is exponential ($y=A_{(0)}*e^{-\alpha*x}$) where $A_{(0)}$ is plotted as 100 nm radial displacement at the point of stimulation (0 μm) and α is the corresponding value in Table 5.4. Wild-type basal CBA/Ca data (blue lines) are plotted for reference.

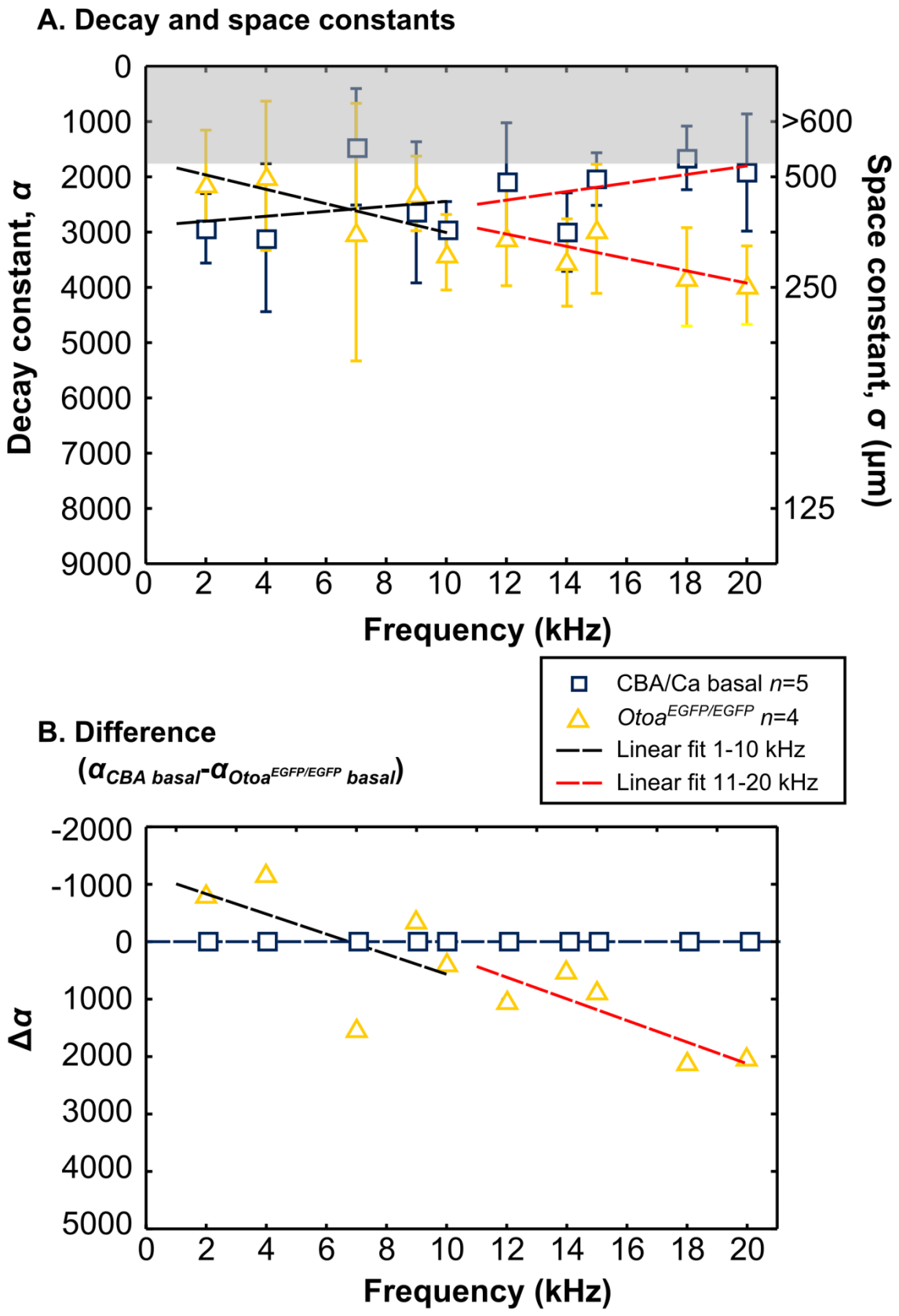

Figure 5.10 Spatial decay as a function of frequency for the *Otoa*$^{EGFP/EGFP}$ basal TM segments. **A**. Mean decay constants, α (and corresponding space constants, σ) for the *Otoa*$^{EGFP/EGFP}$ basal TM segments, with wild-type CBA/Ca basal data plotted for reference. Error bars are standard deviation of α. Dashed black and dashed red regression lines show linear fits to the 1-10 kHz and 11-20 kHz stimulus frequency ranges. **B**. The difference in mean α between the wild-type CBA/Ca basal and *Otoa*$^{EGFP/EGFP}$ basal TM segments ($\alpha_{CBA\ basal}$-$\alpha_{OtoaEGFP/EGFP\ basal}$).

5.3.5 Waveform of the travelling wave

The waveform of the propagating travelling wave is a product of both its wavelength (λ) and amplitude decay (α). The waveform is calculated by fitting a sine wave to the average phase roll-off data at each frequency. The exponential decay functions fit to the amplitude data (plotted as a representative 100 nm radial displacement at 0 µm longitudinal distance) are then applied to the sine wave. Examples of these waveforms are shown in Figure 5.11, A-D (*Tecta*$^{Y1870C/}$ basal^{+}), Figure 5.13, A-D (*Tectb*$^{-/-}$ basal) and Figure 5.15, A-D (*Otoa*$^{EGFP/EGFP}$ basal).

In the *Tecta*$^{Y1870C/+}$ basal TM segments the waveforms consistently lag those from the wild-type CBA/Ca basal TM segments and decayed more rapidly over a shorter longitudinal distance (both effects increasing with stimulus frequency). All waveforms from the *Tecta*$^{Y1870C/+}$ basal TM segments are compared in Figure 5.12, A, with the longitudinal position of the first positive peak plotted in Figure 5.12, B. Across the whole frequency range the first positive peak of the *Tecta*$^{Y1870C/+}$ basal travelling waves occurred at a position ~50% of the distance of the wild-type CBA/Ca basal travelling waves. The travelling waves from the *Tectb*$^{-/-}$ basal TM segments were somewhat similar to those tracked in the *Tecta*$^{Y1870C/+}$ basal TM segments. The waveforms consistently lag those from the wild-type CBA/Ca basal TM segments and decayed more rapidly over a shorter distances (both effects increasing with stimulus frequency). All waveforms from the *Tectb*$^{-/-}$ basal TM segments are compared in Figure 5.14, A with the longitudinal position plotted in Figure 5.14, B. Across the whole frequency range the first positive peak of the *Tectb*$^{-/-}$ basal travelling waves occurred at a position ~50-70% of the distance of the wild-type CBA/Ca basal travelling waves. Overall the *Otoa*$^{EGFP/EGFP}$ basal travelling waves were similar to the other two mutant groups (Figure 5.16, A-B), the first positive peak of the travelling wave occurring at ~60-70% of the distance of those of wild-type CBA/Ca basal TM segments (except at 4 kHz, where there is a corresponding notch in the average phase data).

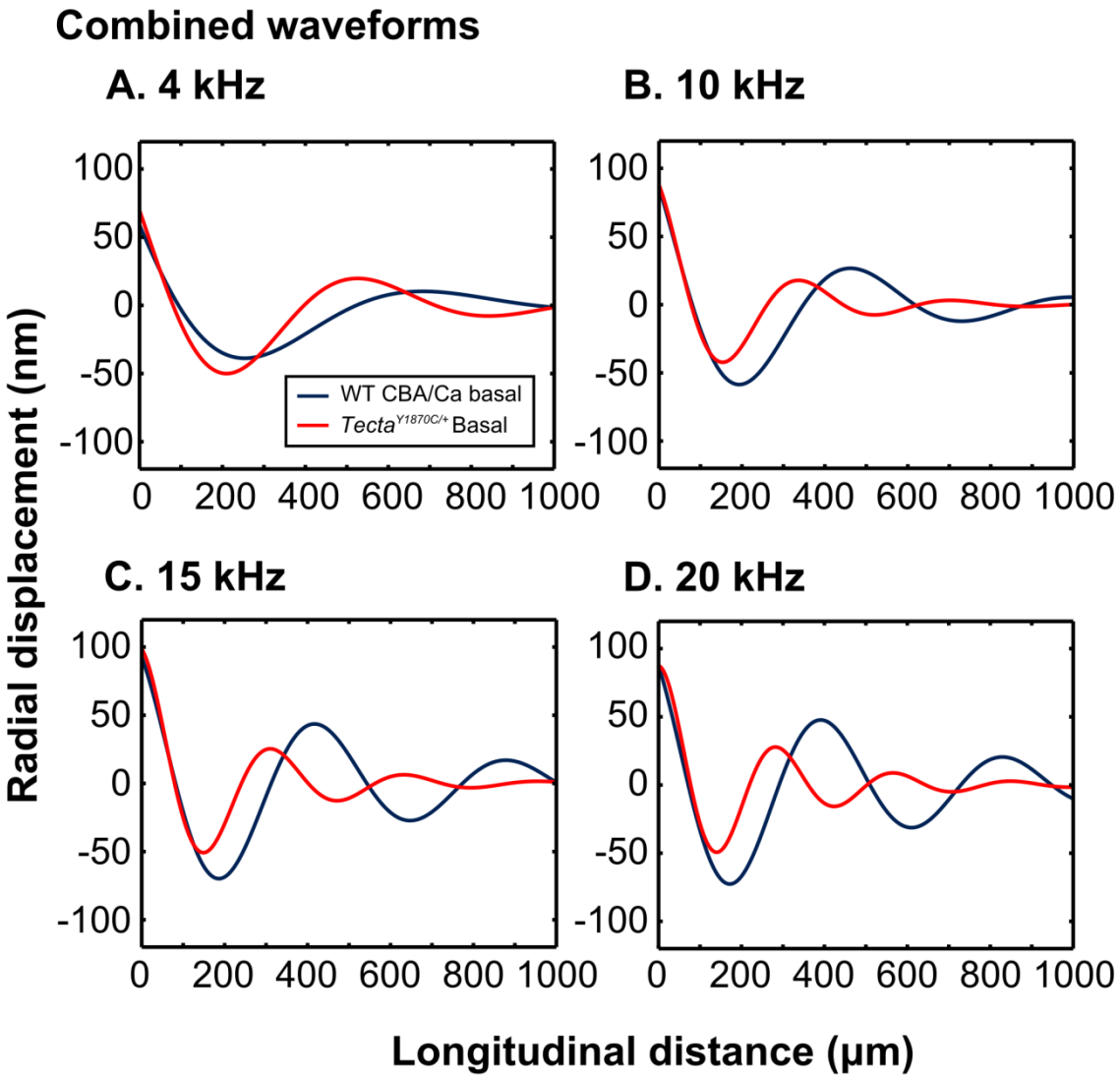

Figure 5.11 Waveforms of the travelling waves for the *Tecta*$^{Y1870C/+}$ basal TM segments. **A-D**. Waveforms from the *Tecta*$^{Y1870C/+}$ basal TM segments (red) for stimulus frequencies 4 (**A**), 10 (**B**), 15 (**C**) and 20 kHz (**D**). Waveforms were calculated from the rate of amplitude decay, α (fit with an exponential decay of the form $y=A_{(0)}*e^{-\alpha*x}$) and the phase data (fit with a sine wave of the form $y=c*\sin(d*x+f)$). Wild-type CBA/Ca basal data (blue) plotted for reference.

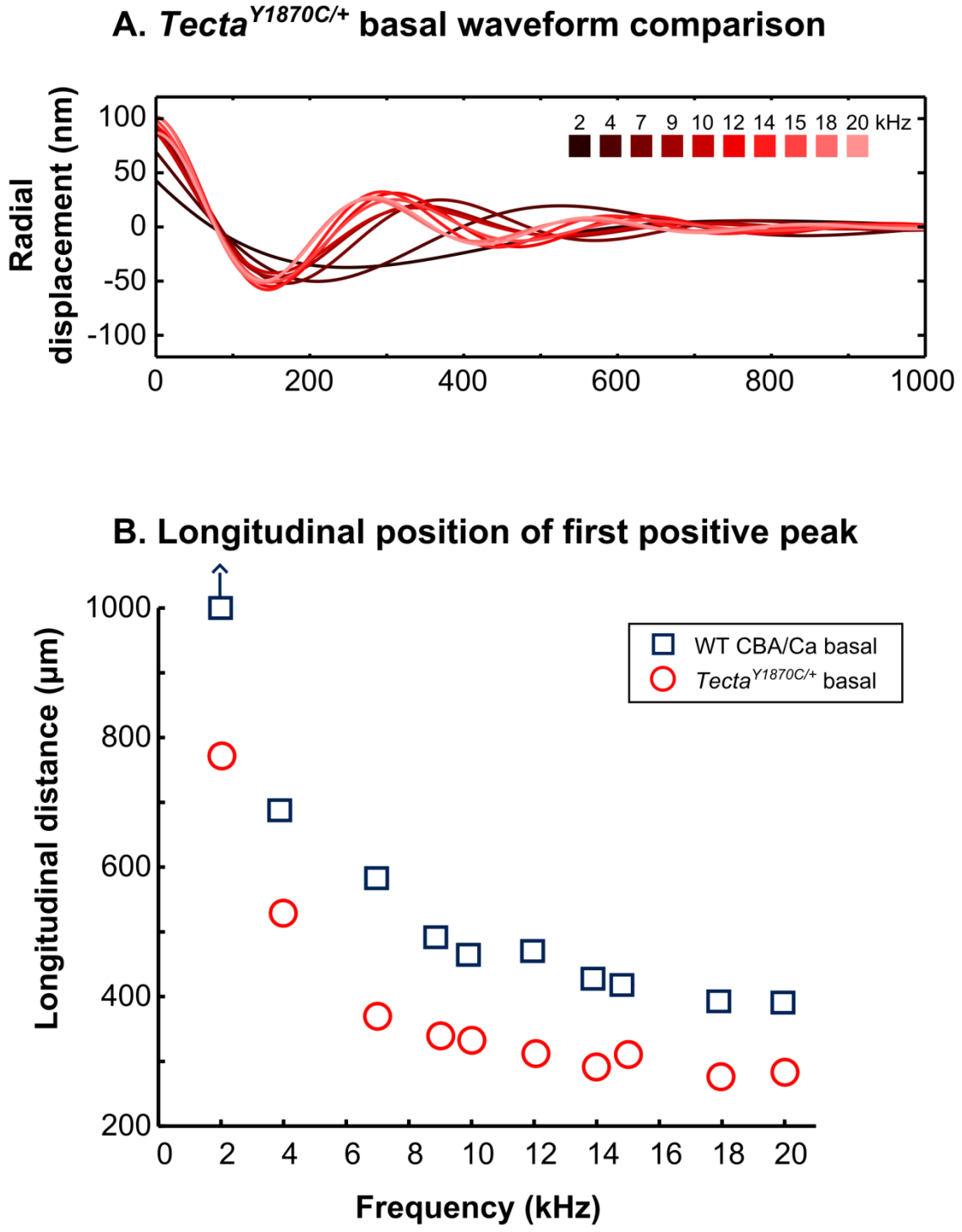

Figure 5.12 Comparison of the waveforms of the travelling waves in the *Tecta*$^{Y1870C/+}$ basal TM segments. **A**. Travelling waveforms for stimulus frequencies 2-20 kHz **B**. The longitudinal position of the first positive peak compared to wild-type CBA/Ca basal TM segments (blue).

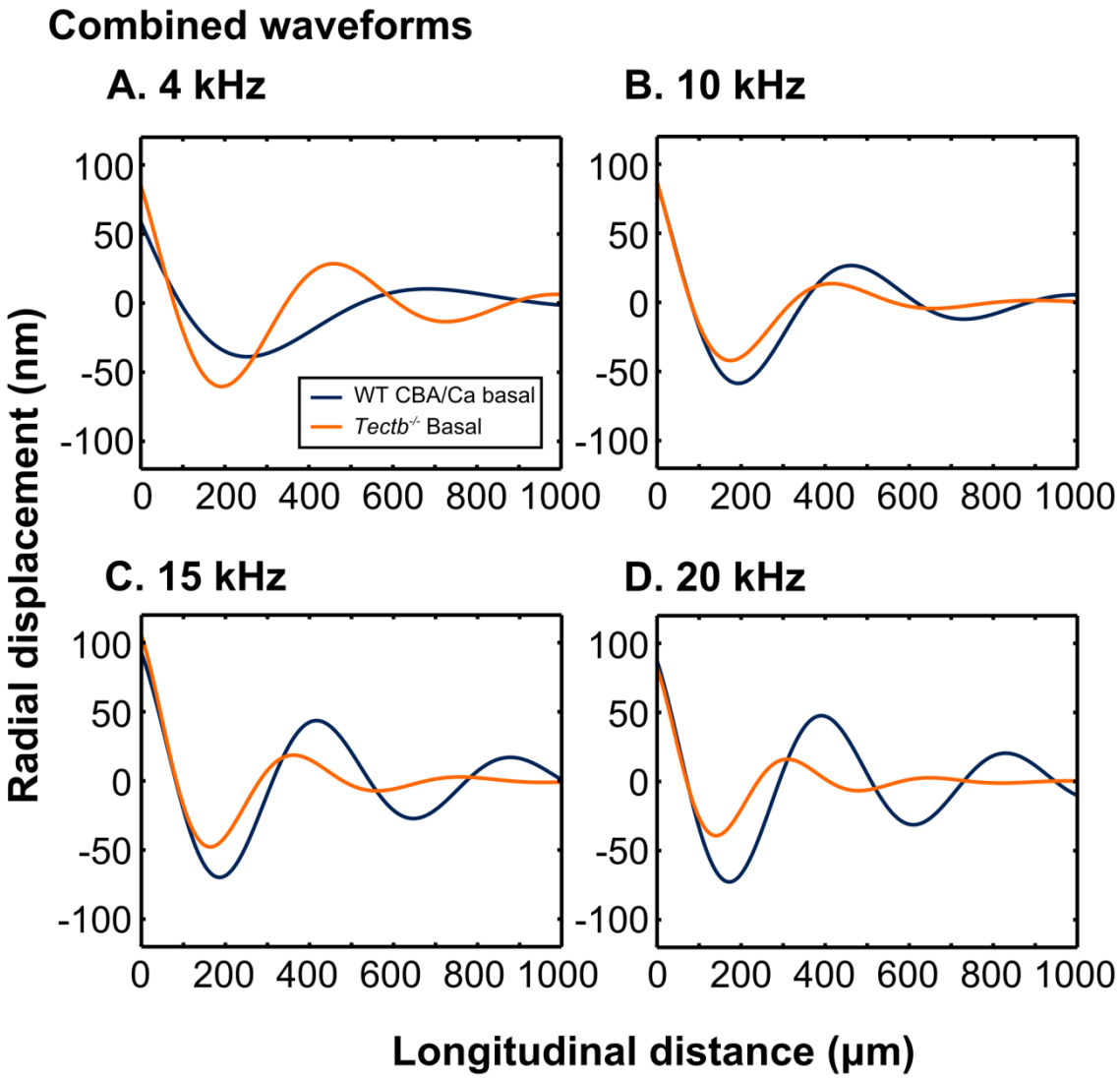

Figure 5.13 Waveforms of the travelling waves in the *Tectb*$^{-/-}$ basal TM segments. **A-D**. Waveforms from the *Tectb*$^{-/-}$ basal TM segments (orange) for stimulus frequencies 4 (**A**), 10 (**B**), 15 (**C**) and 20 kHz (**D**). Waveforms were calculated from the rate of amplitude decay, α (fit with an exponential decay of the form $y=A_{(0)}*e^{-\alpha*x}$) and the phase data (fit with a sine wave of the form $y=c*\sin(d*x+f)$). Wild-type CBA/Ca basal data (blue) plotted for reference.

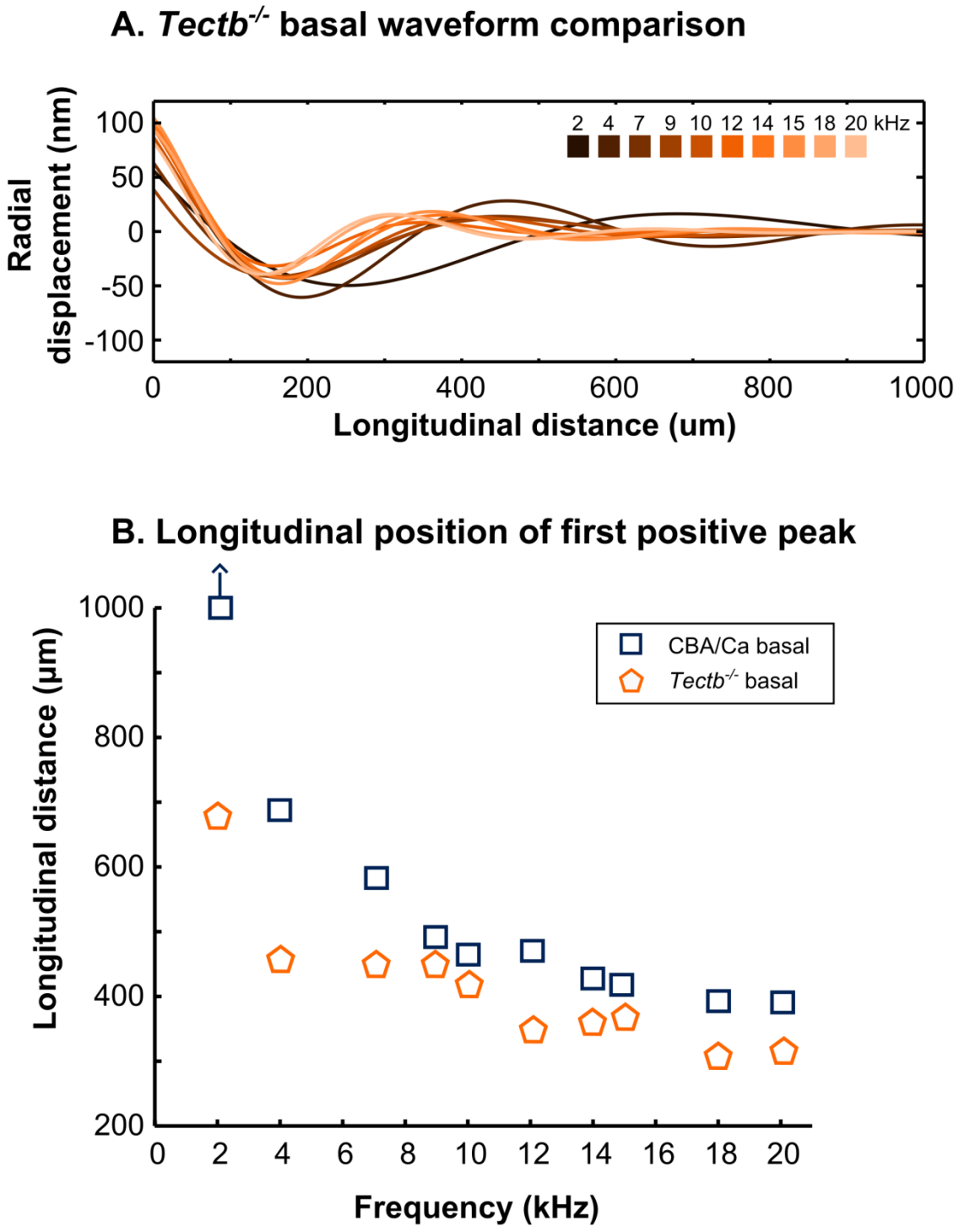

Figure 5.14 Comparison of the waveforms of the travelling waves in the *Tectb*$^{-/-}$ basal TM segments. **A**. Travelling waveforms for stimulus frequencies 2-20 kHz **B**. The longitudinal position of the first positive peak compared to wild-type CBA/Ca basal TM segments (blue).

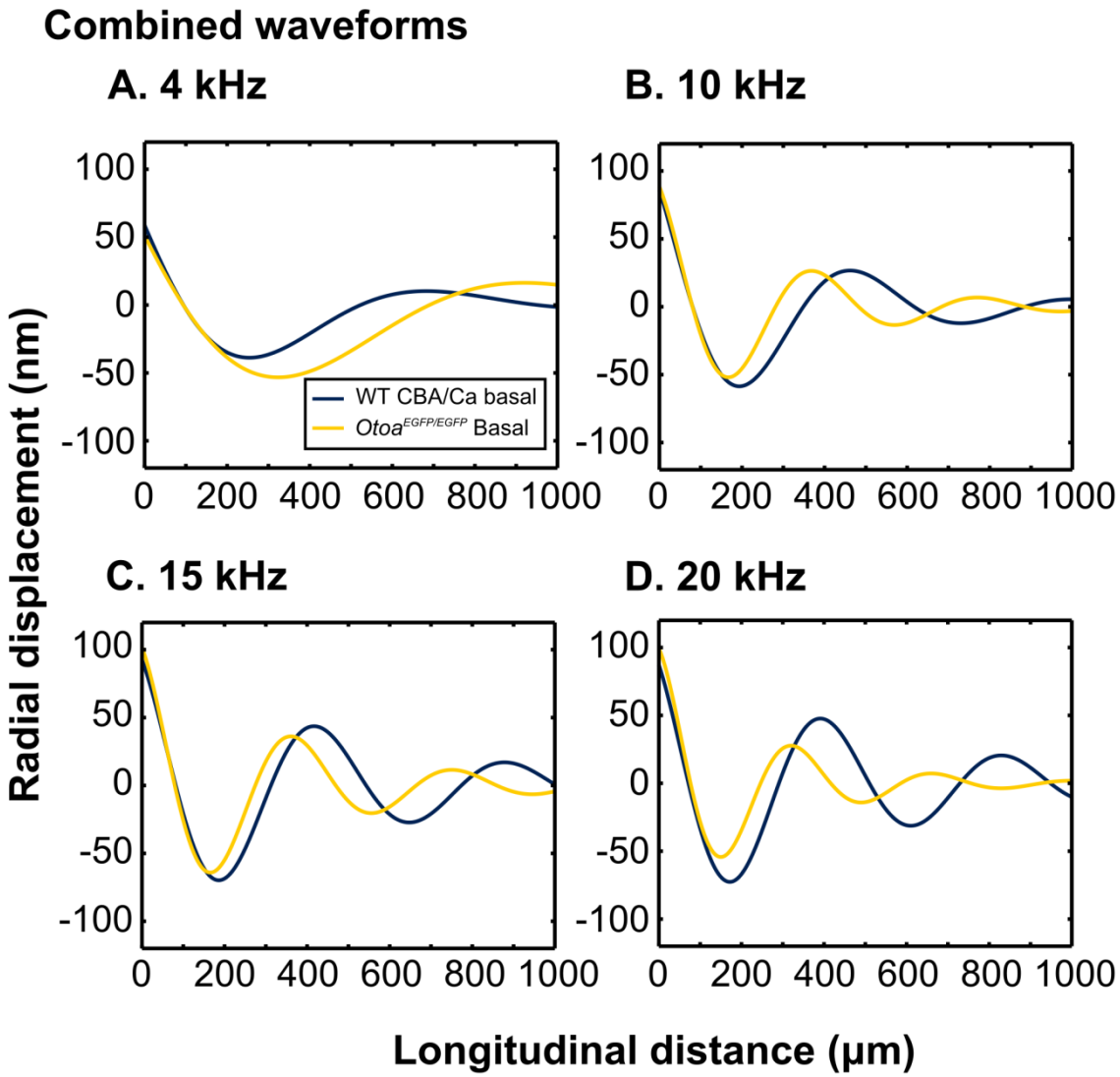

Figure 5.15 Waveforms of the travelling waves in the *Otoa*$^{EGFP/EGFP}$ basal TM segments. **A-D**. Waveforms from the *Otoa*$^{EGFP/EGFP}$ basal TM segments (yellow) for stimulus frequencies 4 (**A**), 10 (**B**), 15 (**C**) and 20 kHz (**D**). Waveforms were calculated from the rate of amplitude decay, α (fit with an exponential decay of the form $y=A_{(0)}*e^{-\alpha*x}$) and the phase data (fit with a sine wave of the form $y=c*\sin(d*x+f)$). Wild-type CBA/Ca basal data (blue) plotted for reference.

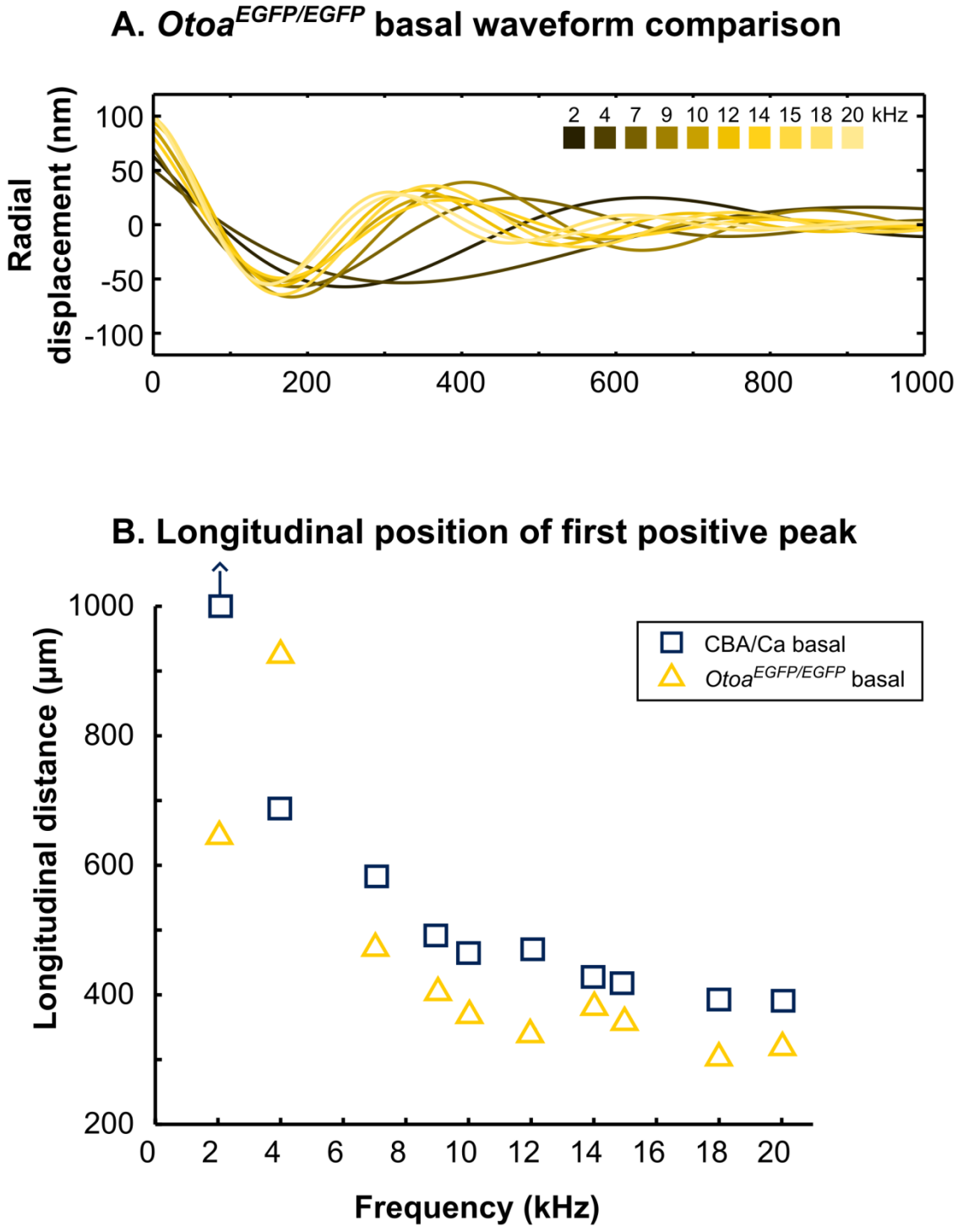

Figure 5.16 Comparison of the waveforms of the travelling waves in the *Otoa*$^{EGFP/EGFP}$ basal TM segments. **A**. Travelling waveforms for stimulus frequencies 2-20 kHz **B**. The longitudinal position of the first positive peak compared to wild-type CBA/Ca basal TM segments (blue).

5.4 Discussion

5.4.1 Summary

The mechanical properties of the isolated TM segments of all three mutant groups studied are different from those of wild-types. The specific characteristics of each group vary, with phase roll-off, travelling wave propagation velocity, and spatial decay of the amplitude of the travelling waves all affected (Figure 5.17). Attributing any particular characteristic change to a structural pathology of the TM is difficult; in the *Tecta*$^{Y1870C/+}$ and *Tectb*$^{-/-}$ mice the striated sheet matrix is known to be disrupted, but how specifically is not known (Legan et al., 2005; Russell et al., 2007). Structural abnormalities of the *Otoa*$^{EGFP/EGFP}$ TMs any are less obvious, although they do lack Hensen's stripe and have possible disruption of the marginal zone (Lukashkin et al., unpublished data).

5.4.2 Wave velocity is reduced in all three mutant groups

Phase rolled-off more quickly with longitudinal distance in the *Tecta*$^{Y1870C/+}$, *Tectb*$^{-/-}$ and *Otoa*$^{EGFP/EGFP}$ basal TM segments than in the wild-type basal TM segments. As a result the calculated travelling wave propagation velocities were significantly lower than those of wild-types (Figure 5.3) and were more similar to the calculated propagation velocities from the wild-type apical TM segments (Figure 4.3, p. 96). Resulting estimates for the viscoelastic properties in these mutants were significantly lower than the CBA/CA basal group for both the shear storage modulus (G') and shear viscosity (η) (Table 5.3). The lower viscoelastic properties (Figure 5.4, A-D) indicate that compared to their wild-type counterparts, the TM segments from the mutant groups (as a result of different structural abnormalities) are less rigid and equally less able to propagate energy longitudinally.

Between the mutant groups more specific differences in the relationship between phase roll-off and stimulus frequency (Figure 5.2) were also observed. In TM segments from both the apical and basal turns of the wild-type CBA/Ca mice, phase roll-off as a function of stimulus frequency varied more quickly for the 1-10 kHz frequency range than for the 11-20 kHz frequency range. This relationship is maintained in the *Tectb*$^{-/-}$ mice, which show a similar, rapid increase in the rate of phase roll-off between 1-10 kHz (dashed black regression lines Figure 5.2, B and D, which appear significantly different to y=0) and a plateauing of the roll-off between 11-20 kHz (dashed red regression lines Figure 5.2, B and D, which do not appear significantly different to y=0). In the *Otoa*$^{EGFP/EGFP}$ basal TM segments, however this relationship is completely lost and rate of phase roll-off varies lineally with stimulus frequency (dashed black and dashed red regression lines Figure 5.2, C and F, which do not appear significantly

different to *y*=0). The *Tecta*$^{Y1870C/+}$ basal TM segments fall somewhere between the extremes of the *Tectb*$^{-/-}$ and *Otoa*$^{EGFP/EGFP}$ in terms of the similarity of their rate of phase roll-off to stimulus frequency relationship to wild-types. Phase measurements from TM segments of *Tecta*$^{Y1870C/+}$ mice show the rapid increase in the rate of phase roll-off over the lower frequency range (dashed black regression lines Figure 5.2, A and D, appear significantly different to *y*=0) characteristic of all the other groups studied (CBA/Ca basal, CBA/Ca apical, S129 basal, *Tectb*$^{-/-}$ basal and *Otoa*$^{EGFP/EGFP}$ basal). However, phase does not plateau at the higher stimulus frequencies (dashed red regression lines Figure 5.2, A and D, which also appears significantly different from *y*=0), although statistically linear, the relationship is statistically and qualitatively not as strong as the linear relationship between rate of phase roll-off and stimulus frequency observed in the *Otoa*$^{EGFP/EGFP}$ TM segments (p=0.015 for the *Tecta*$^{Y1870C/+}$ basal 11-20 kHz fit compared to p<0.001 for the *Otoa*$^{EGFP/EGFP}$ basal 11-20 kHz fit).

5.4.3 Spatial coupling is reduced in all three mutant groups

The longitudinal coupling, indicated by the spatial extent of the travelling waves (space constant, σ) and the amplitude decay of the travelling wave (decay constant, α), is reduced in all three mutant groups by varying amounts, compared to the wild-type CBA/Ca basal data. In all three mutant groups, α increases as a function of stimulus frequency over the 2-20 kHz range, whereas in TM segments isolated from the basal turn of the wild-types, there is no increase in α (or corresponding decrease in σ) over this range of stimulus frequencies (Figure 4.6, A, p. 100).

σ decreases as a function of stimulus frequency for all three mutant groups and the greatest overall reduction in σ is observed in the *Tectb*$^{-/-}$ basal TM segments; at 20 kHz σ=203 µm compared to >600 µm in wild-type CBA/Ca basal TM segments (Table 5.4). At 20 kHz the *Tecta*$^{Y1870C/+}$ and *Otoa*$^{EGFP/EGFP}$ basal TM segments have similar σ values; σ=263 and σ=259 µm, respectively (Table 5.4). Although the σ values are similar for each mutant group at 20 kHz (the error bars of α overlap), the characteristics of the relationship between spatial decay and stimulus frequency vary. The *Otoa*$^{EGFP/EGFP}$ basal TM segments are the most representative of the wild-type CBA/Ca basal group and when fit with linear functions for the 1-10 and 11-20 kHz stimulus frequency ranges (dashed black and dashed red regression lines, Figure 5.4, A) neither appear significantly different to *y*=0 (as in the wild-types). The standard deviation error bars in Figure 5.4, A indicate that the mean *Otoa*$^{EGFP/EGFP}$ basal α is significantly different from that of wild-types at 18 and 20 kHz only. The relationship between stimulus frequency and spatial decay in *Tecta*$^{Y1870C/+}$ and *Tectb*$^{-/-}$ is characteristically different to that of the wild-type CBA/Ca basal and *Otoa*$^{EGFP/EGFP}$ basal data. For both of these groups (*Tecta*$^{Y1870C/+}$ basal and

Tectb$^{-/-}$ basal), α increases rapidly in the 1-10 kHz frequency range and then plateaus in the 11-20 kHz frequency range. This effect is strongest in the *Tectb*$^{-/-}$ basal TM segments (Figure 5.8, A, dashed black and dashed red regression lines), which show the greatest overall reduction in σ, and α appears significantly different from wild-types for stimulus frequencies ≥10 kHz (as indicated by the standard deviation of α, Figure 5.8, A). In the *Tecta*$^{Y1870C/+}$ basal TM segments a similar rapid decrease in spatial coupling is seen in the lower frequency range and a plateau in the higher frequency range (dashed black and dashed red regression lines, Figure 5.6, A). Stimulus frequencies ≥14 kHz appear significantly different from wild-type CBA/Ca basal TM segments (as indicated by the standard deviation of α, Figure 5.6, A).

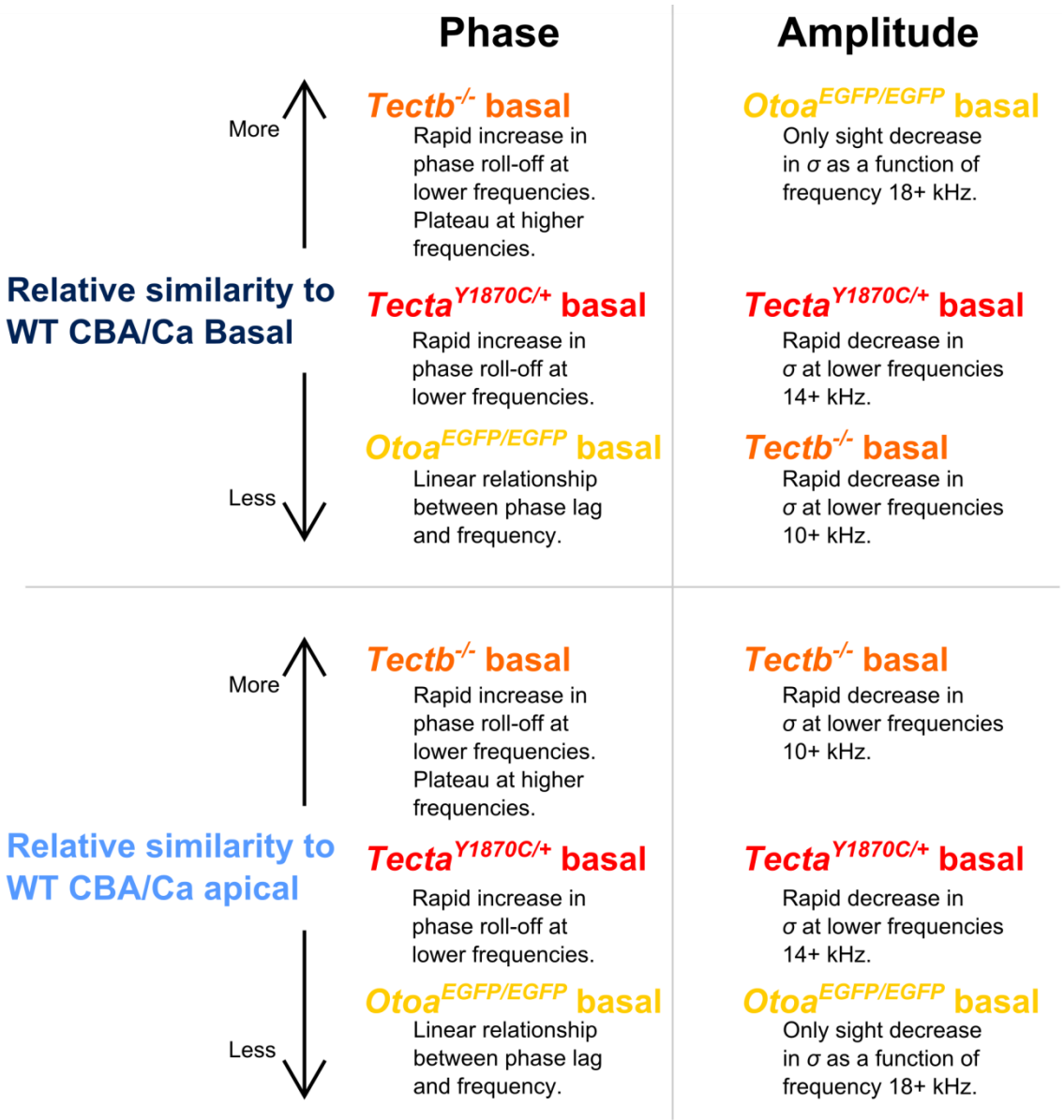

Figure 5.17 Relative similarity of each of the basal mutant TM segments to the apical and basal wild-type TM segments (Chapter 4, p. 87).

5.4.4 Waveforms

The shape of the travelling waves recorded in the isolated TM segments varied between the three mutant groups and wild-types. In each of the mutant groups the waves lag those from the wild-type CBA/Ca basal group, with the first positive peak of the wave occurring at ~50% (*Tecta*$^{Y1870C/+}$ basal, Figure 5.12, B), ~50-70% (*Tectb*$^{-/-}$ basal, Figure 5.14, B) and ~60-70% (*Otoa*$^{EGFP/EGFP}$ basal, Figure 5.16, B) of the longitudinal position relative to the wild-type wave. Although these waves are not representative of a travelling wave *in vivo*, the differences reflect the mechanical differences between the mutant groups and the wild-types.

5.4.5 Comparison to previous data

The data collected from the TM segments of the *Tectb*$^{-/-}$ mice are similar to previously reported values by Ghaffari et al. (2010). In these mice the estimates of the propagation velocity, viscoelastic moduli (using a distributed impedance model) and the space constants of the travelling waves are all reduced. The travelling wave propagation velocities (and increase of propagation velocity as a function of stimulus frequency) are similar to those presented here (~5 ms^{-1} at 20 kHz). There are slight differences between the velocities recorded from wild-types (for example ~6 ms^{-1} compared to ~9 ms^{-1} at 20 kHz). These slight differences may be a result of the methodological approach; the stimulation amplitude (and hence the radial velocity of the stimulating piezo) used with the laser interferometer method is smaller (see Chapter 2.3.4, p. 58), which may have an effect on both the fluid coupling in the TM preparation and the mechanical properties of the TM itself. Despite these slight differences, the velocity data are comparable; the reduction in propagation velocities is within the same order of magnitude. Similarly reductions in the viscoelastic moduli are also observed, although in the basal data presented here, the shear storage modulus dropped from G'=11.0±6.73 kPa (mean±SD) in wild-type CBA/Ca TM segments to around G'=-0.0983±0.0.642 kPa in the *Tectb*$^{-/-}$ mutants compared to a drop of G'=42±10 kPa (wild-type basal, mean±SD) to G'=18±1 kPa (*Tectb*$^{-/-}$ basal) (Ghaffari et al., 2007; Ghaffari et al., 2010). The estimates for reduction in shear viscosity between wild-types and *Tectb*$^{-/-}$ mice are very similar, although are slightly greater (and statistically significant) in the data presented in this chapter: η=0.305±0.0469 Pa·s (wild-type CBA/Ca basal, mean±SD) to η=0.128±0.0153 Pa·s (*Tectb*$^{-/-}$ basal), compared to η=0.23±0.07 Pa·s (wild-type, mean±SD) η=0.17+0.06 Pa·s (*Tectb*$^{-/-}$) (Ghaffari et al., 2007; Ghaffari et al., 2010).

5.4.6 Structural correlates

The mechanical characteristics of each of the mutant groups differ markedly and compare to the wild-type data differently (Figure 5.17). In the *Tecta*$^{Y1870C/+}$ and *Tectb*$^{-/-}$ mice the striated

sheet matrix, created by the α-tectorin and β-tectorin proteins, is disrupted. The striated sheet matrix forms a backbone in the TM against which the radial collagen fibres organise and without it these fibres orientate randomly throughout the TM, likely reducing the radial stiffness of the TM, as well as the longitudinal stiffness. The phase data from the *Tecta*$^{Y1870C/+}$ mice may indicate that the *Tecta*$^{Y1870C/+}$ TMs are less disrupted than the *Tectb*$^{-/-}$ mice, whereas the spatial decay data indicates a greater difference relative to wild-types than the *Tectb*$^{-/-}$. Whatever the specific structural abnormality responsible, the travelling wave velocity and spatial decay properties appear to be affected independently of each other. The *Otoa*$^{EGFP/EGFP}$ show the greatest change relative to wild-types for the phase and velocity data but the least change in spatial decay of the wave. These mice are not reported to have a disrupted striated sheet matrix (although notably do lack Hensen's stripe), but must have some other structural pathology to account for the differences observed compared to the wild-types. It may be reasonable to hypothesise that with the lack of otoancorin and the consequent loss of the attachment to the spiral limbus, that perhaps the limbal zone of the TM is structurally affected. If this is the case, the stark difference in the relationship between phase roll-off and stimulus frequency in the *Otoa*$^{EGFP/EGFP}$ mice, compared to the wild-type mice, would indicate the importance of this zone for travelling wave velocity. Whereas the amplitude data, which is very similar to that of wild-types, would imply that this zone is not required to carry energy longitudinally. Perhaps the limbal zone provides an additional anchor (or pivot) for the radial collagen fibres, affecting how the wave moves between the fibres, whereas the striated sheet matrix carries the energy in the wave.

5.4.7 Conclusions

Generally speaking, the reduction in all the material properties of each of the mutant groups is somewhat analogous to the reduction in these properties seen between the TM segments isolated from the apical and basal turns from the wild-types. The differences between the wild-type basal and *Tectb*$^{-/-}$ basal data most closely mirror the wild-type apical-basal differences, although are caused by a totally different change in structure. In the *Tectb*$^{-/-}$ mice the striated sheet matrix is disrupted, accounting for the changes in the material properties, whereas in the wild-type mice it is not disrupted in either region. It is clear that different structural abnormalities can create TMs with similar mechanical properties, but also that different structural properties can cause completely different TM mechanical properties (for example in the *Otoa*$^{EGFP/EGFP}$ group). While this method does not necessarily demonstrate how a travelling wave may propagate *in vivo* (if at all), it does show the distinct structural

differences between groups that strongly imply that the properties of any *in vivo* TM travelling wave will be affected (such as already demonstrated in the *Tectb*$^{-/-}$ mice) (Russell et al., 2007).

6 REFLECTIVE PROPERTIES OF WILD-TYPE AND MUTANT TECTORIAL MEMBRANES

6.1 Abstract

Tecta$^{Y1870C/+}$, *Tectb*$^{-/-}$ and *Otoa*$^{EGFP/EGFP}$ mice exhibit various changes to tectorial membrane (TM) structure compared to wild-type mice. Gross morphological changes, visible under light microscopy, include loss of Hensen's stripe and enlargement or shrinking of the TM. Disruption to the finer structure of the striated sheet matrix and consequent disorganisation of the collagen fibrils in the TM require greater magnification to visualise. A correlate to these more subtle changes is a change in the amount of light reflected back from the TM when a laser interferometer is focused on the marginal edge. This effect is quantified by averaging uncalibrated amplitude data between multiple experiments (presented in Chapters 4, p. 87 and 5, p. 107) to correct for uncontrolled variables, such as laser angle, fluid opacity, etc. All three mutant groups reflected back more light than the wild-type TM segments, indicating some structural differences exist relative to the wild-types. In the *Tecta*$^{Y1870C/+}$ and *Tectb*$^{-/-}$ mice this is not unexpected as the structural pathologies of the mice have already been observed. However, the nature of the disruption to *Otoa*$^{EGFP/EGFP}$ mice is less clear.

6.2 Introduction

The nanometre-scale surface topology a material can affect its bulk properties, including its optical properties and how it interacts with other materials (Assender et al., 2002). Reflective properties (of both light and sound) can also provide information on the structural state of materials (Antich et al., 1991; Sakhnini et al., 2006). The structural changes to the TMs of the mutant groups presented in Chapter 5 have the effect of changing the reflectance of the TM. In addition, as the TM is somewhat translucent, the amount of light reflected back to the laser is presumably affected by internal structures as well as the surface of the marginal edge where the laser is focused (laser depth of focus=20 µm). During the experiments conducted in Chapters 4 and 5 it was qualitatively observed that *Tecta*$^{Y1870C/+}$ TM segments appeared to be more reflective than those from wild-types. This chapter aims to quantify this observation and to investigate if this effect is exclusive to the *Tecta*$^{Y1870C/+}$ TMs, or is also present in the *Tectb*$^{-/-}$ and *Otoa*$^{EGFP/EGFP}$ TMs. The data analysed here are unable to provide detailed information about the structure, as this was not the original intention of the experiments. However, when compared to values from wild-type TMs changes in reflectance can indicate that structural differences exist between groups.

A number of variables affected the amount of light returned to the laser interferometer during the experiments presented in Chapters 4 and 5 (Table 6.1). Both during the course of a single experiment and between separate experiments these variables changed unpredictably. In order to extract usable amplitude data, these variables were controlled for by calibrating the amplitude of the lasers response at each longitudinal position on the TM. Uncalibrated amplitude data are the product of displacement and reflectivity of the target. Calibration provides a value for reflectance (in Volts) that corresponds to a known displacement. Assuming little variability at the same longitudinal position between collection of the experimental and calibration data, then any variance in reflectance – regardless of cause – is mitigated. The laser interferometer was mounted on a piezo and during calibration runs the size of this displacement of this piezo was stepped up until the response of the laser became non-linear. This point showed the voltage corresponding to 84 nm displacement at the current reflectance of the longitudinal position. The relative amplitude of the laser single from the experimental data was then compared to this point and the actual displacement of the TM calculated (see Chapter 2.3.6, p. 61).

Variable	Varies…	Control	Notes
Angle of viewing window glass	Between experiments (whenever glass is replaced)	Only experiments between changes of glass used	Data collected from experiments between replacements or change to the viewing window glass.
Vertical angle of laser	Between experiments	Average	At the start of the experiment the laser was angled approximately perpendicular relative to the longitudinal direction of the TM. This should not have affected uncalibrated amplitude greatly.
Horizontal angle of laser	Between experiments	Average	At the start of the experiment the laser was angled approximately parallel to the supports in the experimental chamber. Variation from this orientation should not have affected uncalibrated amplitude greatly.
Connection of TM to vibrating support	Between experiments	Average	The better the connection of the TM to the vibrating support the greater the absolute displacement and hence amplitude of the experimental data (but not the calibration data).
Opacity of fluid	During and between experiments	Average	Any debris in the fluid in the experimental chamber had a small, random effect on amplitude. Minor effect.
TM reflectance due to longitudinal position	During experiments	Average	Varies somewhat at each longitudinal point (hence need for calibration at every point). Had an effect on uncalibrated amplitude and maximum recorded amplitude of calibration runs.
TM reflectance due to phenotype	Between groups	N/A	Qualitatively effect of phenotype on reflectance appeared distinguishable from the other variables above, particularly for the *Tecta*$^{Y1870C/+}$ mice.

Table 6.1 Summary of the variables affecting the amplitude of the laser signal.

In order to assess the overall reflectance of the isolated TM segments from each group calibration was not applied to the experimental data and, instead, the calibration and experimental data were treated separately. During each experiment *n*=3-5 frequency runs (1-20 kHz) were collected and *n*=3-5 calibration runs were performed. The uncalibrated experimental data includes individual amplitudes for each frequency (which were a combination of actual displacement and surface reflectance) and the calibration data provides the voltage value of a known displacement at the current reflectance of the surface. Because of the large volume of both raw experimental and calibration data, averaging both groups separately accounted sufficiently for the variables summarised in Table 6.1. As an additional means of verification both the experimental and calibration data were expected to show similar trends (at different absolute values); greater reflectance should cause in greater amplitude values to be recorded in the experimental and calibration data.

6.2.1 Data analysis

Although the chamber design remained the same during the course of the experiments presented in Chapters 4 and 5, the glass of the viewing window was occasionally replaced. Changes in opacity or angle of this glass changed the amount of light reflected back to the laser and to avoid this complication, calibration and experimental data were collected from experiments conducted in the same experimental chamber (ie. between replacements of the glass). This block of experiments included 10 wild-type, 9 $Tectb^{-/-}$, 6 $Tecta^{Y1870C/+}$ and 5 $Otoa^{EGFP/EGFP}$ TM segments. The individual runs for each set of data provided adequate *n*: All calibration data for every longitudinal position for all experiments in the block was collected and the maximum point of reflectance (the point at which the laser support moved 84 nm) was averaged for each group; wild-type CBA/Ca basal n=164, wild-type CBA/Ca apical *n*=152, $Tecta^{Y1870C/+}$ basal *n*=192, $Tectb^{-/-}$ basal *n*=262, and $Otoa^{EGFP/EGFP}$ basal *n*=140. From the experimental data the amplitude of all the stimulus frequencies was averaged at every longitudinal position recorded from during the block of experiments. The data was then averaged for each group; wild-type CBA/Ca basal *n*=246, CBA/Ca apical *n*=228, $Tecta^{Y1870C/+}$ basal *n*=288, $Tectb^{-/-}$ basal *n*=393, and $Otoa^{EGFP/EGFP}$ basal *n*=210.

A one-way ANOVA was performed to assess the significance of the differences observed between groups in Matlab 2006b (The MathWorks, Inc.)

6.2.2 Aims

1. To quantify the qualitative differences noted in the reflective properties of the *Tecta*$^{Y1870C/+}$ mice and analyse statistically.
2. To similarly compare the other mutant groups to wild-types.

6.3 Results

Similar trends were observed in the experimental and calibration data, providing validation for the statistical treatment of the data (Figure 6.1). One way ANOVA (Figure 6.2, A; Figure 6.3, A; summarised in Table 6.2) and comparison of means (Figure 6.2, B; Figure 6.3, B; summarised in Table 6.3 and Table 6.4) in both sets of data indicated there was no significant difference at the p=0.05 level (after correcting for multiple comparisons) in the reflectivity between the wild-type CBA/Ca basal and CBA/Ca apical TM segments, whereas TM segments from all three basal mutant groups were significantly more reflective compared to the wild-type CBA/Ca basal group. The *Tecta*$^{Y1870C/+}$ basal TM segments were the most reflective of the mutant groups, followed by the *Tectb*$^{-/-}$ basal and *Otoa*$^{EGFP/EGFP}$ basal, respectively.

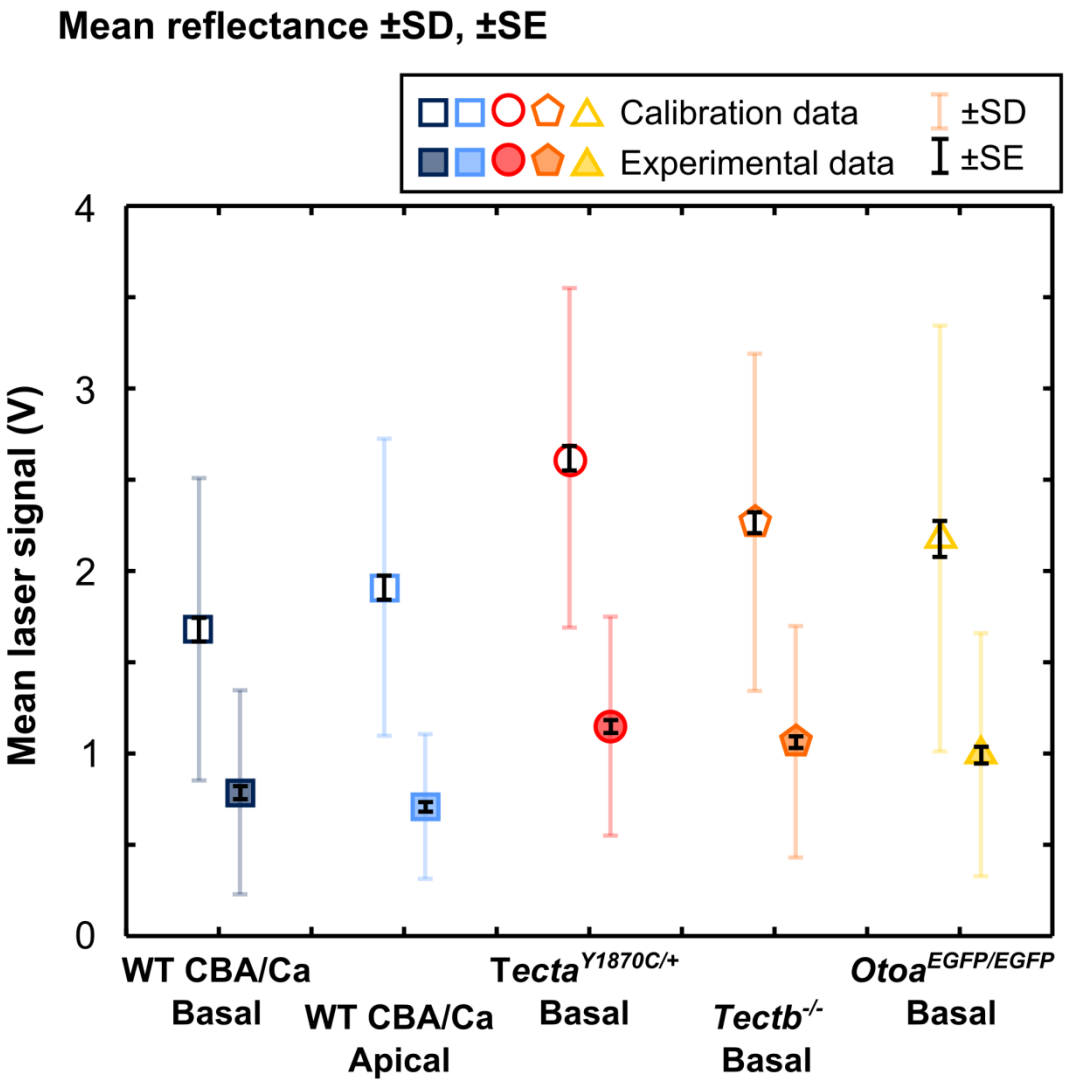

Figure 6.1 Mean laser signal for each group. The relative trend is similar for both data from experimental and calibration runs.

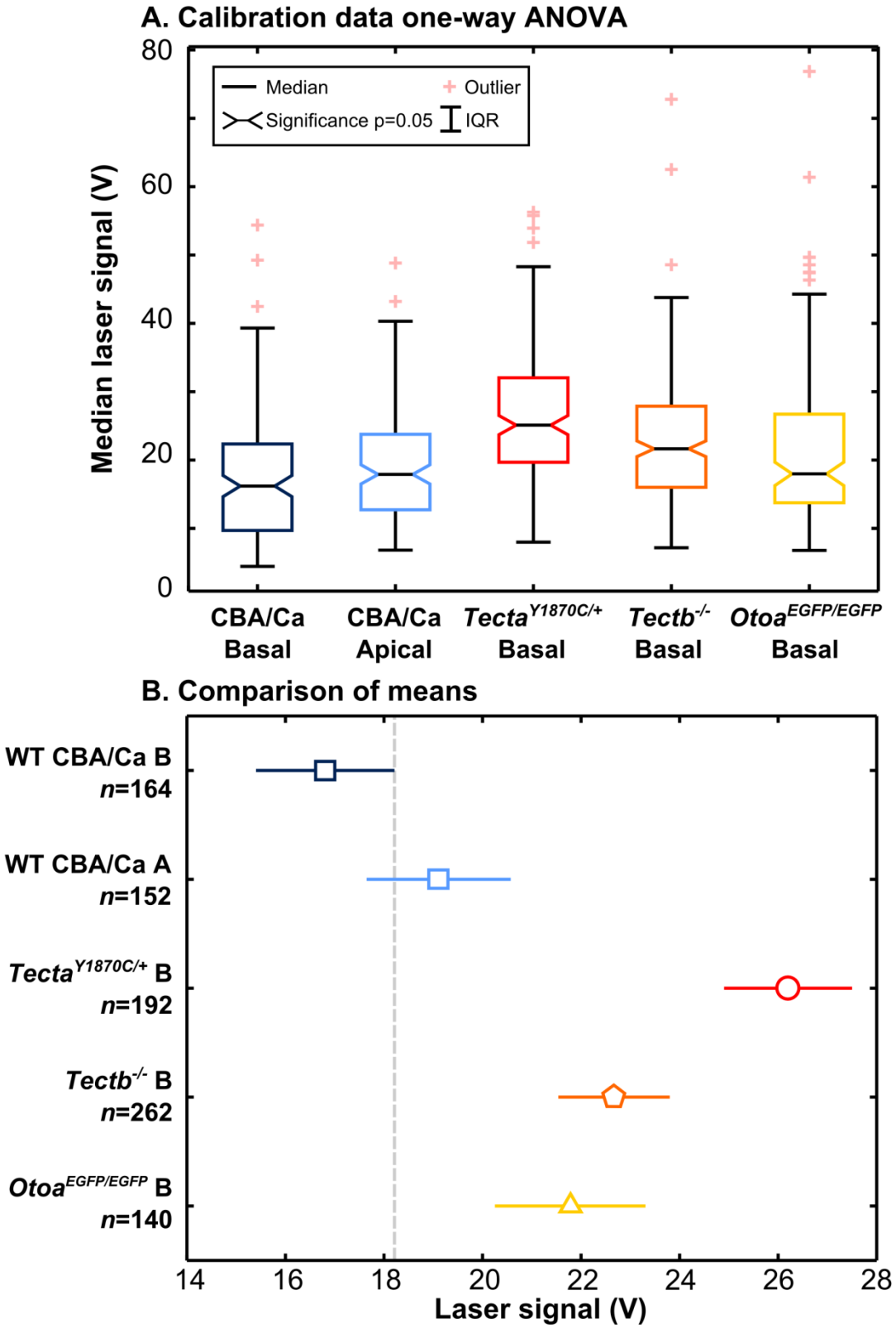

Figure 6.2 One way ANOVA and a graphical comparison of means for the calibration data. **A**. Horizontal black lines indicate the median and the error bars are interquartile range (IQR). The notches indicate significance between groups at $p<0.05$ where they do not overlap. **B**. A visual comparison of means (summarised numerically in Table 6.3). Error bars indicate 95% confidence intervals and correspond to significance at $p<0.05$ (accounting for multiple comparisons) where they do no overlap. The upper 95% confidence for the CBA/Ca basal group overlaps with the lower 95% confidence interval for the CBA/Ca apical group (indicated by the dashed grey line) showing the groups are not significantly different.

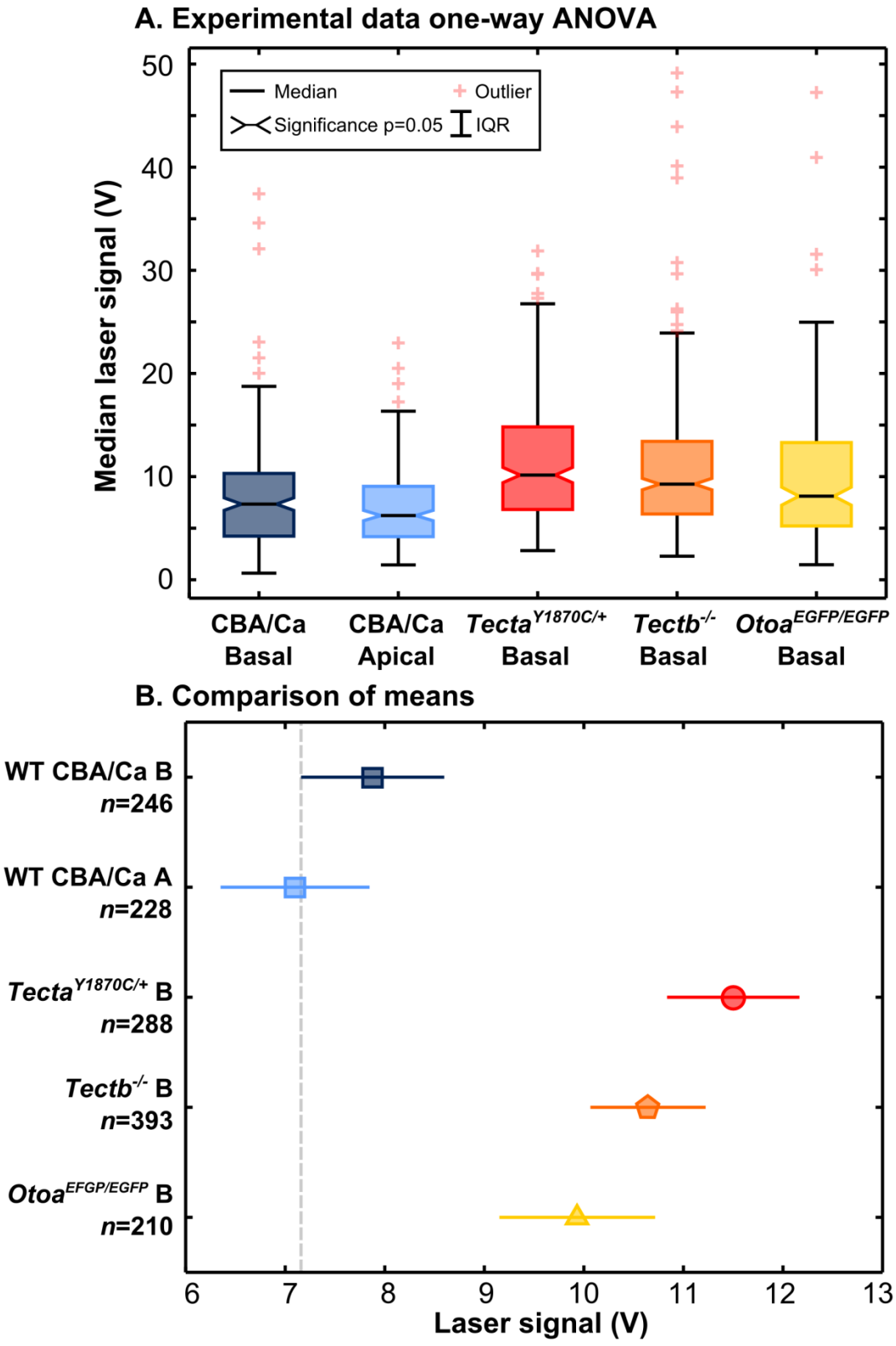

Figure 6.3 One way ANOVA and a graphical comparison of means for the experimental data. **A**. Horizontal black lines indicate the median and the error bars are interquartile range (IQR). The notches indicate significance between groups at $p<0.05$ where they do not overlap. **B**. A visual comparison of means (summarised numerically in Table 6.4). Error bars indicate 95% confidence intervals and correspond to significance at $p<0.05$ (accounting for multiple comparisons) where they do no overlap. The lack of significant difference between the two wild-type groups is indicated by a dashed grey line.

Experimental data					
Source	**Sum of squares between groups**	**Degrees of freedom**	**Mean square between groups**	***F***	***p***
Groups	3646.70	4.00	911.67	26.62	<0.001
Error	46569.60	1360.00	34.24		
Total	50216.40	1364.00			
Calibration Data					
Source	**SS**	**df**	**MS**	***F***	***p***
Groups	9077.90	4.00	2269.48	26.04	<0.001
Error	78889.30	905.00	87.17		
Total	87967.20	909.00			

Table 6.2 Summary of the one-way ANOVAs.

Calibration data

Means

Group	Mean	SE	*n*
CBA/Ca basal	16.8	0.729	164
CBA/Ca apical	19.2	0.757	152
Tecta$^{Y1870C/+}$ basal	26.2	0.674	192
Tectb$^{-/-}$ basal	22.7	0.577	262
Otoa$^{EGFP/EGFP}$ basal	21.8	0.789	140

Comparisons of means

Group 1	Group 2	Difference between means (*sig. at $p \leq 0.05$)	Lower confidence interval (95%)	Upper confidence interval (95%)
CBA/Ca apical	CBA/Ca basal	-2.30	-5.17	0.565
CBA/Ca apical	*Tecta*$^{Y1870C/+}$ basal	**-9.39***	-12.1	-6.69
CBA/Ca apical	*Tectb*$^{-/-}$ basal	**-5.86***	-8.40	-3.33
CBA/Ca apical	*Otoa*$^{EGFP/EGFP}$ basal	**-4.97***	-7.90	-2.04
CBA/Ca basal	*Tecta*$^{Y1870C/+}$ basal	**-7.09***	-9.86	-4.37
CBA/Ca basal	*Tectb*$^{-/-}$ basal	**-3.56***	-6.16	-0.96
CBA/Ca basal	*Otoa*$^{EGFP/EGFP}$ basal	**-2.67***	-5.65	0.314
Tecta$^{Y1870C/+}$ basal	*Tectb*$^{-/-}$ basal	**3.53***	1.11	5.95
Tecta$^{Y1870C/+}$ basal	*Otoa*$^{EGFP/EGFP}$ basal	**4.42***	1.59	7.25
Tectb$^{-/-}$ basal	*Otoa*$^{EGFP/EGFP}$ basal	0.89	-1.78	3.56

Table 6.3 Summary of the means and comparisons of means between each group for the calibration data. Asterisks indicate significance between means at $p \leq 0.05$ after accounting for multiple comparisons (here means are significantly different when the 95% confidence intervals of the difference between a mean do not cross 0).

Experimental data				
Means				
Group	**Mean**	**SE**	***n***	
CBA/Ca basal	7.88	0.373	246	
CBA/Ca apical	7.10	0.388	228	
Tecta$^{Y1870C/+}$ basal	11.5	0.345	288	
Tectb$^{-/-}$ basal	10.6	0.295	393	
Otoa$^{EGFP/EGFP}$ basal	9.93	0.404	210	
Comparisons of means				
Group 1	**Group 2**	**Difference between means (*sig. at $p \leq 0.05$)**	**Lower confidence interval (95%)**	**Upper confidence interval (95%)**
CBA/Ca apical	CBA/Ca basal	0.779	-0.688	2.25
CBA/Ca apical	*Tecta*$^{Y1870C/+}$ basal	**-3.62***	-5.01	-2.24
CBA/Ca apical	*Tectb*$^{-/-}$ basal	**-2.77***	-4.06	-1.47
CBA/Ca apical	*Otoa*$^{EGFP/EGFP}$ basal	**-2.06***	-3.56	-0.556
CBA/Ca basal	*Tecta*$^{Y1870C/+}$ basal	**-4.40***	-5.82	-2.99
CBA/Ca basal	*Tectb*$^{-/-}$ basal	**-3.55***	-4.87	-2.22
CBA/Ca basal	*Otoa*$^{EGFP/EGFP}$ basal	**-2.83***	-4.36	-1.31
Tecta$^{Y1870C/+}$ basal	*Tectb*$^{-/-}$ basal	0.856	-0.382	2.09
Tecta$^{Y1870C/+}$ basal	*Otoa*$^{EGFP/EGFP}$ basal	**1.57***	0.119	3.02
Tectb$^{-/-}$ basal	*Otoa*$^{EGFP/EGFP}$ basal	**0.71***	-0.654	2.08

Table 6.4 Summary of the means and comparisons of means between each group for the experimental data. Asterisks indicate significance between means at $p \leq 0.05$ after accounting for multiple comparisons (here means are significantly different when the 95% confidence intervals of the difference between a mean do not cross 0).

6.4 Discussion

The observed qualitative effect of increased reflectivity relative to wild-types observed in the *Tecta*$^{Y1870C/+}$ basal TM segments is statistically significant, indicating that their TMs are indeed more reflective than those of wild-types. A smaller effect (also statistically significant) is observed in the *Tectb*$^{-/-}$ basal and *Otoa*$^{EGFP/EGFP}$ basal TM segments compared to wild-types.

The variability of the reflective properties of the TM segments from the mutant groups compared to wild-types provides evidence for differences in the structure of each group. Although these data do not necessarily convey detailed information about the underlying structural pathology, the fact that differences exist is interesting, particularly in the case of the *Otoa*$^{EGFP/EGFP}$ mice. These mice lack expression of otoancorin, which, in the developed cochlea, forms part of the attachment of the inner limbal edge of the TM to the spiral limbus. The resulting detachment between the TM spiral limbus is evident during cochlea dissection, where the TM easily disassociates with the organ of Corti. However, these mice are reported to only have minor structural pathology of the TM (Lukashkin et al., unpublished data).

The travelling wave velocity and amplitude decay data in Chapter 5 indicate that there are mechanical (and hence structural) differences between the TM segments from the *Otoa*$^{EGFP/EGFP}$ mice and wild-types. It is reasonable to hypothesise from these data that the limbal zone is somehow affected by the absence of otoancorin (as this is its only permanent expression site in the developed cochlea), implying that the limbal zone has a significant structural role in longitudinal coupling of energy. However, the reflectance data presented in this chapter challenges such reasoning. The laser is focused on the marginal edge of the TM and the majority of the light reflected back to the laser comes from the focal point on the marginal edge and, due to the translucence of the TM, from inside the marginal zone (within the 20 µm depth of field of the laser). The amount of light reflected from the *Otoa*$^{EGFP/EGFP}$ basal TM segments was more similar to the *Tectb*$^{-/-}$ basal TM segments than to the wild-type CBA/Ca TM segments, indicating a structural difference relative to wild-types, somewhere within ~20 µm of the marginal edge. While this difference is not necessarily the disorganisation shown in the striated sheet matrix of the *Tectb*$^{-/-}$ mice, it is present at least in the marginal zone of the TM. During development there is transient expression of otoancorin in the marginal zone where the OHC hair bundles contact with the TM. This expression is absent in the mutants, providing a possible mechanism for structural pathology in this region (which is not necessarily mutually exclusive to pathology in the limbal region). This observation may be

confirmed by the reported possible disorganisation of the marginal band reported in Lukashkin et al. (unpublished data).

The reflective properties of materials can be linked to their material properties (Assender et al., 2002), and the data from the TM mutants presented here show that this relationship is quantifiable using a laser interferometer. This was not the original aim of the experiments on the TM mutants, and as such the method is by no means optimised for such a purpose. Nevertheless the significant differences seen between the *Tecta*$^{Y1870C/+}$ and *Tectb*$^{-/-}$ mutants correlate with the known structural abnormalities for these mutants. The significant difference observed between the *Otoa*$^{EGFP/EGFP}$ mice and wild-types predicts (independently of the data presented in Chapter 5) that their TMs are somewhat abnormal, and perhaps indicates that whatever the abnormality is, it is not necessarily restricted to the limbal region where the otoancorin is mainly expressed. This method could be refined to account for the variables summarised in Table 6.1 experimentally, rather than statistically. For example, by standardising the properties of the experimental chamber that affected light transmission, such as the angle of the glass of the viewing window. Such refinement may yield further insights into the material properties of these mutants, or perhaps provide a means of quickly assaying and comparing different mutants. One interesting potential comparison would be between the basal and apical region of wild-types. If the reflectivity of these areas is statistically different (although not indicated by the data presented here, it does not yet necessarily rule out more subtle changes) then it would be interesting to compare the characteristics of such a change to those of mutants. If there is no significant difference between these regions (as indicated by the data presented here) it is interesting to consider that the travelling wave propagation velocities and spatial decay from the basal region of *Tecta*$^{Y1870C/+}$ and *Tectb*$^{-/-}$ TM segments (Chapter 5) are characteristically similar to the apical region in CBA/Ca wild-types, yet the reflective properties vary greatly (along with the known morphological differences).

7 GENERAL DISCUSSION

7.1 Acoustic sensitivity of the vestibular system

7.1.1 Perceptual level

The results presented in Chapter 3 (p. 70) show that low frequency auditory stimuli can be sensed by the sacculus of the vestibular system in mice. It is unclear if this stimulation reaches the level of perception, which is not necessarily required for the modification of auditory behavioural responses observed in the experiments. The perceptual level of appreciation of auditory stimuli via the vestibular system is potentially vast due to the evolutionary ancient nature of the vestibular system and its resulting extensive connectivity to the rest of the nervous system. If the modification is reflexive the perceptual level does not need to be conscious at all, but this does not preclude the possibility of conscious awareness. It is perhaps possible that the perceptual level of acoustic stimulation via the vestibular system relative to that via the auditory system is analogous to the perception of visual signals via the retina-superior colliculus visual pathway compared to that via the retina-lateral geniculate nucleus-V1 visual pathway. The evolutionary ancient retina-superior colliculus visual pathway is below the level of consciousness but still provides basic visual information, which is most noticeable when the conscious and evolutionarily newer retina-lateral geniculate nucleus-V1 visual pathway is disabled, such as in the case of blindsight patients (Ramachandran and Blakeslee, 1998). Any conscious awareness of the acoustic stimulation of the vestibular system (assuming it is even distinguishable from “normal” vestibular stimulation by linear acceleration or rotation) may not be noticeable when the more salient cochlear-mediated hearing covers the same range, such as in humans.

Regardless of the conscious level of the acoustic-vestibular sensation, it is likely that the retained acoustic ability of the vestibular system is still physiologically relevant in some mammals and not just a vestigial function. Mice, for example, have a cochlea with a large frequency range that evolved to allow mating calls to be made and for mothers to communicate with their pups, without being overheard by predators. This evolutionary pressure may have come at the cost of the loss of the low frequency end of their hearing range; hearing relies on the spatial decomposition of sound, and the hearing apparatus has a finite length. It is possible that the acoustic sensitivity of the vestibular system makes up, in part, for the lack of <~4 kHz hearing – which is part of the auditory spectrum available to most other mammals. Such speculation raises the question about how relevant sensation of acoustic stimulation by the vestibular system may be to animals that do have low frequency

cochlear-mediated hearing. In humans the vibrational sensitivity of the vestibular system may be greater than that of the cochlea at very low frequencies (Todd et al., 2008) and it has been suggested that the vestibular system may be used in monitoring self-vocalisations (Todd et al., 2000), such as during the Lombard effect, where a speaker increases their vocal effort as background noise increases, without the need for conscious awareness (Lane and Tranel, 1971). Dysfunction of the vestibular system also correlates with raised auditory thresholds (at 500-1000 Hz) in noise-exposed individuals (Guest et al., 2011).

Currently there is no reason to believe that every animal with an acoustically sensitive sacculus has evolved to use the information it provides in the same way, particularly when considering the vast variations between mammalian acoustic niches.

7.1.2 Future work

Further determination of the physiological importance of the retained acoustic ability of the vestibular system would be important to our understanding of hearing in general and is of potential benefit to medicine. This work demonstrates a potential functional use in mice, but other mammals may also have a use for low frequency sensitivity to acoustic tones via the vestibular system. In humans, determining the perceptual level of acoustic-vestibular stimulation may elucidate potential functions. If such a behaviourally relevant function exists at the appropriate perceptual level, there is some potential for the information provided by the acoustic stimulation of the vestibular system to be exploited to aid hearing in the hearing impaired.

7.2 Mechanical properties of the tectorial membrane

7.2.1 Introduction

In all of the groups studied, including the mutants, radial stimulation of an isolated segment of tectorial membrane (TM) generated a longitudinally propagating travelling wave. The propagation velocities (v_s) and space constants (σ) of these waves varied with frequency and between groups. Additionally the reflective properties of the TM segments varied between the groups. These differences between each of the mutant groups and the wild-types gives some insight in to the mechanical, and hence structural, properties of the TMs of the *Tecta*$^{Y1870C/+}$, *Tectb*$^{-/-}$ and *Otoa*$^{EGFP/EGFP}$ mice.

7.2.2 Viscoelastic properties

For all groups, the propagation velocity of the travelling wave increased roughly monotonically as a function of frequency (Figure 4.3, p. 96; Figure 5.3, p. 121). The fastest waves at all frequencies were recorded from the basal region of the two wild-type groups (S129 and CBA/Ca), although the increase in propagation velocity between 1-20 kHz was greater in the mutants (Table 7.1). The relationship between propagation velocity and stimulus frequency in the basal region of each of the mutant groups was more similar to the apical region in wild-types than the basal region.

Group	Wave propagation velocity at 1 kHz ±SD (ms^{-1})	Wave propagation velocity at 20 kHz ±SD (ms^{-1})	Increase
S129 basal (*n*=4)	3.95±1.07	10.1±1.40	2.56x
CBA/Ca basal (*n*=18)	4.24±2.60	8.93±2.16	2.11x
CBA/Ca apical (*n*=6)	2.03±0.708	5.94±1.07	2.93x
Tecta$^{Y1870C/+}$ **Basal** (*n*=12)	1.50±1.14	5.44±1.03	3.63x
Tectb$^{-/-}$ **Basal** (*n*=14)	1.41±0.627	5.19±0.881	3.68x
Otoa$^{EGFP/EGFP}$ **Basal** (*n*=12)	1.33±0.574	6.03±1.20	4.53x

Table 7.1 Summary of wave propagation velocities for all groups (wild-types blue, mutants red-yellow).

Estimates of the viscoelastic moduli, shear storage modulus (G'), and shear viscosity (η), quantified the relationships between wave propagation velocity and stimulus frequency (Chen et al., 2004). Decreases of 2.3x for G' and 2x for η were observed between the basal and apical

TM segments from the wild-type CBA/Ca mice. The estimates of the moduli for the CBA/CA basal and CBA/Ca apical TM segments were similar, although generally slightly lower to previous data (Ghaffari et al., 2007). *G'* and *η* were significantly lower in all three mutant groups compared to the wild-type CBA/Ca basal group (Figure 7.1 and Table 7.2). Again, the estimates of the mechanical properties of the *Tectb*$^{-/-}$ basal segments are similar, but somewhat lower than those obtained using a similar experimental method (Ghaffari et al., 2010). Notably, there is no significant difference in the shear viscosity between wild-type basal and *Tectb*$^{-/-}$ basal shown in (Ghaffari et al., 2007; Ghaffari et al., 2010) whereas there is between the wild-type CBA/Ca basal and *Tectb*$^{-/-}$ basal presented in Chapters 4 (p. 87) and 5 (p. 107) (Table 7.2).

It is important to note that the estimates of the viscoelastic moduli presented in this thesis are based solely on the linear Voigt body model from (Chen et al., 2004). Damping by the fluid environment is not accounted for, and it is likely to have a frequency dependant effect, thus skewing the stimulus frequency-propagation velocity relationship and affecting the estimates of *G'* and *η*. The damping of the fluid causes an effective increase in the thickness and mass of the TM, which reduces the velocity of the longitudinal travelling wave (Elliott, 2011).

7.2.3 Space constants

The space constant is the distance over which the amplitude of radial displacement reduced to $A_{(x)}=A_{(0)}*1/e$. For the data normalised to a representative stimulus amplitude of 100 nm at the piezo (0 µm from point of stimulation), it is the longitudinal distance over which amplitude decays to $100*1/e$=36.8 nm.

In the basal region of wild-type mice the space constant does not appear to change as a function of frequency (Figure 4.6, p. 100), at least not within the 1-20 kHz range. With all the other groups the space constant decreases with frequency to differing degrees.

The generally shorter space constants observed in the *Tecta*$^{Y1870C/+}$, *Tectb*$^{-/-}$ and CBA/Ca apical, indicate that these TMs are less stiff and hence less able to couple energy longitudinally than those from CBA/Ca basal mice. This has been suggested as a reason for the sharpened frequency tuning in these mice (Russell et al., 2007; Lukashkin et al., 2009; Ghaffari et al., 2010). However, the spatial extent of the waves in *Tecta*$^{Y1870C/+}$ mice is reduced by a similar amount to the *Tectb*$^{-/-}$ mice (and the viscoelastic properties, also), but DPOAE data from *Tecta*$^{Y1870C/+}$ mice appear to show tuning in these mice is unaffected (Legan et al., 2005).

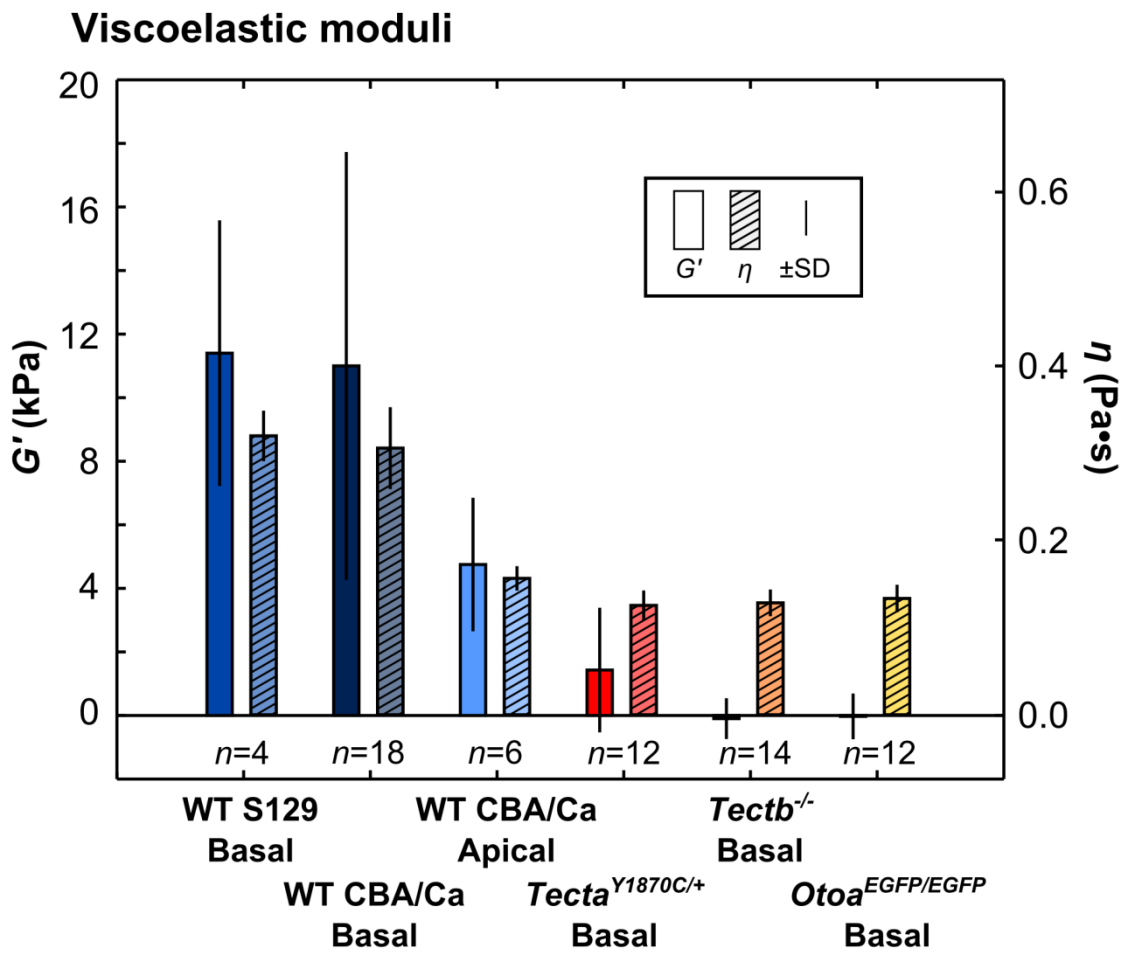

Figure 7.1 Comparison of the estimated viscoelastic moduli for all groups.

Group	*G'* ±SD (kPa)	*η* ±SD (Pa·s)	*λ* at 4, 10, 15, 18, 20 kHz (µm)	*σ* at 4, 10, 15, 18, 20 kHz (µm)
S129 basal	11.4±4.18	0.319±0.0289	-	-
CBA/Ca basal	11.0±6.73	0.305±0.0469	858, 537, 461, 425, 439	323, 340, 490, >600, 521
CBA/Ca apical	4.75±2.10	0.156±0.0140	787, 357, 310, 280, 278	325, 182, 198, 211, 240
Tecta$^{Y1870C/+}$ basal	1.43±1.96	0.125±0.0172	632, 366, 322, 280, 283	340, 212, 233, 204, 248
Tectb$^{-/-}$ basal	-0.0983±0.642	0.128±0.0153	534, 482, 396, 339, 339	355, 214, 210, 180, 191
Otoa$^{EGFP/EGFP}$ basal	-0.0284±0720	0.133±0.0157	1190, 402, 390, 314, 340	505, 298, 340, 262, 253

Table 7.2 Comparison of viscoelastic moduli, wavelength and space constants for all groups (colour coded by group).

7.2.4 Waveforms

The shape of the propagating longitudinal travelling wave along the isolated segments of TM is a product of the rate of change of phase (ie. its wavelength) and the rate of amplitude decay. The shape of the travelling wave differs between the groups (Figure 7.2). Although this does not necessarily represent any TM travelling wave *in vivo*, it does highlight the potential for timing differences between waves. Timing of the radial resonance of the TM and mechanical feedback from outer hair cells (OHCs) is critical. If longitudinal coupling of energy along the TM feeds the radial resonance (~0.5 octaves below the CF), changes in phase of the longitudinal wave may affect the phase of the resonance and hence may determine whether the transverse BM travelling wave is amplified or suppressed (Gummer et al., 1996; Lukashkin et al., 2010).

7.2.5 Reflectivity

The reflective differences between the isolated TM segments of wild-types and each of the mutant groups indicate structural differences exist between their TMs. Although the laser interferometer cannot yet convey detailed information about such differences it could be adapted to work as a quick assay to identify if structural differences exist between a mutant and wild-types. It may also be possible to identify structural correlates to higher or lower reflectivity.

The reflective data obtained from the *Otoa*$^{EGFP/EGFP}$ mice provides further evidence that there is some structural difference in the TMs of this group compared to wild-types. It is unclear exactly what this difference might be, but it is likely to be related to the lack of expression of otoancorin in the limbal and marginal regions.

7.2.6 *Otoa* mice

The phase data, velocity data, estimated viscoelastic moduli, and reflectivity data collected from the *Otoa*$^{EGFP/EGFP}$ mice indicate that these TM are mechanically, and hence structurally, different compared to wild-types. Conversely, of the three mutant groups, the spatial decay data collected from the *Otoa*$^{EGFP/EGFP}$ mice is most similar to wild-types. Also, despite the similarity in estimates of the viscoelastic properties, the *Otoa*$^{EGFP/EGFP}$ phase data is characteristically different from the other mutant groups as well as the wild-types (Figure 5.2, p. 119).

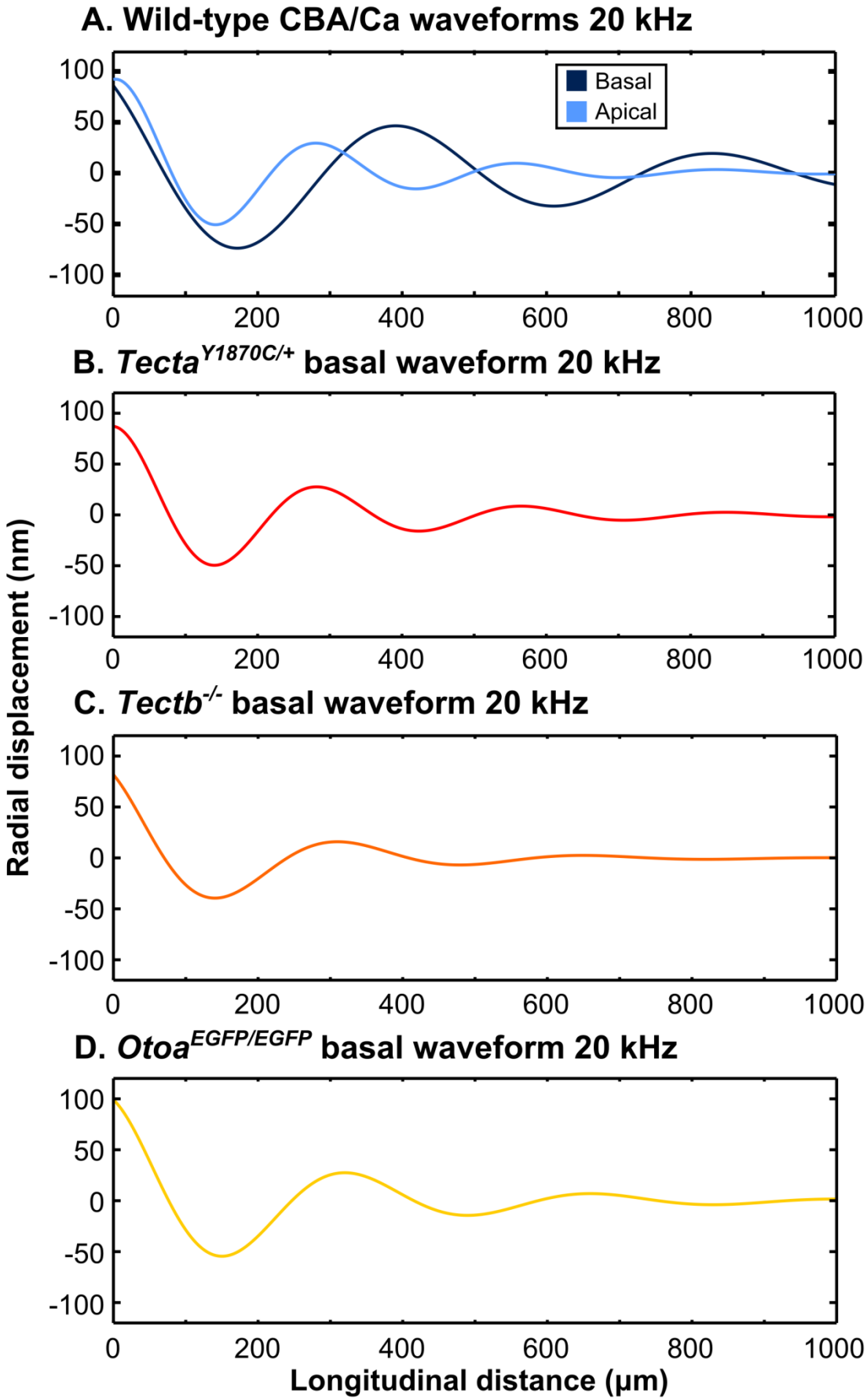

Figure 7.2 Comparison of waveforms. **A**. Between the wild-type CBA/Ca apical and basal TM segments. **B-D**. Between the mutant basal TM segments.

Although otoancorin is a protein mediating the connection of the TM to the organ of Corti, it is not unexpected for it to also affect the structure of the TM. Other connective proteins such as ceacam16 (Zheng et al., 2011) and stereocilin (Verpy et al., 2011), which both mediate the connection between OHCs and Kimura's membrane, are thought to interact with tectorins (particularly α-tectorin), and hence have the potential to affect structure. If only the limbal zone of the *Otoa*$^{EGFP/EGFP}$ TM is affected, as may be implied by it being the only point of permanent expression of otoancorin in the wild-type, the phase, velocity and amplitude decay data, and the estimates of the viscoelastic properties presented in this thesis provide evidence for its structural importance. It would also provide confirmatory evidence of the structural stiffness of the limbal zone, as shown in atomic force microscopy (AFM) probing studies such as (Gueta et al., 2006; Richter et al., 2007). Probing measurements can be potentially questioned on the basis that the AFM technique also tests the compliance of the experimental environment in which the TM is mounted (which is inevitably stiffer than the TM). Proportionally this effect is likely greater in the (transversally) thinnest limbal region, relative to the thicker middle and marginal zones. However, the reflectivity data presented in Chapter 6 (p. 144) may indicate that the marginal zone is affected as well; the *Otoa*$^{EGFP/EGFP}$ TMs are significantly more reflective than those of wild-types and the light returning to the laser is expected to mostly be reflected from the marginal zone. This implies a structural difference within the marginal zone, which may not be entirely unexpected as otoancorin is transiently expressed in the marginal zone during development, at the points where OHC stereocilia attach to the underside of the TM. This observation of disruption in both the limbal and marginal zones fits with current histological analysis of the *Otoa*$^{EGFP/EGFP}$ TM (Lukashkin et al., unpublished data; Weddell et al., 2011a)

7.2.7 Structural correlates

The implication from the differences between some of the measures of the mechanical state of the mutant TMs, and the similarity between others is that the mechanical state of the TM cannot be judged from one type of measurement alone. The least difference between the mutant groups is exhibited in the relationship between stimulus frequency and propagation velocity; this measurement on its own may be able to show that structural pathology exists, but not provide much more detail. The phase data, amplitude decay, and reflectivity data, on the other hand, are distinguishable between groups. This indicates that different structural pathologies of the TM create different mechanical properties (while not ruling out the possibility of different structural pathologies causing the same mechanical effects) and raises

the possibility of correlating the known structural pathologies of a mutant group to specific mechanical changes.

Currently linking the mechanical differences in mutant TMs to the structural changes is difficult for two reasons. The actual disruption to the TMs of the mutant groups on a molecular level, particularly for the *Otoa*$^{EGFP/EGFP}$ mice, is not completely clear. Additionally some of the measurements of the mechanical properties would benefit from more detailed quantification, particularly the amplitude data, than the linear 1-10 and 11-20 kHz stimulus frequency fits used to illustrate them here; perhaps by application of an appropriate model (analogous to the linear Voigt body model used to characterise the propagation velocity data).

7.2.8 TM mechanical properties and relevance to cochlear tuning

The reduction in travelling wave propagation velocity and space constants in the mutant basal TM segments, relative to the wild-type CBA/Ca basal TM segments provides two potential mechanisms that tuning can be affected *in vivo*. Firstly, assuming that TM travelling waves propagate *in vivo*, they will peak at the TM resonance, which is below (physically before) that of the basilar membrane (BM). Interaction between the BM and TM travelling waves can potentially occur and the relative phases of the waves depend on the difference between the physical position of resonance and wave propagation velocity. Travelling wave propagation velocity is shown to be reduced in the mutants studied, and it is not unreasonable to assume that the mechanical properties of the mutant TMs also alter the resonant properties. This means that, in the mutant cochlea, the relative phases of the waves will differ from those in the wild-type cochlea and hence affect timing of feedback. TM vibration and transverse BM vibration controls the excitation and inhibition of the mechanical feedback from the OHCs, and leads to amplification or compression at a given longitudinal location (hence affecting gain and tuning), depending on the relative phase of the two travelling waves. The second mechanism is controlled by the reduced space constant exhibited by mutant TM travelling waves. Not only does the reduced space constant decrease the longitudinal extent of coupling along the TM and hence the total number of OHCs that are coupled near the CF, but it also reduces the longitudinal extent over which interaction between the BM and TM travelling waves can potentially occur.

7.2.9 Limitations

The data presented in Chapters 4 and 5 provide good relative measures of the mechanical difference between the groups, however, lack complete means of analysis. Currently the analytical paradigm limits the interpretation of the experimental data, for example, it is less

able to provide absolute values about the mechanical properties of the TM (because of the fluid damping), or about how travelling waves might propagate *in vivo* (because of the difference in loading on the TM).

7.2.10 Frequency dependence of mechanical properties

The TM is a viscoelastic structure, meaning its mechanical properties vary depending on the stimulation applied to it. The underlying assumption of the Voigt body model (Equation 2.2, p. 66) used for analysis in Chapters 4 and 5, and used along with the distributed impedance model used by Ghaffari et al. (2007, 2008, 2010), is that mechanical properties can be determined by how travelling wave propagation velocity changes over a range of radial stimulation velocities. As described in the methods, the radial velocity of stimulation is mainly determined by the stimulation frequency, but is also affected by the amplitude of stimulation (this inevitably varies slightly when using a piezo, but the magnitude of change is limited by the use of small displacements, Figure 2.9, p 60). Therefore, analysis Equation 2.2 effectively provides estimates for G' and η that are averages for the frequency (and amplitude) of stimulation over the 1-20 kHz range. Such analysis is obviously limited given the viscoelastic nature of the TM, which dictates that its mechanical properties should vary over such a large range. It is likely that frequency dependency of the mechanical properties of the TM is partly responsible for the differences in between static measurements and higher-frequency stimulation; AFM probing studies may only measure the static, structural, stiffness of the TM, whereas higher frequency studies may measure both the structural stiffness and dynamic, frequency dependant, stiffness of the TM. However, the current analysis is unable to show the predicted frequency dependency within the physiologically realistic 1-20 kHz range. Frequency dependency within this range would add another degree of freedom to TM stiffness and hence motion *in vivo*. Such a finding has not been considered in previous models of cochlear mechanics.

7.2.10.1 Fluid damping

The linear Voigt body model (Equation 2.2) used to estimate the viscoelastic moduli does not take in to account the fluid dynamics in the isolated TM preparation. In the experimental chamber the segment of TM is immersed in a fluid with the density of water, and in the estimates of the viscoelastic moduli the density of the TM is assumed to be that of water. As the TM moves through the fluid during stimulation, a viscous boundary layer forms around the TM. This has the effect of increasing the effective shearing thickness by twice the thickness of the vicious boundary layer. For example, at 10 kHz the vicious boundary layer is ~3 μm, increasing the shearing thickness of the TM by 6 μm. This is significant considering the

transverse thickness of the TM varies radially between ~10-30 µm. This effect slows the propagation of the longitudinal travelling wave in a frequency dependant manner and hence skews the relationship between stimulus frequency and propagation velocity, on which the estimates of the viscoelastic moduli are made (Elliott, 2011).

TM dimensions are very similar in the basal region between groups, meaning the proportion of effective added mass is the same for each group at each frequency. Also, the skewing of the stimulus frequency-propagation velocity relationship should be constant between groups. This allows for legitimate comparison of the moduli between groups (and between similar methods) but does limit the absolute interpretation of the values.

7.2.10.2 Physiological relevance of piezo stimulation

The radial stimulation applied to the TM was physiologically unrealistic. *In vivo* travelling waves in the organ of Corti are driven indirectly by the pressure differences between the scala vestibuli and scala tympani and/or mechanical feedback from OHCs. However, the consistency of the (*in vitro*) stimulation between the groups allows for the comparison of mechanical properties between the two groups.

In addition, the experimental paradigm gives no consideration to the radial resonance of the TM. TM segments were extracted from approximate regions (Figure 2.5, p. 56), meaning the frequency range they covered varied and the longitudinal location of resonant points were unknown for each stimulus frequency. Any effect on the propagation of the travelling wave caused by the resonant points was lost in averaging. Also, during the dissection and mounting of the TM it was practically impossible to keep track of the orientation of the isolated segment. In each experiment it was unknown whether the basal or apical end of the isolated segment was attached to the vibrating support, and hence the direction of travel of the wave (relative to when *in situ*), was unknown. This problem may be avoidable by marking each end of the TM during dissection, for example, by cutting at different angles or using a scalpel blade loaded with an appropriate dye, to make each end individually identifiable.

7.2.10.3 In vivo loading

In the organ of corti the TM is loaded by its limbal attachment and attachment to OHC stereocilia. It is also damped by differing fluid environments in the subtectorial space (below) and scala media (above). In the experimental chamber these loads did not exist, and coupled with the unrealistic nature of the stimulation applied to the TM, mean that any conclusions about TM travelling waves *in vivo* are limited. If such waves exist *in vivo*, how they propagate will be very different from *in vitro*. Two modes of TM vibration exist *in vivo*; radial shear of the

TM dominates only between 1 to 0.1 octaves below the CF (near the TM resonance), rather than along the entire length of the TM (Gummer et al., 1996; Hemmert et al., 2000).

7.2.11 Summary

As they are the data presented clearly illustrates the mechanical differences between the apical and basal regions of wild-types and between the basal regions of the three mutant groups and wild-types. The specific differences between each group vary and no single measurement (eg. v_s, G', η, σ, etc.) used to assess the TM is able to fully describe its properties if used alone. Currently there are limitations in interpreting the absolute properties of the TM from these methods, but each provides a reliable way of comparing between groups tested with the same (or similar) methods.

7.2.12 Future work

Future work on the mechanical properties of the TM should focus on solving the limitations described above. These can be approached in two ways.

7.2.12.1 Frequency dependency of mechanical properties

In order to elucidate the absolute mechanical properties of the TM both the effects of fluid damping in the experimental chamber and the frequency dependency of the mechanical properties within the experimental range need to be accounted for. This can be approached mathematically; the effective mass of the TM can be calculated at each frequency, and the velocity of propagation corrected for the reduction due to the extra mass. Estimation of the viscoelastic moduli using the linear Voigt body model would then provide values more comparable to other methods. The analysis could be further improved by the development of a model allowing calculation of G' and η at discreet frequencies, to account for the frequency dependency of G' and η within the experimental range.

Modelling of the phase and amplitude data could also be used to quantify and fully characterise the relationships between stimulation frequency and phase and amplitude, as roughly visualised by the linear fits to the 1-10 kHz and 11-20 kHz frequency ranges. These relationships are defining characteristics between the wild-types and mutants, but currently it is unclear why, for example, the phase roll-off plateaus at 11-20 kHz for the wild-types and *Tecta*$^{Y1870C/+}$ and *Tectb*$^{-/-}$ groups, but does not for the *Otoa*$^{EGFP/EGFP}$ group.

7.2.12.2 Measurement of in vivo travelling waves

A number of recent studies have been published showing the relative motion of organ of Corti structures in various preparations using low-coherence laser interferometry (Choudhury et al.,

2006; Chen et al., 2007; Chen et al., 2011a; Chen et al., 2011b; Choudhury et al., 2011; Nowotny and Gummer, 2011; Ren and He, 2011; Zha et al., 2011). Being able to observe organ of Corti motion in the intact cochlear has the potential to elucidate the complex interactions between structures, particularly the relative motion of the BM and TM that leads to excitation of the OHCs. However, the main focus of most of these studies has been transverse organ of Corti motion, rather than radial. Radial vibration of the TM and its interaction with transverse vibration of the BM is more important than transverse vibration of the TM near the CF and is responsible for either the excitation or inhibition of the OHCs. Measuring TM radial vibration over an appropriate longitudinal segment has the potential to demonstrate the *in vivo* existence of TM travelling waves, and to give more insight into the interaction between BM and TM motion. Measuring TM travelling waves *in vivo* would be technically challenging and another suitable approach may involve opening the cochlea and using a laser interferometer to measure displacement at multiple longitudinal positions of the TM *in situ*. Although opening the cochlea compromises the endocochlear potential, the physical loading by other cochlear structures on the TM still remain. Measuring the spatial extent of energy propagation in the TM would help confirm or negate hypotheses about reduced longitudinal coupling causing the sharpening in tuning observed in the *Tectb*$^{-/-}$ mice.

REFERENCES

ABNET, C. C. 1998. *Measuring Mechanical Properties of the Tectorial Membrane with a Magnetizable Bead.* phD, Massachusetts Institude of Technology.

ABNET, C. C. & FREEMAN, D. M. 2000. Deformations of the isolated mouse tectorial membrane produced by oscillatory forces. *Hearing Research,* 144**,** 29-46.

ALLEN, J. B. 1980. Cochlear micromechanics---A physical model of transduction. *The Journal of the Acoustical Society of America,* 68**,** 1660-1670.

ALLEN, J. B. & FAHEY, P. F. 1993. A second cochlear-frequency map that correlates distortion product and neural tuning measurements. *The Journal of the Acoustical Society of America,* 94**,** 809-816.

ANGELAKI, D. E. & CULLEN, K. E. 2008. Vestibular System: The Many Facets of a Multimodal Sense. *Annual Review of Neuroscience,* 31**,** 125-150.

ANTICH, P. P., ANDERSON, J. A., ASHMAN, R. B., DOWDEY, J. E., GONZALES, J., MURRY, R. C., ZERWEKH, J. E. & PAK, C. Y. C. 1991. Measurement of mechanical properties of bone material in vitro by ultrasound reflection: Methodology and comparison with ultrasound transmission. *Journal of Bone and Mineral Research,* 6**,** 417-426.

ASHMORE, J., AVAN, P., BROWNELL, W. E., DALLOS, P., DIERKES, K., FETTIPLACE, R., GROSH, K., HACKNEY, C. M., HUDSPETH, A. J., JÜLICHER, F., LINDNER, B., MARTIN, P., MEAUD, J., PETIT, C., SANTOS SACCHI, J. R. & CANLON, B. 2010. The remarkable cochlear amplifier. *Hearing Research,* 266**,** 1-17.

ASSENDER, H., BLIZNYUK, V. & PORFYRAKIS, K. 2002. How Surface Topography Relates to Materials' Properties. *Science,* 297**,** 973-976.

BALOH, R. W. 2003. Vestibular Neuritis. *New England Journal of Medicine,* 348**,** 1027-1032.

BÉKÉSY, G. V. 1952. Resting Potentials Inside the Cochlear Partition of the Guinea Pig. *Nature,* 169**,** 241-242.

BÉKÉSY, G. V. 1953. Description of Some Mechanical Properties of the Organ of Corti. *The Journal of the Acoustical Society of America,* 25**,** 770-785.

BÉKÉSY, G. V. 1960. *Experiments in hearing*, McGraw-Hill Book Company.

BÉKÉSY, G. V. 1970. Travelling Waves as Frequency Analysers in the Cochlea. *Nature,* 225**,** 1207-1209.

BEURG, M., FETTIPLACE, R., NAM, J.-H. & RICCI, A. J. 2009. Localization of inner hair cell mechanotransducer channels using high-speed calcium imaging. *Nat Neurosci,* 12**,** 553-558.

BICKFORD, R. G., JACOBSON, J. L. & CODY, D. T. R. 1964. Nature of Average Evoked Potentials to Sound and Other Stimuli in Man. *Annals of the New York Academy of Sciences,* 112**,** 204-218.

BILLONE, M. & RAYNOR, S. 1973. Transmission of radial shear forces to cochlear hair cells. *The Journal of the Acoustical Society of America,* 54**,** 1143-1156.

BOHNKE, F. & ARNOLD, W. 1998. Nonlinear mechanics of the organ of Corti caused by Deiters cells. *Biomedical Engineering, IEEE Transactions on,* 45**,** 1227-1233.

BROWN, J. S., KALISH, H. I. & FARBER, I. E. 1951. Conditioned fear as revealed by magnitude of startle response to an auditory stimulus. *Journal of Experimental Psychology,* 41**,** 317-328.

BROWNELL, W. E., BADER, C. R., BERTRAND, D. & DE RIBAUPIERRE, Y. 1985. Evoked mechanical responses of isolated cochlear outer hair cells. *Science,* 227**,** 194-196.

BURIAN, M. & GSTOETTNER, W. 1988. Projection of primary vestibular afferent fibres to the cochlear nucleus in the guinea pig. *Neuroscience Letters,* 84**,** 13-17.

CARLSON, S. & WILLOTT, J. F. 2001. Modulation of the Acoustic Startle Response by background sound in C57BL/6J mice. *In:* WILLOTT, J. F. (ed.) *Handbook of Mouse Auditory Research: From Behavior to Molecular Biology.* CRC Press LLc.

CAZALS, Y., ARAN, J.-M. & ERRE, J.-P. 1983a. Intensity difference thresholds assessed with eighth nerve and auditory cortex potentials: Compared values from cochlear and saccular responses. *Hearing Research,* 10**,** 263-268.

CAZALS, Y., ARAN, J.-M., ERRE, J.-P., GUILHAUME, A. & AUROUSSEAU, C. 1983b. Vestibular Acoustic Reception in the Guinea Pig: A Saccular Function? *Acta Oto-laryngologica,* 95**,** 211-217.

CHEN, F., CHOUDHURY, N., ZHENG, J., MATTHEWS, S., NUTALL, A. L. & JACQUES, S. L. 2007. In vivo imaging and low-coherence interferometry of organ of Corti vibration. *Journal of Biomedical Optics,* 12**,** 021006-9.

CHEN, F., ZHA, D., CHOUDHURY, N., FRIDBERGER, A. & NUTTALL, A. L. 2011a. Vibration Measurement on Reticular Lamina and Basilar Membrane at Multiple Longitudinal Locations. *AIP Conference Proceedings,* 1403**,** 389-390.

CHEN, F., ZHA, D., FRIDBERGER, A., ZHENG, J., CHOUDHURY, N., JACQUES, S. L., WANG, R. K., SHI, X. & NUTTALL, A. L. 2011b. A differentially amplified motion in the ear for near-threshold sound detection. *Nat Neurosci,* 14**,** 770-774.

CHEN, S., FATEMI, M. & GREENLEAF, J. F. 2004. Quantifying elasticity and viscosity from measurement of shear wave speed dispersion. *The Journal of the Acoustical Society of America,* 115**,** 2781.

CHOUDHURY, N., CHEN, F., FRIDBERGER, A., ZHA, D., JACQUES, S. L., WANG, R. K. & NUTTALL, A. L. 2011. Imaging Organ of Corti Vibration Using Fourier-Domain OCT. *AIP Conference Proceedings,* 1403**,** 391-395.

CHOUDHURY, N., SONG, G., CHEN, F., MATTHEWS, S., TSCHINKEL, T., ZHENG, J., JACQUES, S. L. & NUTTALL, A. L. 2006. Low coherence interferometry of the cochlear partition. *Hearing Research,* 220**,** 1-9.

CODY, D. T. R. & BICKFORD, R. G. 1969. Averaged evoked myogenic responses in normal man. *The Laryngoscope,* 79**,** 400-416.

COHEN-SALMON, M., EL-AMRAOUI, A., LEIBOVICI, M. & PETIT, C. 1997. Otogelin: A glycoprotein specific to the acellular membranes of the inner ear. *Proceedings of the National Academy of Sciences,* 94**,** 14450-14455.

COLEBATCH, J. G., HALMAGYI, G. M. & SKUSE, N. F. 1994. Myogenic potentials generated by a click-evoked vestibulocollic reflex. *Journal of Neurology, Neurosurgery & Psychiatry,* 57**,** 190-197.

CRAWFORD, A. C., EVANS, M. G. & FETTIPLACE, R. 1991. The actions of calcium on the mechano-electrical transducer current of turtle hair cells. *The Journal of Physiology,* 434**,** 369-398.

CRAWFORD, A. C. & FETTIPLACE, R. 1981. An electrical tuning mechanism in turtle cochlear hair cells. *The Journal of Physiology,* 312**,** 377-412.

DALLOS, P. 1992. The active cochlea. *The Journal of Neuroscience,* 12**,** 4575-4585.

DALLOS, P., BILLONE, N. C., DURRANT, J. D., WANG, C. Y. & RAYNOR, S. 1972. Cochlear Inner and Outer Hair Cells: Functional Differences. *Science,* 177**,** 356-358.

DAVIS, H. 1958. A mechano-electrical theory of cochlear action. *Trans Am Otol Soc.,* 46**,** 180-96.

DAVIS, H. 1965. A Model for Transducer Action in the Cochlea. *Cold Spring Harbor Symposia on Quantitative Biology,* 30**,** 181-190.

DAVIS, H. 1983. An active process in cochlear mechanics. *Hearing Research,* 9**,** 79-90.

DAVIS, M. 1974. Sensitization of the rat startle response by noise. *Journal of Comparative and Physiological Psychology,* 87**,** 571-581.

DAVIS, M., FALLS, W. A., CAMPEAU, S. & KIM, M. 1993. Fear-potentiated startle: A neural and pharmacological analysis. *Behavioural Brain Research,* 58**,** 175-198.

DAVIS, M., WALKER, D. L. & LEE, Y. 1997. Roles of the Amygdala and Bed Nucleus of the Stria Terminalis in Fear and Anxiety Measured with the Acoustic Startle Reflex. *Annals of the New York Academy of Sciences,* 821**,** 305-331.

DAVIS, R. L. 2003. Gradients of Neurotrophins, Ion Channels, and Tuning in the Cochlea. *The Neuroscientist,* 9**,** 311-316.

DIDIER, A. & CAZALS, Y. 1989. Acoustic responses recorded from the saccular bundle on the eighth nerve of the guinea pig. *Hearing Research,* 37**,** 123-127.

EATOCK, R. A. & SONGER, J. E. 2011. Vestibular Hair Cells and Afferents: Two Channels for Head Motion Signals. *Annual Review of Neuroscience,* 34**,** 501-534.

EGOROVA, M., EHRET, G., VARTANIAN, I. & ESSER, K.-H. 2001. Frequency response areas of neurons in the mouse inferior colliculus. I. Threshold and tuning characteristics. *Experimental Brain Research,* 140**,** 145-161.

ELLIOTT, S. J. 24.08.2011 2011. *RE: Personal Communication.*

EVANS, B. N. & DALLOS, P. 1993. Stereocilia displacement induced somatic motility of cochlear outer hair cells. *Proceedings of the National Academy of Sciences,* 90**,** 8347-8351.

FERBER-VIART, C., DUBREUIL, C. & DU, R. 1999. Vestibular Evoked Myogenic Potentials in Humans: a Review. *Acta Oto-laryngologica,* 119**,** 6-15.

FERNANDEZ, C. & GOLDBERG, J. M. 1976a. Physiology of peripheral neurons innervating otolith organs of the squirrel monkey. I. Response to static tilts and to long-duration centrifugal force. *Journal of Neurophysiology,* 39**,** 970-984.

FERNANDEZ, C. & GOLDBERG, J. M. 1976b. Physiology of peripheral neurons innervating otolith organs of the squirrel monkey. II. Directional selectivity and force-response relations. *Journal of Neurophysiology,* 39**,** 985-995.

FERNANDEZ, C. & GOLDBERG, J. M. 1976c. Physiology of peripheral neurons innervating otolith organs of the squirrel monkey. III. Response dynamics. *Journal of Neurophysiology,* 39**,** 996-1008.

FETTIPLACE, R. & HACKNEY, C. M. 2006. The sensory and motor roles of auditory hair cells. *Nature Reviews Neuroscience,* 7**,** 19-29.

FETTIPLACE, R. & RICCI, A. J. 2003. Adaptation in auditory hair cells. *Current Opinion in Neurobiology,* 13**,** 446-451.

FLOCK, Å. 1965. Transducing Mechanisms in the Lateral Line Canal Organ Receptors. *Cold Spring Harbor Symposia on Quantitative Biology,* 30**,** 133-145.

FLOCK, A. & CHEUNG, H. C. 1977. Actin filaments in sensory hairs of inner ear receptor cells. *The Journal of Cell Biology,* 75**,** 339-343.

FREEMAN, D. M., ABNET, C. C., HEMMERT, W., TSAI, B. S. & WEISS, T. F. 2003a. Dynamic material properties of the tectorial membrane: a summary. *Hearing Research,* 180**,** 1-10.

FREEMAN, D. M., MASAKI, K., MCALLISTER, A. R., WEI, J. L. & WEISS, T. F. 2003b. Static material properties of the tectorial membrane: a summary. *Hearing Research,* 180**,** 11-27.

FREEMAN, D. M. & WEISS, T. F. 1990a. Hydrodynamic forces on hair bundles at high frequencies. *Hearing Research,* 48**,** 31-36.

FREEMAN, D. M. & WEISS, T. F. 1990b. Hydrodynamic forces on hair bundles at low frequencies. *Hearing Research,* 48**,** 17-30.

FREEMAN, D. M. & WEISS, T. F. 1990c. Superposition of hydrodynamic forces on a hair bundle. *Hearing Research,* 48**,** 1-15.

GAVARA, N. & CHADWICK, R. S. 2009. Collagen-Based Mechanical Anisotropy of the Tectorial Membrane: Implications for Inter-Row Coupling of Outer Hair Cell Bundles. *PLoS ONE,* 4**,** e4877.

GAVARA, N., MANOUSSAKI, D. & CHADWICK, R. S. 2011. Auditory mechanics of the tectorial membrane and the cochlear spiral. *Current Opinion in Otolaryngology & Head and Neck Surgery,* 19.

GEISLER, C. D. 1998. *From Sound to Synapse*, OUP USA.

GHAFFARI, R. 2008. *The Functional Role of the Mammalian Tectorial Membrane in Cochlear Mechanics.* phD, Massachusetts Institute of Technology.

GHAFFARI, R., ARANYOSI, A. J. & FREEMAN, D. M. 2007. Longitudinally propagating traveling waves of the mammalian tectorial membrane. *Proceedings of the National Academy of Sciences,* 104**,** 16510-16515.

GHAFFARI, R., ARANYOSI, A. J., RICHARDSON, G. P. & FREEMAN, D. M. 2010. Tectorial membrane travelling waves underlie abnormal hearing in Tectb mutant mice. *Nature Communications,* 1.

GLUECKERT, R., WIETZORREK, G., KAMMEN-JOLLY, K., SCHOLTZ, A., STEPHAN, K., STRIESSNIG, J. & SCHROTT-FISCHER, A. 2003. Role of class D L-type Ca2+ channels for cochlear morphology. *Hearing Research,* 178**,** 95-105.

GOLD, T. 1948. Hearing. II. The Physical Basis of the Action of the Cochlea. *Proceedings of the Royal Society of London. Series B, Biological Sciences,* 135**,** 492-498.

GOODYEAR, R. J., MARCOTTI, W., KROS, C. J. & RICHARDSON, G. P. 2005. Development and properties of stereociliary link types in hair cells of the mouse cochlea. *The Journal of Comparative Neurology,* 485**,** 75-85.

GOODYEAR, R. J. & RICHARDSON, G. P. 2002. Extracellular matrices associated with the apical surfaces of sensory epithelia in the inner ear: Molecular and structural diversity. *Journal of Neurobiology,* 53**,** 212-227.

GOVAERTS, P. J., CEULAER, G. D., DAEMERS, K., VERHOEVEN, K., CAMP, G. V., SCHATTEMAN, I., VERSTREKEN, M., WILLEMS, P. J., SOMERS, T. & OFFECIERS, F. E. 1998. A New Autosomal-Dominant Locus (DFNA 12) Is Responsible for a Nonsyndromic, Midfrequency, Prelingual and Nonprogressive Sensorineural Hearing Loss. *Otology & Neurotology,* 19.

GROSH, K., ZHENG, J., ZOU, Y., DE BOER, E. & NUTTALL, A. L. 2004. High-frequency electromotile responses in the cochlea. *The Journal of the Acoustical Society of America,* 115**,** 2178-2184.

GU, J. W., HEMMERT, W., FREEMAN, D. M. & ARANYOSI, A. J. 2008. Frequency-Dependent Shear Impedance of the Tectorial Membrane. *Biophysical Journal,* 95**,** 2529-2538.

GUEST, M., BOGGESS, M., D'ESTE, C., ATTIA, J. & BROWN, A. 2011. An Observed Relationship Between Vestibular Function and Auditory Thresholds in Aircraft-Maintenance Workers. *Journal of Occupational and Environmental Medicine,* 53.

GUETA, R., BARLAM, D., SHNECK, R. Z. & ROUSSO, I. 2006. Measurement of the mechanical properties of isolated tectorial membrane using atomic force microscopy. *Proceedings of the National Academy of Sciences,* 103**,** 14790-14795.

GUETA, R., LEVITT, J., XIA, A., KATZ, O., OGHALAI, JOHN S. & ROUSSO, I. 2011. Structural and Mechanical Analysis of Tectorial Membrane Tecta Mutants. *Biophysical Journal,* 100**,** 2530-2538.

GUETA, R., TAL, E., SILBERBERG, Y. & ROUSSO, I. 2007. The 3D structure of the tectorial membrane determined by second-harmonic imaging microscopy. *Journal of Structural Biology,* 159**,** 103-110.

GUMMER, A. W., HEMMERT, W. & ZENNER, H. P. 1996. Resonant tectorial membrane motion in the inner ear: its crucial role in frequency tuning. *Proceedings of the National Academy of Sciences,* 93**,** 8727-8732.

HE, D. Z. Z., JIA, S. & DALLOS, P. 2004. Mechanoelectrical transduction of adult outer hair cells studied in a gerbil hemicochlea. *Nature,* 429**,** 766-770.

HEMMERT, W., ZENNER, H.-P. & GUMMER, A. W. 2000. Three-Dimensional Motion of the Organ of Corti. *Biophysical Journal,* 78**,** 2285-2297.

HIGHSTEIN, S. M. & HOLSTEIN, G. R. 2006. The Anatomy of the vestibular nuclei. *In:* BÜTTNER-ENNEVER, J. A. (ed.) *Progress in Brain Research.* Elsevier.

HOFFMAN, H. S. & FLESHLER, M. 1963. Startle Reaction: Modification by Background Acoustic Stimulation. *Science,* 141**,** 928-930.

HOFFMAN, H. S. & ISON, J. R. 1980. Reflex Modification in the Domain of Startle I. Some Empirical Findings and Their Implications for How the Nervous System Processes Sensory Input. *Psychological Review,* 87(2)**,** 175-189.

HOLY, T. E. & GUO, Z. 2005. Ultrasonic Songs of Male Mice. *PLoS Biol,* 3**,** e386.

HUDSPETH, A. J. & JACOBS, R. 1979. Stereocilia mediate transduction in vertebrate hair cells (auditory system/cilium/vestibular system). *Proceedings of the National Academy of Sciences,* 76**,** 1506-1509.

ISON, J. R. & HOFFMAN, H. S. 1983. Reflex modification in the domain of startle: II. The anomalous history of a robust and ubiquitous phenomenon. *Psychological Bulletin,* 94**,** 3-17.

ISON, J. R. & RUSSO, J. M. 1990. Enhancement and depression of tactile and acoustic startle reflexes with variation in background noise level. *Psychobiology,* 18**,** 96-100.

JOHNSON, STUART L., BEURG, M., MARCOTTI, W. & FETTIPLACE, R. 2011. Prestin-Driven Cochlear Amplification Is Not Limited by the Outer Hair Cell Membrane Time Constant. *Neuron,* 70**,** 1143-1154.

JOHNSTONE, J. R. & JOHNSTONE, B. M. 1966. Origin of Summating Potential. *The Journal of the Acoustical Society of America,* 40**,** 1405-1413.

JONES, G., RUSSELL, I. & LUKASHKIN, A. 2011. Laser Interferometer Measurements of the Viscoelastic Properties of Tectorial Membrane Mutants. *AIP Conference Proceedings,* 1403**,** 419-420.

JONES, G. P., LUKASHKINA, V. A., RUSSELL, I. J. & LUKASHKIN, A. N. 2010. The Vestibular System Mediates Sensation of Low-Frequency Sounds in Mice. *Journal of the Association for Research in Otolaryngology,* 11**,** 725-732-732.

KANDEL, E. R., SCHWARTZ, J. H. & JESSELL, T. M. 2000. *Principles of Neural Science*, McGraw-Hill Medical.

KAZMIERCZAK, P., SAKAGUCHI, H., TOKITA, J., WILSON-KUBALEK, E. M., MILLIGAN, R. A., MULLER, U. & KACHAR, B. 2007. Cadherin 23 and protocadherin 15 interact to form tip-link filaments in sensory hair cells. *Nature,* 449**,** 87-91.

KEMP, D. T. 1978. *Stimulated acoustic emissions from within the human auditory system*, ASA.

KEMP, D. T. & CHUM, R. 1980. Properties of the generator of stimulated acoustic emissions. *Hearing Research,* 2**,** 213-232.

KENNEDY, H. J., CRAWFORD, A. C. & FETTIPLACE, R. 2005. Force generation by mammalian hair bundles supports a role in cochlear amplification. *Nature,* 433**,** 880-883.

KENNEDY, H. J., EVANS, M. G., CRAWFORD, A. C. & FETTIPLACE, R. 2006. Depolarization of Cochlear Outer Hair Cells Evokes Active Hair Bundle Motion by Two Mechanisms. *The Journal of Neuroscience,* 26**,** 2757-2766.

KIMURA, R. S. 1966. Hairs of the Cochlear Sensory Cells and Their Attachment to the Tectorial Membrane. *Acta Oto-laryngologica,* 61**,** 55-72.

KJELLEN, L. & LINDAHL, U. 1991. Proteoglycans: Structures and Interactions. *Annual Review of Biochemistry,* 60**,** 443-475.

KOCH, M. 1999. The neurobiology of startle. *Progress in Neurobiology,* 59**,** 107-128.

KÖSSL, M. & RUSSELL, I. J. 1992. The phase and magnitude of hair cell receptor potentials and frequency tuning in the guinea pig cochlea. *The Journal of Neuroscience,* 12**,** 1575-1586.

KRONESTER-FREI, A. 1978. Ultrastructure of the different zones of the tectorial membrane. *Cell and Tissue Research,* 193**,** 11-23.

KROS, C. J. 1996. *Physiology of Mammalian Cochlear Hair Cells*, Springer-Verlag.

KROS, C. J., RUSCH, A. & RICHARDSON, G. P. 1992. Mechano-Electrical Transducer Currents in Hair Cells of the Cultured Neonatal Mouse Cochlea. *Proceedings of the Royal Society of London. Series B: Biological Sciences,* 249**,** 185-193.

LANE, H. & TRANEL, B. 1971. The Lombard Sign and the Role of Hearing in Speech. *Journal of Speech and Hearing Research,* 14**,** 677-709.

LANG, P. J., BRADLEY, M. M. & CUTHBERT, B. N. 1990. Emotion, Attention, and the Startle Reflex. *Psychological Review,* 97**,** 377-395.

LEGAN, P. K., LUKASHKINA, V. A., GOODYEAR, R. J., KÖSSL, M., RUSSELL, I. J. & RICHARDSON, G. P. 2000. A Targeted Deletion in [alpha]-Tectorin Reveals that the Tectorial Membrane Is Required for the Gain and Timing of Cochlear Feedback. *Neuron,* 28**,** 273-285.

LEGAN, P. K., LUKASHKINA, V. A., GOODYEAR, R. J., LUKASHKIN, A. N., VERHOEVEN, K., VAN CAMP, G., RUSSELL, I. J. & RICHARDSON, G. P. 2005. A deafness mutation isolates a second role for the tectorial membrane in hearing. *Nature Neuroscience,* 8**,** 1035-1042.

LEGAN, P. K., RAU, A., KEEN, J. N. & RICHARDSON, G. P. 1997. The Mouse Tectorins. *Journal of Biological Chemistry,* 272**,** 8791-8801.

LI, L., STEIDL, S. & YEOMANS, J. S. 2001. Contributions of the vestibular nucleus and vestibulospinal tract to the startle reflex. *Neuroscience,* 106**,** 811-821.

LI, L. & YEOMANS, J. S. 1999. Summation between acoustic and trigeminal stimuli evoking startle. *Neuroscience,* 90**,** 139-152.

LIM, D. J. 1972. Fine morphology of the tectorial membrane. Its relationship to the organ of Corti. *Arch Otolaryngol,* 96**,** 199-205.

LIM, D. J. 1980. *Cochlear anatomy related to cochlear micromechanics. A review*, ASA.

LIM, D. J. 1986. Functional structure of the organ of Corti: a review. *Hearing Research,* 22**,** 117-146.

LOWENSTEIN, O. & ROBERTS, T. D. M. 1951. The localization and analysis of the responses to vibration from the isolated elasmobranch labyrinth. A contribution to the problem of the evolution of hearing in vertebrates. *The Journal of Physiology,* 114**,** 471-489.

LUKASHKIN, A., LUKASHKINA, V., RICHARDSON, G. P. & RUSSELL, I. J. 2009. Does the cochlea compromise on sensitivity and frequency selectivity? *In:* COOPER, N. P. & KEMP, D. T. (eds.) *Concepts and Challenges in the Biophysics of Hearing.* World Scientific Publishing Company.

LUKASHKIN, A. N., BASHTANOV, M. E. & RUSSELL, I. J. 2005. A self-mixing laser-diode interferometer for measuring basilar membrane vibrations without opening the cochlea. *Journal of Neuroscience Methods,* 148**,** 122-129.

LUKASHKIN, A. N., LEGAN, P. K., LUKASHKINA, V. A., WEDDELL, T. D., GOODYEAR, R., WELSTEAD, L., PETIT, C., RUSSELL, I. J. & RICHARDSON, G. P. 2011. Otoancorin knockout mice reveal inertia is the force for hearing, unpublished data.

LUKASHKIN, A. N., RICHARDSON, G. P. & RUSSELL, I. J. 2010. Multiple roles for the tectorial membrane in the active cochlea. *Hearing Research,* 266**,** 26-35.

LUKASHKIN, A. N., WALLING, M. N. & RUSSELL, I. J. 2007. Power Amplification in the Mammalian Cochlea. *Current Biology,* 17**,** 1340-1344.

MAMMANO, F. & NOBILI, R. 1993. Biophysics of the cochlea: Linear approximation. *The Journal of the Acoustical Society of America,* 93**,** 3320-3332.

MARTIN, P., BOZOVIC, D., CHOE, Y. & HUDSPETH, A. J. 2003. Spontaneous Oscillation by Hair Bundles of the Bullfrog's Sacculus. *The Journal of Neuroscience,* 23**,** 4533-4548.

MASAKI, K., GHAFFARI, R., GU, J. W., RICHARDSON, G. P., FREEMAN, D. M. & ARANYOSI, A. J. 2010. Tectorial Membrane Material Properties in TectaY1870C/+ Heterozygous Mice. *Biophysical Journal,* 99**,** 3274-3281.

MASAKI, K., WEISS, T. F. & FREEMAN, D. M. 2006. Poroelastic Bulk Properties of the Tectorial Membrane Measured with Osmotic Stress. *Biophysical Journal,* 91**,** 2356-2370.

MCCUE, M. P. & GUINAN, J. J. 1994. Acoustically responsive fibers in the vestibular nerve of the cat. *The Journal of Neuroscience,* 14**,** 6058-6070.

MCCUE, M. P. & GUINAN, J. J. 1995. Spontaneous activity and frequency selectivity of acoustically responsive vestibular afferents in the cat. *Journal of Neurophysiology,* 74**,** 1563-1572.

MCGUIRT, W. T., PRASAD, S. D., GRIFFITH, A. J., KUNST, H. P. M., GREEN, G. E., SHPARGEL, K. B., RUNGE, C., HUYBRECHTS, C., MUELLER, R. F., LYNCH, E., KING, M.-C., BRUNNER, H. G., CREMERS, C. W. R. J., TAKANOSU, M., LI, S.-W., ARITA, M., MAYNE, R., PROCKOP, D. J., CAMP, G. V. & SMITH, R. J. H. 1999. Mutations in COL11A2 cause non-syndromic hearing loss (DFNA13). *Nat Genet,* 23**,** 413-419.

MEAUD, J. & GROSH, K. 2010. The effect of tectorial membrane and basilar membrane longitudinal coupling in cochlear mechanics. *The Journal of the Acoustical Society of America,* 127**,** 1411-1421.

MEAUD, J. & GROSH, K. 2011. Coupling Active Hair Bundle Mechanics, Fast Adaptation, and Somatic Motility in a Cochlear Model. *Biophysical Journal,* 100**,** 2576-2585.

MELLADO LAGARDE, M. M. 2008. *A Role for Prestin in Amplification, Otoacoustic Emissions, and Shaping Mechanical Tuning in the Cochlea.* DPhil, University of Sussex.

MELLADO LAGARDE, M. M., DREXL, M., LUKASHKIN, ANDREI N., ZUO, J. & RUSSELL, I. J. 2008. Prestin's Role in Cochlear Frequency Tuning and Transmission of Mechanical Responses to Neural Excitation. *Current Biology,* 18**,** 200-202.

MENSINGER, A. F., CAREY, J. P., BOYLE, R. & HIGHSTEIN, S. M. 1997. Differential central projections of physiologically characterized horizontal semicircular canal vestibular nerve afferents in the toadfish, Opsanus tau. *The Journal of Comparative Neurology,* 384**,** 71-85.

MEREDITH, G. E. & BUTLER, A. B. 1983. Organization of eighth nerve afferent projections from individual endorgans of the inner ear in the teleost, Astronotus ocellatus. *The Journal of Comparative Neurology,* 220**,** 44-62.

MIDDLEBROOKS, J. C. & GREEN, D. M. 1991. Sound Localization by Human Listeners. *Annual Review of Psychology,* 42**,** 135-159.

MOFFAT, A. J. M. & CAPRANICA, R. R. 1976. Auditory sensitivity of the saccule in the American toad (Bufo americanus). *Journal of Comparative Physiology A: Neuroethology, Sensory, Neural, and Behavioral Physiology,* 105**,** 1-8-8.

MOLLER, A. R. 1963. Transfer Function of the Middle Ear. *The Journal of the Acoustical Society of America,* 35**,** 1526-1534.

MORAVEC, W. J. & PETERSON, E. H. 2004. Differences Between Stereocilia Numbers on Type I and Type II Vestibular Hair Cells. *Journal of Neurophysiology,* 92**,** 3153-3160.

MOUNTAIN, D. C. & CODY, A. R. 1999. Multiple modes of inner hair cell stimulation. *Hearing Research,* 132**,** 1-14.

MÜLLER, M., HUNERBEIN, K., HOIDIS, S. & SMOLDERS, J. 2005. A physiological place frequency map of the cochlea in the CBA/J mouse. *Hearing Research,* 202**,** 63-73.

MUNYER, P. D. & SCHULTE, B. A. 1991. Immunohistochemical identification of proteoglycans in gelatinous membranes of cat and gerbil inner ear. *Hearing Research,* 52**,** 369-378.

MUROFUSHI, T., IWASAKI, S., TAKAI, Y. & TAKEGOSHI, H. 2005a. Sound-evoked neurogenic responses with short latency of vestibular origin. *Clinical Neurophysiology,* 116**,** 401-405.

MUROFUSHI, T., IWASAKI, S., TAKAI, Y. & TAKEGOSHI, H. 2005b. Sound-evoked neurogenic responses with short latency: are they of vestibular origin? *International Congress Series,* 1278**,** 433-436.

NEELY, S. T. & KIM, D. O. 1983. An active cochlear model showing sharp tuning and high sensitivity. *Hearing Research,* 9**,** 123-130.

NEELY, S. T. & KIM, D. O. 1986. A model for active elements in cochlear biomechanics. *The Journal of the Acoustical Society of America,* 79**,** 1472-1480.

NETTEN, S. M. V. & KROS, C. J. 2000. Gating energies and forces of the mammalian hair cell transducer channel and related hair bundle mechanics. *Proceedings of the Royal Society of London. Series B: Biological Sciences,* 267**,** 1915-1923.

NILSEN, K. E. & RUSSELL, I. J. 1999. Timing of cochlear feedback: spatial and temporal representation of a tone across the basilar membrane. *Nature Neuroscience,* 2**,** 642-648.

NILSSON, H. G. 1978. A comparison of models for sharpening of the frequency selectivity in the coachlea. *Biological Cybernetics,* 28**,** 177-181.

NOWOTNY, M. & GUMMER, A. W. 2006. Nanomechanics of the subtectorial space caused by electromechanics of cochlear outer hair cells. *Proceedings of the National Academy of Sciences of the United States of America,* 103**,** 2120-2125.

NOWOTNY, M. & GUMMER, A. W. 2011. Vibration responses of the organ of Corti and the tectorial membrane to electrical stimulation. *The Journal of the Acoustical Society of America,* 130**,** 3852-3872.

NYBY, J. 2001. Auditory communication among adults. *In:* WILLOTT, J. F. (ed.) *Handbook of Mouse Auditory Research: From Behavior to Molecular Biology.* CRC Press LLC.

OLSON, E. S. 1998. *Observing middle and inner ear mechanics with novel intracochlear pressure sensors*, ASA.

PAFFENHOLZ, R. 2004. Vestibular defects in head-tilt mice result from mutations in Nox3, encoding an NADPH oxidase. *Genes & Development,* 18**,** 486-491.

PARHAM, K. & WILLOTT, J. F. 1988. Acoustic startle response in young and aging C57BL6J and CBAJ Mice. *Behavioral Neuroscience,* 102(6)**,** 881-886.

PFISTER, M., THIELE, H., VAN CAMP, G., FRANSEN, E., APAYDIN, F., AYDIN, Ö., LEISTENSCHNEIDER, P., DEVOTO, M., ZENNER, H. P., BLIN, N., NÜRNBERG, P., OZKARAKAS, H. & KUPKA, S. 2004. A Genotype-Phenotype Correlation with Gender-Effect for Hearing Impairment Caused by TECTA Mutations. *Cellular Physiology and Biochemistry,* 14**,** 369-376.

PICKLES, J. O. 2008. *An Introduction to the Physiology of Hearing*, Academic Press.

PICKLES, J. O., COMIS, S. D. & OSBORNE, M. P. 1984. Cross-links between stereocilia in the guinea pig organ of Corti, and their possible relation to sensory transduction. *Hearing Research,* 15**,** 103-112.

PLANTINGA, R. F., BROUWER, A. P. M., HUYGEN, P. L. M., KUNST, H. P. M., KREMER, H. & CREMERS, C. W. R. J. 2006. A Novel TECTA Mutation in a Dutch DFNA8/12 Family Confirms Genotype–Phenotype Correlation. *Journal of the Association for Research in Otolaryngology,* 7**,** 173-181.

PLAPPERT, C. F. & PILZ, P. K. D. 2002. Difference in anxiety and sensitization of the acoustic startle response between the two inbred mouse strains BALB/cAN and DBA/2N. *Genes, Brain and Behavior,* 1**,** 178-186.

PLAPPERT, C. F., PILZ, P. K. D. & SCHNITZLER, H.-U. 1993. Acoustic Startle Response and Habituation in Freezing and Nonfreezing Rats. *Behavioral Neuroscience,* 107**,** 981-987.

POPPER, A. N. & FAY, R. R. 1973. *Sound detection and processing by teleost fishes: a critical review*, ASA.

POPPER, A. N., PLATT, C. & SAIDEL, W. M. 1982. Acoustic functions in the fish ear. *Trends in Neurosciences,* 5**,** 276-280.

PURVES, D., AUGUSTINE, G. J., FITZPATRICK, D., KATZ LAWRENCE, C., LAMANTIA, A.-S., MCNAMARA, J. O. & WILLIAMS, M. 2001. *Neuroscience*, Sinauer Associates Inc., U.S.

RAMACHANDRAN, V. & BLAKESLEE, S. 1998. *Phantoms in the Brain,* London, Fourth Estate.

RAPOPORT, S., SUSSWEIN, A., UCHINO, Y. & WILSON, V. J. 1977. Synaptic actions of individual vestibular neurones on cat neck motoneurones. *The Journal of Physiology,* 272**,** 367-382.

REN, T. 2002. Longitudinal pattern of basilar membrane vibration in the sensitive cochlea. *Proceedings of the National Academy of Sciences,* 99**,** 17101-17106.

REN, T. & HE, W. 2011. Measurement of Basilar Membrane, Reticular Lamina, and Tectorial Membrane Vibrations in the Intact Mouse Cochlea. *AIP Conference Proceedings,* 1403**,** 423-429.

REN, T., HE, W. & GILLESPIE, P. G. 2011a. Measurement of cochlear power gain in the sensitive gerbil ear. *Nat Commun,* 2**,** 216.

REN, T., HE, W. & PORSOV, E. 2011b. Localization of the Cochlear Amplifier in Living Sensitive Ears. *PLoS ONE,* 6**,** e20149.

REN, T. & NUTTALL, A. L. 2001. Basilar membrane vibration in the basal turn of the sensitive gerbil cochlea. *Hearing Research,* 151**,** 48-60.

RHODE, W. S. & GEISLER, C. D. 1967. Model of the Displacement between Opposing Points on the Tectorial Membrane and Reticular Lamina. 42**,** 185-190.

RICCI, A. J., CRAWFORD, A. C. & FETTIPLACE, R. 2000. Active Hair Bundle Motion Linked to Fast Transducer Adaptation in Auditory Hair Cells. *The Journal of Neuroscience,* 20**,** 7131-7142.

RICCI, A. J., CRAWFORD, A. C. & FETTIPLACE, R. 2003. Tonotopic Variation in the Conductance of the Hair Cell Mechanotransducer Channel. *Neuron,* 40**,** 983-990.

RICCI, A. J., RENNIE, K. J., COCHRAN, S. L., KEVETTER, G. A. & CORREIA, M. J. 1997. Vestibular type I and type II hair cells. 1: morphometric identification in the pigeon and gerbil. *Journal of Vestibular Research,* 7**,** 393-406.

RICHARDSON, G. P., DE MONVEL, J. B. & PETIT, C. 2011. How the Genetics of Deafness Illuminates Auditory Physiology. *Annual Review of Physiology,* 73**,** 311-334.

RICHARDSON, G. P., LUKASHKIN, A. N. & RUSSELL, I. J. 2008. The tectorial membrane: one slice of a complex cochlear sandwich. *Current Opinion in Otolaryngology & Head and Neck Surgery,* 16.

RICHARDSON, G. P., RUSSELL, I. J., DUANCE, V. C. & BAILEY, A. J. 1987. Polypeptide composition of the mammalian tectorial membrane. *Hearing Research,* 25**,** 45-60.

RICHTER, C.-P., EMADI, G., GETNICK, G., QUESNEL, A. & DALLOS, P. 2007. Tectorial Membrane Stiffness Gradients. *Biophysical Journal,* 93**,** 2265-2276.

ROBINSON, D. A. 1968. The oculomotor control system: A review. *Proceedings of the IEEE,* 56**,** 1032-1049.

ROBLES, L. & RUGGERO, M. A. 2001. Mechanics of the Mammalian Cochlea. *Physiological Reviews,* 81**,** 1305-1352.

RUGGERO, M. A. & RICH, N. C. 1991. Furosemide alters organ of corti mechanics: evidence for feedback of outer hair cells upon the basilar membrane. *The Journal of Neuroscience,* 11**,** 1057-1067.

RUSSELL, I. J., CODY, A. R. & RICHARDSON, G. P. 1986a. The responses of inner and outer hair cells in the basal turn of the guinea-pig cochlea and in the mouse cochlea grown in vitro. *Hearing Research,* 22**,** 199-216.

RUSSELL, I. J., KOSSL, M. & RICHARDSON, G. P. 1992. Nonlinear Mechanical Responses of Mouse Cochlear Hair Bundles. *Proceedings of the Royal Society of London. Series B: Biological Sciences,* 250**,** 217-227.

RUSSELL, I. J., LEGAN, P. K., LUKASHKINA, V. A., LUKASHKIN, A. N., GOODYEAR, R. J. & RICHARDSON, G. P. 2007. Sharpened cochlear tuning in a mouse with a genetically modified tectorial membrane. *Nature Neuroscience,* 10**,** 215-223.

RUSSELL, I. J. & NILSEN, K. E. 1997. The location of the cochlear amplifier: Spatial representation of a single tone on the guinea pig basilar membrane. *Proceedings of the National Academy of Sciences,* 94**,** 2660-2664.

RUSSELL, I. J. & RICHARDSON, G. P. 1987. The morphology and physiology of hair cells in organotypic cultures of the mouse cochlea. *Hearing Research,* 31**,** 9-24.

RUSSELL, I. J., RICHARDSON, G. P. & CODY, A. R. 1986b. Mechanosensitivity of mammalian auditory hair cells in vitro. *Nature,* 321**,** 517-519.

RUSSELL, I. J., RICHARDSON, G. P. & KÖSSL, M. 1989. The responses of cochlear hair cells to tonic displacements of the sensory hair bundle. *Hearing Research,* 43**,** 55-69.

RUSSELL, I. J. & SELLICK, P. M. 1978. Intracellular studies of hair cells in the mammalian cochlea. *The Journal of Physiology,* 284**,** 261-290.

RUSSELL, I. J. & SELLICK, P. M. 1983. Low-frequency characteristics of intracellularly recorded receptor potentials in guinea-pig cochlear hair cells. *The Journal of Physiology,* 338**,** 179-206.

SAKHNINI, L., DAIRI, M., AL-TAITOON, N. & EXCEL, M. 2006. Determining mechanical properties of rabbit skin with light reflection technique verified with latex. *Journal of Biomedical Optics,* 11**,** 014030.

SALT, A. N., THALMANN, R., MARCUS, D. C. & BOHNE, B. A. 1986. Direct measurement of longitudinal endolymph flow rate in the guinea pig cochlea. *Hearing Research,* 23**,** 141-151.

SAUNDERS, J. C. & JOHNSTONE, B. M. 1972. A Comparative Analysis of Middle-Ear Function in Non-Mammalian Vertebrates. *Acta Oto-laryngologica,* 73**,** 353-361.

SCHMID, A., KOCH, M. & SCHNITZLER, H. U. 1995. Conditioned Pleasure Attenuates the Startle Response in Rats. *Neurobiology of Learning and Memory,* 64**,** 1-3.

SHAH, D. M., FREEMAN, D. M. & WEISS, T. F. 1995. The osmotic response of the isolated, unfixed mouse tectorial membrane to isosmotic solutions: effect of Na+, K+, and Ca2+ concentration. *Hearing Research,* 87**,** 187-207.

SHEYKHOLESLAMI, K. & KAGA, K. 2002. The otolithic organ as a receptor of vestibular hearing revealed by vestibular-evoked myogenic potentials in patients with inner ear anomalies. *Hearing Research,* 165**,** 62-67.

SHOELSON, B., DIMITRIADIS, E. K., CAI, H., KACHAR, B. & CHADWICK, R. S. 2004. Evidence and Implications of Inhomogeneity in Tectorial Membrane Elasticity. *Biophysical Journal,* 87**,** 2768-2777.

SIMMLER, M.-C., COHEN-SALMON, M., EL-AMRAOUI, A., GUILLAUD, L., BENICHOU, J.-C., PETIT, C. & PANTHIER, J.-J. 2000a. Targeted disruption of Otog results in deafness and severe imbalance. *Nat Genet,* 24**,** 139-143.

SIMMLER, M.-C., ZWAENEPOEL, I., VERPY, E., GUILLAUD, L., ELBAZ, C., PETIT, C. & PANTHIER, J.-J. 2000b. Twister mutant mice are defective for otogelin, a component specific to inner ear acellular membranes. *Mammalian Genome,* 11**,** 961-966-966.

STEEL, K. P. 1983. The tectorial membrane of mammals. *Hearing Research,* 9**,** 327-359.

STEIN, B. M. & CARPENTER, M. B. 1967. Central projections of portions of the vestibular ganglia innervating specific parts of the labyrinth in the rhesus monkey. *American Journal of Anatomy,* 120**,** 281-317.

STERKERS, O., FERRARY, E. & AMIEL, C. 1988. Production of inner ear fluids. *Physiological Reviews,* 68**,** 1083-1128.

STRELIOFF, D. & FLOCK, Å. 1984. Stiffness of sensory-cell hair bundles in the isolated guinea pig cochlea. *Hearing Research,* 15**,** 19-28.

SUGIYAMA, S., SPICER, S. S., MUNYER, P. D. & SCHULTE, B. A. 1992. Ultrastructural localization and semiquantitative analysis of glycoconjugates in the tectorial membrane. *Hearing Research,* 58**,** 35-46.

TABERNER, A. M. & LIBERMAN, M. C. 2005. Response Properties of Single Auditory Nerve Fibers in the Mouse. *Journal of Neurophysiology,* 93**,** 557-569.

TANAKA, T. 1981. Gels. *Scientific American,* 244**,** 124-136.

TASAKI, I. & SPYROPOULOS, C. S. 1959. Stria Vascularis as Source of Endocochlear Potential. *Journal of Neurophysiology,* 22**,** 149-155.

THALMANN, I., MACHIKI, K., CALABRO, A., HASCALL, V. C. & THALMANN, R. 1993. Uronic Acid-Containing Glycosaminoglycans and Keratan Sulfate Are Present in the Tectorial Membrane of the Inner Ear: Functional Implications. *Archives of Biochemistry and Biophysics,* 307**,** 391-396.

THALMANN, I., THALLINGER, G., COMEGYS, T. H. & THALMANN, R. 1986. Collagen – The Predominant Protein of the Tectorial Membrane. *ORL,* 48**,** 107-115.

TILNEY, L. G., DEROSIER, D. J. & MULROY, M. J. 1980. The organization of actin filaments in the stereocilia of cochlear hair cells. *The Journal of Cell Biology,* 86**,** 244-259.

TODD, N. 2001. Evidence for a behavioral significance of saccular acoustic sensitivity in humans. *The Journal of the Acoustical Society of America,* 110**,** 380.

TODD, N. P. M. & CODY, F. W. 2000. Vestibular responses to loud dance music: A physiological basis of the "rock and roll threshold''? *The Journal of the Acoustical Society of America,* 107**,** 496-500.

TODD, N. P. M., CODY, F. W. J. & BANKS, J. R. 2000. A saccular origin of frequency tuning in myogenic vestibular evoked potentials?: implications for human responses to loud sounds. *Hearing Research,* 141**,** 180-188.

TODD, N. P. M., ROSENGREN, S. M. & COLEBATCH, J. G. 2008. Tuning and sensitivity of the human vestibular system to low-frequency vibration. *Neuroscience Letters,* 444**,** 36-41.

TODD, N. P. M. A., ROSENGREN, S. M. & COLEBATCH, J. G. 2003. A short latency vestibular evoked potential (VsEP) produced by bone-conducted acoustic stimulation. *Journal of the Acoustical Society of America,* 114**,** 3264-3272.

VATER, M. & KÖSSL, M. 2011. Comparative aspects of cochlear functional organization in mammals. *Hearing Research,* 273**,** 89-99.

VERHOEVEN, K., LAER, L. V., KIRSCHHOFER, K., LEGAN, P. K., HUGHES, D. C., SCHATTEMAN, I., VERSTREKEN, M., HAUWE, P. V., COUCKE, P., CHEN, A., SMITH, R. J. H., SOMERS, T., OFFECIERS, F. E., HEYNING, P. V. D., RICHARDSON, G. P., WACHTLER, F., KIMBERLING, W. J., WILLEMS, P. J., GOVAERTS, P. J. & CAMP, G. V. 1998. Mutations in the human [alpha]-tectorin gene cause autosomal dominant non-syndromic hearing impairment. *Nat Genet,* 19**,** 60-62.

VERPY, E., LEIBOVICI, M., MICHALSKI, N., GOODYEAR, R. J., HOUDON, C., WEIL, D., RICHARDSON, G. P. & PETIT, C. 2011. Stereocilin connects outer hair cell stereocilia to one another and to the tectorial membrane. *The Journal of Comparative Neurology,* 519**,** 194-210.

VOSS, S. E., ROSOWSKI, J. J. & PEAKE, W. T. 1996. *Is the pressure difference between the oval and round windows the effective acoustic stimulus for the cochlea?*, ASA.

WALKER, D. L. & DAVIS, M. 1997. Double Dissociation between the Involvement of the Bed Nucleus of the Stria Terminalis and the Central Nucleus of the Amygdala in Startle Increases Produced by Conditioned versus Unconditioned Fear. *The Journal of Neuroscience,* 17**,** 9375-9383.

WALSH, T., ABU RAYAN, A., ABU SA'ED, J., SHAHIN, H., SHEPSHELOVICH, J., LEE, M., HIRSCHBERG, K., TEKIN, M., SALHAB, W., AVRAHAM, K., KING, M. & KANAAN, M. 2006.

Genomic analysis of a heterogeneous Mendelian phenotype: multiple novel alleles for inherited hearing loss in the Palestinian population. *Human Genomics,* 2**,** 201-11.

WANG, S.-J. & YOUNG, Y.-H. 2003. Vestibular evoked myogenic potentials using simultaneous binaural acoustic stimulation. *Hearing Research,* 185**,** 43-48.

WATANUKI, K. & SCHUKNECHT, H. 1976. A morphological study of human vestibular sensory epithelia. *Arch Otolaryngol,* 102**,** 853-858.

WECKER, J. & ISON, J. 1986. Effects of motor activity on the elicitation and modification of the startle reflex in rats. *Learning & Behavior,* 14**,** 287-292-292.

WEDDELL, T. D., LEGAN, P. K., LUKASHKINA, V. A., GOODYEAR, R., WELSTEAD, L., PETIT, C., RUSSELL, I. J., LUKASHKIN, A. N. & RICHARDSON, G. P. Year. Otoancorin knockout mice reveal intertia is the force for hearing. *In:* SHERA, C. A. & OLSON, E. S., eds. 11th International Mechanicas of Hearing Workshop, 2011a Williamstown, Massachusetts. American Institute of Physics.

WEDDELL, T. D., MELLADO-LAGARDE, M., LUKASHKINA, V. A., LUKASHKIN, A. N., ZUO, J. & RUSSELL, I. J. 2011b. Prestin links extrinsic tuning to neural excitation in the mammalian cochlea. *Current biology : CB,* 21**,** R682-R683.

WEISS, T. F. & FREEMAN, D. M. 1997. Equilibrium behavior of an isotropic polyelectrolyte gel model of the tectorial membrane: effect of pH. *Hearing Research,* 111**,** 55-64.

WILLOTT, J. F. 2001. *Handbook of Mouse Auditory Research: From Behavior to Molecular Biology*, CRC Press.

WIT, H. P., BLEEKER, J. D. & MULDER, H. H. 1984. Responses of pigeon vestibular nerve fibers to sound and vibration with audiofrequencies. *The Journal of the Acoustical Society of America,* 75**,** 202-208.

XIA, A., GAO, S. S., YUAN, T., OSBORN, A., BRESS, A., PFISTER, M., MARICICH, S. M., PEREIRA, F. A. & OGHALAI, J. S. 2010. Deficient forward transduction and enhanced reverse transduction in the alpha tectorin C1509G human hearing loss mutation. *Disease Models and Mechanisms,* 3**,** 209-223.

YEOMANS, J. S., LI, L., SCOTT, B. W. & FRANKLAND, P. W. 2002. Tactile, acoustic and vestibular systems sum to elicit the startle reflex. *Neuroscience & Biobehavioral Reviews,* 26**,** 1-11.

YOUNG, E. D., FERNÁNDEZ, C. & GOLDBERG, J. M. 1977. Responses of Squirrel Monkey Vestibular Neurons to Audio-Frequency Sound and Head Vibration. *Acta Oto-laryngologica,* 84**,** 352-360.

YU, N. & ZHAO, H.-B. 2009. Modulation of Outer Hair Cell Electromotility by Cochlear Supporting Cells and Gap Junctions. *PLoS ONE,* 4**,** e7923.

ZHA, D., CHEN, F., FRIDERBERG, A., CHOUDHURY, N. & NUTTALL, A. 2011. Acoustically Evoked Different Vibration Pattern Across the Width of the Cochlea Partition. *AIP Conference Proceedings,* 1403**,** 434-437.

ZHENG, J., MILLER, K. K., YANG, T., HILDEBRAND, M. S., SHEARER, A. E., DELUCA, A. P., SCHEETZ, T. E., DRUMMOND, J., SCHERER, S. E., LEGAN, P. K., GOODYEAR, R. J., RICHARDSON, G. P., CHEATHAM, M. A., SMITH, R. J. & DALLOS, P. 2011. Carcinoembryonic antigen-related cell adhesion molecule 16 interacts with α-tectorin and is mutated in autosomal dominant hearing loss (DFNA4). *Proceedings of the National Academy of Sciences,* 108**,** 4218-4223.

ZHENG, J., SHEN, W., HE, D. Z., LONG, K. B., MADISON, L. D. & DALLOS, P. 2000. Prestin is the motor protein of cochlear outer hair cells. *Nature,* 405**,** 149-155.

ZUREK, P. M. 1981. *Spontaneous narrowband acoustic signals emitted by human ears*, ASA.

ZWAENEPOEL, I. 2002. Otoancorin, an inner ear protein restricted to the interface between the apical surface of sensory epithelia and their overlying acellular gels, is defective in autosomal recessive deafness DFNB22. *Proceedings of the National Academy of Sciences,* 99**,** 6240-6245.

ZWISLOCKI, J. J. 1986. Analysis of cochlear mechanics. *Hearing Research,* 22**,** 155-169.

ZWISLOCKI, J. J. & CEFARATTI, L. K. 1989. Tectorial membrane II: Stiffness measurements in vivo. *Hearing Research,* 42**,** 211-227.

ZWISLOCKI, J. J., CHAMBERLAIN, S. C. & SLEPECKY, N. B. 1988. Tectorial membrane I: Static mechanical properties in vivo. *Hearing Research,* 33**,** 207-222.

ZWISLOCKI, J. J. & KLETSKY, E. J. 1979. Tectorial membrane: a possible effect on frequency analysis in the cochlea. *Science,* 204**,** 639-641.

APPENDIX 1

The attached CD contains video recorded during the dissection of the mouse cochlea and shows the opening of the cochlea and removal of the tectorial membrane. Also included are higher resolution versions of the figures used in this thesis, including some in Scalable Vector Graphics (.svg) format.

Cochlear dissection

The included video files are in .mp4 format and are encoded with Xvid and for convenience a portable copy of the open-source video player, VLC media player (VideoLAN Organization), which is capable of displaying the video files is also included on the CD (run vlc.exe in the vlc-1.1.11 folder). The version of VLC media player is 1.1.11 (Windows 32-bit) downloaded from http://www.videolan.org/vlc/ and distributed in accordance with the GPL license (the source code is included also). If needed, alternative versions are available from http://www.videolan.org/vlc/#download (including for Mac and Linux).

Set up

The videos were recorded in 1080p HD and at 30 fps using a Contour HD camera (Contour Inc.) mounted on a stereoscopic microscope (Leica Microsystems). The camera was connected to a C-mount on the microscope using a specially shaped falcon tube lid, rubber washers, microscope eyepiece and insulation tape (see accompanying picture).

The rubber washer ensured the lens of the camera was the correct distance from the microscope eyepiece. The same eyepieces were used for the camera and microscope head to make sure the focus and picture were consistent.

Dissection

The three video files are from the same dissection of a *Tectb*$^{-/-}$ cochlea. The dissection is rough and the resulting TM segments were not used in any experiments. The videos are unedited and are presented in real time.

File	Notes (time in minutes)
FILE0025_xvid.mp4 (*Tectb*$^{-/-}$)	**00:00** Isolated inner ear in petri dish **02:34** Cochlea clearly visible **03:05** Stapes removed **05:36** Exposed organ of Corti **06:12** Tungsten probe used to remove TM **11:50** Isolated TM
FILE0026_xvid.mp4 (*Tectb*$^{-/-}$)	**0:00** Continues from FILE0025 and shows isolated TM under varying light and focal conditions. **03:14** TM cut in to segments with a scalpel (somewhat shorter than those used in the experiments)
FILE0027_xvid.mp4 (*Tectb*$^{-/-}$)	**00:00** Continues from FILE0026 after a break and shows the TM segments under varying light and focal conditions.

Additional figures

Higher resolution figures are included on the CD in \Additional figures in .png format. All the figures in this thesis were created using Inkscape 0.48 (http://inkscape.org/), an open-source vector image editor that uses the Scalable Vector Graphics format (Windows 32-bit version included, downloaded from http://inkscape.org/download/ and distributed in accordance with the GNU General Public License Version 2). Some figures include .svg versions that can be used to easily modify the figures and may be used for any purpose, with acknowledgment. Also included is an incredibly useful Matlab script by Juerg Schwizer that allows for the export of Matlab figures to .svg format (included with permission and in accordance with the BSD license). The most up to date version of this script is also available online at http://www.mathworks.com/matlabcentral/fileexchange/7401.